Stony Brook University

Cryo Soft X-ray Diffraction Microscopy with Biological Specimens

A Dissertation Presented

by

Xiaojing Huang

to

The Graduate School

in Partial Fulfillment of the Requirements

for the Degree of

Doctor of Philosophy

in

Physics

Stony Brook University

December 2009

Stony Brook University

The Graduate School

Xiaojing Huang

We, the dissertation committee for the above candidate for the Doctor of Philosophy degree, hereby recommend acceptance of this dissertation.

Chris Jacobsen – Dissertation Advisor
Professor, Department of Physics and Astronomy

Jacobus Verbaarschot – Chairperson of Defense
Professor, Department of Physics and Astronomy

Vladimir J. Goldman
Professor, Department of Physics and Astronomy

Qun Shen
Senior Scientist, Brookhaven National Laboratory

This dissertation is accepted by the Graduate School.

Lawrence Martin
Dean of the Graduate School

Abstract of the Dissertation

Cryo Soft X-ray Diffraction Microscopy with Biological Specimens

by

Xiaojing Huang

Doctor of Philosophy

in

Physics

Stony Brook University

2009

X-ray diffraction microscopy (XDM) is a lensless imaging technique well suited to studying thick biological samples at high resolution. Because x-rays have relatively short wavelengths, x-ray microscopes have the potential to achieve higher resolution than visible light microscopes. X-rays have high penetration ability, which enables x-ray microscopes to image samples that are too thick for electron microscopes. X-ray photons can be considered to interact with objects only once in most cases, which simplifies the data analysis process. Furthermore, by dispensing with the resolution and efficiency limitations imposed by x-ray optics, XDM can provide images with a resolution only confined by the maximum diffraction angle that can be collected and the sample's radiation tolerance.

We demonstrated through numerical simulations that XDM has the capability to deliver equivalent resolution images using fewer photons, compared with conventional x-ray microscopy. This is an important advantage for studying radiation-sensitive biological and soft matter specimens.

We applied XDM on a chemically dried yeast cell with 750 eV x-rays, and obtained images at 10 different rotation angles. They provided partial 3D structure information of the complex object. However, radiation damage imposed on the specimen prevented the taking of more data as required for a full 3D reconstruction.

We obtained the first image of an intact, frozen hydrated eukaryotic yeast cell using soft x-ray diffraction microscopy. Frozen hydrated samples are interesting because they are close to the cell's natural, hydrated state without dehydration artifacts, and they are radiation hard. By plunge-freezing the specimen into liquid ethane and maintaining it below -170°C, artifacts due to dehydration, ice crystallization, and radiation damage are greatly reduced. In this example, coherent diffraction data using 520 eV x-rays were recorded and reconstructed to reveal a budding yeast cell at a resolution better than 25 nm. This demonstration represents an important step towards high resolution imaging of cells in their natural, hydrated state.

To my wife Lin, my parents and my brother.

Contents

List of Figures

List of Tables

Acknowledgements

"A word is dead / When it is said, / Some say. / I say it just / Begins to live / That day." – Emily Dickinson

It is a long and exciting journey that brings me to this dissertation. I am grateful to a long list of people for helping and supporting me to accomplish my goals and dreams. This is my attempt to thank everyone who boosts me on my way.

My first heartfelt "thank you" goes out to my advisor, Prof. Chris Jacobsen. It is a great honor and pleasure to work with him. When I need to be inspired, advised, guided or encouraged, he is always there with kindness and patience, even though his schedule is already over-occupied. I'm deeply impressed by his passion for work, and I wish that I can carry on the flame into the future. There is a scene marked in my memory that Chris headed to his office directly from an overnight flight and discussed with me about the running project. Besides his intelligence and talents, I guess his red eyes and impressive coffee consuming amount also partially explain why he is able to manage all his duties.

I'd like to thank Prof. Janos Kirz for his generous and brilliant advices. Janos is a master of explaining complex problems with simple words. I always feel refreshed after talking with him. It was fantastic to have Janos at the beamline. When we were stuck, he always had the capability to ignite us by a magic touch or a unique suggestion.

I started working on frozen hydrated cells with Enju Lima and Huijie Miao. They taught me how to "cook" yeasts using liquid nitrogen. I also bugged them a lot with silly questions in my early days working at the beamline. I enjoyed myself very much by working with Andrew Stewart, Johanna Nelson, Jan

Steinbrener and Joshua Turner, who gradually joined the diffraction project. Besides the endless beam shifts, it is an unforgettable adventure to explore new restaurants around Berkeley area with them. It is also indelible to have the mini but special celebration for Johanna's and my birthdays at the no-food-drink-allowed beamline. Johanna and Jan shared the D-123 office with me for most of the time. Thanks a lot for all the sparkling conversations and mutual help. I'll miss the foosball games in D-123 too, although I'm still not good at it.

In this great group, I also benefited from the stimulating discussions with the past and current group members: Holger Fleckenstain, Lisseth Gavilan, Marc Häming, Christian Holzner, Benjamin Hornberger, Bjorg Larson, Mirna Lerotić, Ming Lu, Rachel Mak, Simon Moser and Robert Towers. Thank Rachel for carefully proofreading part of my thesis. I want to thank Sue Wirich, who is so nice and helpful. She always gave me warm welcome at the NSLS beamline X1A, and helped me intensively on taking STXM images.

The experiments at ALS were aided a lot by David Shapiro and Stefano Marchesini. I also enjoyed the enlightening discussions with them. Tony Warwich, Richard Celestre and George Meigs at ALS helped me to design the ACD and make sure it works properly. Thank Kenneth Downing and Eva Nogales at Berkeley for their helps on freezing cells.

I want to thank my closest friends, Ying Xu and Zhenhua Yu, for sharing their inspiring thoughts, long-term physical and mental supports. I'd like to thank Lei Zhu and Xiaowan Huang, who helped me settle down at Stony Brook from the first day when I arrived at US. Thank them for all the free rides, happy weekend diners, funny talks, and countless helps in my daily life. My friends at Stony Brook Physics Department make my study very delightful: Yu-tin Huang, Tao Sun, Feng Guo, Sung Tae Cho, Mark Stanford, Shu Lin, Wei Zhou, Xiao Shen, Yan Zhang, Ping Lin, Trung Le... I cannot possibly name all of them here, but thank you all very much.

Walter Schmeling, Mark Jablonski and Jeffrey Slechta at the Physics machine shop helped me a lot on fabricating components of the ACD and the liquid nitrogen filling system. Chuck Pancake at the Physics electronics shop designed and built the valve controller box for the refilling system. Pete Davis

taught me many tricks on working with liquid nitrogen.

The XDM biological imaging project was supported by the National Institute for General Medical Services at the National Institutes for Health under contract 5R21EB6134. The instrumentation development was supported by the Division of Materials Sciences and Engineering, Office of Basic Energy Sciences, at the Department of Energy under contract DE-FG02-07ER46128. All the diffraction experiments were performed at the Advanced Light Source, which is supported by the Director, Office of Science, Office of Basic Energy Sciences, of the U.S. Department of Energy under Contract No. DE-AC02-05CH11231.

I thank my parents and brother back in China, for their continuous support and encourage through my life. Their ardent expectation on me and their pride on every step that I have accomplished become the powerful motivations to drive me moving forward.

Finally, I'd like to thank my wife, Lin. Thank you so much for the love and the care, for the laughter that you bring into my life, for exploring new recipes and all the delicious dishes, for all the efforts to make our living space comfortable, for every moment that we spend together... Thank you for being with me.

Chapter 1

Microscopy with x-rays

X-ray microscopy has been used for high resolution imaging, because of its unique characteristics of short wavelength and deep penetration ability. This chapter describes x-ray interactions with matter, the production of coherent x-rays from synchrotron light sources, and the advantages and challenges of x-ray microscopies.

1.1 X-ray spectral region

The x-ray region is located between the ultraviolet and gamma ray regions in the electromagnetic spectrum. As shown in Fig. 1.1, "soft" x-rays commonly mean x-rays from an energy about 100 eV to several keV, with typical attenuation lengths of a few microns for low-Z elements which make up the main part of the mass of biological specimens. The "hard" x-rays are commonly from several keV to about 100 keV with attenuation lengths up to millimeters. Soft x-rays with energies lower than 1 keV are considered in this thesis work.

The x-ray photon energy E and wavelength λ are related by

$$E = h\nu = h\frac{c}{\lambda}, \tag{1.1}$$

where h is the Planck's constant 6.626×10^{-34} J·sec or 4.136×10^{-15} eV·sec, ν is the wave frequency, and c is the speed of light in vacuum 3.0×10^{8} m/sec. X-ray wavelengths vary from 10^{-2} nm to about 10 nm.

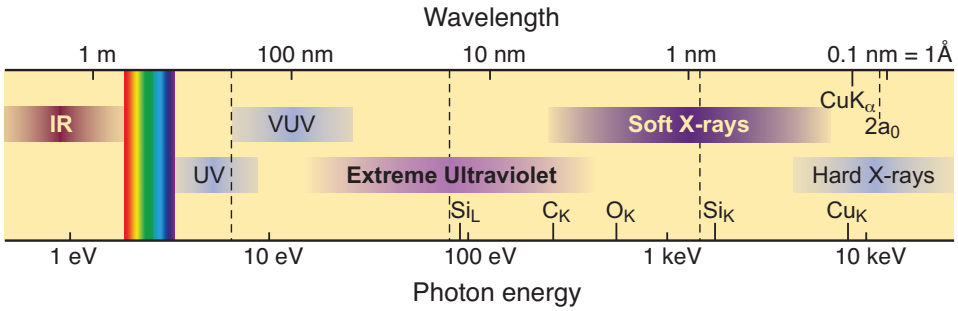

Figure 1.1: A portion of the electromagnetic spectrum extending from the infrared to the x-ray region [1].

The high penetration ability of x-rays has attracted scientific attention since they were discovered, as they can interact with internal structures rather than the surface features. Moreover, because they have relatively short wavelengths, x-rays can be used to distinguish small structures as in microscopy. The first ever Nobel Prize in Physics was awarded to W. Röntgen in 1901 for the discovery of these remarkable rays with exceptional importance.

1.2 X-ray refractive index

1.2.1 Propagation in vacuum

The propagation of all electromagnetic waves, including x-rays, is described by Maxwell's equations [2, 3]:

$$\nabla \times \boldsymbol{H} = \frac{\partial \boldsymbol{D}}{\partial t} + \boldsymbol{J} \qquad \text{Ampere's law,} \tag{1.2}$$

$$\nabla \times \boldsymbol{E} = -\frac{\partial \boldsymbol{B}}{\partial t} \qquad \text{Faraday's law,} \tag{1.3}$$

$$\nabla \cdot \boldsymbol{B} = 0, \tag{1.4}$$

$$\nabla \cdot \boldsymbol{D} = \rho \qquad \text{Coulomb's law,} \tag{1.5}$$

where $\boldsymbol{H}$ is the magnetic field vector, $\boldsymbol{D}$ is the electric displacement, $\boldsymbol{J}$ is the current density, $\boldsymbol{E}$ is the electric field vector, $\boldsymbol{B}$ is the magnetic density, and ρ is the charge density.

Considering the waves in vacuum, the constitutive relations take the form

$$\boldsymbol{D} = \epsilon_0 \boldsymbol{E}, \tag{1.6}$$

$$\boldsymbol{B} = \mu_0 \boldsymbol{H}, \tag{1.7}$$

where ϵ_0 is the permittivity (dielectric constant), and μ_0 is the magnetic permeability in vacuum.

Electromagnetic waves are solutions to Maxwell's equations. The vector wave equation can be obtained from Eqs. 1.2–1.7 as

$$\left(\frac{\partial^2}{\partial t^2} - c^2\nabla^2\right)\boldsymbol{E}(\boldsymbol{r},t) = -\frac{1}{\epsilon_0}\left[\frac{\partial \boldsymbol{J}(\boldsymbol{r},t)}{\partial t} + c^2\nabla\rho(\boldsymbol{r},t)\right], \tag{1.8}$$

where $c = 1/\sqrt{\epsilon_0\mu_0}$ is identified as the velocity of an electromagnetic wave in vacuum.

1.2.2 Interaction with bound electrons

X-ray propagation in a medium can be explained on the basis of interaction with bound electrons.

In the semi-classical model, an atom can be represented as a massive, positively charged $(+Ne)$ nucleus surrounded by N low mass, negatively charged electrons bound at discrete energies. When an external electromagnetic wave (for instance, an incident x-ray wave) passes through this atom as shown in Fig. 1.2, the bound electrons will oscillate, driven by the imposed electromagnetic field in the presence of the nuclear restoring force. An electron's response to the external electromagnetic field depends on both the electron's resonant frequency ω_s and the frequency of external wave ω.

The equation of motion of the bound electrons with oscillation mode ω_s can be written following Newton's second law of motion as

$$m_e \frac{d^2 \boldsymbol{x}_s}{dt^2} + m_e \gamma_{ds} \frac{d\boldsymbol{x}_s}{dt} + m_e \omega_s^2 \boldsymbol{x}_s = -e(\boldsymbol{E_i} + \boldsymbol{v}_s \times \boldsymbol{B_i}), \tag{1.9}$$

where m_e is the mass of electron, $\boldsymbol{x}_s$ is the displacement, and γ_{ds} is the damping ratio. The first term in Eq. 1.9 is the acceleration contribution, the second term is the dissipative force term which accounts for energy loss, and the third term is caused by the restoring force for an oscillator of resonant frequency ω_s. The term on the right side is the Lorentz force imposed by the external field.

As the oscillation is driven by the incident electromagnetic field, the displacement $\boldsymbol{x}_s$, velocity $\boldsymbol{v}_s = \partial \boldsymbol{x}_s / \partial t$, and acceleration $\partial^2 \boldsymbol{x}_s / \partial t^2$ all have the same time dependence $\exp(-i\omega t)$ as the incident field, along with possible constant phase offsets. For non-relativistic oscillation velocities $\boldsymbol{v}_s$, the $\boldsymbol{v}_s \times \boldsymbol{B_i}$ term is negligible. In that case, Eq. 1.9 can be simplified to

$$m_e(-i\omega)^2 \boldsymbol{x}_s + m_e \gamma_{ds}(-i\omega)\boldsymbol{x}_s + m_e \omega_s^2 \boldsymbol{x}_s = -e\boldsymbol{E_i}. \tag{1.10}$$

Combining factors, the harmonic displacement is given by

$$\boldsymbol{x}_s = \frac{e}{m_e} \frac{1}{\omega^2 - \omega_s^2 + i\gamma_{ds}\omega} \boldsymbol{E_i}. \tag{1.11}$$

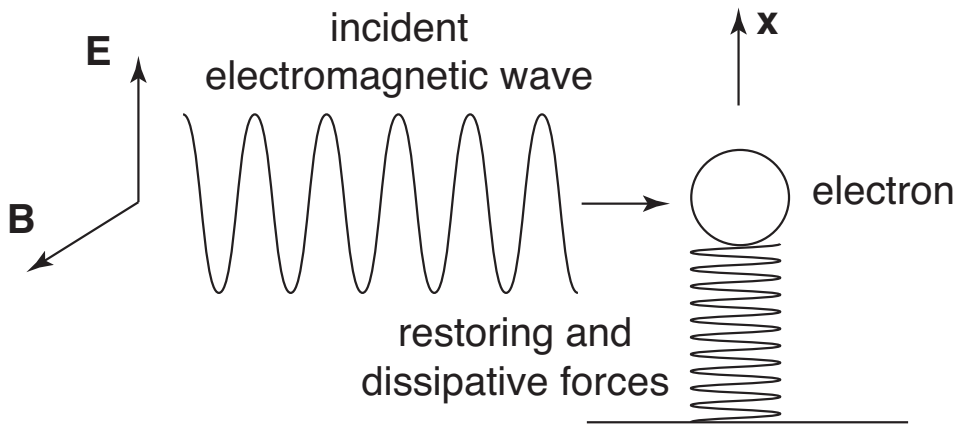

Figure 1.2: Schematic illustration of a bound electron oscillation mode response to an incident electromagnetic wave in the presence of restoring and dissipative forces.

The oscillation velocity is thus

$$\boldsymbol{v}_s = \frac{e}{m_e}\frac{1}{\omega^2 - \omega_s^2 + i\gamma_{ds}\omega}\frac{\partial \boldsymbol{E_i}}{\partial t}. \tag{1.12}$$

1.2.3 Refractive index

For the propagation of a transverse wave, where the electric field plane is perpendicular to the propagation direction, only the component of the current density in the transverse plane $\boldsymbol{J}_\mathrm{T}$ contributes. Supposing that there is no net charge density in the medium, the $\nabla\rho$ term in the wave equation Eq. 1.8 can be dropped. In this condition, Eq. 1.8 can be rewritten as

$$\left(\frac{\partial^2}{\partial t^2} - c^2\nabla^2\right)\boldsymbol{E}(\boldsymbol{r},t) = -\frac{1}{\epsilon_0}\frac{\partial \boldsymbol{J}_\mathrm{T}(\boldsymbol{r},t)}{\partial t}. \tag{1.13}$$

The transverse current density $\boldsymbol{J}_\mathrm{T}$ contributed from many electrons is a summation over all electrons at different resonance frequencies in the medium

$$\boldsymbol{J}_\mathrm{T}(\boldsymbol{r},t) = -en_a\sum_s g_s\boldsymbol{v}_s(\boldsymbol{r},t), \tag{1.14}$$

where n_a is the average density of atoms, and g_s is the oscillator strength which

is the number of electrons associated with a given resonance frequency ω_s in an atom. The sum of the oscillator strengths for all resonances is equal to the total number of electrons in the atom

$$\sum_s g_s = Z, \tag{1.15}$$

where Z is the total number of electrons per atom.

Substituting Eqs. 1.12, 1.14 and 1.15 into Eq. 1.13, we have

$$\left(\frac{\partial^2}{\partial t^2} - c^2\nabla^2\right)\boldsymbol{E}(\boldsymbol{r},t) = \frac{e^2 n_a}{\epsilon_0 m_e}\sum_s \frac{g_s}{\omega^2 - \omega_s^2 + i\gamma_{ds}\omega}\frac{\partial^2 \boldsymbol{E}(\boldsymbol{r},t)}{\partial t^2}, \tag{1.16}$$

which can be reorganized in the standard form of a wave equation as

$$\left[\frac{\partial^2}{\partial t^2} - \frac{c^2}{n^2(\omega)}\nabla^2\right]\boldsymbol{E}(\boldsymbol{r},t) = 0, \tag{1.17}$$

where the refractive index $n(\omega)$ is defined as

$$n(\omega) = \left[1 - \frac{e^2 n_a}{\epsilon_0 m_e}\sum_s \frac{g_s}{\omega^2 - \omega_s^2 + i\gamma_{ds}\omega}\right]^{1/2}. \tag{1.18}$$

In x-ray region, ω^2 is very large compared to the quantity $e^2 n_a/\epsilon_0 m_e$, so the second term in the square brackets is much smaller than 1. The index of refraction can be written using the first order approximation of the Taylor Series ($\sqrt{1-\varepsilon} \simeq 1 - \frac{1}{2}\varepsilon$ with $\varepsilon \ll 1$) as

$$n(\omega) = 1 - \frac{1}{2}\frac{e^2 n_a}{\epsilon_0 m_e}\sum_s \frac{g_s}{\omega^2 - \omega_s^2 + i\gamma_{ds}\omega}. \tag{1.19}$$

The complex scattering factor is usually denoted as $f(\omega)$ with the form

$$f(\omega) = \sum_s \frac{g_s}{\omega^2 - \omega_s^2 + i\gamma_{ds}\omega}, \tag{1.20}$$

which can be written in terms of the complex components

$$f(\omega) = f_1(\omega) - if_2(\omega) \tag{1.21}$$

with

$$f_1(\omega) = \sum_s \frac{g_s(\omega^2 - \omega_s^2)}{(\omega^2 - \omega_s^2)^2 + (\gamma_{ds}\omega)^2}, \; f_2(\omega) = \sum_s \frac{g_s\gamma_{ds}\omega}{(\omega^2 - \omega_s^2)^2 + (\gamma_{ds}\omega)^2}. \tag{1.22}$$

For x-rays, the refractive index deviates slightly from unity. It is common to express it in the form:

$$n(\omega) = 1 - \delta + i\beta, \tag{1.23}$$

where the negative sign before δ is determined by choosing the propagation direction as the forward direction, and this sign will be flipped if the forward direction is defined oppositely. Combined with Eqs. 1.19, 1.20 and 1.21, we obtain

$$\delta = \frac{1}{2}\frac{e^2 n_a}{\epsilon_0 m_e} f_1(\omega), \tag{1.24}$$

$$\beta = \frac{1}{2}\frac{e^2 n_a}{\epsilon_0 m_e} f_2(\omega). \tag{1.25}$$

We note that both δ and β are dependent on incident x-ray frequency ω, or the x-ray energy. As an example, Table 1.1 shows the δ and β values of carbon and protein at different x-ray energies [4]. As it will be discussed in Sec. 1.2.4, δ is related to phase shift, and β is related to absorption. We can see that at higher x-ray energies, both the absorption and phase shift contrasts are significantly reduced. It's also noticeable that the phase factor can be orders of magnitude larger than absorption. Because of this fact, most samples show mainly phase rather than absorption contrast at high x-ray energies.

Table 1.1: Refractive index of carbon and protein with a composition of $H_{48.6}C_{32.9}N_{8.9}S_{0.3}$ and a density of 1.35 g/cm^3.

X-ray energy	δ (carbon)	β (carbon)	δ (protein)	β (protein)
520 eV	1.76606×10^{-3}	5.31843×10^{-4}	9.89096×10^{-4}	2.64519×10^{-4}
750 eV	8.81000×10^{-4}	1.45286×10^{-4}	5.43095×10^{-4}	1.04496×10^{-4}
1 keV	4.94676×10^{-4}	4.94325×10^{-5}	3.10657×10^{-4}	3.63702×10^{-5}
1.5 keV	2.16575×10^{-4}	1.04040×10^{-5}	1.37252×10^{-4}	7.89374×10^{-6}
5 keV	1.88883×10^{-5}	8.42194×10^{-8}	1.20456×10^{-5}	9.00700×10^{-8}
10 keV	4.69771×10^{-6}	4.60272×10^{-9}	2.99445×10^{-6}	5.39158×10^{-9}

1.2.4 Absorption and phase shift

Because the x-ray wave interacts with the medium in which it propagates, the wave front will be modified to have the amplitude decreased and the phase advanced or retarded.

Let's consider these effects on a plane wave

$$\boldsymbol{\psi}(\boldsymbol{r},t) = \psi_0 e^{-i(\omega t - \boldsymbol{k}\cdot\boldsymbol{r})}, \tag{1.26}$$

where ψ_0 is the initial amplitude, and the propagation direction of this plane is defined as the forward direction which is consistent with the refractive index definition in Eq. 1.23. In the propagation direction, we have $\boldsymbol{k}\cdot\boldsymbol{r} = kz$, where z is the distance which the wave has traversed in the medium. The wave number k in the medium can be obtained from the complex dispersion relation, which is defined as

$$\frac{\omega}{k} = \frac{c}{n} = \frac{c}{1-\delta+i\beta}. \tag{1.27}$$

Substituting Eq. 1.27 into Eq. 1.26, we have

$$\boldsymbol{\psi}(z,t) = \psi_0 e^{-i\omega(t-z/c)} e^{i(2\pi/\lambda)\delta z} e^{-(2\pi/\lambda)\beta z}, \tag{1.28}$$

where $\omega/c = 2\pi/\lambda$ is used. The first exponential term in Eq. 1.28 represents the phase advance of vacuum propagation, the second term represents the phase shift due to interactions with the medium, and the third term represents a decay of the wave amplitude due to absorption.

Eq. 1.28 can be considered as the near field exit wave from a medium with thickness z and refractive index n. The intensity of this exit wave can be calculated by

$$I(z) = \boldsymbol{\psi}^* \cdot \boldsymbol{\psi} = I_0 e^{-2(2\pi/\lambda)\beta z} = I_0 e^{-\mu z}, \tag{1.29}$$

where $I_0 = \psi_0^2$, μ is the attenuation coefficient which is defined by the Lambert-Beer law as

$$\mu = \frac{4\pi\beta}{\lambda}. \tag{1.30}$$

The attenuation length is the distance into a medium when the wave intensity drops to $1/e$ of its initial magnitude.From Eq. 1.29, the attenuation length is the inverse of the attenuation coefficient or $1/\mu$.

1.3 Synchrotron x-ray source

A number of x-ray sources have been invented. One motivation for the evolution of x-ray sources is the pursuit of higher brightness. The spectral brightness $\mathcal{B}$ is defined as the photon flux per unit phase space volume, which is the photon number ΔN_{photon} per second s, per source area ΔA, per solid angle $\Delta\Omega$, and per 0.1% bandwidth BW, or

$$\mathcal{B} = \frac{\Delta N_{\text{photon}}}{s \cdot \Delta A \cdot \Delta\Omega \cdot 0.1\%\text{BW}}. \tag{1.31}$$

Table 1.2 shows the typical brightnesses of several different types x-ray sources.

For the diffraction experiments described in this dissertation, the spectral brightness and coherence of the x-ray beam are of great importance. The time-averaged brightnesses are listed in Table 1.2, except for free electron laser (FEL), for which it refers to the peak brightness. As we can see, the FEL provides the highest brightness. However, the photons from an FEL are so tightly compressed into ultrashort pulses that they may cause significant heating of a specimen, so that some specimens, especially biological samples, could be easily destroyed by a single pulse exposure. Without a beam splitter to provide multiple viewing directions for one pulse, FELs may have challenges

Table 1.2: Typical brightnesses of x-ray sources. The time-averaged brightnesses are listed, except for free electron laser (FEL), for which it refers to the peak brightness.

X-ray source	Brightness (photons/s/mm^2/mrad^2/0.1%BW)
X-ray tube	10^9 [5, 6]
X-ray emitting plasma	10^7 [7]
Bending magnet	10^{14} [8]
Wiggler	10^{16} [9]
Undulator	10^{19} [10]
Free electron laser	10^{30} [11]

for 3D imaging of biological specimens. On the other hand, undulators, one type of magnetic structure used to generate synchrotron radiation, have the ability to produce discrete, spectrally narrow, intense and continuous x-ray beams. They match our experimental requirements very well.

1.3.1 Undulator radiation

An undulator is a periodic magnetic structure, as illustrated in Fig. 1.3. When the relativistic electron beam traverses the alternating magnetic field in the axial direction, it oscillates harmonically in the transverse plane with angular excursions which are called undulations. With a relatively weak magnetic field, the amplitude of these angular excursions are small, which can generate narrow radiation cones.

Let's consider the characteristics of undulator radiation in a little more detail. Suppose the electron beam speed is v, which is close to the light speed in vacuum c. The Lorentz factor γ is defined as $1/\sqrt{(1-v^2/c^2)}$. If the period of the undulator is λ_u, according to Lorentz contraction of length, the new period in the electron's reference frame is

$$\lambda' = \frac{\lambda_u}{\gamma}. \tag{1.32}$$

In this reference frame, the frequency of the emitted radiation is $f' = c/\lambda' = c\gamma/\lambda_u$. In the laboratory reference frame, this frequency is modified by the

relativistic form of the Doppler frequency formula as

$$f = \frac{f'}{\gamma(1-\beta\cos\theta)} = \frac{c}{\lambda_u(1-\beta\cos\theta)}, \tag{1.33}$$

where $\beta = v/c$, and θ is the angle between the observation direction and the moving direction of electron beam. For small angles off axis, the first order approximation of Taylor expansion for $\cos\theta$ is $1-\theta^2/2$, so that Eq. 1.33 can be simplified as

$$f = \frac{c/\lambda_u}{1-\beta(1-\theta^2/2)} = \frac{2c\gamma}{\lambda_u(1+\gamma^2\theta^2)}, \tag{1.34}$$

where $1-\beta \simeq 1/2\gamma^2$ with $\beta \simeq 1$ is used for the second equality. The radiation wavelength in the laboratory reference frame is then

$$\lambda = \frac{c}{f} = \frac{\lambda_u}{2\gamma^2}(1+\gamma^2\theta^2). \tag{1.35}$$

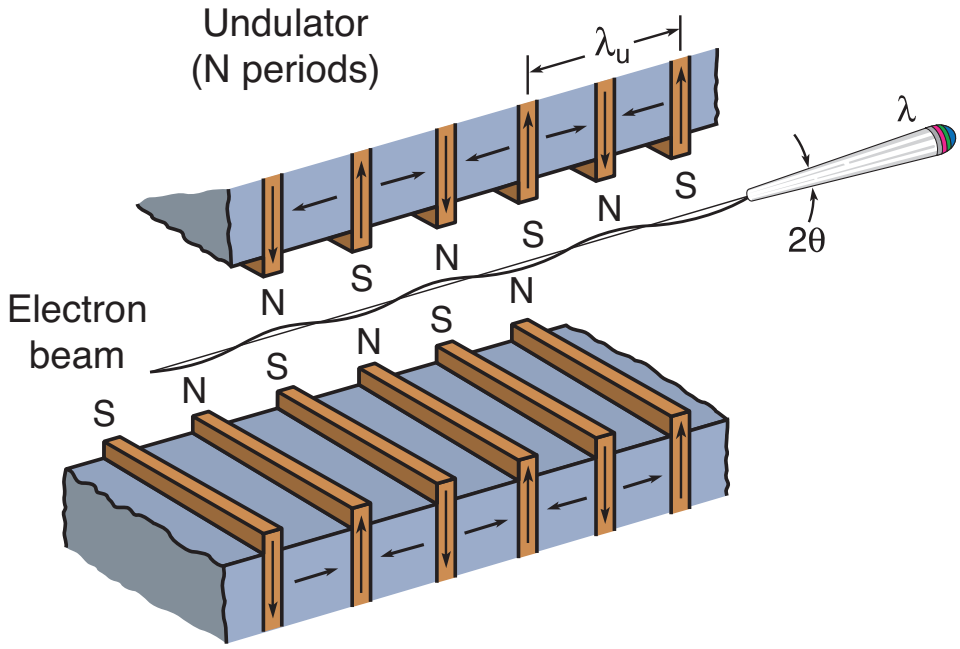

Figure 1.3: Schematic of an undulator: a narrow cone of radiation generated by deflecting relativistic electron beam with alternating magnetic structure.

As we can see in Fig. 1.3, the electron oscillation in the transverse plane

leads to a longer traveling path than the initial circular trajectory. As a result, the axial velocity is reduced. By solving the equation of motion of the oscillating electrons [1], the effective value of the Lorentz factor can be found as

$$\gamma^* = \frac{\gamma}{\sqrt{1 + K^2/2}}, \tag{1.36}$$

where K is the non-dimensional magnetic strength parameter of an undulator, which is defined as

$$K = \frac{eB_0\lambda_u}{2\pi m_e c}, \tag{1.37}$$

where B_0 is the peak magnetic field.

Replacing γ in Eq. 1.35 with γ^* in Eq. 1.36, we obtain the undulator equation for the fundamental mode:

$$\lambda = \frac{\lambda_u}{2\gamma^2}(1 + \frac{K^2}{2} + \gamma^2\theta^2). \tag{1.38}$$

The bandwidth of the emitted radiation is determined by the number of oscillation period N as [12]

$$\frac{\Delta\lambda}{\lambda} = \frac{1}{N}. \tag{1.39}$$

For mth harmonics, both the frequencies and oscillation cycles are enhanced by a factor of m. The corresponding undulator equation is

$$\lambda_m = \frac{\lambda_u}{2\gamma^2 m}(1 + \frac{K^2}{2} + \gamma^2\theta^2), \tag{1.40}$$

and the band width is

$$\frac{\Delta\lambda}{\lambda} = \frac{1}{mN}. \tag{1.41}$$

1.3.2 Undulator gap

The magnetic field produced by the permanent magnet arrays in an undulator (as shown in Fig. 1.3) is determined by its parameters such as the remanent magnetic field B_r, the period length λ_u, the height of magnet blocks h_u, the number of magnet blocks in each period in upper or lower branch M', and

the tunable gap between those two branches g. For many purposes, their rigorously expressed relationship given by [13] can be simplified by a sine wave with period λ_u and amplitude [14]

$$B_0 = 2B_r e^{-\pi g/\lambda_u} \frac{\sin(\pi/M')}{\pi/M'} [1 - e^{-2\pi h_u/\lambda_u}], \tag{1.42}$$

where we note that all the variables on the right side are fixed with the magnetic structure, except for the undulator gap g. Therefore Eq. 1.42 can be rewritten as a function of g as

$$B_0 \propto e^{-\pi g/\lambda_u}. \tag{1.43}$$

From Eq. 1.37, K varies linearly with B_0 or $K \propto B_0$. Substituting this result into Eq. 1.43, we have

$$K = C_u e^{-\pi g/\lambda_u}, \tag{1.44}$$

which can be rewritten specifically with one unknown constant as

$$g = \frac{\lambda_u}{\pi} \ln \frac{C_u}{K}, \tag{1.45}$$

where C_u is a constant that needs to be determined.

1.3.3 ALS beamline 9.0.1 undulator

The experimental apparatus [15] used in this dissertation is stationed at Beamline 9.0.1 at Advanced Light Source (ALS) at Lawrence Berkeley National Laboratory, where the x-ray radiation is produced by undulator U10. The engineering design parameters of U10 are listed in Table 1.3 [16][17].

We operated the microscope at 520 and 750 eV energies for diffraction experiments using the third harmonic of the undulator. The x-ray energy is selected by adjusting undulator gap to the specific setting. To determine the required gap value, we first calculate the fundamental energy E_f from the

Table 1.3: Engineering design parameters of undulator U10 at ALS

Period length	10 cm
Number of period	43
Effective field range	0.98–0.05 T
Energy range (at 1.9 GeV ring energy)	8–1500 eV
Gap range	2.27–11.6 cm
Gap step resolution	2.8 μm
Operation pressure	10^{-9} torr

target energy E_t and harmonic number m using Eq. 1.40 and $E = 2\pi\hbar c/\lambda$ as

$$E_f = \frac{E_t}{m}. \tag{1.46}$$

We then calculate the undulator parameter K on axis ($\theta = 0$) using the energy form of the undulator equation Eq. 1.38, which gives

$$E_f(\text{keV}) = \frac{0.9496 E_e^2(\text{GeV})}{\lambda_u(\text{cm})\left(1 + \frac{K^2}{2}\right)}, \tag{1.47}$$

where E_e is the electron energy in the synchrotron storage ring. Eq. 1.47 can be reorganized to be

$$K = \sqrt{2\left[\frac{0.9496 E_e^2(\text{GeV})}{E_f(\text{keV})\lambda_u(\text{cm})} - 1\right]}. \tag{1.48}$$

Finally, the undetermined constant parameter C_u in the relationship between K and g in Eq. 1.45 is calibrated from fitting the measured field strength of this undulator, giving $C_u = 19.573$. The calibration also gives a multiplicative correction factor 0.935 to Eq. 1.45, which reflecting the characteristics of the actual device as opposed to an ideal model of it.

Using these undulator parameters for the ALS operated at 1.9 GeV, we find that to obtain 530 eV radiation from the third harmonic, a gap of 7.91 cm and a K of 1.37 is required, while for 750 eV x-rays a gap of 9.29 cm and a K of 0.86 is required.

1.4 X-ray microscopy for biological samples

There are three major microscopy techniques for biological imaging: visible light microscopy, electron microscopy and x-ray microscopy. Each type has strengths that make it well suited for one circumstance, and weaknesses that limit its application in other cases. Visible light microscopy allows one to study biological samples in their natural state and with maximum ease of use, but its achievable resolution is severely limited by the wavelength of the illumination. Electron microscopy has the ability to achieve extremely high resolution, but it can only penetrate less than a half micron into biological materials; it cannot image micron size objects in their entirety. X-ray microscopy fills a resolution and fidelity gap between the other two microscopies. It can be used for the imaging of unsectioned biological samples which are too thick to be viewed in electron microscopy, and it has the potential for achieving much higher spatial resolution than the most advanced optical microscopy. In this last section of Chapter 1, we discuss some basic and important considerations of x-ray microscopy.

1.4.1 Resolution

Resolution is one of the key characteristics to judge the performance of microscopes.

If two objects are brought close, the intensity between them rises in the image, so it becomes difficult to resolve each individual object. The transverse resolution δ_t, which is the permitted separation that can be distinguished, is defined by the Rayleigh criterion, which states that two circular objects are minimally resolved when the central peak of the Airy pattern from one object is located at the first minimum ring of the Airy pattern from the other displaced δ_t away. In this condition, the overlapped intensity of the central Rayleigh dip is 26.5% off from each single peak.

Suppose that the Airy patterns are collected on a screen placed at a distance z from a round object with diameter d, which is illuminated by light with wavelength λ. The radius of the first minimum ring in its Airy pattern can be

calculated by

$$r_{\text{null}} = \frac{1.22\lambda z}{d}. \tag{1.49}$$

We introduce another important concept, the numerical aperture (N.A.), which is defined as the product of the medium's refractive index and the sine of the angle between the optical axis and the outermost light direction, or N.A. $= n \sin\theta$. The refractive index equals 1 in air, and in small angle approximation $\sin\theta \simeq \theta$, so N.A. is $d/2z$ in this case. The transverse resolution $\delta_t = r_{\text{null}}$ can then expressed from Eq. 1.49 as

$$\delta_t = \frac{0.61\lambda}{\text{N.A.}}. \tag{1.50}$$

The longitudinal resolution δ_l, or depth of focus, is the maximum displacement from the focal plane, when the intensity is decreased by a amount which does not affect resolution. It is shown [3] that the intensity on-axis decreases by about 20% (comparable to 26.5% in Rayleigh criterion) when the observation plane displaced by an amount of $\pm\lambda/(2(\text{N.A.})^2)$. Based on this consideration, the longitudinal resolution δ_l is obtained as

$$\delta_l = \frac{\lambda}{2(\text{N.A.})^2}. \tag{1.51}$$

1.4.2 Water window

Table 1.1 shows that, in general, the higher the x-ray energy, the less interaction with the medium. However, a side effect of the increase in penetration power is the loss in image contrast. Therefore, the x-ray energy has to be carefully chosen according to the properties of the specimen to be studied. Regarding biological samples, where carbon and oxygen are the most abundant atoms, there is an exceptional spectral region to work with called "the water window" between the carbon and oxygen K absorption edges (284 eV and 544 eV, respectively) [18], where the contrast of organic materials is optimized with low absorption in water. This is shown in Fig. 1.4.

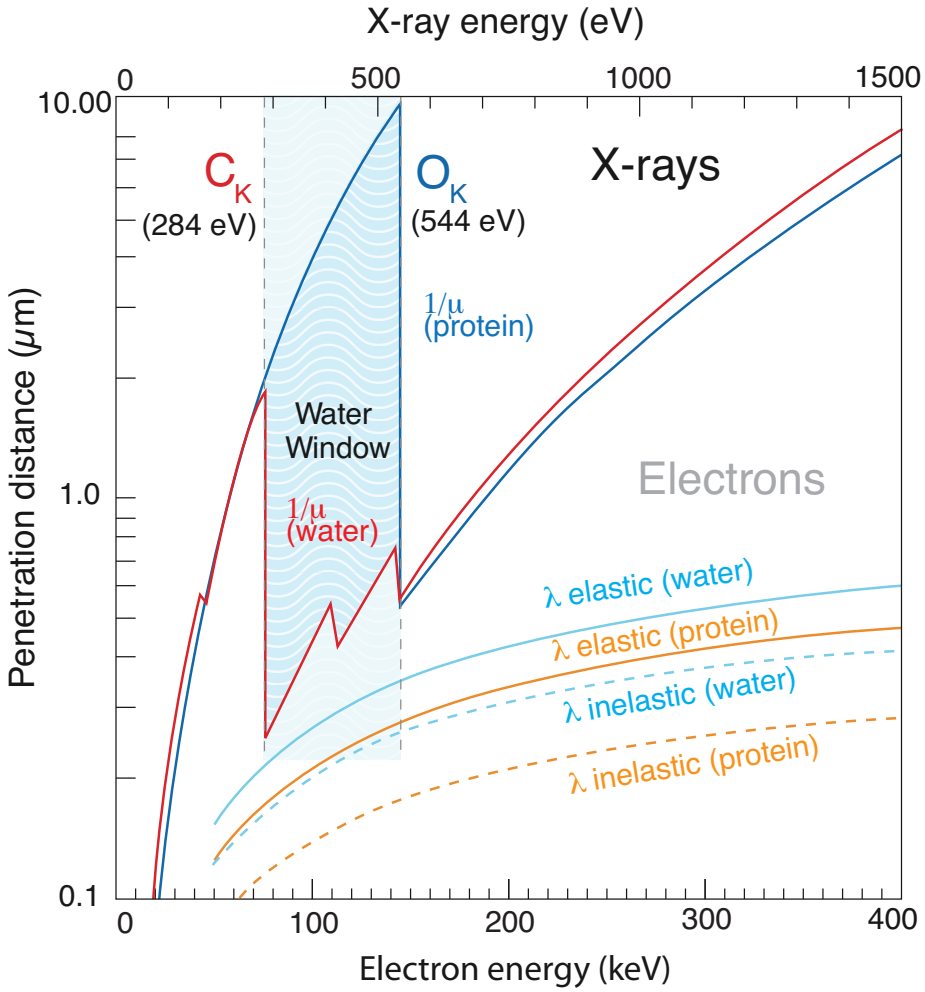

Figure 1.4: Penetration distances on x-rays and electrons in water and protein as a function of energy [19]. The blue curve is for oxygen, and the red curve is for carbon. The spectral region between carbon and oxygen K absorption edges give best contrast of carbon against oxygen (water). This region is known as the "water window".

1.4.3 Radiation damage

Radiation damage results when materials are subject to ionizing illuminations. Depending on the energy level of the incident radiation, the interactions with electrons in the material can be described in three forms: Photoelectric, Auger, or Compton effects. They are known as the primary damage. In hydrated materials, the energetic electrons generated by the primary reactions can create free radicals, which can diffuse and change the chemical states of the object, causing secondary damage.

To measure the intensity of radiation exposures, the radiation dose is defined as the absorbed energy per mass with an SI unit of Gray (Gy). One Gray equals to 1 Joule of energy absorbed by 1 kilogram of material. Consider a specimen that is illuminated by an average of $\bar{n}$ photons per pixel, with a pixel dimension of Δ_r (and thus an areal exposure of $\bar{n}/\Delta_r^2$). If an incident beam is attenuated according to the Lambert-Beer law (Eq. 1.29 and Eq. 1.30), then the fraction of energy absorbed per thickness is given by $-dI/dz = \mu\, I_0 \exp(-\mu z)$, where z is the distance into which the beam has already penetrated the specimen. We can therefore describe the "skin dose" D at $z = 0$ by

$$D = \frac{\bar{n} E_{\text{photon}} \mu}{\Delta_r^2 \rho}, \tag{1.52}$$

where ρ is the density of the specimen material and E_{photon} is the photon energy. The skin dose D calculation above assumes no escaped energy, which is usually the case for soft x-ray microscopy because of the short range of secondary electrons produced following x-ray absorption and the very low fluorescence yield of the low-Z elements that make up the main part of the mass of biological specimens. The relative biological effectiveness or RBE factor is considered to be equal to unity as usually the case with x-ray photons. Based on the above, we assume a direct proportionality between photons per pixel $\bar{n}$, areal exposure $\bar{n}/\Delta_r^2$, and absorbed dose D.

Theoretical calculations [20] and experimental data [21] show that higher illumination dose is required to resolve higher resolution. It has also been shown [21, 22] that the radiation damage effects limit the achievable resolution. The battle between dose and radiation damage sets a resolution limit for

biological x-ray microscopy to be around 10 nm, as shown in Fig. 1.5.

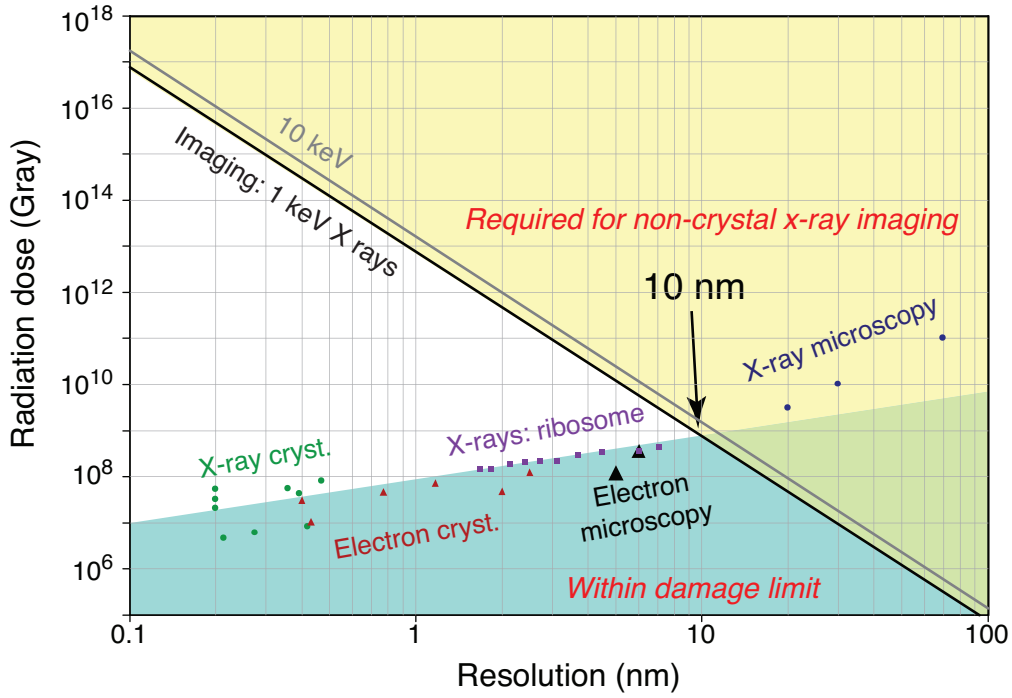

Figure 1.5: Radiation dose requirement for achievable resolutions, together with the maximum tolerable dose before damage [21]. The required doses are calculated for protein against water background at 1 keV and 10 keV x-ray energies. The maximum tolerable doses are summarized from published literatures. The decreasing Dose vs Resolution line crosses with the increasing Dose vs Damage line at a resolution about 10 nm.

Chapter 2

X-ray Diffraction Microscopy

X-ray diffraction microscopy (XDM) is a novel imaging method, which involves no optics in the imaging system. As a result, it dispenses with the technological limitations of lens efficiency and resolution. The achievable resolution is only limited by the maximum collected diffraction angle and the radiation tolerance of the sample. In this chapter, we will discuss the principles of lens-based microscopy and lensless XDM, and the approximations and limitations of XDM.

2.1 Lens-based imaging

In conventional microscopes, the scattered signal from an object illuminated by an incident beam is collected and phased to form an image in real space by a lens or a combination of lenses, as shown in Fig. 2.1. We are going to briefly review the principles of the lens-based microscopy before we discuss the advantages of lensless imaging system.

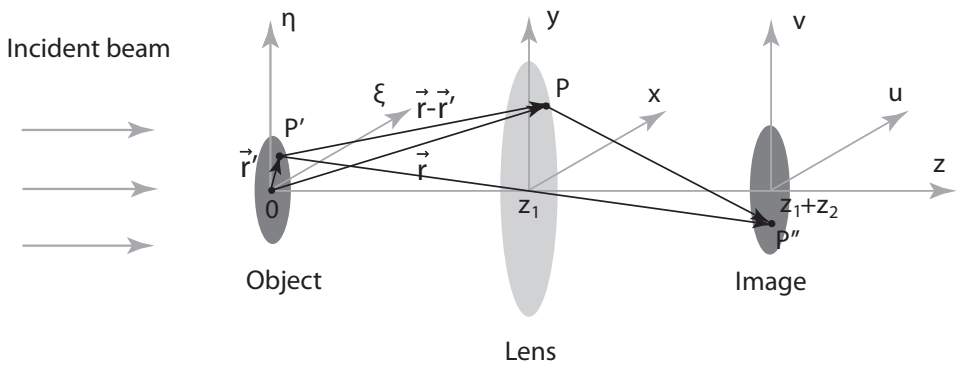

Figure 2.1: Geometry for lens-based imaging formation.

2.1.1 Fresnel diffraction

Assume the object is located in the $(\xi, \eta, 0)$ plane, and the illumination is along the positive $\hat{\boldsymbol{z}}$ direction, as shown in Fig. 2.1. The exit wave from the object can be considered as a collection of Huygens point sources. Each point source propagates towards the lens plane (x, y, z_1) independently. The wave front in front of the lens can be obtained by summing up the amplitude from all those point sources, as

$$\begin{aligned} \boldsymbol{\psi}(x,y) &= \int\int \boldsymbol{\psi}(\xi,\eta)\frac{\exp\left(ik|\boldsymbol{r}-\boldsymbol{r'}|\right)}{|\boldsymbol{r}-\boldsymbol{r'}|}\cos\theta d\xi d\eta \\ &= z_1\int\int \boldsymbol{\psi}(\xi,\eta)\frac{\exp\left(ik|\boldsymbol{r}-\boldsymbol{r'}|\right)}{|\boldsymbol{r}-\boldsymbol{r'}|^2}d\xi d\eta, \end{aligned} \tag{2.1}$$

where θ is the angle between $\boldsymbol{r}-\boldsymbol{r'}$ and $\hat{\boldsymbol{z}}$, and $\cos\theta$ equals $z_1/|\boldsymbol{r}-\boldsymbol{r'}|$.

We apply the Fresnel approximation ($(x-\xi)^2+(y-\eta)^2 \ll z^2$) to simplify

Eq. 2.1. In this condition, using the Taylor expansion approximation of the square root function, we have

$$\begin{aligned} |\boldsymbol{r}-\boldsymbol{r'}| &= z_1\sqrt{1+\left(\frac{x-\xi}{z_1}\right)^2+\left(\frac{y-\eta}{z_1}\right)^2} \\ &\approx z_1\left[1+\frac{1}{2}\left(\frac{x-\xi}{z_1}\right)^2+\frac{1}{2}\left(\frac{y-\eta}{z_1}\right)^2\right]. \end{aligned} \tag{2.2}$$

The accurate expression of the Fresnel approximation requires that the phase change induced by ignoring the third term in Taylor expansion is much less than 1 radian, which gives $\pi[(x-\xi)^2+(y-\eta)^2]^2/(4\lambda) \ll z^3$.

Eq. 2.1 then becomes

$$\boldsymbol{\psi}(x,y) = \frac{e^{ikz_1}}{z_1} e^{\frac{ik}{2z_1}(x^2+y^2)} \int\int \boldsymbol{\psi}(\xi,\eta) e^{\frac{ik}{2z_1}(\xi^2+\eta^2)} e^{\frac{-ik}{z_1}(x\xi+y\eta)} d\xi d\eta. \tag{2.3}$$

2.1.2 Impulse response and lens law

For a linear system, the superposition property gives

$$\boldsymbol{\psi}(x,y) = \int\int \boldsymbol{\psi}(\xi,\eta)\delta(x-\xi,y-\eta)d\xi d\eta, \tag{2.4}$$

which guarantees that the image can be obtained by summing each individual impulse response as

$$\begin{aligned} \boldsymbol{\psi}_i(x,y) &= \mathcal{S}\left\{\int\int \boldsymbol{\psi}_o(\xi,\eta)\delta(x-\xi,y-\eta)d\xi d\eta\right\} \\ &= \int\int \boldsymbol{\psi}_o(\xi,\eta)\mathcal{S}\left\{\delta(x-\xi,y-\eta)\right\}d\xi d\eta \\ &= \int\int \boldsymbol{\psi}_o(\xi,\eta)h(x,y;\xi,\eta)d\xi d\eta, \end{aligned} \tag{2.5}$$

where the operator $\mathcal{S}$ represents the system function operating on an input object to produce an output image, and h is the imaging system response to one point source, *i.e.*, the impulse response, which is also known as the point spread function.

Let's consider what h looks like for the Fresnel imaging system. Consider one point on the object at coordinates $(\xi, \eta, 0)$. The corresponding incident wave front before entering the lens can be described as a spherical wave diverging from that point, or

$$\begin{aligned} \boldsymbol{\psi}_l^{(p)}(x,y) &= \frac{1}{|\boldsymbol{r}-\boldsymbol{r'}|} e^{ik|\boldsymbol{r}-\boldsymbol{r'}|} \\ &= \frac{e^{ikz_1}}{z_1} \exp\left\{\frac{ik}{2z_1}\left[(x-\xi)^2+(y-\eta)^2\right]\right\}, \end{aligned} \tag{2.6}$$

where the simplification step Eq. 2.2 under the Fresnel approximation is applied in the second equality. The same result can be obtained by substituting $\boldsymbol{\psi}(\xi, \eta)$ in Eq. 2.3 with $\delta(\xi - \xi', \eta - \eta')$ which represents this point source.

The function of a lens with a focal length f_l can be expressed as a phase transformation factor $\exp\left[-ik(x^2+y^2)/2f_l\right]$ due to the thickness variance, and a pupil function $P(x, y)$ because of the finite radius. Then, the wave front from a pulse after the lens takes the form

$$\boldsymbol{\psi}_l'^{(p)}(x,y) = \frac{e^{ikz_1}}{z_1} P(x,y) \exp\left[-\frac{ik}{2f_l}(x^2+y^2)\right] \exp\left\{\frac{ik}{2z_1}\left[(x-\xi)^2+(y-\eta)^2\right]\right\}. \tag{2.7}$$

This wave front exiting the lens can be again treated as a collection of Huygens point sources. Then, the wave front at the image plane $(u, v, z_1 + z_2)$ can be calculated using Fresnel diffraction formula Eq. 2.3. We note that this image is formed by an impulse input, so it is the point spread function of the imaging system h, which is

$$\begin{aligned} h(u,v;\xi,\eta) &= \frac{e^{ik(z_1+z_2)}}{z_1 z_2} \exp\left[\frac{ik}{2z_2}(u^2+v^2)\right] \exp\left[\frac{ik}{2z_1}(\xi^2+\eta^2)\right] \\ &\times \int\int P(x,y) \exp\left[\frac{ik}{2}\left(\frac{1}{z_1}+\frac{1}{z_2}-\frac{1}{f_l}\right)(x^2+y^2)\right] \\ &\times \exp\left\{-ik\left[\left(\frac{\xi}{z_1}+\frac{u}{z_2}\right)x+\left(\frac{\eta}{z_1}+\frac{v}{z_2}\right)y\right]\right\} dxdy. \end{aligned} \tag{2.8}$$

The quadratic phase factor in the integral is eliminated when the object dis-

tance z_1 and the image distance z_2 satisfy

$$\frac{1}{z_1} + \frac{1}{z_2} = \frac{1}{f_l}, \tag{2.9}$$

which is known as the lens law.

If the impulse response of the system depends only on the distance between the excitation point and the response point, *i.e.*, $(x-\xi)$ and $(y-\eta)$, $h(x, y; \xi, \eta)$ can be written as $h(x-\xi, y-\eta)$. In the case of Eq. 2.8, h is determined by $(u - M\xi)$ and $(v - M\eta)$, where $M = -z_2/z_1$ is the system magnification. Under this condition, Eq. 2.5 shows that the image equals the convolution of the object with the point spread function of the system, or

$$\boldsymbol{\psi}_i = \boldsymbol{\psi}_o \otimes h, \tag{2.10}$$

where the symbol $\otimes$ denotes the convolution of two functions.

2.1.3 Modulation transfer function

Considering a full-field transmission x-ray microscope (TXM) operating in brightfield incoherent imaging mode, this is done by using a condenser lens to illuminate the specimen, and an objective lens to collect the scattered light and deliver a phased, magnified, real-space image to a detector. In this incoherent circumstance, Eq. 2.10 becomes the intensity convolution relationship

$$I_i = I_o \otimes |h|^2. \tag{2.11}$$

The Fourier transform of the intensity of the point spread function, $\mathcal{F}(|h|^2)$ (where $\mathcal{F}$ denotes the Fourier transform operation), is defined as the Modulation Transfer Function, or MTF. The MTF can be calculated [23] as

$$\text{MTF} = \begin{cases} \frac{2}{\pi}\left[\cos^{-1}\left(\frac{f}{f_0}\right) - \frac{f}{f_0}\sqrt{1-\left(\frac{f}{f_0}\right)^2}\right] & f \le f_0 \\ 0 & f > f_0, \end{cases} \tag{2.12}$$

where f represents spatial frequency, and f_0 is the spatial frequency cutoff.

Using the convolution theorem of Fourier transforms $\mathcal{F}\{\}$, the image intensity can be represented as

$$I_i = \mathcal{F}^{-1}\Big\{\mathcal{F}\{I_o\} \cdot \mathcal{F}\{|h|^2\}\Big\} = \mathcal{F}^{-1}\Big\{\mathcal{F}\{I_o\} \cdot \mathrm{MTF}\Big\}. \tag{2.13}$$

2.1.4 Zone plate

For x-rays, Fresnel zone plates are utilized as diffractive lenses, because it is difficult in practice to make normal optical lenses with materials of refractive indices close to unity in the x-ray spectral region.

A Fresnel zone plate consists of alternate transparent and opaque rings. The radius of the mth zone is given by

$$r_m^2 = m f_{\mathrm{zp}} \lambda + m^2 \lambda^2 / 4, \tag{2.14}$$

where f_{zp} is the first order focal length. f_{zp} can be calculated by

$$f_{\mathrm{zp}} = 4 N dr_N^2 / \lambda, \tag{2.15}$$

where N is the number of zones, and dr_N is the outermost zone width. The numerical aperture, transverse resolution and depth of focus of the zone plate are given by

$$\mathrm{N.A._{zp}} = \frac{\lambda}{2 dr_N}, \tag{2.16}$$

$$\delta_t^{\mathrm{zp}} = 0.61 \frac{\lambda}{\mathrm{N.A._{zp}}} = 1.22 dr_N, \tag{2.17}$$

$$\delta_l^{\mathrm{zp}} = 1.22 \frac{\lambda}{\mathrm{N.A._{zp}^2}} = 4.88 \frac{dr_N^2}{\lambda}. \tag{2.18}$$

For example, for 520 eV x-rays with $\lambda = 2.38$ nm, a zone plate with 20 nm outermost zone width, the achievable transverse resolution and depth of focus are 24.4 nm and 0.82 μm, respectively.

As we can see, the performance of TXM is highly restricted by the zone plate quality. Although TXM has been routinely used for high resolution

imaging of biological specimens in both 2D [24–26] and more recently in 3D via tomography [27, 28], and the Fresnel zone plate-based scanning transmission x-ray microscopes (STXM) have been successfully applied as 2D and 3D structure determination methods [29–31], the technical difficulty in the fabrication of high resolution and efficiency zone plates becomes a major limitation. Most soft x-ray experiments use zone plates with an outermost zone width of 25 to 30 nm, and efficiencies of about 10%. Higher resolution zone plates have been fabricated, but with lower efficiency; for example, 15 nm outermost zone width was demonstrated in 2005 with an efficiency of 4% [32], and this record was pushed forward to 12 nm in 2009, but with an efficiency of 0.6% [33]. Considering such low efficiencies, these zone plates are not feasible for imaging radiation sensitive samples, such as biological and soft matter specimens. Therefore, an alternative, lensless microscope can complement TXM and STXM for high resolution imaging with no optics-imposed losses on either the efficiency, or finite numerical aperture (and thus resolution limitations).

2.2 Lensless imaging: XDM

XDM is a lensless method for imaging isolated nonperiodic objects at high resolutions. It was proposed by Sayre in 1980 as an extension of crystallography to non-crystalline samples [34]. Unlike conventional x-ray microscopies, this imaging system employs no x-ray optics (such as Fresnel zone plates). Instead, the isolated object is illuminated by a coherent plane-wave incident x-ray beam, and the properly sampled far field diffraction pattern is collected directly by a charge-coupled device (CCD) placed downstream, as shown in Fig. 2.2. Without a lens to sample and phase the diffraction signal, the object image in real space is reconstructed by iterative phase retrieval algorithms from the measured diffraction intensity. In this section, we will go through the basic ideas in XDM.

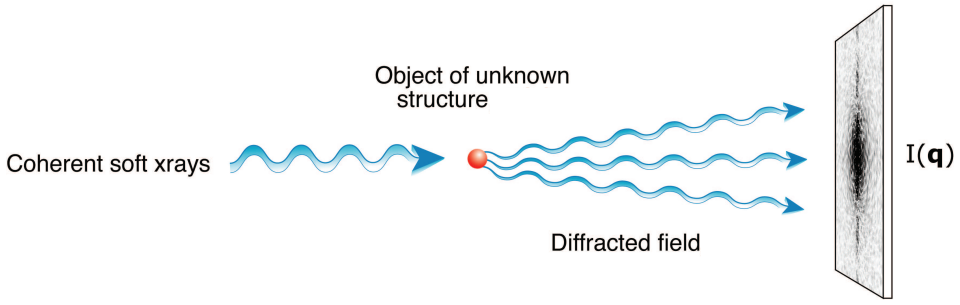

Figure 2.2: Schematic layout of XDM experimental setup (adapted from [35]).

2.2.1 Far field diffraction pattern

When an incident x-ray plane wave interacts with a nonperiodic object, the wave front will be modified by the scattering with electrons and nuclei in the object. We can consider the exit wave from the object (expressed by Eq. 1.28) as a collection of Huygens point sources located at the object exit plane, and derive what the far field exit wave looks like by letting it propagate a relatively long distance.

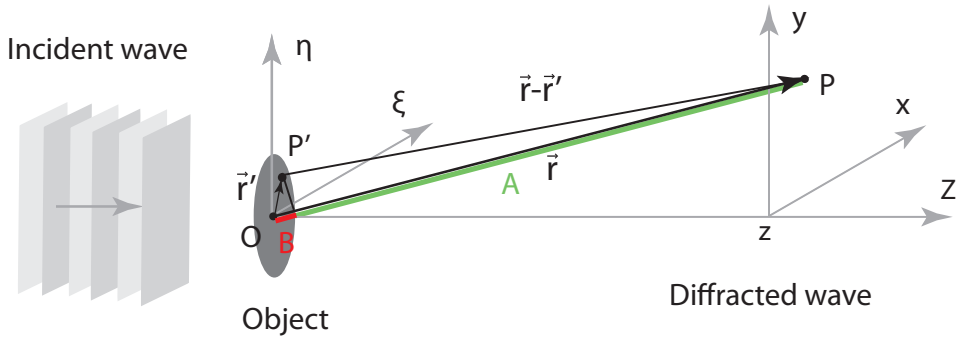

Figure 2.3: Illustration of incident plane scattered by an object.

We follow Born's approach instead to derive the far field wave front [3], since it is more convenient for describing the essence of XDM. Assuming an incident coherent plane wave traveling along the $\hat{z}$ direction diffracted by an object, as shown in Fig. 2.3, the exit wave front satisfies the wave equation Eq. 1.17. Of course the plane wave has a time dependence of $\exp(-i\omega t)$, as seen in Eq. 1.26, but this term will not be shown in the following discussions.

Eq. 1.17 can then be expressed as

$$\nabla^2\boldsymbol{\psi}(\boldsymbol{r}) + k^2 n^2(\boldsymbol{r})\boldsymbol{\psi}(\boldsymbol{r}) = 0, \tag{2.19}$$

where k is the wave number in vacuum, with $\hat{\boldsymbol{k}}$ in the $\hat{\boldsymbol{z}}$ direction and $k = \omega/c$. For convenience, we rewrite Eq. 2.19 in the form

$$\nabla^2\boldsymbol{\psi}(\boldsymbol{r}) + k^2\boldsymbol{\psi}(\boldsymbol{r}) = -4\pi\boldsymbol{F}(\boldsymbol{r})\boldsymbol{\psi}(\boldsymbol{r}), \tag{2.20}$$

where $\boldsymbol{F}(\boldsymbol{r})$ is called the scattering potential, defined as

$$\boldsymbol{F}(\boldsymbol{r}) = \frac{1}{4\pi}k^2\left[n^2(\boldsymbol{r}) - 1\right] \approx \frac{1}{2\pi}k^2\left[-\delta(\boldsymbol{r}) + i\beta(\boldsymbol{r})\right]. \tag{2.21}$$

As the refractive index n is expressed by $1-\delta+i\beta$ as in Eq. 1.23, and both δ and β are very small numbers in the x-ray spectral range (as shown in Table 1.1), n^2 can be approximated as $1 + 2(-\delta + i\beta)$, which is used in the last equality of Eq. 2.21.

Because the interaction between the incident wave and the object is relatively weak, the incident wave is partially diffracted by the scattering potential of the object with the remaining and strongest part transmitted without diffraction. We can then express the far field wave front $\boldsymbol{\psi}(\boldsymbol{r})$ as the summation of the unscattered incident wave $\boldsymbol{\psi}^{(i)}(\boldsymbol{r})$ and the scattered wave $\boldsymbol{\psi}^{(s)}(\boldsymbol{r})$ as

$$\boldsymbol{\psi}(\boldsymbol{r}) = \boldsymbol{\psi}^{(i)}(\boldsymbol{r}) + \boldsymbol{\psi}^{(s)}(\boldsymbol{r}). \tag{2.22}$$

The unscattered plane wave $\boldsymbol{\psi}^{(i)}(\boldsymbol{r})$ satisfies the Helmholtz equation

$$(\nabla^2 + k^2)\boldsymbol{\psi}^{(i)}(\boldsymbol{r}) = 0. \tag{2.23}$$

Substituting Eq. 2.22 and Eq. 2.23 into Eq. 2.20, we obtain

$$(\nabla^2 + k^2)\boldsymbol{\psi}^{(s)}(\boldsymbol{r}) = -4\pi\boldsymbol{F}(\boldsymbol{r})\boldsymbol{\psi}(\boldsymbol{r}). \tag{2.24}$$

Solving this equation using Green's function [3], and noting that the incident plane wave takes the form $\psi_0 \exp(ik\hat{\boldsymbol{z}}\cdot\boldsymbol{r})$, we see that the far field wave front

$\boldsymbol{\psi}(\boldsymbol{r})$ can be obtained as

$$\boldsymbol{\psi}(\boldsymbol{r}) = \psi_0 e^{ik\hat{\boldsymbol{z}}\cdot\boldsymbol{r}} + \int_V \boldsymbol{F}(\boldsymbol{r'})\boldsymbol{\psi}(\boldsymbol{r'})\frac{e^{ik|\boldsymbol{r}-\boldsymbol{r'}|}}{|\boldsymbol{r}-\boldsymbol{r'}|}d^3\boldsymbol{r'}, \tag{2.25}$$

where $\hat{\boldsymbol{z}}$ and $\hat{\boldsymbol{r}}$ are the direction units, and $\boldsymbol{r'}$ goes through all points located in the volume V occupied by the object.

For far field diffraction, the so-called Fraunhofer approximation condition is satisfied, or $|\boldsymbol{r}| \gg |\boldsymbol{r'}|$, or $z^2 \gg \xi^2 + \eta^2$. The accurate expression of the Fraunhofer approximation is $z \gg \pi(\xi^2 + \eta^2)/\lambda$, which is stronger than the Fresnel approximation. As shown in Fig. 2.3, $|\boldsymbol{r} - \boldsymbol{r'}|$ is approximately equal to the length of $\boldsymbol{A}$, while $|\boldsymbol{A}| = |\boldsymbol{r}| - |\boldsymbol{B}|$, where $\boldsymbol{B}$ is the projection of $\boldsymbol{r'}$ on to $\boldsymbol{r}$, *i.e.*, $|\boldsymbol{B}| = \boldsymbol{r'} \cdot \hat{\boldsymbol{r}}$. In that case, $|\boldsymbol{r} - \boldsymbol{r'}|$ can be approximated as

$$|\boldsymbol{r} - \boldsymbol{r'}| \approx |\boldsymbol{r}| - \boldsymbol{r'} \cdot \hat{\boldsymbol{r}}, \tag{2.26}$$

where $\hat{\boldsymbol{r}}$ can be calculated as $\boldsymbol{r}/|\boldsymbol{r}|$. Eq. 2.25 can then be simplified to

$$\boldsymbol{\psi}(\boldsymbol{r}) = \psi_0 e^{ik\hat{\boldsymbol{z}}\cdot\boldsymbol{r}} + \frac{e^{ik|\boldsymbol{r}|}}{|\boldsymbol{r}|}\int_V \boldsymbol{F}(\boldsymbol{r'})\boldsymbol{\psi}(\boldsymbol{r'})e^{-ik\boldsymbol{r'}\cdot\hat{\boldsymbol{r}}}d^3\boldsymbol{r'}. \tag{2.27}$$

2.2.2 Born approximation

By applying the Fraunhofer approximation, we obtain an integral equation of $\boldsymbol{\psi}(\boldsymbol{r})$ as in Eq. 2.27. In general cases, it is very difficult to find the solutions for integral equations of arbitrary integrand $\boldsymbol{\psi}(\boldsymbol{r})$. Fortunately, there are approximation methods available.

As discussed in Sec. 1.2.3, the refractive indices are usually very close to unity in x-ray region. From Eq. 2.21, we can see that the scattering potentials are small when n is slightly off from 1, which implies the object diffracts weakly. In this circumstance, we can use the lowest-order approximation as in perturbation expansion, where the successive terms can be calculated by iteration from previous terms. By replacing the total wave front term $\boldsymbol{\psi}$ ($\boldsymbol{\psi}^{(i)} + \boldsymbol{\psi}^{(s)}$) inside the intergral with the incident plane wave front $\boldsymbol{\psi}^{(i)}$ or $\psi_0 e^{ik\hat{\boldsymbol{z}}\cdot\boldsymbol{r}}$, the first approximation to the solution of the integral equation of Eq. 2.27 can

be obtained as

$$\boldsymbol{\psi}(\boldsymbol{r}) = \psi_0 e^{ik\hat{\boldsymbol{z}}\cdot\boldsymbol{r}} + \psi_0 \frac{e^{ik|\boldsymbol{r}|}}{|\boldsymbol{r}|} \int_V \boldsymbol{F}(\boldsymbol{r'}) e^{-ik(\hat{\boldsymbol{r}}-\hat{\boldsymbol{z}})\cdot\boldsymbol{r'}} d^3\boldsymbol{r'}. \tag{2.28}$$

The solution given by Eq. 2.28 is referred to as the Born approximation. We note that the integral in this solution is a Fourier transform of the object's scattering potential $\boldsymbol{F}$. As illustrated by Fig. 2.4, the end points of the vector $k(\hat{\boldsymbol{r}} - \hat{\boldsymbol{z}})$ lies on a sphere with radius k, which is known as the Ewald sphere.

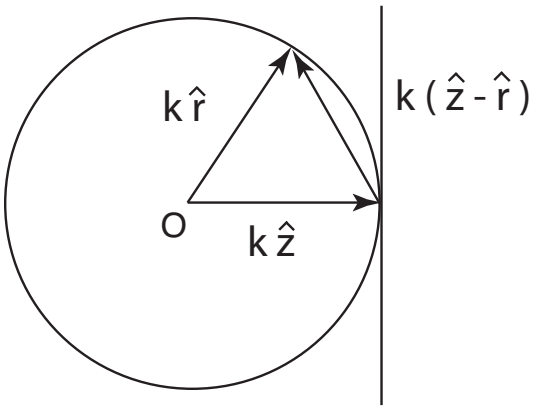

Figure 2.4: Ewald sphere of far field diffraction.

The validity limit of the Born approximation requires [36]

$$T|n-1| < 2\pi\lambda C_b, \tag{2.29}$$

where T is the thickness of the object and C_b is a constant ~ 0.2 [37]. For instance, at 520 eV ($\lambda = 2.38$ nm), the maximum thickness of protein within the Born approximation requirement is about 3 μm. Considering nearly 50% of the real cell is occupied by protein, this estimation roughly gives the maximum cell size that satisfies the Born approximation, which is about 6 μm.

Let's emphasize one more time that as defined by Eq. 2.22, the first term in Eq. 2.28 is the unscattered incident wave, and the second term is the scattered wave. By using the Born approximation, the incident wave is applied to the integral of the scattered term as the first order approximation, which means the incident beam is considered to be scattered only once under this condition.

For nonperiodic objects, the far field diffraction obtained by Eq. 2.28 does not distribute scattered signals into discrete Bragg peaks; instead it spreads out into a more continuous diffraction pattern.

When considering the diffraction pattern near the incident wave propagation axis ($\hat{\boldsymbol{z}}$ in the current discussion), the arc of the Ewald sphere can be modeled as a straight line, as shown in Fig. 2.4. In XDM experiments, the far field scattered wave front is collected by a CCD pixel array. In other words, the continuous diffraction pattern is sampled by a grid in Cartesian coordinates. For further analysis, we denote $\boldsymbol{r}$ and $\boldsymbol{r'}$ using Cartesian coordinate components as (x, y, z) and $(\xi, \eta, 0)$. The $\boldsymbol{r'} \cdot (\hat{\boldsymbol{r}} - \hat{\boldsymbol{z}})$ term in Eq. 2.28 can then be expressed as

$$\boldsymbol{r'} \cdot (\hat{\boldsymbol{r}} - \hat{\boldsymbol{z}}) = \frac{x\xi}{|\boldsymbol{r}|} + \frac{y\eta}{|\boldsymbol{r}|} \approx \frac{x\xi}{z} + \frac{y\eta}{z}. \tag{2.30}$$

where $|\boldsymbol{r}| \approx z$ is used for near axis condition.

Substituting Eq. 2.30 into Eq. 2.28, for a 2D measurement, we have

$$\boldsymbol{\psi}(x, y, z) = \psi_0 e^{ikz} + \psi_0 \frac{e^{ikz}}{z} e^{ik\frac{x^2+y^2}{2z}} \int\int \boldsymbol{F}(\xi, \eta) e^{-2\pi i(f_x\xi + f_y\eta)} d\xi d\eta, \tag{2.31}$$

where $k = 2\pi/\lambda$ is used, the spatial frequencies are defined as $f_x = x/(\lambda z)$ and $f_y = y/(\lambda z)$, and the label for the object area V is taken off, because the scattering potential function $\boldsymbol{F}$ is zero outside. $\boldsymbol{F}(\xi, \eta)$ represents the overall scattering potential of $\boldsymbol{F}(\boldsymbol{r'})$ viewed along the illumination direction.

In experiments with wavelengths shorter than microwaves, the detector can only record the intensities of the far field wave; the phase is lost. Furthermore, since scattering by the object tends to fall off with spatial frequency as f^{-4}, the dynamic range of the scattered radiation exceeds that of many detectors, so that the unscattered incident wave (the first term at the right side of Eq. 2.31) is usually blocked by a beamstop. We can then see that the measured intensity is proportional to the square of the Fourier transform modulus of the object's scattering potential, or

$$\begin{aligned} I(x, y) &= |\boldsymbol{\psi}(x, y, z)|^2 \\ &= \frac{{\psi_0}^2}{z^2} \left|\mathcal{F}\left[\boldsymbol{F}(\xi, \eta)\right]\right|^2, \end{aligned} \tag{2.32}$$

where I is the measured far field diffraction intensity. More specifically, as the scattering potential $\boldsymbol{F}$ is determined by the δ and β parameters in the refractive index (Eq. 2.21), we have

$$I(x,y) = C_F \left|\mathcal{F}\left[-\delta(\xi,\eta) + i\beta(\xi,\eta)\right]\right|^2, \tag{2.33}$$

where $C_F = k^4{\psi_0}^2/(4\pi^2 z^2)$ is a constant. From now on, the "object" o is denoted by $-\delta + i\beta$ of the specimen.

Suppose the CCD array size is N×N with pixel size $\Delta \times \Delta$ and corresponding pixel size $\Delta_r \times \Delta_r$ in real space. Eq. 2.33 can be rewritten using the form of discrete Fourier transform as

$$I(p\Delta, q\Delta) = \left|\sum_{n=0}^{N-1}\sum_{m=0}^{N-1} o(n\Delta_r, m\Delta_r) e^{-2\pi i(p\Delta\frac{n}{N} + q\Delta\frac{m}{N})}\right|^2, \tag{2.34}$$

where p and q are array pixel indices. Eq. 2.34 is accurate up to the multiplicative complex constant C_F.

2.2.3 Oversampling

In XDM experiments, only the magnitude (square root of intensity) of the diffraction pattern is measured, while all the phase information is lost. This is known as the phase problem. In order to reconstruct the object, the phase part needs to be recovered. This process cannot be done by using Eq. 2.34 itself. Other *a priori* information (constraints) is required for the object reconstruction.

According to Eq. 2.34, N^2 equations are given by the intensity measurement. Considering that a complex object has both δ and β values at each pixel, there are $2N^2$ unknown variables. So, the equations can only be solved by reducing the number of unknown variables by at least a factor of 2. This can be satisfied by requiring that the object is finite and isolated in an optically empty space from other scatterers. The area occupied by the object is commonly called "support"; the support area is required to be smaller than half size of the field of view, and this requirement is known as a finite support

constraint. If the object is purely real, according to the Friedel's law [38], its diffraction intensity is centrally symmetric, where the number of independent equations is N/2 with N unknown variables. The object is still required to be finite to reduce the unknown variable number by at least a factor of 2. As a result, in both cases the object needs to be localized in an area which is at most half the size of the entire array. This conclusion holds for 1D, 2D and 3D objects.

Let's consider how finely a CCD should sample the continuous diffraction pattern to ensure that all information is recorded. This question is answered by the Nyquist-Shannon sampling theorem [39, 40]. It states that the signal can be completely reconstructed when the sampling frequency is at least twice the highest frequency of the input signal.

Assume that the object in the current consideration is finite within a $n \times n$ array, or within the range of $[-n\Delta_r/2, n\Delta_r/2]$ in each direction, with pixel size in real space of Δ_r. The minimum signal period in reciprocal space from this object can be calculated by

$$p_{\text{min}} = \frac{2}{n\Delta_r}. \tag{2.35}$$

Suppose that the entire array size is N×N. So the pixel size in reciprocal space, or the sampling period, is

$$p_{\text{sampling}} = \frac{1}{N\Delta_r}. \tag{2.36}$$

The Nyquist-Shannon sampling theorem requires p_{sampling} is at most half of p_{min}, which gives

$$n \leq N. \tag{2.37}$$

As mentioned before, in order to have the phase information retrieved, the object size should be smaller than half of the entire array. In this 2D example, it requires $n^2 \leq N^2/2$, which is

$$n \leq \frac{N}{\sqrt{2}}. \tag{2.38}$$

We can see that Eq. 2.38 restricts the allowed object size more strongly than the Nyquist-Shannon sampling. In fact, further restrictions of the object size are helpful, and are characterized by an oversampling ratio σ_o [41]

$$\sigma_o = \frac{\text{entire image size}}{\text{object size}}, \tag{2.39}$$

which must be at least ≥ 2 for successful reconstructions. In the current example,

$$\sigma_o = \left(\frac{N\Delta_r}{n\Delta_r}\right)^2 = \frac{N^2}{n^2}. \tag{2.40}$$

The oversampling ratio can be determined in reciprocal space too. The diffraction speckles are sampled by CCD pixels. So, the oversampling ratio can also be obtained by

$$\sigma_o = \frac{\text{speckle size}}{\text{CCD pixel size}}. \tag{2.41}$$

Suppose that the CCD is located at a distance of z away from the object. The speckle dimension of the diffraction pattern can be calculated as

$$\Delta_s = \frac{\lambda z}{n\Delta_r}. \tag{2.42}$$

The CCD pixel size is related to the dimension of the field of view as

$$N\Delta_r = \frac{\lambda z}{\Delta}. \tag{2.43}$$

Then, using Eq. 2.42 and Eq. 2.43, the oversampling ratio calculated with the definition in Eq. 2.41 is

$$\sigma_o = \left(\frac{\Delta_s}{\Delta}\right)^2 = \frac{N^2}{n^2}, \tag{2.44}$$

which is consistent with the result from Eq. 2.39.

It should be mentioned that increasing the oversampling ratio does not give more information about the object, but adds more zero-value pixels outside the support area in real space. However, a larger oversampling ratio indeed helps to retrieve phases with less difficulty.

2.2.4 Phase retrieval

Phase recovery from the oversampled intensities is performed by iterative phase retrieval algorithms. The first phase recovery algorithm was invented by Gerchberg and Saxton [42], where it was used to recover phase from simultaneous intensity measurements in real and Fourier spaces. For recovery from Fourier plane data alone, various generalizations of the Gerchberg-Saxton algorithm have been proposed by Fienup [43, 44], Elser [45], and others [46–50].

The phase retrieval algorithms take different forms, but they share the same characteristics of iterating between pre-defined constraints. The most commonly used constraints are the Fourier modulus constraint in reciprocal space and the support constraint in real space. They are determined by two sets of *a priori* information: the measured diffraction magnitude (the Fourier modulus in reciprocal space), and the object being isolated in a finite area (the support area in real space).

Consider the output of each iteration as a point in Euclidean space, and the constraints as the subspaces satisfying corresponding requirements. Then the applications of constraints can be modeled as projection operators. These projection operators have two major properties: one is that their actions take the minimized path to project a point to the subspaces of the constraint sets, the other is that applying projections twice gives the same results as applying them once. For instance, the Fourier modulus projection π_m sets the magnitudes of a complex diffraction pattern to the measured values and maintain the phases in reciprocal space, and the support projection π_s is to set all the pixel values outside the support to zero in real space.

Various phase retrieval algorithms have been generated by using those defined projection operators. They are summarized in Table 2.1 with the algorithm list of error reduction (ER) [42], solvent flipping (SF) [46], hybrid input-output (HIO) [43], difference map (DM) [45], averaged successive reflections (ASR) [47], hybrid projection reflection (HPR) [48], relaxed averaged alternating reflectors (RAAR) [49], and relaxed averaged successive reactor (RASR) [50]. The reflectors of π_m and π_s are defined as $R_m = 2\pi_m - I$ and $R_s = 2\pi_s - I$, where I is the unity array.

Table 2.1: Various phase retrieval algorithms expressed in projection operators.

Algorithm	$o^{(n+1)}$
ER	$\pi_s\pi_m o^{(n)}$
SF	$R_s\pi_m o^{(n)}$
HIO	$[I-\beta\pi_m+\pi_s(\pi_m-I+\beta\pi_m)]o^{(n)}$
DM	$\{I+\beta\pi_s[(1+\gamma_s)\pi_m-\gamma_s I]$ $-\beta\pi_m[(1+\gamma_m)\pi_s-\gamma_m I]\}o^{(n)}$
ASR	$\frac{1}{2}(R_sR_m+I)o^{(n)}$
HPR	$\frac{1}{2}\{R_s[R_m+(\beta-1)\pi_m]$ $+I+(1-\beta)\pi_m\}o^{(n)}$
RAAR	$\left[\frac{1}{2}\beta(R_sR_m+I)+(1-\beta)\pi_m\right]o^{(n)}$
RASR	$(\pi_m-\beta R_m+\beta\pi_sR_m)o^{(n)}$

We note that when the algorithm parameter β equals 1, HIO, ASR, HPR, RAAR and RASR coincide. For DM algorithm, as the optimized values for γ_m and γ_s are β^{-1} and $-\beta^{-1}$ respectively, HIO becomes a special case of DM with $\beta=1$. Simulations on the comparisons between these algorithms [51, 52] conclude that the hybrid input-output (and hence the difference map as well) is the most efficient algorithm in the presence of noise.

2.3 Limitations and requirements of XDM

In a lens-based imaging system, the image quality is limited by the property of the lens. In this section, we will discuss the factors that limit the image quality in a lensless XDM system in terms of spatial resolution and depth of focus, what coherence level is required, and how to handle the missing data at the diffraction center and the floating phase ambiguity.

2.3.1 Resolution and depth of focus

The transverse spatial resolution is limited by the x-ray wavelength and the numerical aperture of the imaging system, which is determined by the maximum diffraction angle recorded for XDM. As shown in Fig. 2.5, with a N×N CCD of $\Delta\times\Delta$ pixel size which is placed at a distance of z away from the

object, the diffraction angle of the smallest feature that can be identified (normally, we consider the half-period transverse resolution σ_t, which has the half size of the smallest feature) is

$$\theta_{\max} \approx \sin(\theta_{\max}) = \frac{\lambda}{2\sigma_t}. \tag{2.45}$$

The maximum diffraction angle can also be calculated from the CCD size and CCD-to-sample distance as

$$\theta_{\max} \approx \tan(\theta_{\max}) = \frac{\frac{1}{2}N\Delta}{z}. \tag{2.46}$$

Combining Eq. 2.45 and Eq. 2.46, the diffraction limited transverse resolution of XDM can be obtained as

$$\sigma_t = \frac{\lambda z}{N\Delta}. \tag{2.47}$$

Note that σ_t equals the pixel size in real space Δ_r as calculated by Eq. 2.43, and this result differs from the resolution defined by the Rayleigh criterion (as discussed in Sec. 1.4.1) by a factor of 1.22.

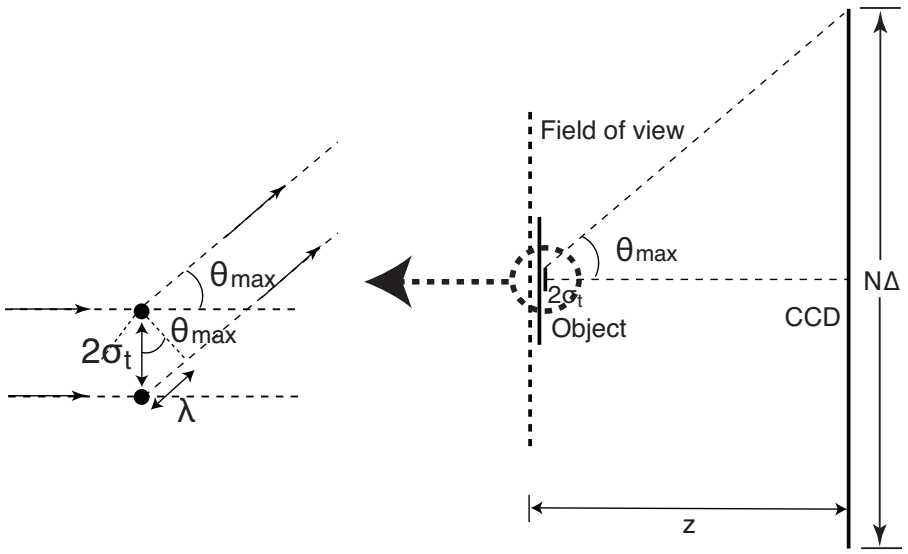

Figure 2.5: Schematic geometry of XDM resolution calculation.

The longitudinal resolution σ_l, or the depth of focus, can be calculated using Eq. 1.51. Using the experimental parameters, the numerical aperture is

N.A. $\approx \theta_{\max} = N\Delta/2z$. Then, σ_l is

$$\sigma_l = \frac{2\lambda z^2}{N^2\Delta^2}. \tag{2.48}$$

As an example, for 520 eV x-rays with λ =2.38 nm, z =15 cm, N = 1024 and Δ = 20 μm, which are typical for the XDM experiments described in this dissertation, the maximum achievable transverse resolution is about 17 nm, and the depth of focus is 0.26 μm. The field of view can be calculated using $N\sigma_t$ or Eq. 2.43, which gives 18 μm. We note that the depth of focus in this case is shorter than the typical cell dimension ($\sim$ 3 μm). However, the focal plane can be adjusted by refining the support shape or propagating the reconstructed wave front in real space.

2.3.2 Coherence requirement

X-ray sources in reality are quasi-monochromatic and finite in size, so that the well-defined phase relationships between points at the wave front are restricted to a finite region of coherence. This region is determined by dimensions in 2 directions: the temporal coherence (or longitudinal coherence) in the propagation direction, and the spatial coherence (or transverse coherence) in the transverse direction, as shown in Fig. 2.6.

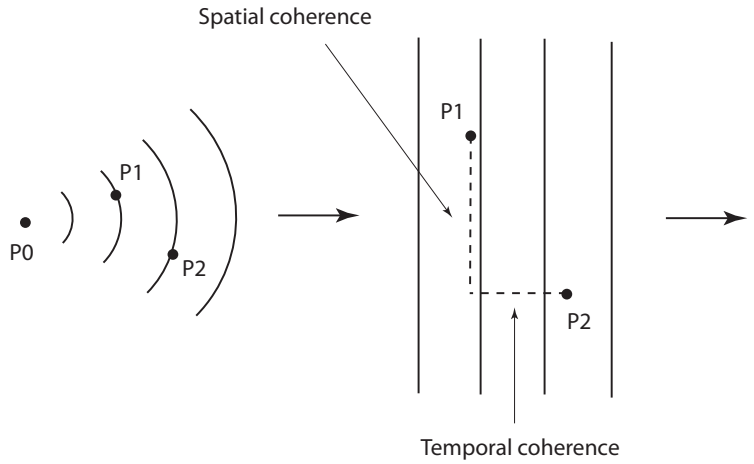

Figure 2.6: Spatial and temporal coherence.

The XDM experiments require that the spatial coherence length is at least the same size as the object. According to the van Cittert-Zernike theorem [3], a partially coherent source can be obtained from a non-coherent source by using an aperture. The illumination within the half radius of the central Airy disk of the pinhole aperture can be considered to be coherent. This approach was used in our XDM experiments. Using Eq. 1.49, we obtain the spatial coherence t_{coh} as

$$t_{\mathrm{coh}} = \frac{0.61\lambda z_{\mathrm{ph}}}{d_{\mathrm{ph}}}, \tag{2.49}$$

where z_{ph} is the distance from the pinhole to the sample, and d_{ph} is the diameter of the pinhole.

In the experiments, we placed a 5 μm pinhole 2.5 cm upstream of the specimen grid, so with 520 eV x-rays, $\lambda = 2.38$ nm, the spatial coherence width is about 14.5 μm. This satisfies the requirement of the typical specimen size which is about 3 μm.

The temporal coherence l_{coh} is defined as the length that causes a π phase shift for wave fronts with wavelengths differing by $\Delta\lambda$. Suppose that the wave front with wavelength λ travels m cycles in a distance of l_{coh}, or

$$l_{\mathrm{coh}} = m\lambda, \tag{2.50}$$

while the wave front with $\lambda + \Delta\lambda$ travels $m - 1/2$ cycles, or

$$l_{\mathrm{coh}} = (m - \frac{1}{2})(\lambda + \Delta\lambda). \tag{2.51}$$

Solving l_{coh} from Eq. 2.50 and Eq. 2.51, we have

$$l_{\mathrm{coh}} = \frac{\lambda^2}{2\Delta\lambda}. \tag{2.52}$$

We see the temporal coherence l_{coh} is proportional to $\lambda/\Delta\lambda$, which relates to the object size a and maximum diffraction angle θ_{max} by [53]

$$\frac{\lambda}{\Delta\lambda} \geq \frac{a}{\lambda}\sqrt{2\left[1 - \cos\left(2\theta_{\mathrm{max}}\right)\right]}. \tag{2.53}$$

Because the maximum diffraction angle $\theta_{\max}$ relates to the transverse spatial resolution σ_t by Eq. 2.45, Eq. 2.53 can be simplified in the small angle approximation as

$$\begin{aligned} \frac{\lambda}{\Delta\lambda} &\geq \frac{a}{\lambda}\sqrt{2\left[1-\cos\left(\frac{\lambda}{\sigma_t}\right)\right]} \\ &\approx \frac{a}{\sigma_t}. \end{aligned} \tag{2.54}$$

For instance, to achieve 10 nm resolution from a 3 μm specimen, it requires $\lambda/\Delta\lambda \geq 300$.

2.3.3 Missing center

The intense direct x-ray beam is blocked by a beamstop in XDM experiments. This leaves an area with no data value in the center of the diffraction pattern. The size of this missing center is typically 20×20 pixels. To reconstruct an object with a finite support, the lack of data in the diffraction center can bring ambiguities. As an example, considering that the Fourier transform of a Gaussian function is a Gaussian function, if the initial Gaussian function is sufficiently broad and within the support region in real space, its Fourier transform can be narrow enough to fit into the missing center in reciprocal space. In this case, this Gaussian function satisfies both the support constraint and the Fourier modulus constraint (as shown in Fig. 2.7), so it is unconstrained by known information in either space, and can potentially dominate the reconstructed image. Of course, other Fourier transform pairs beyond Gaussians can give rise to the same problem.

A method to select the unconstrained intensities was proposed by ranking the eigenvalues of a set of "constrained power operators" [54, 55] and subtracting the least constrained powers from the reconstructed images. An alternative method is to apply a high-pass filter to the diffraction pattern with a missing center to remove the intensity abruption caused by the beam stop [36]. The

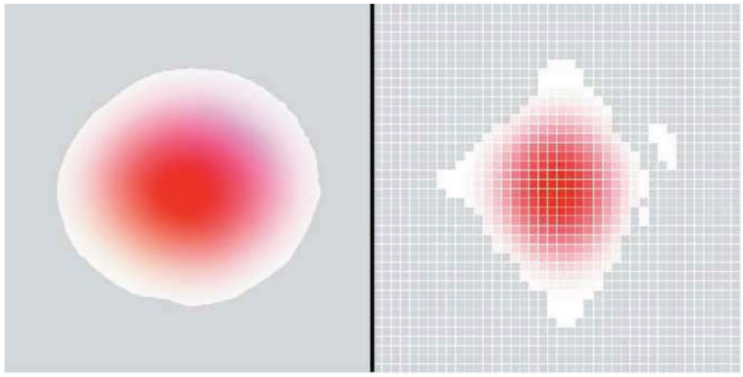

Figure 2.7: An example of a Gaussian function fitting both the support constraint in real space (left) and the Fourier modulus constraint in reciprocal space (right) [54].

filter function is

$$\text{Filter}(f) = \begin{cases} d_f + (1 - d_f)(f/r)^4 \exp\left(2 - 2f^2/r^2\right) & f < r \\ 1 & \text{otherwise,} \end{cases} \tag{2.55}$$

where f is the spatial frequency in reciprocal space, d_f is the depth of the filter with a value between 0 and 1 (smaller number means deeper), and r is the filter radius, which is normally less than 10% of the array width. The effect of this filter function is equivalent to the coherent image generated by a lens with a center stop, but it also convolves the image with the Fourier transform of the filter. It could increase the negative magnitude in the image, and cause the support to be slightly larger.

2.3.4 Global phase

Another type of ambiguity comes from the fact that only the intensity of the diffraction pattern is measured. It is because the measured far field diffraction pattern, or the Fourier modulus of the object as expressed by Eq. 2.34, is not sensitive to multiplicative constant phase factors, translations and twin images

(complex conjugation plus 180° rotation), or

$$\begin{aligned} |\mathcal{F}[o(x,y)]| &= \left|\mathcal{F}\left[e^{i\phi}o(x-x_0,y-y_0)\right]\right| \\ &= \left|\mathcal{F}\left[e^{i\phi}o^*(-x-x_0,-y-y_0)\right]\right|. \end{aligned} \tag{2.56}$$

In an image reconstruction process, if the support is well defined in real space, the translation ambiguity is then removed. If the object shape is not central symmetric, there will be no twin image problem. However, the arbitrary phase offset factor $\exp(i\phi)$ always exists.

This random phase variation has to be adjusted to a common value to minimize the magnitude reduction during the averaging process in reconstruction. We calculate this global phase following Fienup's method [56]. Consider the normalized difference caused by the phase factor $\exp(i\phi)$

$$\begin{aligned} E^2 &= \frac{\sum \left|e^{i\phi}o - o\right|^2}{\sum |o|^2} \\ &= \frac{2\sum |o|^2 - \left(e^{i\phi}\sum oo^* + c.c.\right)}{\sum |o|^2} \\ &= \frac{2\sum |o|^2 - 2\mathcal{R}\left(e^{i\phi}\sum oo^*\right)}{\sum |o|^2}, \end{aligned} \tag{2.57}$$

where *c.c.* denotes for complex conjugate of the preceding term, and $\mathcal{R}$ stands for the real part of a complex value. To minimize this error, we should maximize the second term in the numerator by setting $\phi = -\varphi$, where φ is the phase of the complex value $\sum oo^*$.

If $o^{(n)}$ is the first term in the averaging process, the initial phase factor ϕ_0 is set to be the phase of $\sum o^{(n)}o^{*(n+1)}$ with the opposite sign. Similarly, the phase factors ϕ_m for subsequent terms are the phases of $\sum o^{(n)}o^{*(m)}$ with the opposite sign.

Chapter 3

Simulations on XDM

The previous chapter described the beauties as well as the challenges of x-ray diffraction microscopy (XDM), in this chapter we discuss some subtleties of this technique through numerical simulations, including comparison with conventional x-ray microscopy in the aspect of signal-to-noise ratio, radiation dose requirement for achieving given resolution, how phase retrieval algorithms handle improperly defined supports, and the stagnation caused by the missing center in reciprocal space.

3.1 Signal-to-noise ratio comparison

Using a signal-to-noise ratio estimation based on correlations between multiple simulated images, we compare the dose efficiency of two soft x-ray imaging systems: incoherent brightfield imaging using zone plate optics in a transmission x-ray microscope (TXM), and x-ray diffraction microscopy (XDM). In XDM one must computationally phase weak diffraction signals; in TXM one suffers signal losses due to the finite numerical aperture and efficiency of the optics.

In this section we address the following question through simulations: which approach yields more information on example biological specimens for a given radiation dose? This is an important consideration for radiation-sensitive specimens such as frozen hydrated cells, since similar to electron microscopy radiation damage is the resolution-limiting factor. We find that XDM has the potential for delivering equivalent resolution images using fewer photons. This can be an important advantage for studying radiation-sensitive biological and soft matter specimens. This SNR simulation and the dose requirement calculation discussed in Sec. 3.2 have been published [57].

3.1.1 Signal and noise in images

The signal-to-noies ratio, or SNR, of 2D images was defined by Rose [58, 59] as the square root of the total number of photons removed from or added into an object area. The SNR calculated from this definition is not sensitive to the structure variations inside the object, and in reality the dimension of the object is unknown in advance. Instead, we estimate SNR of images based on image correlations in the presence of signal-dependent noise. This method gives SNR values that scale with incident photon number as expected, and it is used in subsequent SNR calculations on simulated images.

SNR, and object detection

We wish to consider the signal-to-noise ratio for the detection of an object with a specified contrast. We follow here the treatment of Glaeser [60] and of Sayre *et al.* [61]. Our goal is to distinguish measurements (such as image pixels) in the

case that a unit-incident-flux measurement would lead to a measured intensity of I. To detect an object, assume that the signal is given by the difference between an intensity with a feature present I_f, and the background intensity I_b; that is, the average signal is $\bar{n}|I_f - I_b|$ when each measurement is made with $\bar{n}$ incident photons. In the Gaussian approximation to the Poisson distribution for event counting, the noise can be expressed as the square root variance of each measurement $\sqrt{\bar{n}I}$, and if the noise is uncorrelated from measurement to measurement (which is the case for photon noise) the total noise will be given by the root mean square sum. As a result, the expected signal-to-noise ratio (SNR) is

$$\mathrm{SNR} = \frac{\mathrm{Signal}}{\mathrm{Noise}} = \frac{\bar{n}|I_f - I_b|}{\sqrt{(\sqrt{\bar{n}I_f})^2 + (\sqrt{\bar{n}I_b})^2}} = \sqrt{\bar{n}}\frac{|I_f - I_b|}{\sqrt{I_f + I_b}} = \sqrt{\bar{n}}\,\Theta, \tag{3.1}$$

where Θ of

$$\Theta = \frac{|I_f - I_b|}{\sqrt{I_f + I_b}} \tag{3.2}$$

is a contrast parameter [61] which differs slightly from the usual definition of contrast C as

$$C = \frac{|I_f - I_b|}{I_f + I_b}. \tag{3.3}$$

Based on Eq. 3.1, a log-log plot of SNR versus incident photon number $\bar{n}$ should follow a straight line with a slope of 1/2 and an ordinate intercept of $\log_{10}\Theta$:

$$\log_{10}\mathrm{SNR} = \log_{10}(\sqrt{\bar{n}}\Theta) = \frac{1}{2}\log_{10}\bar{n} + \log_{10}\Theta. \tag{3.4}$$

SNR estimation from image correlations

The easiest way to measure signal-to-noise ratio is to compare measured images of an object against the known object itself. While this approach can be used in simulations, we wish to employ a method that can be used in experiments where the object is not known except through images that have been obtained. An intuitive approach is to calculate the cross correlation coefficient of two independent images of the same object, so as to compare features that are

reproduced against those that fluctuate. We summarize here an approach described by Bershad and Rockmore [62] and first used in electron microscopy by Frank and Al-Ali [63]. We extend this method to signal-dependent noise cases, and without the requirement of zero-mean signal.

Let us consider two separate 2D intensity measurements I_1 and I_2 of the same signal array S with stochastic noise arrays N_1 and N_2, or

$$I_1 = S + N_1 \qquad \text{and} \qquad I_2 = S + N_2, \tag{3.5}$$

where the mean value of S over all 2D pixels is $\langle S \rangle$, and N_1 and N_2 come from the same source obeying the same Gaussian distribution with zero mean value ($\langle N_1 \rangle = \langle N_2 \rangle = 0$). Consequently, $\langle I_1 \rangle = \langle I_2 \rangle = \langle S \rangle$. Detailed derivation steps can be found in Appendix B.

For 2D images, the object visibility depends on how much the signal differs from noise level and its background. Based on this consideration, we define the total signal and total noise for the entire 2D image by their variances:

$$\text{Signal}^2 = \langle (S - \langle S \rangle)(S - \langle S \rangle)^* \rangle = \langle S^2 \rangle - \langle S \rangle^2, \tag{3.6}$$

$$\text{Noise}^2 = \langle (N_{1,2} - \langle N_{1,2} \rangle)(N_{1,2} - \langle N_{1,2} \rangle)^* \rangle = \langle N_{1,2}^2 \rangle, \tag{3.7}$$

where $\langle N_{1,2} \rangle = 0$ has been used in the final equality of Eq. 3.7. Again, the average is done over all pixel indices of the 2D image, which differs from variance calculation for each pixel with a stack of images. The variances of images I_1 and I_2 can be calculated as

$$\begin{aligned} {\sigma_{1,2}}^2 &= \langle (I_{1,2} - \langle I_{1,2} \rangle)(I_{1,2} - \langle I_{1,2} \rangle)^* \rangle \\ &= \langle S^2 \rangle + \langle N_{1,2}^2 \rangle - \langle S \rangle^2, \end{aligned} \tag{3.8}$$

where we used the fact that the cross terms $\langle S N_{1,2}^* \rangle$ and $\langle S^* N_{1,2} \rangle$ are in practice negligible compared to $\langle S S^* \rangle$. This would be expected for low contrast objects, but in practice it also applies to cases with objects with high contrast; in simulations, we find that $\langle S N_{1,2}^* \rangle$ and $\langle S^* N_{1,2} \rangle$ are several orders of magnitude lower than $\langle S S^* \rangle$ even with full contrast object. As a result, we are able

to drop the terms $\langle SN_{1,2}^* \rangle$ and $\langle S^* N_{1,2} \rangle$ in Eq. 3.8 to obtain the final result listed above. Since N_1 and N_2 obey the same Gaussian distribution, they have identical variances ($\langle N_1^2 \rangle = \langle N_2^2 \rangle$). So, we can denote $\sigma_1 = \sigma_2 = \sigma$. The covariance between I_1 and I_2 can be derived following analogous steps:

$$\begin{aligned} r\sigma_1\sigma_2 = r\sigma^2 &= \langle (I_1 - \langle I_1 \rangle)(I_2 - \langle I_2 \rangle)^* \rangle \\ &= \langle S^2 \rangle - \langle S \rangle^2, \end{aligned} \tag{3.9}$$

where r is the correlation coefficient. It can be calculated as

$$r = \frac{\langle (I_1 - \langle I_1 \rangle)(I_2 - \langle I_2 \rangle)^* \rangle}{\sqrt{\langle (I_1 - \langle I_1 \rangle)^2 \rangle \langle (I_2 - \langle I_2 \rangle)^2 \rangle}}. \tag{3.10}$$

Combining Eqs. 3.6 and 3.7 with Eq. 3.8, we have

$$\sigma^2 = (\langle S^2 \rangle - \langle S \rangle^2) + \langle N_{1,2}^2 \rangle = \text{Signal}^2 + \text{Noise}^2. \tag{3.11}$$

From Eqs. 3.6 and 3.9, we have

$$r\sigma^2 = \langle S^2 \rangle - \langle S \rangle^2 = \text{Signal}^2. \tag{3.12}$$

From Eq. 3.11 and Eq. 3.12, we see that the signal-to-noise ratio can be calculated from the correlation coefficient r as

$$\text{SNR} = \sqrt{\frac{\text{Signal}^2}{\text{Noise}^2}} = \sqrt{\frac{r}{1-r}}. \tag{3.13}$$

which is the square root of the expression $\alpha = r/(1-r)$ used by Frank and Al-Ali [63].

Simulation of signal-dependent noise in images

To explore signal to noise effects in photon-limited imaging, we need to be able to generate images with simulated noise. We begin with an image with K pixels and a set of intensities $\{I_k\}$ before noise is added. To include signal-dependent noise, we employ two alternative approaches for implementation in

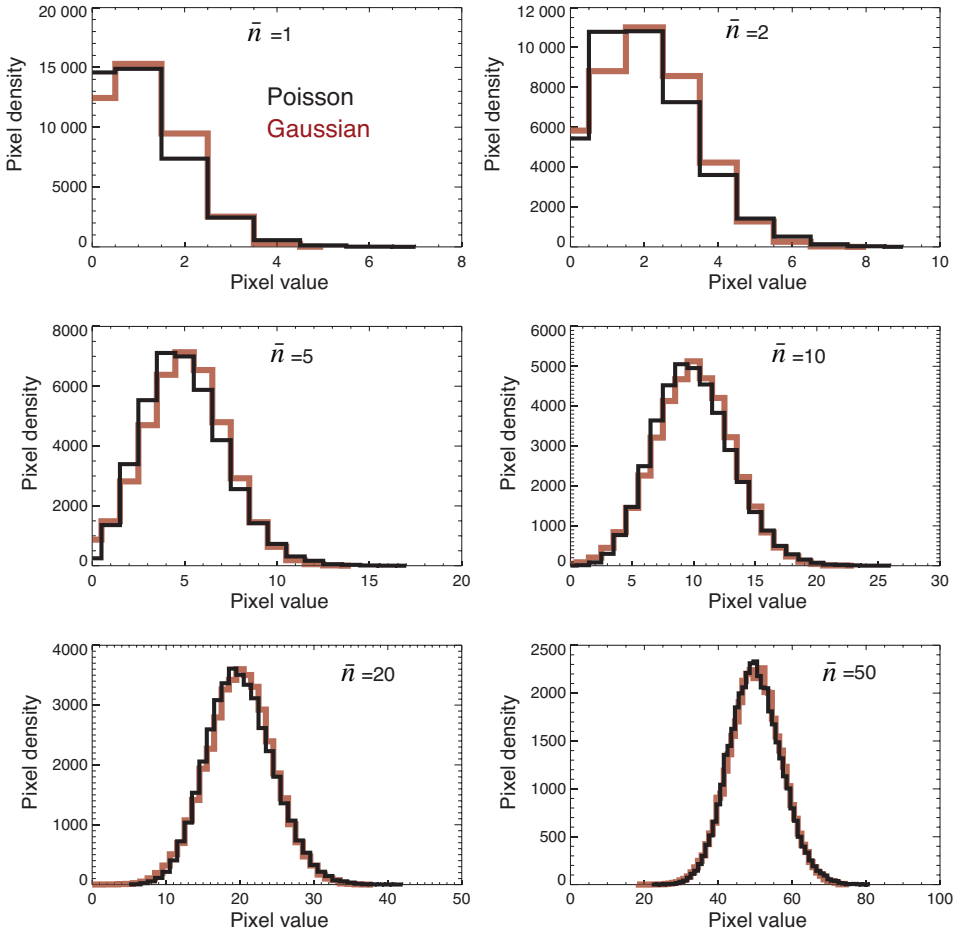

Figure 3.1: Histograms of photon noise simulated according to the two approaches described in the main text. A Gaussian approximation works very well for $\bar{n} \geq 10$. The histograms for these simulated images are identical to the expected distribution.

the IDL programming environment (Research Systems, Inc.):

1. One approach is to use IDL's `randomn()` routine with the `poisson` keyword. For this case, we have to give `randomn()` each value I_k to generate a noise-included value $I_{n,k}$, and thereby arrive at a noise-included set $\{I_{n,k}\}$.

2. Another approach is to use the fact that the Gaussian approximation provides a very good representation of the Poisson distribution for expected counts of $\bar{n} \geq 20$. Since in the Gaussian approximation the variance of the photon noise σ_d^2 is equal to the number of photons I_k in each of K pixels, we can approximate the set of signal-dependent noise values $\{N_{d,k}\}$ as

$$\{N_{d,k}\} = \sqrt{\{I_k\}} \cdot \{r_{d,k}\}, \tag{3.14}$$

   where we use a Gaussian-distributed zero-mean random number set $\{r_d\}$ in the calculation as provided by the IDL routine `randomn()`. We then arrive at a noise-included set of

$$\{I_{n,k}\} = \{I_k\} + \{N_{d,k}\}, \tag{3.15}$$

   which we must then constrain to have non-negative values to correct for possible "tails" of the Gaussian distribution at small values of I_k.

In both cases, the `randomn()` routine is used with an initial seed generated from the system clock as `seed=long(systime(/seconds))`. In Fig. 3.1, we show the histograms of flatfield images with 200^2 pixels and various values of $\bar{n}$ using both of the methods mentioned above.

Test with Lena's picture

To confirm that Eq. 3.13 provides a good measure of the SNR from multiple noisy images of identical objects, we used simulations to explore its scaling with photon number. As an "object" we used the well-known "Lena" image with transparency I normalized between 0 and 1. For each calculational run we multiplied the image by a value of $\bar{n}$, and then added to each pixel p

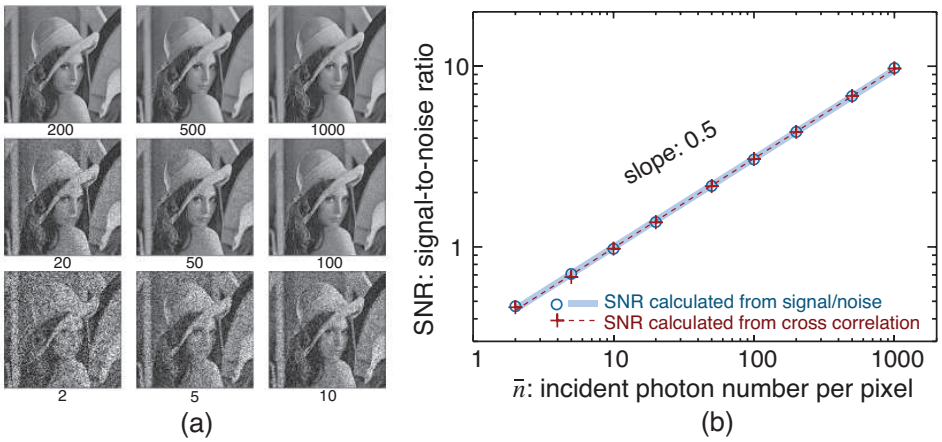

Figure 3.2: (a) Images with noise simulated according to different mean photon numbers per pixel $\bar{n}$. Without noise, each pixel p has a value I_p of between 0 and 1. With illumination of $\bar{n}$ photons per pixel, each pixel has a starting value of $\bar{n}I_p$ photons which was used on a pixel-by-pixel basis to generate an image using signal-dependent noise calculated using the positive-integer-truncated Gaussian method described. (b) signal-to-noise ratio (SNR) calculated from the images versus incident photon number per pixel $\bar{n}$. The signal-to-noise ratio was calculated both by comparison of the noisy image with the noise-free original image described in Eqs. 3.6 and 3.7, and by using the two-noisy-image correlation method described in Eqs. 3.10 and 3.13. Since a fit of the data on a log-log plot of SNR versus $\bar{n}$ shows a slope of 0.5 as expected from Eq. 3.4, both image SNR methods give the expected scaling of SNR versus exposure $\bar{n}$.

a pseudo-random noise value based on a positive-integer-truncated Gaussian approximation of the true Poisson distribution for each pixel's value of $\bar{n}I_p$. By repeating this process, we obtained two images of an identical object but with different signal-dependent noise added, allowing us to measure the image SNR using the cross-correlation result of Eqs. 3.10 and 3.13. Figure 3.2(a) shows the resulting images with noise corresponding to the indicated number $\bar{n}$ of incident photons per pixel. Figure 3.2(b) shows that a log-log plot of the calculated SNR values as a function of $\bar{n}$ has slope of 1/2 as expected from Eq. 3.4, reflecting the $\sqrt{\bar{n}}$ dependence of SNR on incident exposure expected from Eq. 3.1. Finally, we also show in Fig. 3.2(b) the signal-to-noise ratio calculated by comparison of the original, noise-free image with a noise-included version at each photon exposure $\bar{n}$ using Eqs. 3.6 and 3.7. We can see that the SNR values calculated with the definitions of signal and noise are identical to those calculated from the correlation method. However, in subsequent calculations we use the two-noisy-image correlation method of Eqs. 3.10 and 3.13 because it is applicable to a broader range of cases including experiments where the noise-free object is not known.

3.1.2 Simulations with defined "cells"

Having established the positive-integer-truncated Gaussian method for adding signal-dependent noise to data recordings, and the image correlation method of Eqs. 3.10 and 3.13 for estimating SNR from image pairs, we now turn to simulations of the two experimental approaches to be compared (Fig. 3.3): lens-based imaging (incoherent brightfield imaging in a TXM), and lensless imaging (x-ray diffraction microscopy or XDM).

Defined "cells" A and B

We generated two different types of biological-cell-like defined objects for our simulations, which we will call cell A and cell B (see Fig. 3.4). In both cases we assumed an x-ray energy of 520 eV (within the "water window" [18, 61] between the carbon and oxygen K absorption edges), and values of the refractive index calculated according to the tabulation of Henke *et al.* [4] using

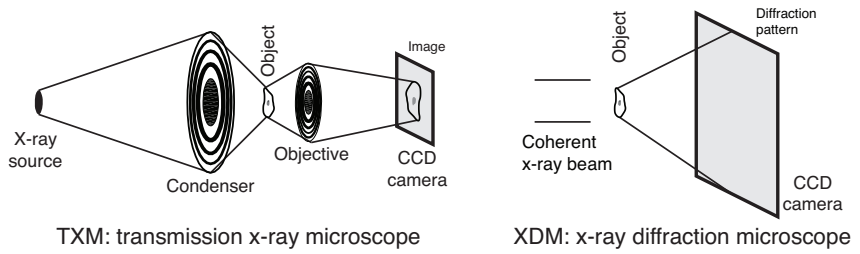

Figure 3.3: Schematic of the two x-ray imaging systems considered in simulations. In the TXM or transmission x-ray microscope at left, incoherent brightfield imaging is assumed where the numerical aperture of the condenser is 1.5 times the numerical aperture of the objective lens; a magnified image is recorded on a detector such as a CCD. The TXM objective is a zone plate with 30 nm outermost zone width and 10% diffraction efficiency. In XDM or x-ray diffraction microscopy at right, the specimen is assumed to be illuminated by a fully coherent beam and the far-field x-ray diffraction pattern is recorded on a detector such as a CCD. A reconstructed image is obtained by computational phasing of the coherent diffraction pattern.

an assumed stoichiometric composition of $H_{48.6}C_{32.9}N_{8.9}O_{8.9}S_{0.3}$ and density of $\rho = 1.35$ g/cm^3 for protein, and $H_{62.5}C_{31.5}O_{6.3}$ with $\rho = 1.0$ g/cm^3 for lipid [64]. The two objects were defined as follows:

Cell A is modeled as a 2D continuous region with irregular boundary and random protein thicknesses over a range of 0 to 500 nm inside (Fig. 3.4(a)). The entire image is a 256×256 pixel array with a pixel size of 15 nm.

Cell B is embedded in the center of a $400 \times 400 \times 400$ pixel ice cube, also with a pixel size of 15 nm. The cell-like object has a diameter of 200 pixels, or 3 microns, with a 3 pixel or 45 nm thick lipid membrane as boundary. Inside the object, several 225 nm diameter protein rods were placed (1.8 μm long for the vertical bars, and 1.35 μm long for the horizontal bars), along with some protein ellipsoids (the larger ones are 0.9×0.45 μm, and the smaller ones are 0.68×0.45 μm in size). A "bud" with a diameter of 1.2 μm was added to the top right shoulder of this fake cell, both in order to break the rotational symmetry for eliminating potential problems with enantiomorphs in XDM, and to approximate the appearance of a budding yeast cell. This object was then assumed to be illuminated by a plane wave, and a multislice propagation

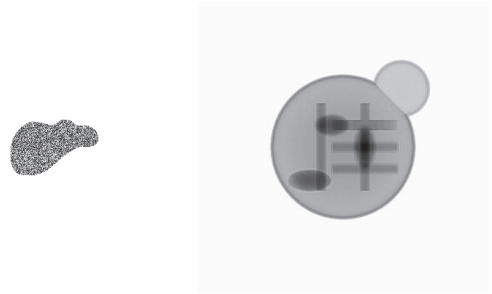

Figure 3.4: Defined objects used for image simulations. Shown here is the magnitude of the simulated exit wave resulting from plane wave illumination of the object. Cell A has random protein thicknesses within an irregular boundary, while Cell B has a lipid membrane and several protein bars and ellipses inside.

process [54, 65] was used to generate an exit wave (400×400 pixels across) leaving the cube.

In the case of cell A, we have a defined object with broad spatial frequency content due to the random thickness variations inside. In the case of cell B, we have an object with readily recognized structures. The two defined objects are shown in real space in Fig. 3.4, and in Fourier space in Fig. 3.5. To compare zone plate imaging with diffraction microscopy, we simulated both imaging techniques on these two different defined objects.

Zone plate imaging process

X-ray microscopes using synchrotron radiation and Fresnel zone plates for full-field imaging have been in existence for some time [24], and are finding considerable success for 25–40 nm resolution imaging applications and tomographic imaging of frozen hydrated cells [27, 28, 66], with commercial laboratory source versions now becoming available [67]. We model here a representative microscope with a Fresnel zone plate with 30 nm outermost zone width and 10% diffraction efficiency [68], used in incoherent brightfield mode with a 100% efficient detector. In this case the recorded image intensity can be obtained using Eq. 2.13.

For a zone plate with outermost zone width of dr_N (set to be 30 nm in

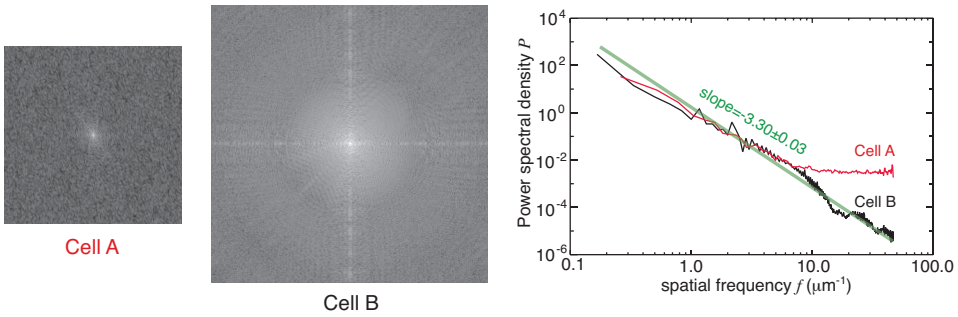

Figure 3.5: Diffraction patterns of the exit waves from the two defined objects, cell A and cell B, and their azimuthally averaged, unit-integral-normalized power spectral densities. In both cases the exit wave amplitude was Fourier transformed and then squared to yield the diffraction intensity. Both defined objects have the signal decline with spatial frequency in a power law relationship with a slope of about 3.3 over most frequencies. For cell A, this trend then levels off at a spatial frequency of about 10 μm^{-1} where the pixel-by-pixel uncorrelated protein thickness dominate the diffraction pattern; this yields a flat power spectrum corresponding to a delta (δ) function in real space. For cell B, the overall round shape of the object gives rise to Airy rings in the diffraction pattern which show up at spatial frequencies above 10 μm^{-1}.

simulation), the cutoff of the incoherent MTF is at a spatial frequency of $f_0 = 1/dr_N$. The integral of Eq. 2.12 has a numerical value of 0.20 compared to the integral of a MTF of 1 for all frequencies up to a cutoff at f_0. The resulting image intensity was then multiplied by 0.10 to account for a typical zone plate focusing efficiency of 10% (while theoretical efficiencies can approach 20%, 10% is representative of the best experimental measurements). Finally, the resulting image was multiplied by an exposure of $\bar{n}$ photons per pixel, and simulated photon noise was added using the positive-integer-truncated Gaussian approach to yield a final image.

Reconstruction from diffraction pattern

In x-ray diffraction microscopy, the image is reconstructed from the far-field diffraction intensity of a coherently illuminated object which is assumed to be within a finite support (area of non-zero optical interaction). To simulate the imaging process, the complex exit wave amplitude leaving the defined object

was multiplied by $\sqrt{\bar{n}}$ to account for an exposure of $\bar{n}$ photons per pixel, after which it was Fourier transformed to yield the far-field diffraction amplitude. This diffraction amplitude was then squared to yield the diffraction intensity, and simulated photon noise was added using the positive-integer-truncated Gaussian approach to produce a simulated data recording. The diffraction patterns were assumed to be recorded in the far field, with proper Shannon sampling between the real-space object array and the Fourier plane detector array (that is, 256^2 detector pixels for Cell A, and 400^2 detector pixels for Cell B). The pixel size in the reconstructed image is 15 nm. To reconstruct the image, we took the square root of the noisy diffraction intensity to revert to Fourier amplitude, and then reconstructed the image using the difference map algorithm developed by Elser [45] with $\beta = 1.15$.

3.1.3 SNR simulation results

We carried out simulation runs for each of the two defined objects (cell A and cell B), using both TXM and XDM, and using incident photon per pixel values of $\bar{n} = \{1, 2, 5\} \times 10^{\{1,2,3,4,5\}}$ and 1×10^6 (that is, exposures of 1×10^1, 2×10^1, ..., 1×10^6). Fig. 3.6 shows some examples of simulated zone plate and reconstructed diffraction images. For each incident photon number $\bar{n}$, we calculated 10 TXM images and 10 XDM images, each with separate simulated signal-dependent photon noise in the intensity recording. From each set of 10 images, one can form 45 separate two-image pairs for calculating the SNR using the method of Eqs. 3.10 and 3.13 over the region where the object is located (that is, inside the object's support for both the XDM and TXM cases). The final SNR value was calculated from the average of these 45 measurements.

Figure 3.7 shows a plot of $\log_{10}(\text{SNR})$ versus $\log_{10}(\bar{n})$ for the set of image simulations of both defined objects. As can be seen, in all cases the slope of the fitted line is near 1/2, as expected from Eq. 3.4; in other words, the signal-to-noise ratio is proportional to $\sqrt{\bar{n}}$ as expected from Eq. 3.1. An important difference is that x-ray diffraction microscopy gives a higher SNR for a given photon exposure $\bar{n}$ in these simulations. For zone plates of 10% efficiency and an incoherent brightfield MTF integral about 0.2 as described in Sec. 3.1.2,

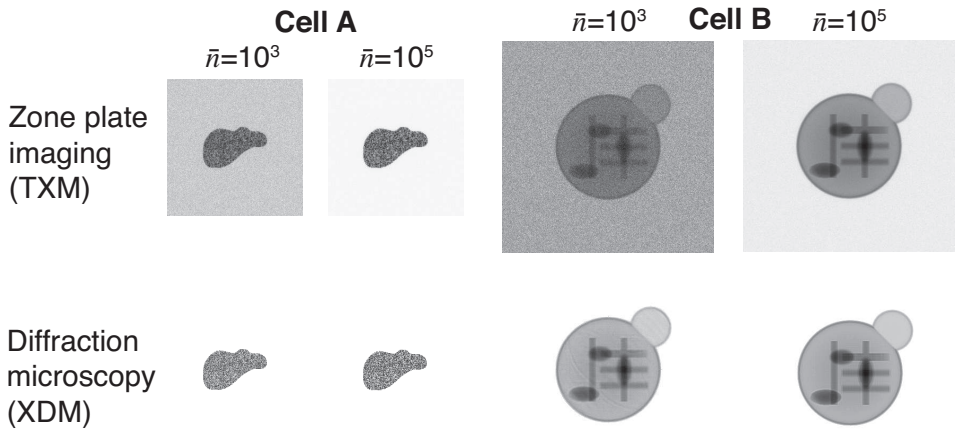

Figure 3.6: Images resulting from the simulations. Shown here are both TXM (top row) and XDM (bottom row) images calculated for the two defined objects, cells A and B, with exposures of $\bar{n} = 1 \times 10^3$ and $\bar{n} = 1 \times 10^5$ photons per pixel. The lack of "salt and pepper" shot noise in background region outside of the cell in the XDM reconstructions is a result of the imposition of a finite support constraint in the reconstruction process.

one might expect an improvement of about $1/(0.1 \times 0.2) = 50$ in signal, or an improvement of $\sqrt{50} \simeq 7$ in the signal-to-noise ratio. The fitted lines of Fig. 3.7 are indeed higher for x-ray diffraction microscopy versus transmission x-ray microscopy, with an improvement of XDM/TXM of 7.2 ± 1.6 for cell A, and 6.3 ± 2.1 for cell B. This means that the iterative reconstruction algorithms used in x-ray diffraction microscopy are able to phase even weak diffracted signals with significant signal-dependent photon noise present; this is consistent with an early observation by Fienup [43] who found that finite support phase retrieval algorithms appeared to be quite robust in the presence of signal-independent noise added to the Fourier magnitudes.

As noted in Fig. 3.7, the $\log_{10}(\mathrm{SNR})$ versus $\log_{10}(\bar{n})$ dependence of cell B shows some oscillations about the linear trend. This oscillation corresponds to successive Airy rings in the diffraction pattern of the overall spherical shape of cell B, as shown in Fig. 3.5. In the dark bands between Airy rings corresponding to the far-field diffraction pattern of a disk, the signal is lower than the ring-free trend would suggest so the addition of more photons is less helpful

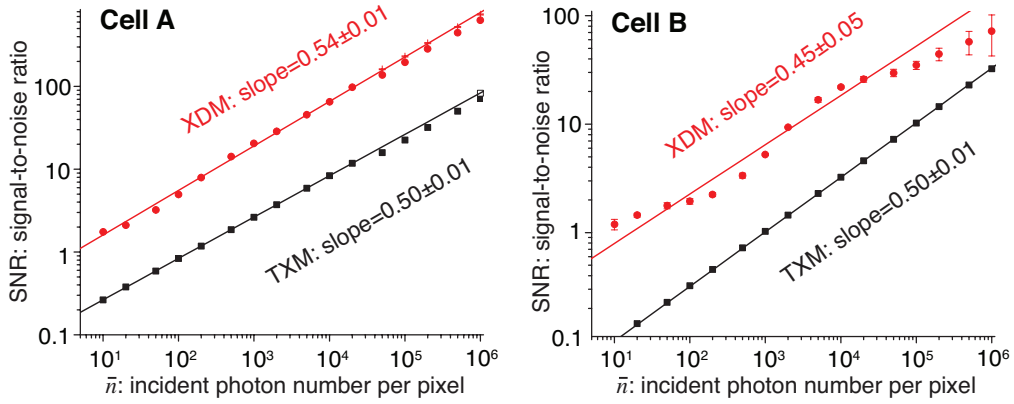

Figure 3.7: Plot of the signal-to-noise ratio SNR as a function of incident photons per pixel $\bar{n}$ for our simulation set. The results at left are for the defined object "cell A", while those at right are for "cell B" (see Fig. 3.4). The results for both x-ray diffraction microscopy (XDM) and transmission x-ray microscopy (TXM) are shown. In all cases a slope of about 1/2 is observed in the $\log_{10}(\text{SNR})$ versus $\log_{10}(\bar{n})$ plot (Eq. 3.4), and for both objects the SNR for x-ray diffraction microscopy is about 7 times higher than it is for transmission x-ray microscopy. For x-ray diffraction microscopy of cell B, the SNR curve oscillates around the straight line fit. This oscillation corresponds to providing enough signal to phase data in successive Airy rings in the diffraction pattern of the overall spherical shape of cell B, as shown in Fig. 3.5.

until the next Airy ring begins to be filled in. A different effect can be seen in the $\log_{10}(\text{SNR})$ versus $\log_{10}(\bar{n})$ curve for cell A: as shown in Fig. 3.5, the normalized power spectrum for cell A "levels off" at a constant value of about 10^{-2} at spatial frequencies f above about 10 μm^{-1}. This suggests that when the incident photon number $\bar{n}$ is larger than 100, all the diffraction intensity pixel values approach 1 so that all spatial frequencies above 10 μm^{-1} have measurable, single-photon or larger intensities. and start to contribute to increase reconstruction quality. This may explain the slight flattening of the $\log_{10}(\text{SNR})$ versus $\log_{10}(\bar{n})$ curve at the lowest photon exposures for cell A in x-ray diffraction microscopy (XDM).

Although in these simulations we had perfect knowledge of the object that was "imaged," we chose to adopt a cross-correlation method for quantitative comparisons that is better suited to experimental work with unknown objects. Following the work of Bershad and Rockmore [62], we modified the signal-to-noise measure of Frank and Al-Ali [63] with the result that our measure gives the expected scaling with incident photon number $\bar{n}$. We then used this measure to compare incoherent brightfield imaging in a transmission x-ray microscope with a zone plate objective lens of specified efficiency versus x-ray diffraction microscopy using an iterative phase retrieval algorithm for image reconstruction. In these simulations, x-ray diffraction microscopy gave a higher signal-to-noise ratio for equivalent dose, with a gain consistent with the losses imposed by the modulation transfer function and overall efficiency of the zone plate objective.

Of course these simulations are idealized; real imaging experiments involve a number of factors not accounted for here. One of them is that transmission x-ray microscopy has the significant advantage of providing images immediately, unlike x-ray diffraction microscopy where one must use sophisticated image reconstruction algorithms, and specimens that satisfy a finite-support constraint (though we note that ptychography can remove that latter limitation [69]). A limitation of transmission x-ray microscopy as well as its scanning "cousin" is that the resolution-determining outermost zones on zone plates usually have a lower diffraction efficiency than the coarser, inner zones. In x-ray diffraction microscopy, complications include undesired scattering from nearby

high-contrast objects such as specimen support grid bars, and the detrimental effects of partial coherence which can contribute noise to reconstructed images [70]. Nevertheless, the simulations shown here illustrate how x-ray diffraction microscopy has the potential to deliver images with higher resolution when studying dose-sensitive specimens.

3.2 Radiation dose requirement

In Sec. 1.4.3, we showed that the radiation dose D is proportional to the incident photon number per pixel $\bar{n}$, as expressed in Eq. 1.52. When combined with a method to estimate resolution of reconstructed images from the phase retrieval transfer function [55], the simulated images for SNR comparison can be actually used to study how much dose is required for achieving certain resolution. This question is important, because radiation damage is one of the major effects that limits the achievable resolution for radiation sensitive specimens, such as biological or soft matter samples.

3.2.1 Power density curve slope

As shown in Fig. 3.5, the azimuthally-averaged diffracted signal $P(f)$ in our defined objects declines in a power law relationship of $\log_{10} P(f) = m \log_{10} f + b$ or

$$P(f) = 10^b f^m \tag{3.16}$$

with $m = -3.3$ (azimuthal averaging smooths out the sharp variations due to individual speckles to reveal an overall scattering trend). Theoretical estimates for signal decline in x-ray diffraction microscopy have ranged from $m = -4$ [21], to $m = -3$, -4, and -6 for various specimen models [20]. In small angle x-ray scattering, Porod's law suggests that the diffraction signal should decline with spatial frequency as f^m with $m = -4$, while measured power spectra tend to have positive deviations from this dependence (*i.e.*, values of m of -3 to -4).

As the diffracted signal for a particular length scale declines, the available number of photons for reconstructing structure at that length scale decreases; the signal-to-noise ratio then worsens as a result (as illustrated in Fig. 3.2).

Since images become unrecognizable when a minimum signal-to-noise ratio is not satisfied [58], this suggests a direct relationship between achievable resolution $\Delta_{\min}$ and some minimum signal level $S_{\min}$. Since the signal scales with incident photons per pixel $\bar{n}$ yet declines with spatial frequency f in the Fourier domain, we will assume that the minimum reconstructable signal level is reached at a cutoff spatial frequency f_c, or

$$S_{\min} = \bar{n}P(f_c). \tag{3.17}$$

Associating the minimum object size $\Delta_{\min}$ with the half-period of a grating at the maximum resolvable spatial frequency f_c, we obtain

$$f_c = \frac{1}{2\Delta_{\min}}. \tag{3.18}$$

Inserting the diffracted signal trend of Eq. 3.16 evaluated at frequency f_c into Eq. 3.17 and then employing Eq. 3.18 leads to

$$S_{\min} = \bar{n}10^b(2\Delta_{\min})^{-m_r}, \tag{3.19}$$

where we have used m_r to denote the power law dependence in reconstructed images even though we expect it to be the same as the specimen diffracted power scaling m of Eq. 3.16. The result of Eq. 3.19 can then be rearranged to give

$$\log_{10}\bar{n} = m_r\ \log_{10}(\Delta_{\min}) + m_r \log_{10} 2 + \log_{10} S_{\min} - b \tag{3.20}$$

where we have chosen to place $\Delta_{\min}$ on the abscissa and $\bar{n}$ on the ordinate for comparison with the dose-versus-resolution plots estimated by Howells *et al.* [21] and Shen *et al.* [20].

The above arguments suggest that the required dose (proportional to exposure $\bar{n}$) for achieving a desired resolution $\Delta_{\min}$ should have the same log-log slope m_r as the scaling m in object's diffracted signal (because of the use of Eq. 3.17 in deriving Eq. 3.20).

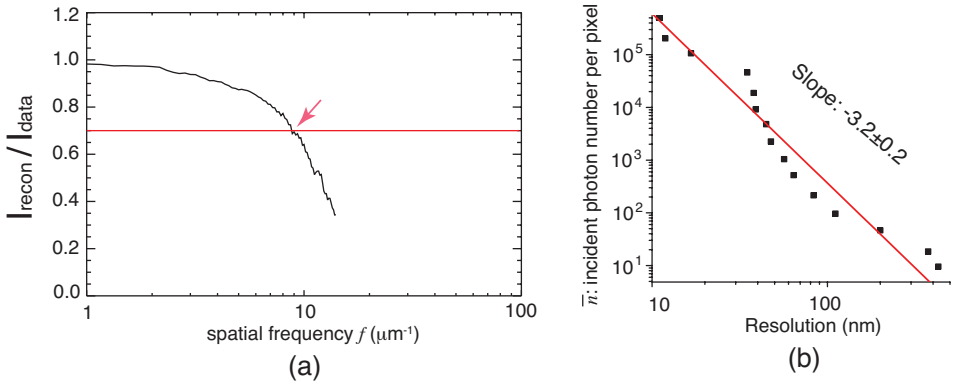

Figure 3.8: Investigation of the dose versus resolution trend for x-ray diffraction microscopy of defined object B. (a) The ratio $\langle I_{\rm recon}(f)\rangle/\langle I_{\rm data}(f)\rangle$ for the example case of incident photon number $\bar{n} = 1000$. This ratio measures how consistent the reconstructed intensity I_{recon} averaged over many iterates compared to the recorded intensity I_{data}. We chose a cutoff value of 0.7 as providing an estimate of the resolution of the reconstructed image. (b) The resulting trend of incident photon number $\bar{n}$ versus resolution $\Delta_{\rm min}$, along with a straight line fit to determine the dose versus resolution scaling parameter m_r. The value of $m_r = -3.2\pm0.2$ is consistent with the scaling of $m = -3.30\pm0.03$ shown in Fig. 3.5 for the diffracted signal from this object.

3.2.2 Dose simulation result

We therefore explored the scaling parameter m_r in our simulations of imaging defined cell B using x-ray diffraction microscopy. The spatial frequency dependent ratio $\langle I_{\text{recon}}(f)\rangle/\langle I_{\text{data}}(f)\rangle$ provides a good measure of the resolution in diffraction microscopy reconstructions [54, 55] (similar to a phase retrieval transfer function [36]), and in our simulations we used a value of 0.7 for this ratio as way to identify the cutoff spatial frequency f_c and thus the resolution $\Delta_{\text{min}} = 1/(2f_c)$. The resulting data of signal level $\bar{n}$ required to achieve a given resolution Δ_{min} are shown in Fig. 3.8; a linear fit of the data gives a value of $m_r = -3.2 \pm 0.2$. Since defined cell B has a signal that scales like $P(f) \propto f^m$ with $m = -3.30 \pm 0.03$ as shown in Fig. 3.5, these simulation results are consistent with the expected result: the scattering strength of the specimen determines the dose versus resolution trend for imaging the specimen. The same conclusion is also obtained from cell A.

While Fig. 3.8 shows a good overall agreement between the dose-versus-resolution slope m_r and the scattering-versus-angle slope m, there are "local" departures from this "global" trend. That is, the power law fit of Fig. 3.8 is done over a very large, 10^5:1 dynamic range in incident photons per pixel $\bar{n}$; this is the "global" trend. If one were instead to carry out the fit over a smaller exposure dynamic range, a different, "local" power law dependance might be observed. Given that the Airy ring characteristics of our defined object B produce departures from a simple power law relationship as seen in Fig. 3.5 (due to concentration of extra diffraction signal into certain spatial frequency ranges), we expect that both computer simulations and experimental observations can have somewhat different dose-versus-resolution slopes m_r over particular exposure ranges.

3.3 Incorrect support tolerance

As discussed in Sec. 2.2.4, phase retrieval algorithms are able to reconstruct the complex object using support constraint in real space and Fourier modulus constraint in the reciprocal space. The Fourier modulus constraint is well

defined, because it is determined by the measured diffraction intensity. On the other hand, it takes a lot of effort to find the correct support in real space. Once the support is accurately defined, the solution for the reconstruction is then obtained.

An image reconstruction process usually starts by running iterative algorithms with an initial support provided from a thresholded version of the autocorrelation function. The output reconstructed image is then used to refine the support towards the correct shape. One method of refinement of the support is through the use of a low pass filter and threshold operation called the "shrinkwrap" algorithm [71], but manual support adjustment can also be required.

In this section, we compare the performances of 4 different phase retrieval algorithms: Error Reduction (ER) [42], Hybrid Input-Output (HIO) [43], Difference Map (DM) [45] and Relaxed Averaged Successive Reactor (RASR) [50], with incorrectly defined supports in real space through numerical simulation.

3.3.1 Support simulation setup

In order to understand the effects of erroneous supports, we used the exit wave of Cell B with $\bar{n} = 10^4$ incident photon number per pixel at a photon energy of 520 eV as defined in Sec. 3.1.2. The diffraction intensity was calculated from this fake cell, photon noise was added, and the XDM reconstruction process was simulated in the same way as in Sec. 3.1.2. For DM algorithm, we set $\beta = 1.15$, $\gamma_m = \beta^{-1}$ and $\gamma_s = -\beta^{-1}$. For HIO and RASR, we set $\beta = 0.9$ for this simulation.

The test supports were generated from the correct support as shown in Fig. 3.9 (b). The first incorrect support, the "bump-out" support, was obtained by including a number of pixels outside the correct support at a local area (Fig. 3.9 (c)). The second one, the "bite-in" support, excludes some pixels inside the correct support at a local area (Fig. 3.9 (d)). The third one, the "loose" support, increases the size of the correct support uniformly by 2 pixels (Fig. 3.9 (e)). The forth one, the "tight" support, reduces the correct support size uniformly by 2 pixels (Fig. 3.9 (f)).

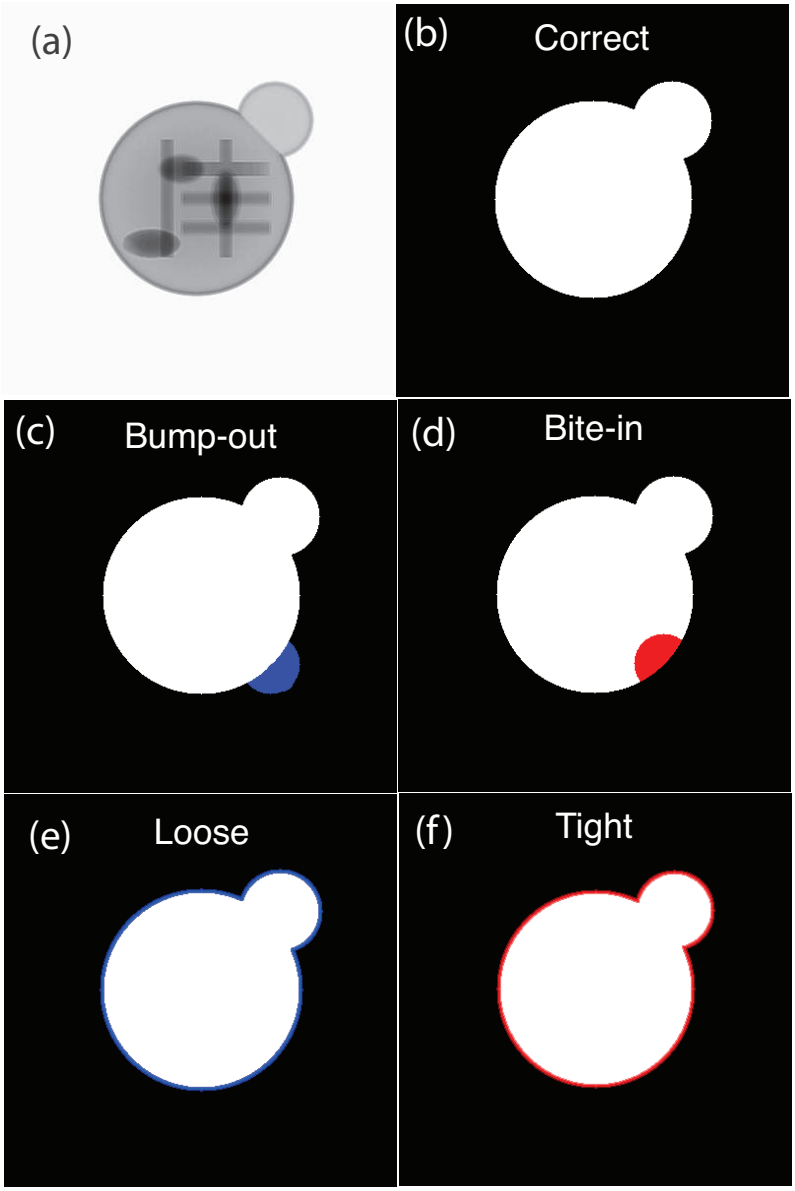

Figure 3.9: The blue area denotes the region removed from the correct support. The error area denotes the region added to the correct support. (a) The exit wave of the simulated cell. (b) The correct support. (c) The "bump-out" support generated by including a number of pixels outside the correct support at a local area. (d) The "bite-in" support generated by excluding some pixels intside the correct support at a local area. (e) The "loose" support generated by increasing the size of the correct support uniformly by 2 pixels. (f) The "tight" support generated by reducing the correct support size uniformly by 2 pixels.

The error function to monitor the convergence of each algorithm is defined differently. In this simulation, in order to make a consistent comparison, a universal error metric was introduced for all these 4 testing algorithms, which was calculated from the difference between the output of the current iteration and that of the next, or

$$E_n = \frac{\sqrt{\sum |o_{n+1} - o_n|^2}}{\sqrt{\sum |o_n|^2}}. \tag{3.21}$$

Note that 2 pairs of Fourier transforms are applied in a DM iteration, while 1 pair is applied in a HIO, ER and RASR iteration. To get the number of Fourier transforms the same for all algorithms, the iteration numbers of the latter 3 algorithms were doubled from that of DM. In the simulation, DM was run by 1000 iterations and starts to average after 800 iterations with an interval of 2. The other 3 algorithms were run by 2000 iterations and start averaging after 1600 iterations with an interval of 4. The reconstruction of each algorithm was performed 5 times with individual random starts, and the final image was averaged from those 5 reconstructions.

3.3.2 Simulated images and comparison

The reconstructed images for the correct, bump-out and bite-in supports are shown in Fig. 3.10, the corresponding error metric curves are shown in Fig. 3.12, and the phase retrieval transfer function curves are shown in Fig. 3.14.

All the algorithms give good reconstructions for the correct support. As the basic shape and major part of the support are kept for both bump-out and bite-in supports, a lot of information are retrieved from those supports too. Especially, for the bump-out support, because the extra support area does not bring translation ambiguity, the reconstruction quality is not affected significantly. For the bite-in support, as the support excludes a part of object area, the reconstruction algorithms try to place all the diffraction intensities inside. The reconstructed image quality thus become worse.

This effect could be used in a support-refining process. If a part of the reconstruction support is not defined with sufficient confidence, we can en-

large the support in this area and keep the rest of support untouched. The reconstruction with this new support could give a new boundary of the object in the target area. Based on that, the new support boundary can be refined in that region.

A similar conclusion can be drawn out from the error and PRTF curves. The error curves for the correct and bump-out supports are almost converged to the same level with small error values. The bite-in support increases the error convergent level and also involves larger fluctuations, especially for DM algorithm, which indicates that the algorithms are struggling to fit the diffraction information into the cropped support. The PRTF curves for the correct and bump-out supports are almost overlapping, while the PRTF from bite-in support stays at an abnormal high level. This is because the intensity outside this bite-in support is also filled into the smaller area, which increases the intensity in the reconstructed image incorrectly.

The reconstructed images for the correct, loose and tight supports are shown in Fig. 3.11, the corresponding error metric curves are shown in Fig. 3.13, and the phase retrieval transfer function curves are shown in Fig. 3.15.

We found the loose support gives good reconstruction too, especially with the application of centering the image to remove the translation ambiguity, which is done by maximizing the convolution between sequential images. This centering process keeps linear phase shifts from building up and giving "false" errors from the reconstructed object shifting off of the support. But, the PRTF curves from loose support drops earlier and stays at a lower level than those from the correct support, which gives a worse reconstruction resolution. The image quality decreases significantly for tight support, because the support constraint is not satisfied very well. This violation is even worse than the bite-in support, where the mismatching only happens at one local position.

5 images are simulated for each case. From those 5 images, there are 10 ways to calculate SNR from image pairs. The averaged SNR value for each case is summarized in Table. 3.1. We can see that the correct and bump-out supports give the best reconstruction, the SNR for loose support decreases slightly, and the SNR given by bite-in and tight supports are not quite consistent. This inconsistency implies that with insufficient large supports, the

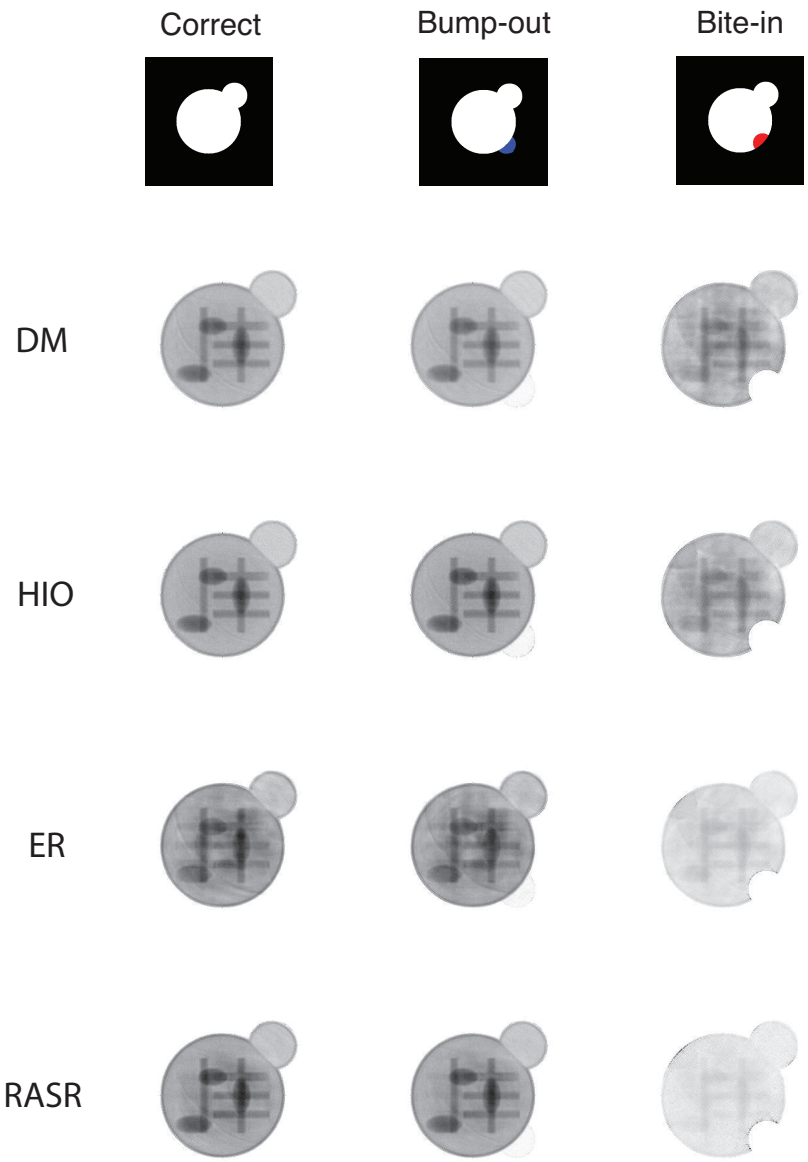

Figure 3.10: Reconstructed images with DM, HIO, ER and RASR with correct, "bump-out", and "bite-in" supports.

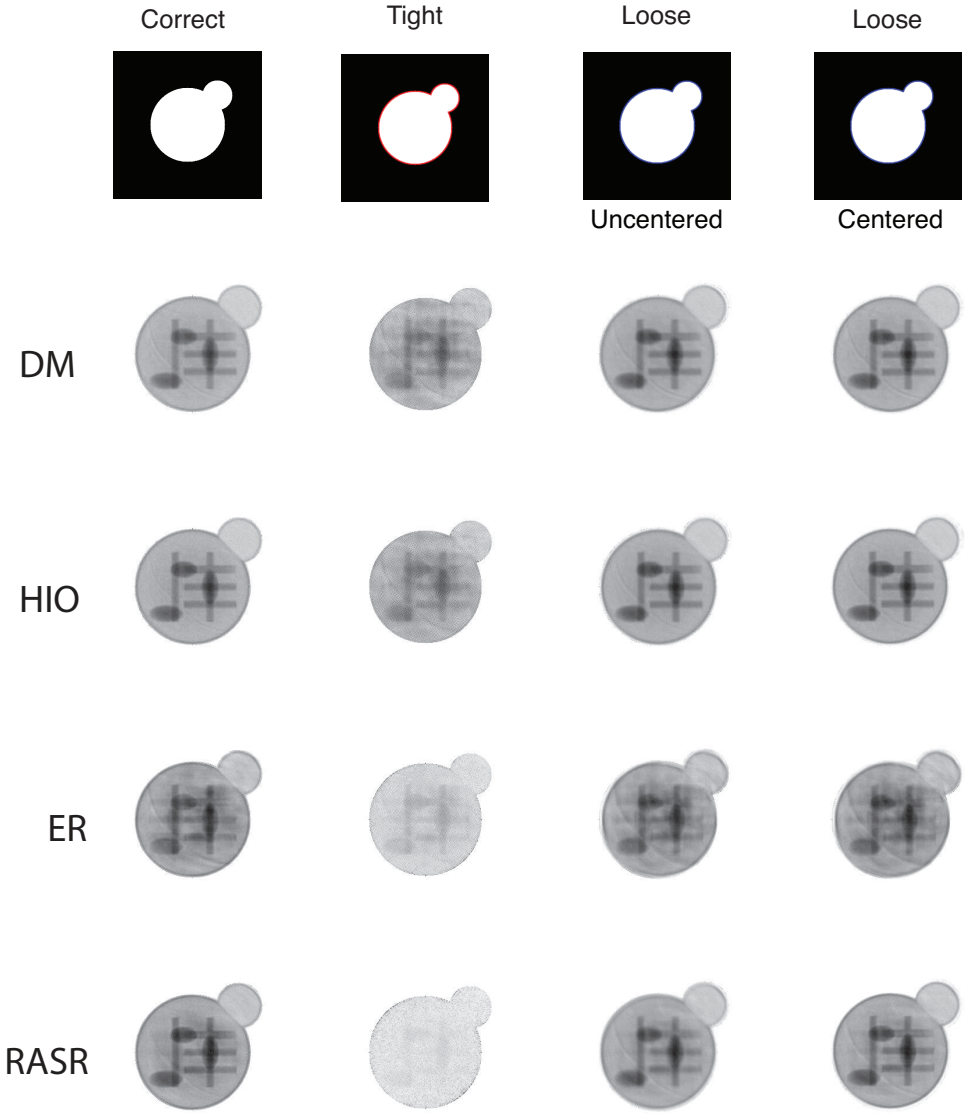

Figure 3.11: Reconstructed images with DM, HIO, ER and RASR with correct, "tight", and "loose" supports. For the loose support, a centering process was applied to remove the translation ambiguity, which is done by maximizing the convolution between sequential images. The corresponding result is labeled with "Centered". The one without the centering process is labeled with "Uncentered".

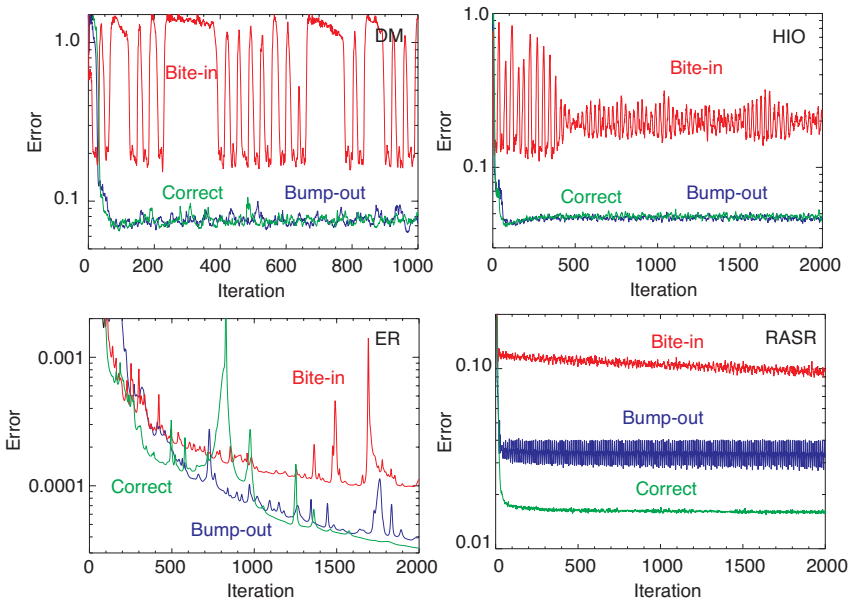

Figure 3.12: Error curves from reconstruction with DM, HIO, ER and RASR with correct, "bump-out", and "bite-in" supports.

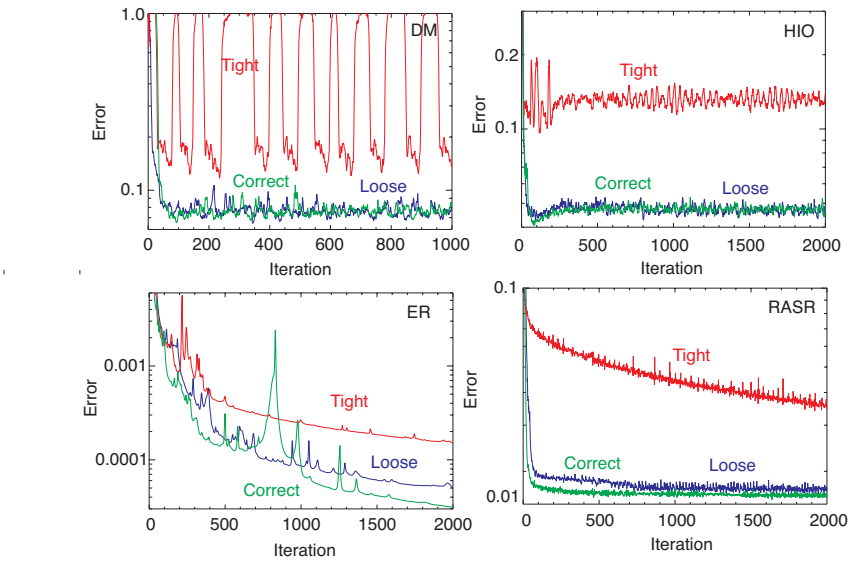

Figure 3.13: Error curves from reconstruction with DM, HIO, ER and RASR with correct, "loose", and "tight" supports.

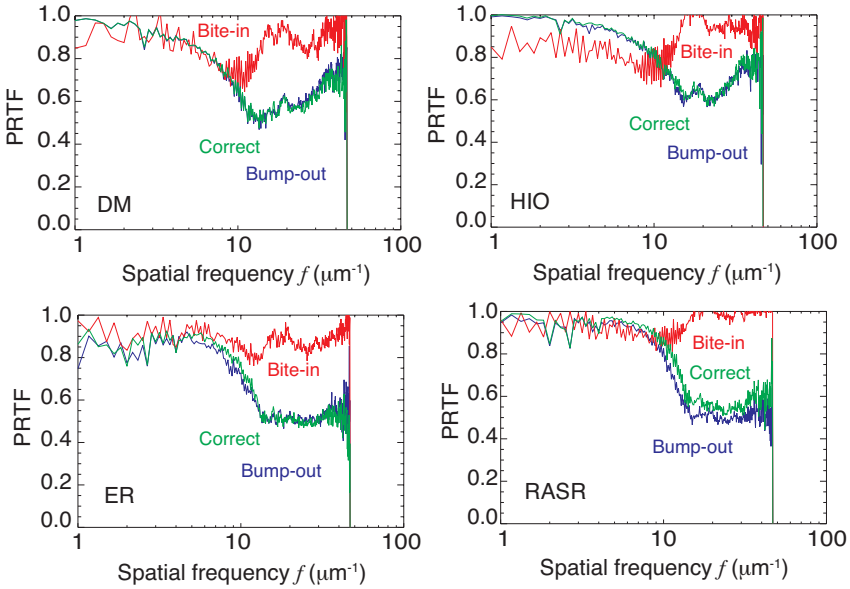

Figure 3.14: PRTF curves from reconstruction with DM, HIO, ER and RASR with correct, "bump-out", and "bite-in" supports.

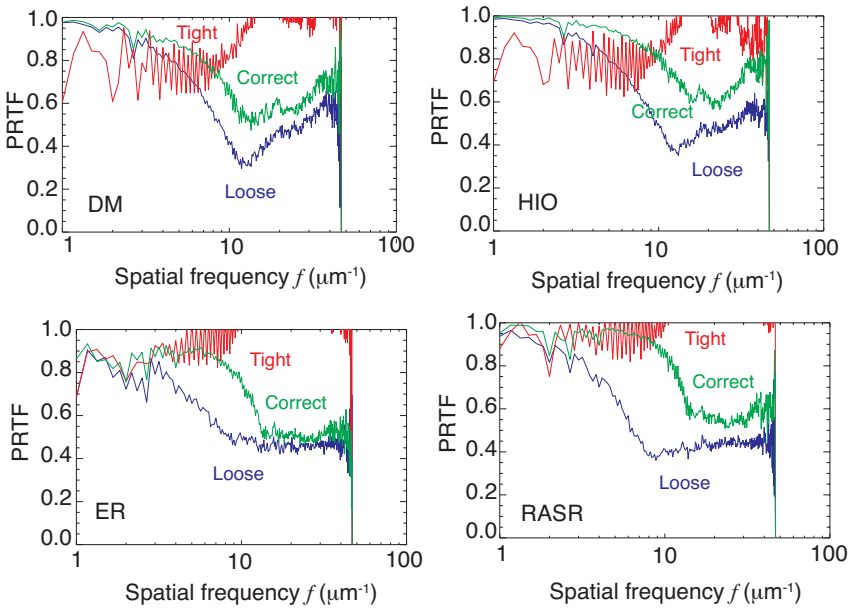

Figure 3.15: PRTF curves from reconstruction with DM, HIO, ER and RASR with correct, "loose", and "tight" supports.

reconstruction algorithms keep outputting reconstructions at a stagnation position. The poor quality of these images can be justified by eyes, but they could have high similarity and give high SNR values.

From this simulation, the smaller supports could cause convergence problems for all reconstruction algorithms. The overall performances of DM and HIO are better than ER and RASR. They give higher reconstruction qualities at most cases.

Table 3.1: SNR of reconstructed images with different supports.

DM	Correct	8.1	Loose (centered)	6.6
	Bump-out	9.4	Loose	4.6
	Bite-in	2.3	Tight	1.8
HIO	Correct	8.0	Loose (centered)	5.2
	Bump-out	8.2	Loose	4.3
	Bite-in	47.0	Tight	24.6
ER	Correct	2.4	Loose (centered)	1.7
	Bump-out	1.9	Loose	1.7
	Bite-in	2.8	Tight	3.6
RASR	Correct	3.2	Loose (centered)	3.5
	Bump-out	3.0	Loose	2.5
	Bite-in	33.2	Tight	10.3

3.4 Missing center tolerance

In Sec. 2.3.3, we discussed that the missing data in the center of the diffraction array can allow unconstrained modes which satisfy both Fourier modulus and support constraints. When the missing data area is large enough, it can hinder successful reconstructions. In experiments with a normal CCD, the intense direct beam has to be blocked by a beamstop; as a result, the center remains at least partially missing, although the size of the missing center can be reduced by assembling data from multiple beamstop positions.

In this section, we compare the performances of phase retrieval algorithms: ER, HIO, DM and RASR with varying sizes of missing centers in diffraction patterns.

3.4.1 Missing center simulation setup

We used the exit wave of Cell B (defined in Sec. 3.1.2) with 520 eV x-rays and 10^4 incident photon number per pixel as the test sample again. The diffraction pattern calculation, addition of photon noise and reconstruction settings are identical to Sec. 3.3.1.

A varying number of pixels are removed from the diffraction pattern. The sizes of the test missing centers are 5×5, 10×10, 20×20 and 50×50 pixels, which are shown in Fig. 3.16. Considering the oversampling ratio of Cell B is about 4.6 (obtained by dividing the array size divided with the number of pixels inside the correct support), the corresponding missing speckles inside the missing centers are 5, 22, 87 and 543, respectively.

3.4.2 Simulated images and comparison

The reconstructed images are shown in Fig. 3.17. We found that the reconstruction quality is significantly affected with 10×10 missing center for all testing algorithms. ER and RASR cannot have the objected reconstructed with missing center size larger than 5×5, while DM and HIO fail to converge when the missing area is larger than 10×10 missing area, which corresponds to about 22 missing speckles.

The error curves are shown in Fig. 3.18, where we see that with increasing size of missing center, the convergence speed slows down, and the convergence level raises up for all testing algorithms. A constant worsen trend can be found from the PRTF curves too (shown in Fig. 3.19). For DM and HIO, PRTF curves collapse after 10×10 missing size, and for ER and RASR, PRTF curves fell off after 5×5 missing size.

The signal-to-noise ratio of reconstructed image for each case is summarized in Table. 3.2. With increasing size of the missing data area, SNR values decrease. DM and HIO give higher image quality in terms of SNR, which is consistent with conclusion obtained from error and PRTF curves.

In Sec. 2.3.3, we mentioned that a high pass filter function can be used to mitigate the ambiguity caused by missing center. We applied a filter with 0.5 depth and 10% width of the entire array to the reconstructed images. They

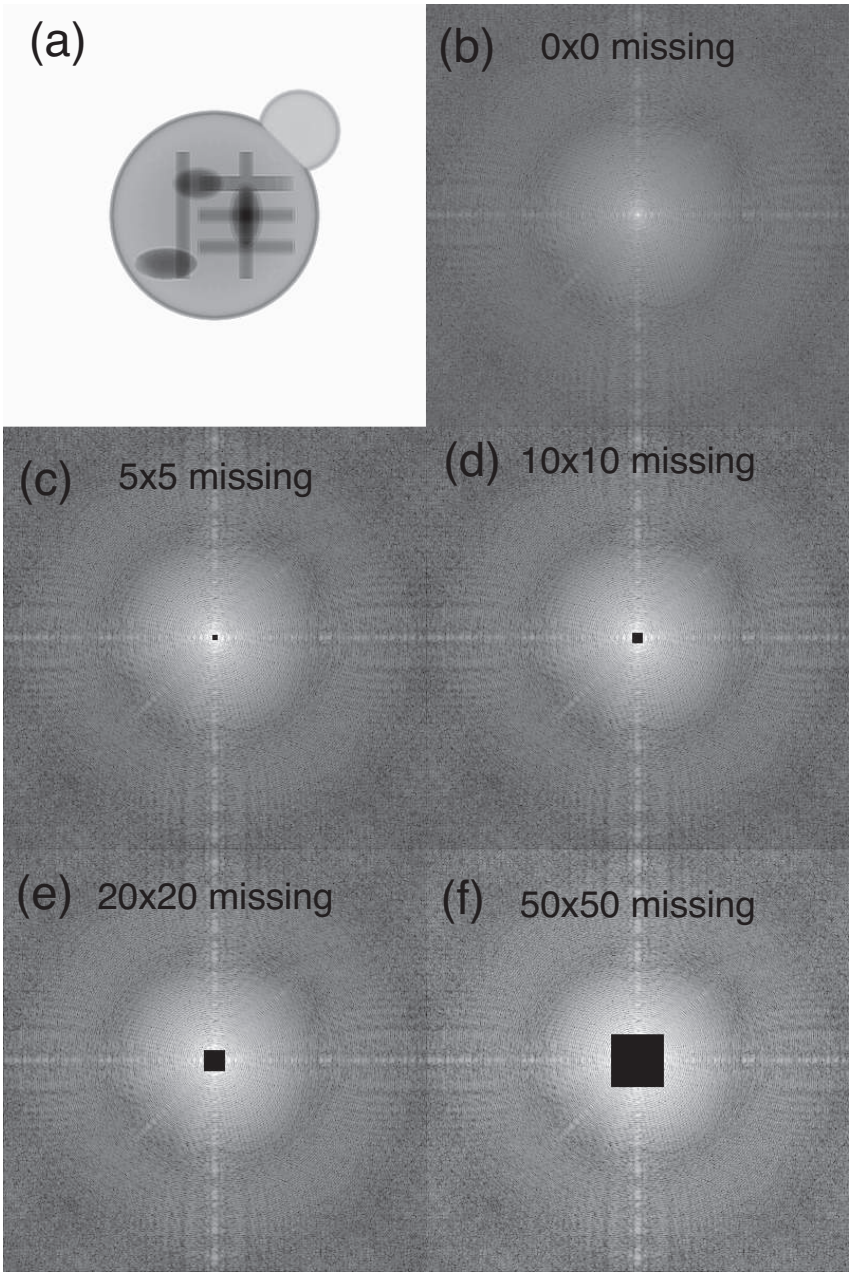

Figure 3.16: (a) Exit wave of Cell B. (b) Diffraction pattern of Cell B. (c-d) Diffraction patterns of Cell B with 5×5, 10×10, 20×20 and 50×50 missing centers, respectively.

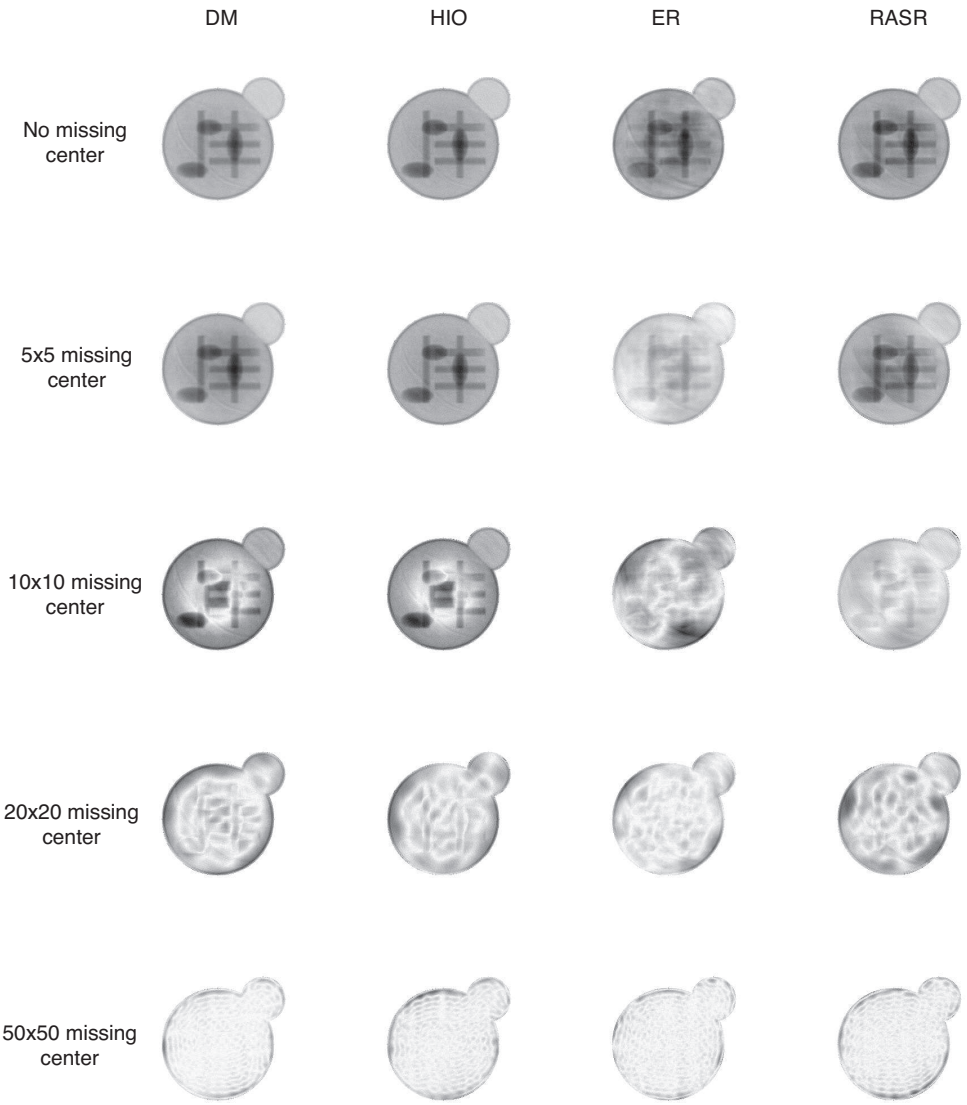

Figure 3.17: Reconstructed images from DM, HIO, ER and RASR for Cell B with 0, 5×5, 10×10, 20×20 and 50×50 missing centers.

Table 3.2: SNR of reconstructed images with varying size of missing center.

Missing area	0	5×5	10×10	20×20	50×50
Missing speckle	0	5	22	87	543
DM	8.1	4.7	2.7	1.4	1.1
HIO	8.0	6.3	1.9	1.0	1.1
ER	2.0	0.8	0.7	0.8	0.9
RASR	3.2	2.0	0.6	0.6	1.0

are displayed in Fig. 3.20, where we see that for the cases with larger missing area in diffraction patterns, the improvement provided by the high pass filter is very limited. Reducing the size of the missing center to a very small value is necessary to achieve good reconstructions.

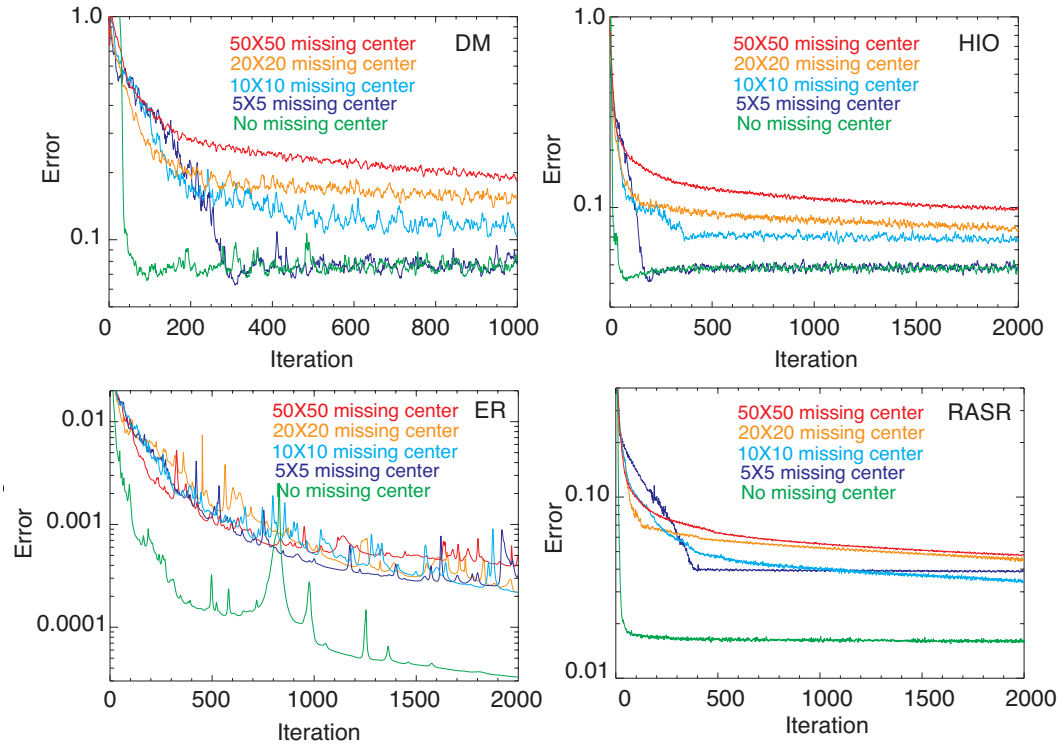

Figure 3.18: Error curves of reconstructions from DM, HIO, ER and RASR for Cell B with 0, 5×5, 10×10, 20×20 and 50×50 missing centers.

From the SNR values listed in Table. 3.1 and Table. 3.2, combined with the reconstructed images shown in Fig. 3.10, Fig. 3.11 and Fig. 3.17, as well as the

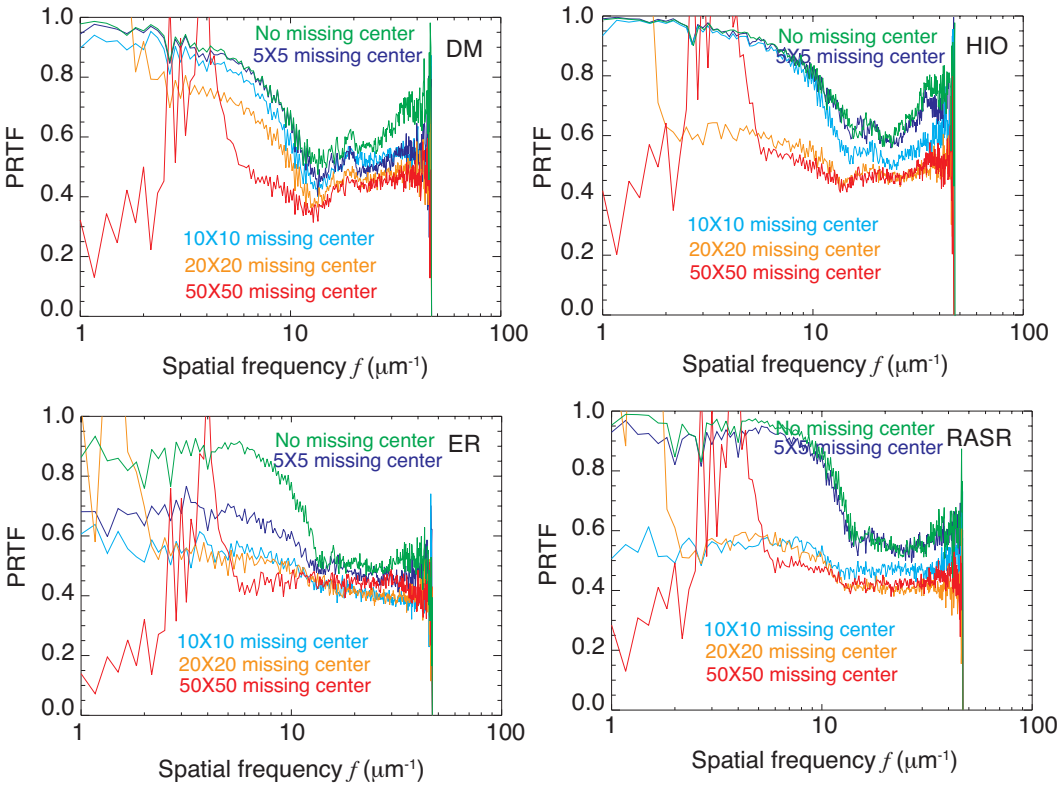

Figure 3.19: PRTF of reconstructions from DM, HIO, ER and RASR for Cell B with 0, 5×5, 10×10, 20×20 and 50×50 missing centers.

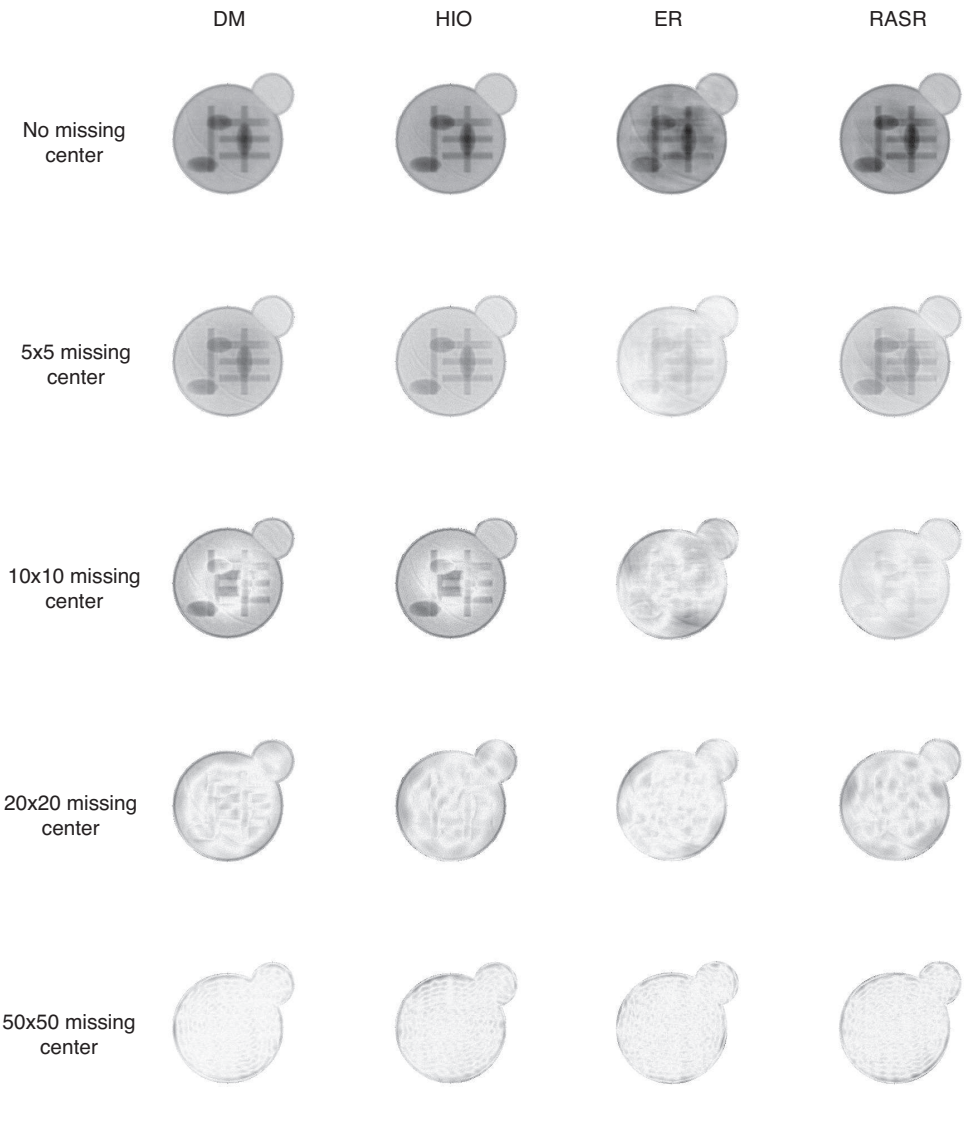

Figure 3.20: High pass filtered reconstructed images from DM, HIO, ER and RASR for Cell B with 0, 5×5, 10×10, 20×20 and 50×50 missing centers.

error and PRTF curves in Fig. 3.12, Fig. 3.13, Fig. 3.14, Fig. 3.15, Fig. 3.18 and Fig. 3.19, we found that when phase retrieval algorithms give reasonably good reconstructions, the corresponding SNR values are about ≥ 2. We mentioned previously that when the reconstruction algorithm trapped into a stagnation position, it is possible to give abnormally high SNR values. This situation can be eliminated by checking the reconstructed images directly.

From the incorrect support and missing center simulations, we found that the DM and HIO algorithms are more robust in handling incorrect support guess and incomplete diffraction data with missing centers than ER and RASR. When the support size is smaller than the actual object size, reconstruction algorithms do not converge well, while a loose support can be used to generate fairly good reconstructions, from which the shape of the support can be refined further. The missing data in the center of diffraction pattern not only brings ambiguities into reconstruction, but also prevents convergence when too many speckles are blocked by the missing center. DM and HIO work well up to about 22 missing speckles, while ER and RASR give reasonably good reconstructions up to about 5 missing speckles.

Chapter 4

XDM experiment on dried yeast cells

In this chapter, we use XDM to image a chemically-dried yeast cell using 750 eV x-rays. A series of 2D reconstructions are obtained at 10 different angles. In this chapter, we will discuss the sample preparation, data collection, image reconstructions, achieved resolutions and associated limitations.

4.1 Imaging whole, eukaryotic cells with XDM

The goal for our experiments is to image whole, eukaryotic biological cells at high resolutions. The size of cells could be a few microns, which is too thick for electron microscopes [72–74]. Cells also provide interesting structures in the range of 5-10 nm, which is beyond the resolution limit of visible light microscopes. Cells do not come in crystalline arrays of identical structures, and they are sensitive to radiation damage.

It has been suggested that x-ray microscopes are well suited for imaging thick biological samples [72, 75, 76]. They have the capability to bridge the gap between electron microscopy and visible light microscopy. In particular, XDM removes the limitations imposed by optics, and it can work with unique objects (single cells) in a way that crystallography cannot. It has the potential to image biological specimens with a resolution limited only by the collected maximum diffraction angle and the radiation tolerance of the samples.

XDM has been successfully applied on biological imaging of bacteria [77], yeasts [55], malaria-infected erythrocytes [78], herpes virions [79] and chromosomes [80] since it was first experimentally demonstrated in 1999 [81]. We contribute to this fast-improving progress in XDM by performing experiments on whole, eukaryotic cells at multiple viewing angles towards 3D, which will be discussed in this chapter, and in their natural, hydrated status, which is going to be discussed in the following chapter.

In this chapter, the sample preparation and data recording were carried out as part of a team effort involving Johanna Nelson, David Shapiro and Stefano Marchesini; the reconstructions shown here were obtained by the thesis author.

4.2 Chemically-dried cell preparation

We imaged *Saccharomyces cerevisiae* yeast cells carrying the *whi5* mutation. The size of the wild type of yeast cells is about 6-7 μm, which is too large for XDM by violating the Born approximation requirement (Eq. 2.29). The *whi5* mutation produces smaller yeast cells [82], normally with a diameter of about 3-4 μm, which satisfies our present-day experimental limitations.

4.2.1 Fixation

Following the recipe described previously [35, 83], the cell colony was initially cultured on a YPD agar plate. Before using, we incubated the cells in YPD solution at 30°C for 8 hours, changed with fresh YPD solution, let them grow for another 8 hours, and repeated this cycle several times.

The purpose of a chemical drying process is to prevent surface-tension-caused structural collapse by gradually replacing water with acetone.

Formaldehyde solution is a widely used fixative. We fixed the cells by suspending them in 37% Formaldehyde YPD solution for 30 minutes at room temperature. In this process, the Formaldehyde solution can be replaced with 3% Glutaraldehyde, 10% NaCu, 0.5% $CaCl_2$ in water.

To remove the fixative, we washed the fixed cells in water, spun them down in centrifuge, discarded the liquid, and resuspended them in fresh water. This process was repeated 3 times.

4.2.2 Dehydration

After the cellular structures were fixed, the water in cells was gradually replaced by acetone. This was done by suspending the cell in an acetone solution with increasing concentrations. The water molecules were gradually diffused and removed.

The protocol of this process is as following:

1. Suspend cells in 30% acetone, 70% water for 10 minutes, repeat.
2. Suspend cells in 50% acetone, 50% water for 10 minutes, repeat.
3. Suspend cells in 70% acetone, 30% water for 10 minutes, repeat.
4. Suspend cells in 90% acetone, 10% water for 10 minutes, repeat.
5. Suspend cells in 100% acetone for 10 minutes, repeat.

Each step was repeated means that the acetone solution was replaced with fresh solution by spinning down the cells, discarding the liquid, and resuspending the cells in fresh solution.

This dehydration process is done slowly, which helps to preserve much of the cells' larger scale structure.

There was still a small amount of water left inside cells after the acetone dehydration process. To remove water as much as possible, the cells were then washed with Hexamethyldisilazane or HMDS. After the last step in the acetone dehydration process, we centrifuged the cells in 100% acetone solution, discarded the liquid, and resuspended cells in HMDS. We then added a droplet of this solution onto the grid coated with a formvar film. The HMDS is highly volatile, so it evaporates almost immediately. We then added another drop of pure HMDS on the grid, allowed it to evaporate, and repeated with a second drop of pure HMDS. Although HMDS evaporates rapidly, we found it does not break or harm the formvar film.

We note that because a lot of cells could be lost during this multiple-step dehydration process, there is not a good way to monitor the cell concentration in the final stage. However, the requirement of a finite support constraint means that a low cell density is preferred.

4.3 Experimental setup

The microscope chamber [15] is stationed at Beamline 9.0.1 of the Advanced Light Source at Lawrence Berkeley National Laboratory. The basic concept of this microscope is to select and deliver coherent x-ray illumination onto a well isolated specimen on the sample grid, and collect the far field diffraction pattern with a CCD located downstream.

4.3.1 Zone plate monochromator

The x-ray energy is selected from the undulator radiation spectrum by a combination of a monochromatic zone plate and a pinhole. This microscope uses an off axis zone plate monochromtor, which was initially designed by Howells [84]. Instead of using a full zone plate, a segment of the zone plate, which contains 1000 outermost zones, vertically disperses photons with different energies and focuses them onto different focal planes, as shown in Fig. 4.1.

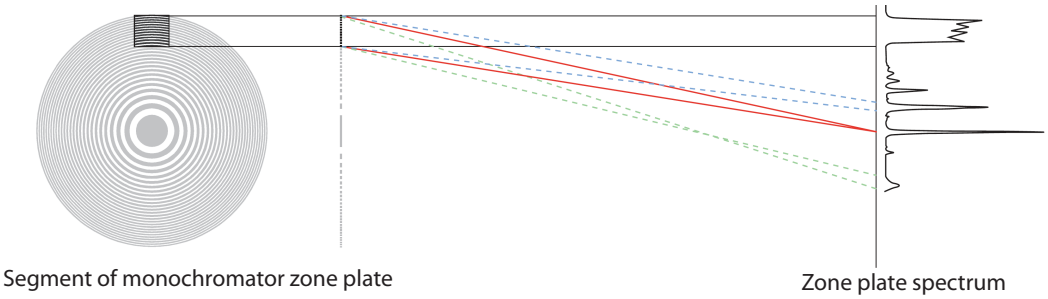

Figure 4.1: Energy selection by off axis zone plate monochromator. A segment of the full zone plate vertically disperses photons with different energy and focuses them onto different focal planes. Place a pinhole in the focal plane of the given energy, and scan it vertically to locate the correct peak. This picture is adapted from [35].

A 5 μm diameter pinhole is placed in the focal plane for the desired x-ray energy, which is 750 eV for this experiment. Scanning this pinhole vertically gives the spectrum dispersed from the zone plate. Considering the radius of the full zone plate is about 3.6 mm and the segment is off-axis by 3.35 mm, the separation between the focal peak to the edge of the unscattered direct beam is about 3.35 mm. Another phenomenon to identify the correct energy is that usually the strength of the peak in focus is higher and its width is narrower than other peaks, as seen in Fig. 4.1.

As we discussed in Sec. 2.3.2, to achieve 10 nm resolution from a 3 μm specimen, the required spectral resolution $\lambda/\Delta\lambda$ is at least 300, as calculated from Eq. 2.54. This should be the minimum spectral resolving power that the monochromatic zone plate should provide. The spectral resolution is related to the number of zones N_{zp} as [85, 86]

$$\frac{\lambda}{\Delta\lambda} = N_{\mathrm{zp}}. \tag{4.1}$$

We obtained the same result for gratings in Eq. 1.39. For the zone plate used in our experiment, there are 1000 zones in the segment, which gives $\lambda/\Delta\lambda = 1000$. This spectral resolving power satisfies the experimental requirement sufficiently. In other words, the temporal coherence l_{coh} is sufficient, according to Eq. 2.52.

4.3.2 Pinhole, corner and beamstop

The further down stream experimental setup from the pinhole is illustrated in Fig. 4.2. The x-ray peak selected by the pinhole propagates through and illuminates the specimen grid. As discussed in Sec. 2.3.2, a pinhole scattering generates the Airy pattern, and the illumination within the half radius of the central Airy disk can be considered to be coherent.

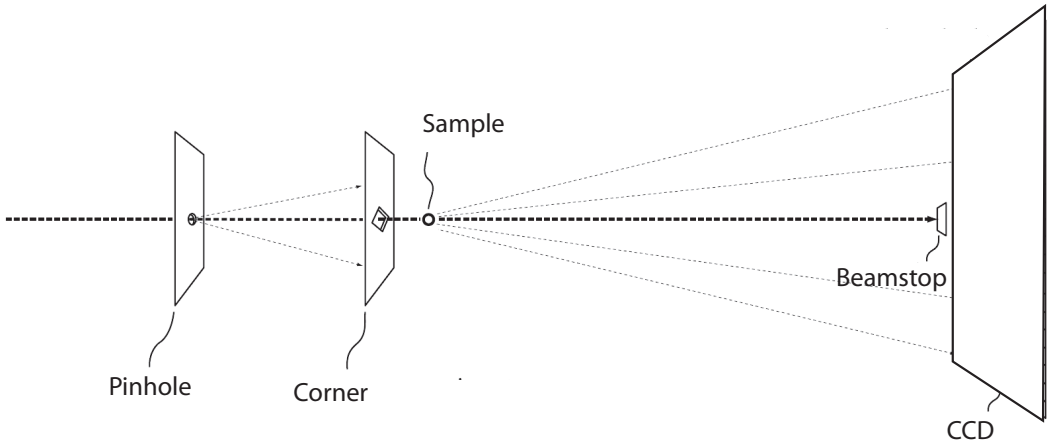

Figure 4.2: Illustration of XDM experimental setup. The focused x-ray peak is selected by a pinhole, which illuminates the sample. A corner window blocks most of the pinhole scattering and leaves clean diffraction pattern collected on CCD. This picture is adapted from [35].

The pinhole we used in the experiment is 5 μm in diameter. The sample grid is placed 2.5 cm down stream from the pinhole. For 750 eV x-rays, we have $\lambda = 1.65$ nm, so this setting gives a theoretical spatial coherence of 10 μm, calculated from Eq. 2.49. The experimental measurement of the coherence width at Beamline 9.0.1 is about 5.3 ± 1.1 μm [87] with 50% fringe visibility, which implies the beamline provides very good coherence up to 5.3 μm.

The Airy rings from the pinhole scattering can project onto the CCD and contaminate the diffraction pattern from the specimen. A silicon piece with a square window, which is called as "corner", is used to block most of the pinhole scattering. The size of the corner opening area is about 200×200 μm. The center part of the Airy pattern goes through the corner, interacts with the specimen, and generates diffraction signal on the CCD.

The CCD we used in this experiment is PI-MTE 2048B CCD from Princeton Instruments. The entire CCD array pixel number is 2048×2048, with 13.5 μm pixel size [88]. The CCD is located 13.6 cm away from the sample grid.

The edges of the corner also scatters. This signal is blocked by a beamstop in front of CCD. The size of the beamstop is about 2×2 mm, corresponding to about 100×100 pixels. It is aligned with the corner to block the projection of corner scattering, and leave the outside area with clean diffraction pattern from the specimen alone. The procedures for fabrication of the silicon corner and beamstop can be found in Appendix C.

As we mentioned before, the beamstop also blocks the intense undiffracted direct beam. To deal with the limited CCD dynamic range and widely distributed diffraction signal, and for the purpose of reducing the "missing central region" where no data is recorded, we aligned the corner and beamstop with the beam direction at several positions: aligning the beam with the centers of the corner and beamstop for long exposure times and thus producing high spatial frequency signal, and aligning the beam with the diagonal corners of the corner and beamstop for short exposure times and producing low spatial frequency signal. The final diffraction pattern is assembled from images taken with both long and short exposures.

The sample grid is motorized by a goniometer system [83, 89], which provides translation ability in X, Y and Z directions, and rotation over a range of -80° to +80°. The microscope thus has the capability for 3D data acquisition.

4.4 Diffraction data and reconstructions

We collected diffraction data from a chemically-dried yeast cell with 750 eV x-rays at 10 different angles: from -40° to 50° with 10° step size. We obtained a 2D reconstructed complex image for each angle.

4.4.1 Diffraction data

Studies [83] show that dried cells suffer from an initial collapse when exposed by x-ray beam, and then they enter a stage with uniform and slow shrinkage.

To make sure the cell is settled down without rapid structure changes, we illuminated the specimen for 20 minutes with direct x-ray beam which corresponds to a dose of about 8.2×10^9 Gray, until we did not see significant changes in speckle pattern.

The corner and beamstop were aligned at 4 different locations for long and short exposures. These locations are called top low and bottom low where x-ray beam is aligned close to diagonal corners of the corner and beamstop for short exposures and low spatial frequency signal, and top high and bottom high where x-ray beam is aligned near the centers the corner and beamstop for long exposures and high spatial frequency signal. We used 0.002 sec, 0.01 sec and 0.1 sec for the exposure times for low positions, and 4 sec, 30 sec for high positions. To increase the photon statistics and partially remove the shot noise, 4 diffraction patterns were taken at each position and for each exposure time setting. The final data array is assembled from 40 images, and 136.448 sec total exposure time.

To obtain a "clean" data set for each angle, the scattering from the corner, the formvar film, and sometimes the sample grid bars have to be removed from the scattering signal from the specimen. Considering that the diameter of the center Airy disk of the pinhole illumination used in this experiment is about 10 μm, we moved the sample grid 50 μm away from the cell for background data taking. This spot is about 10 times of the coherence length ($\sim$ 5 μm) away, which avoids the interference with scattering from the specimen. In this case, the background intensity can be simply subtracted.

The data arrays and background arrays were assembled separately. The final data sets were obtained by subtracting the background arrays from the data arrays, and setting negative pixel values to zero. The assembled diffraction data for all of the 10 angles are displayed in Fig. 4.3. The final array size is 1800×1800 pixels, which is cut from the initial 2048×2048 CCD array. The missing center is about 34×34 pixels. Considering the oversampling ratio of this specimen is about 18, the missing speckle number is 64. According to the simulation result in Sec. 3.4, the difference map algorithm could have difficulty to give good reconstructions under this condition. The recorded diffraction pattern extends to a spatial frequency, which is obtained by di-

viding the diffraction angle with wavelength, of about 54 μm^{-1} at the edges and 77 μm^{-1} at the corners. The spatial frequency at the edges of 54 μm^{-1} corresponds to a half-period pixel size in real space of about 9.2 nm.

The black regions in the assembled data pictures indicate pixels with zero values. The vertical black line in the center of the top half plane is caused by overlapping of the beamstop arm at two high resolution positions. The black streaks emanating from the center come from the mismatching between the data and background. Their locations are almost the same for all angles. The mismatching gets worse for higher rotation angles, for instance, 50°, −30° and −40°. This is partially because the grid bars are closer to the direct beam at higher angles, they diffract strongly, and these diffractions are more difficult to be removed by background subtraction. Another reason could be the reproducibility of rotation motor is worse at higher angles.

Fig. 4.4 shows the power spectral density (PSD) curve of the diffraction data at 10°. The PSD curves from other angles are very similar. We can see the diffraction pattern intensity extends to over 6 orders of magnitude.

4.4.2 Dose calculation

The direct x-ray beam flux through the pinhole measured by a photodiode in front of CCD is about 120 nA. Considering that the energy $E_{\mathrm{e-h}}$ needed to create an electron-hole pair is 3.63 eV, the number of 750 eV photons per second delivered by the incident x-ray beam can be estimated by

$$n_{\mathrm{photon}} = \frac{I/e}{E_{\mathrm{photon}}/E_{\mathrm{e-h}}}, \tag{4.2}$$

where I is the flux current measured on photodiode, e is the charge of an electron in Coulombs (1.6×10^{-19} C), E_{photon} is the photon energy (750 eV in this case). Substituting all the numbers into Eq. 4.2, we obtain that the incident photon number is 3.6×10^{9} /sec.

The major part of this incident illumination is focused within the center Airy disk from the pinhole. Using Eq. 1.49, for a 5 μm pinhole placed 2.5 cm away from the sample grid, the radius of the center Airy ring with 750 eV

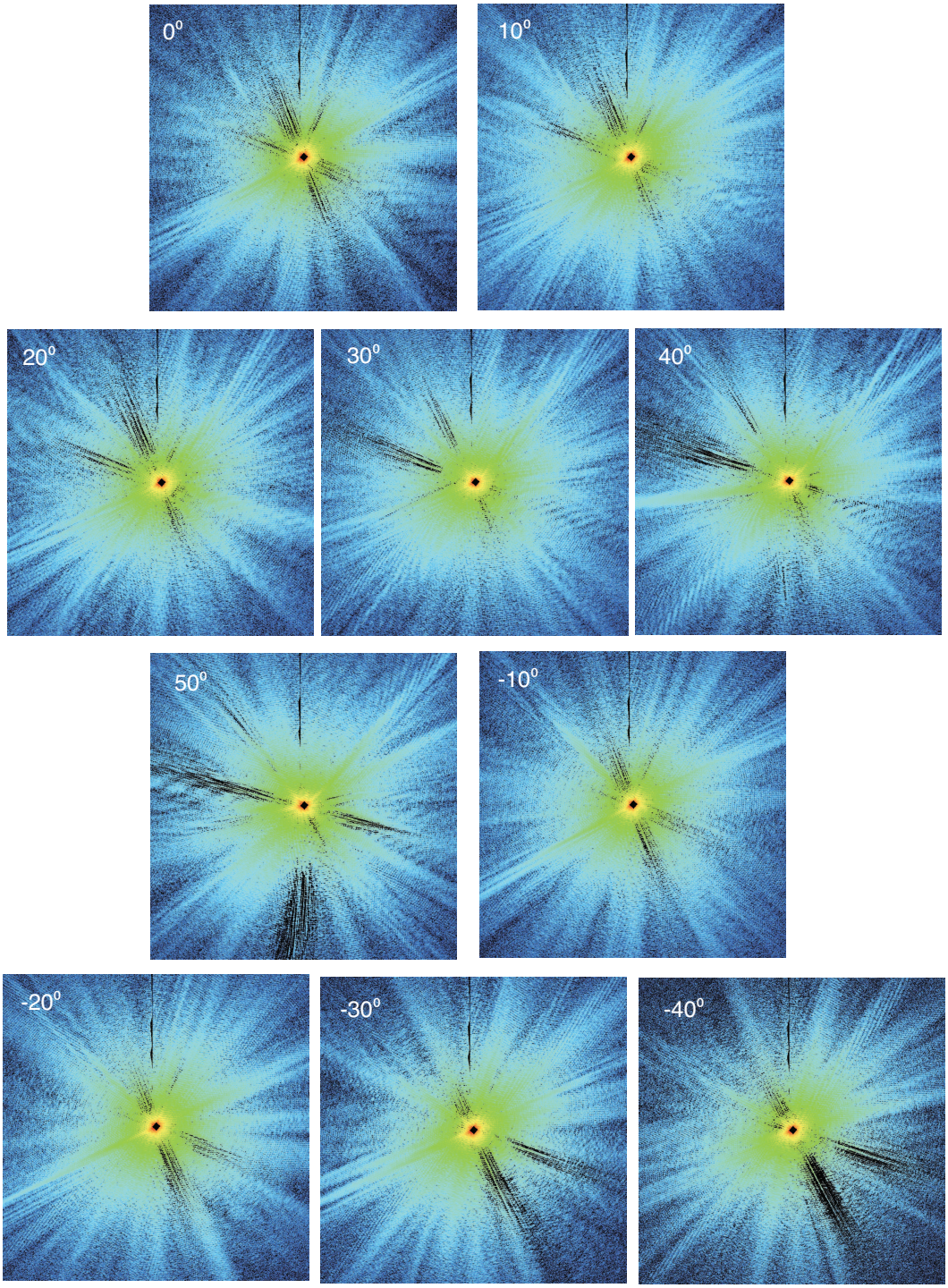

Figure 4.3: Assembled diffraction data from the chemically dried cell at 10 different angles, from -40 to +50 degrees with 10 degree step size.

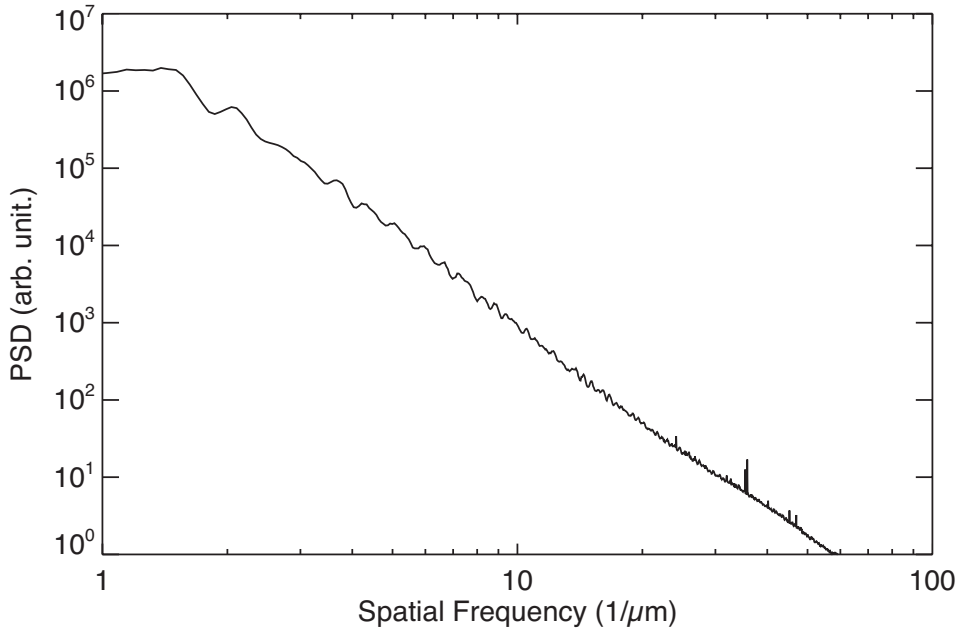

Figure 4.4: Power spectral density curve of assembled diffraction data from the chemically dried cell at 10°. The diffraction pattern intensity extends to over 6 orders of magnitude.

x-rays ($\lambda = 1.65$ nm) is 5 μm. Considering a cell with a radius about 1.5 μm located in the center of the Airy pattern from the pinhole, about 20% of the total photon flux is distributed in the cell area according to the calculation in [3]. So, the photon flux in the sample region per unit area can be calculated by $3.6 \times 10^9 \times 20\%/(\pi \times 1.5^2) = 1.0 \times 10^8$ /sec/μm^2.

The radiation dose imposed on the sample can be estimated using Eq. 1.52, where D will be in Gray (Joule/kg) with the other quantities in MKS units:

$$
\begin{aligned}
&E_{\text{photon}} = 750 \text{ eV} = 750 \times 1.6 \times 10^{-19} \text{ Joule} = 1.2 \times 10^{-16} \text{ Joule}, \\
&\frac{\bar{n}}{\Delta^2} = 4.6 \times 10^7 \text{ /sec/}\mu\text{m}^2 \times 136.448 \text{ sec} = 6.3 \times 10^{21} \text{ /m}^2, \\
&\rho = 1.35 \text{ g/cm}^3 = 1.35 \times 10^3 \text{ kg/m}^3, \\
&\mu = \frac{4\pi\beta}{\lambda} = \frac{4\pi \times 1.0 \times 10^{-4}}{1.65 \text{ nm}} = 7.6 \times 10^5/\text{m}, \qquad (4.3)
\end{aligned}
$$

where the β value for protein at 750 eV is listed in Table. 1.1. Substituting values obtained by Eq. 4.3 into Eq. 1.52, we estimate that the radiation dose

for each 2D diffraction data set is about 9.1×10^8 Gray.

4.4.3 Image reconstruction

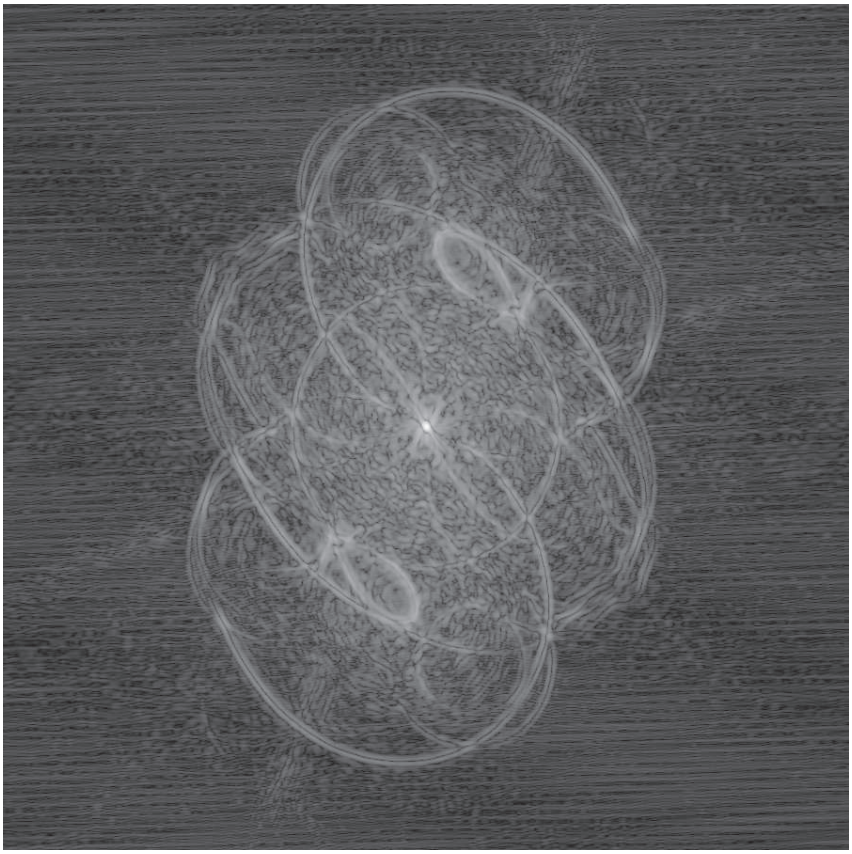

Figure 4.5: Autocorrelation image of the chemically dried cell from assembled diffraction data collected at 10°. The size and shape of the ghost image are the same as those of the object in real space.

We used the Difference Map algorithm to reconstruct the cell images. We started the reconstructions with initial supports defined from the autocorrelation functions (obtained by squaring the Fourier transform of the recorded data intensities and applying a high-pass Fourier filter to the result) at different angles. Fig. 4.5 shows the autocorrelation function at 10°. We see a pair of ghost images in the autocorrelation image. The size of the ghost image should be the same as that of the object in real space.

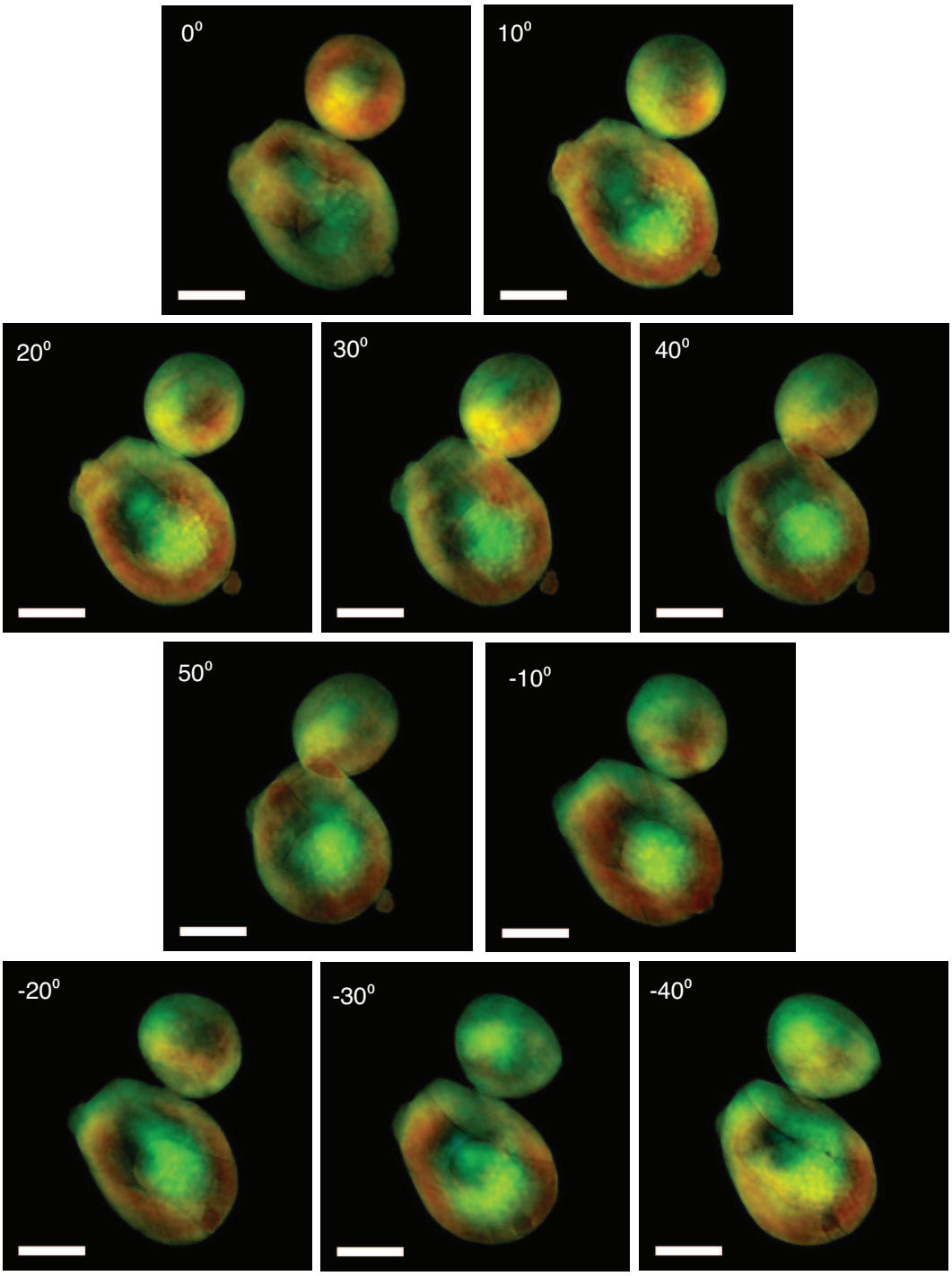

Figure 4.6: Reconstructed images from the chemically dried cell at 10 different angles. The scale bar is 1 μm.

The supports were then refined manually using the first-round reconstruction results. The support refining process was repeated several times until a correct support was obtained with confidence for each angle. The confidence is judged from the reconstruction reproducibility with different random starts, the PRTF level, convergence speed and error metric level.

With the best supports, 10 iterative reconstructions were run with 10 different random starts for each angle. Each of these 10 reconstructions consists of 10,000 iterations. When the iteration number exceeds 8,000, the outputs from every 2 iterations are averaged together to improve statistics of pixel values. The outputs from 10 reconstruction runs are then averaged to generate the final reconstruction image. During the averaging process, a global phase is applied in the way described in Sec. 2.3.4. A high pass filter was applied to the final averaged image following the way described in Sec. 2.3.3. The reconstructed images at those 10 angles are displayed in Fig. 4.6. These images show that we imaged a budding cell with a small bud sitting on the shoulder of the parent cell.

After taking x-ray diffraction data, we imaged the cell specimen in a scanning electron microscope, or SEM. The SEM images are quite consistent with the XDM reconstructions, as shown in Fig. 4.7. The scars from previous budding processes are resolved in the XDM image, which match the SEM image. A small object attached to the parent cell can be also seen in both the SEM and XDM images.

By looking at the 10 images series, especially the reconstructions from 10° to 50°, we can see the bud, the attached small object and some sub-cellular structures rotating systematically between different angles. This gives partial 3D structural information of the cell. The movie file, contained on the multimedia CD, shows how the reconstructed real space images rotate through those 10 different angles.

4.4.4 Reconstruction analysis

The reconstructed images in real space give both the magnitude and phase information of the cell specimen. Fig. 4.8 shows the magnitude and phase

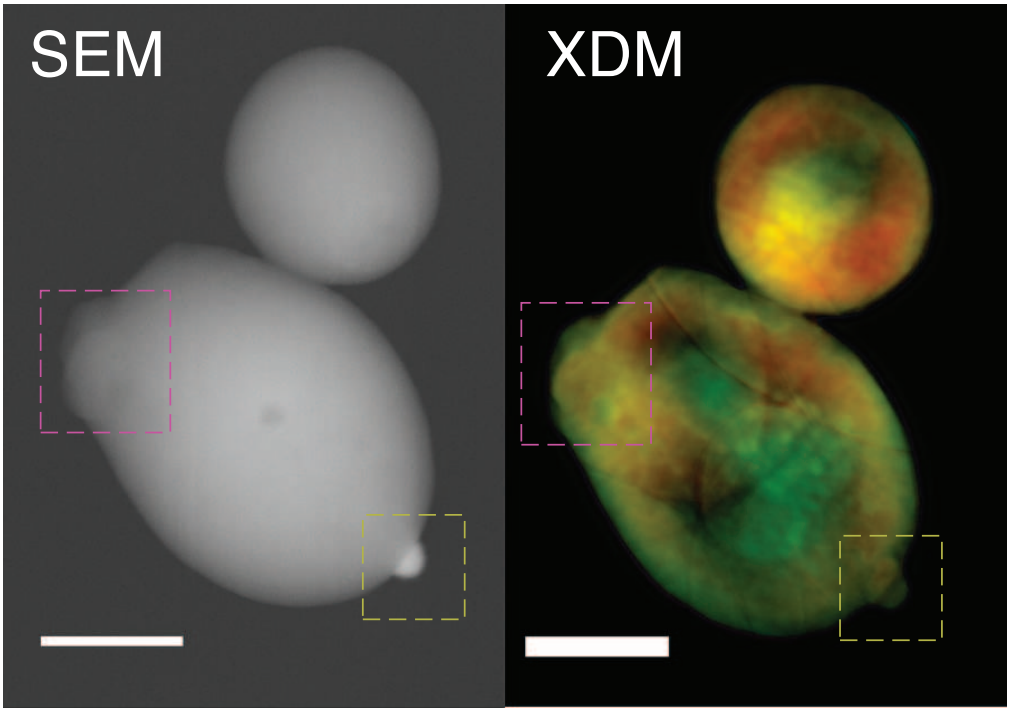

Figure 4.7: The SEM and XDM reconstruction images of the chemically dried cell. The scale bar is 1 μm. The red box locates the position of budding scars. The yellow box locates a small object attaching to the big cell.

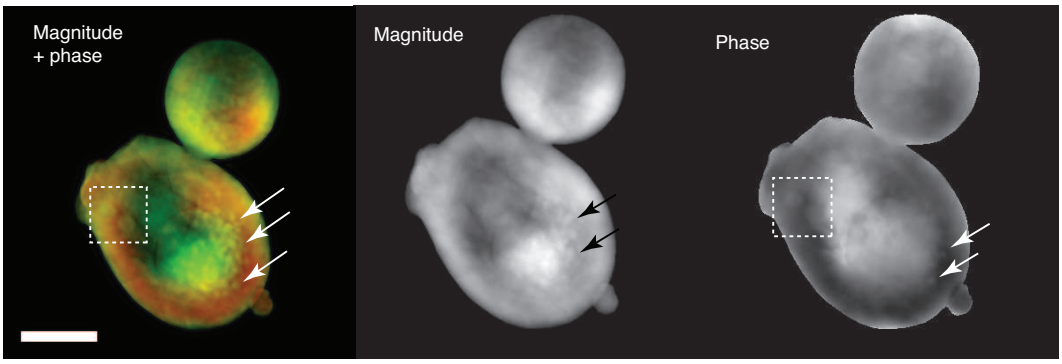

Figure 4.8: Reconstructed magnitude and phase of the chemically dried cell at 10°. The magnitude varies from 0 to 668 (arb. unit), and the phase varies from 0 to 0.8π. Both the magnitude and phase are displayed in the left image, where brightness demonstrates magnitude and hue demonstrates phase. The scale bar is 1 μm. The box and arrows locate the lipid balls in the cell.

parts, respectively, for the reconstruction at 10°. A number of lipid balls can be identified in the reconstructed images. These strong diffracting lipid droplets were consistent with the observation in TXM 3D tomography [28].

To estimated the reconstruction resolution, we picked a line in the reconstructed image, as shown in Fig. 4.9. For the reconstruction at 10°, a Gaussian fit over this lineout gives a half width at half maximum of about 19 nm. We also checked the PRTF curves of the reconstructions. For the 10° reconstruction, the PRTF level stays above 0.5 up to a half period resolution of 20 nm, as shown in Fig. 4.10. Based on the lineout Gaussian fit and the PRTF criterion, we estimate that the reconstruction resolution at 10° is about 20 nm. The resolution for other angles are estimated following the same steps. The reconstruction resolutions for all angles are summarized in Table. 4.1. From the assembled diffraction data images, we saw that the data quality varies for different angles, the estimation of reconstruction resolutions shows that the best resolutions are achieved at 10°-50°

Table 4.1: Reconstruction resolutions at 10 different angles for the chemically dried yeast cell.

Angle	0°	10°	20°	30°	40°
Resolution	33 nm	20 nm	25 nm	28 nm	25 nm
Angle	50°	-10°	-20°	-30°	-40°
Resolution	22 nm	33 nm	33 nm	28 nm	33 nm

Although the outline of the parent cell and the bud are resolved in the reconstruction, as well as the sub-cellular lipid balls, some other major sub-cellular organs, such as the nucleus and the vacuole, are not seen clearly in the reconstructed images. The main reason comes from the large size of the missing centers in the diffraction patterns. Simulations described in Sec. 3.4 show that the reconstruction algorithm cannot give reliable reconstructions with 64 missing speckles.

Another reason is the existence of enantiomorphs in the reconstructions, shown in Fig. 4.11. In most the reconstructed images, we see a bright round blob in the parent cell. It is the twin image of the bud. We can also see that a part of the parent cell boundary reflects inside. These unexpected structures

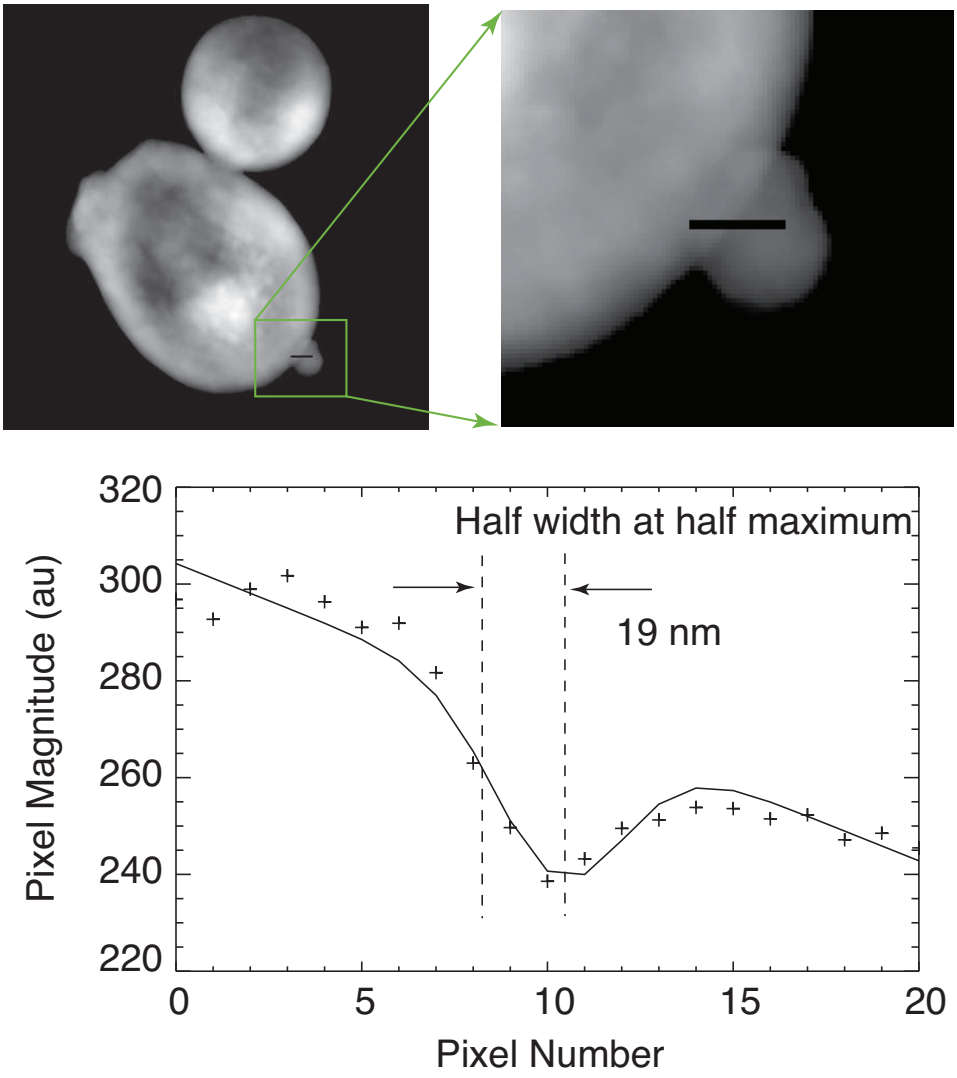

Figure 4.9: Top: a line was picked in the reconstructed image of the chemically dried yeast cell at 10°. Bottom, a Gaussian fit over this line gives a half width at half maximum of about 19 nm.

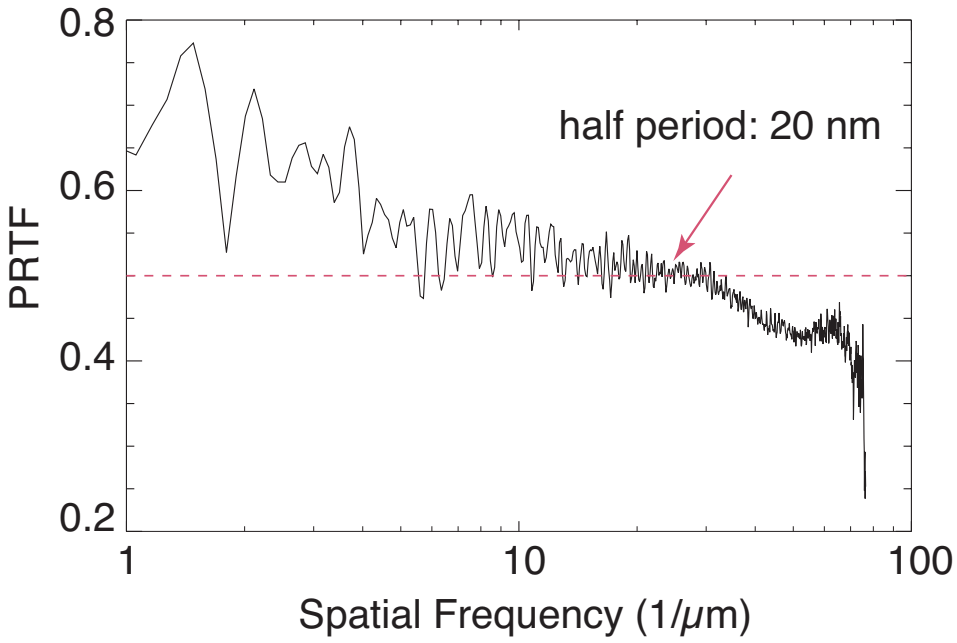

Figure 4.10: PRTF curve of the reconstruction at 10° for the chemically dried yeast cell. Up to 20 nm half period resolution, the PRTF level is above 0.5.

are embedded in the parent cell, which prevent the nucleus and the vacuole from being seen in reconstructions.

It is suggested that the enantiomorphs could be removed by the following strategy [90]: at the beginning at the iterative reconstruction process, replace the correct support with a temporary one, which covers part of the correct support area, perform a few iterations, and then replace back to the correct support to continue with the iterations. We tried this method for the current reconstructions, but It did not help remove the enantiomorphs. The simulation with fake cells shows that the enantiomorphs could be caused by noisy diffraction pattern. This implies that a better beamstop and corner alignment and a better matched background data set are needed to generate a clean diffraction pattern and thus a clear reconstruction.

This partial 3D data set collected at 10 rotation angles is not sufficient for performing a 3D reconstruction. One of the major reasons is that the data is rather sparsely sampled in angle. Another reason comes from radiation damage. The study on a dried yeast cell [83], as plotted in Fig. 5.2, shows

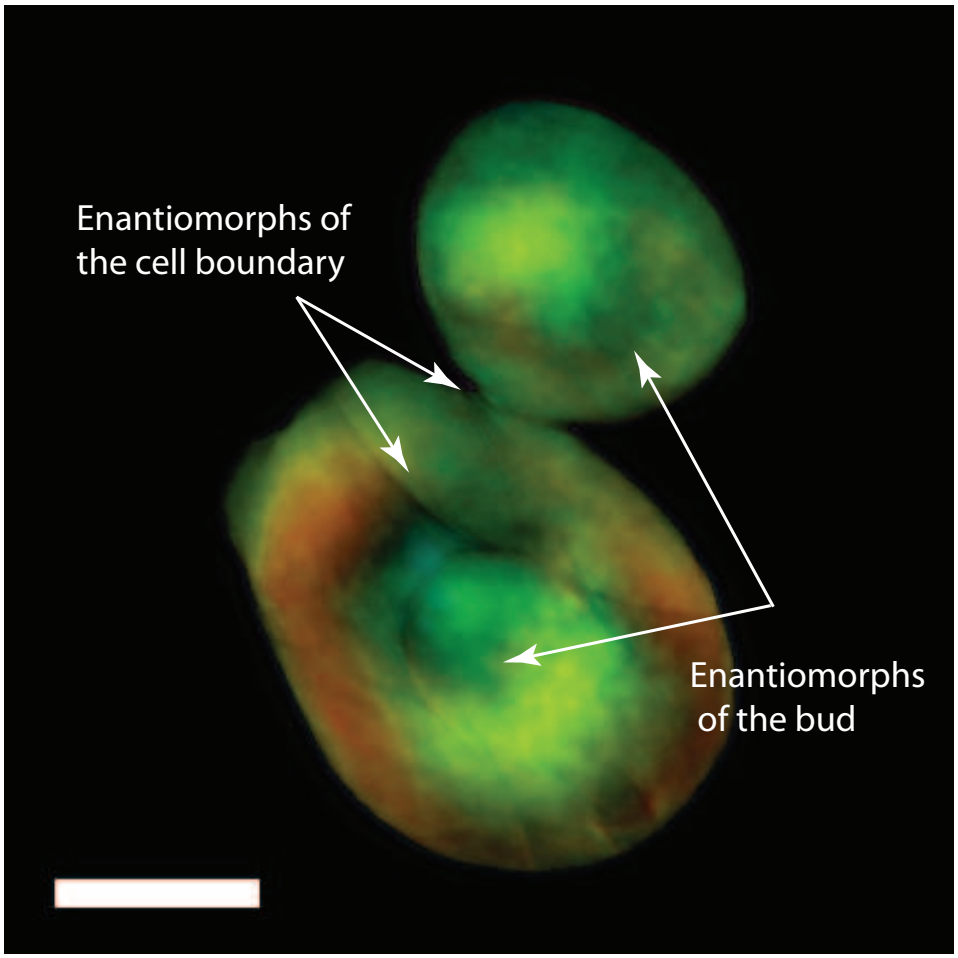

Figure 4.11: Enantiomorphs of the bud and the cell boundary are embedded in the parent cell in the reconstruction at -30°.

that the dried cell starts to shrink at a radiation dose level around 5×10^8 Gray. In this experiment, because the radiation dose for one set of 2D data is about 9.1×10^9 Gray, the cell's structure is quite possible to have been changed due to the accumulated radiation dose. The data acquisition process at multiple angles could involve more dramatic deformations.

Chapter 5

XDM experiment on frozen hydrated cells

Rapid freezing of cells allows one to preserve them with minimum structural changes and no dehydration artifacts. Frozen hydrated cells are also very robust against radiation damage. We applied XDM to a frozen hydrated yeast cell, and obtained the first image of a whole, eukaryotic cell using XDM. In this chapter, we discuss the motivation to work with frozen hydrated samples, how to prepare sample grids, data collection, image reconstruction, and the effort to improve the current experiment.

5.1 Motivation for frozen hydrated samples

Because XDM combines the benefits of x-ray microscopy (short wavelength and high penetration ability) with the advantages of dispensing with the technological limits on lens efficiency and resolution, XDM and the related diffraction-based approaches have been used as important biological imaging techniques by a growing number of groups, including demonstrations of imaging bacteria [77], yeast [55], herpes virions [79], malaria-infected erythrocytes [78], and chromosomes in 2D and 3D [80].

A remarkable limitation of all the previous XDM demonstrations of cells, chromosomes and virons is that they have all involved dehydrated specimens at room temperature. As an example, Nishino *et al.* [80] have obtained an exciting 3D XDM image of a dehydrated chromosome, but they also note significant resolution degradation due to accumulated radiation dose.

Because water is the most abundant component in biological samples, any dehydration process can cause structural artifacts. Dehydrated samples usually suffer from structural collapse, shrinkage, and distortion, with relatively poor preservation of sub-cellular morphology.

The frozen hydrated samples can solve problems in both aspects by mitigating the radiation damage problem and eliminating dehydration artifacts.

5.1.1 Elimination of dehydration artifacts

Chemically dried, freeze-dried and air dried biological samples have been successfully imaged by XDM. They are easier to work with, and more easily satisfy the finite support or isolated specimen constraint.

However, the removal of water from the cells cannot avoid structural changes [92]. For dissolved molecules, they tend to adhere to the closest solid neighborhood, and cause shrinkage and collapse. For the insoluble structures, such as proteins, are compact solid, so they do not always shrink or collapse, but they can undergo aggregations and conformational changes. Normally-hydrated organic molecules and supramolecular assemblies can change their shapes and collapse upon drying.

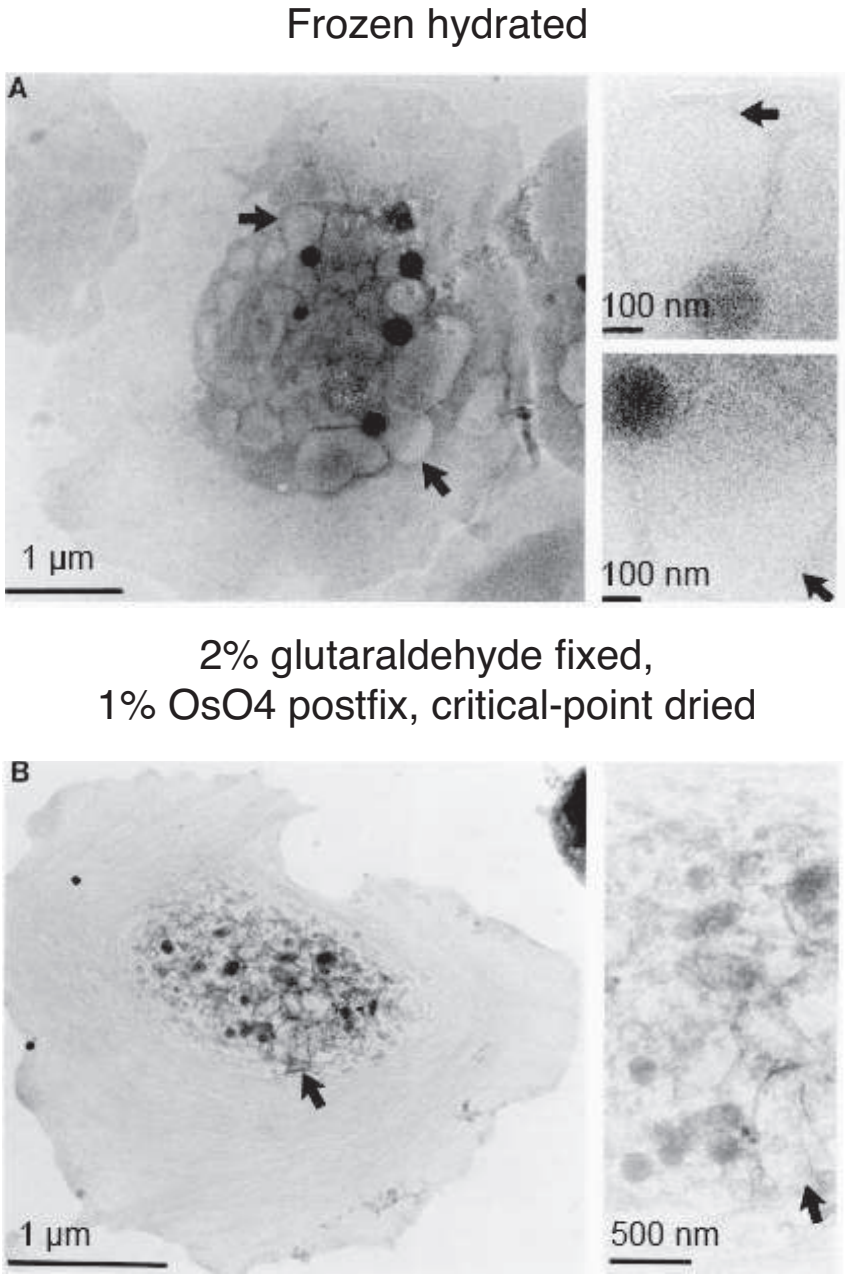

Figure 5.1: 1 MeV TEM images of human blood platelets from [91]. One is frozen hydrated, the other is chemically fixed and critical-point dried. The fixed and dried specimen is smaller and shows considerable collapse and aggregation of sub-cellular structures.

Electron microscope studies have shown that the cellular structures are faithfully preserved in frozen hydrated specimens [93–96]. Fig. 5.1 shows TEM images of frozen hydrated and chemically-fixed critical-point-dried human blood platelets, where we can see that the size of the dried sample is shrunk, the shape is distorted, the connections between sub-cellular organelles are extracted and collapsed. As a comparison, the frozen hydrated sample preserves most of the structures very close to the cell's living state.

5.1.2 Better radiation tolerance

As discussed in Sec. 1.4.3, radiation damage sets an ultimate limit for high resolution imaging with ionizing radiation. The radiation dose required to achieve high resolution can cause immediate changes in the samples, especially biological specimens, and produce remarkable mass loss and shrinkage.

In electron microscopy, stability against radiation damage has long been solved by imaging the specimen at cryogenic temperatures [93, 94, 97]. Electron microscopy studies of fixed and dried versus frozen hydrated blood platelets [91] reveal tremendous differences in structural preservation as shown in Fig. 5.1. However, because of the thickness limitations of electron microscopy on frozen hydrated specimens [72–74], only thin, peripheral regions of whole, unsectioned eukaryotic cells have been imaged in a frozen hydrated state using electron microscopy [98, 99].

Cryo x-ray microscopy experiments at 113 K do not show observable mass loss at 50 nm resolution level with radiation dose up to 10^{10} Gray [26, 30]. A radiation damage study with PMMA using cryo-STXM also shows that cryogenic conditions are very effective for reducing mass loss, although chemical bonds are broken at comparable rates at cryo and room temperatures [100].

The benefits of cryo methods for XDM have been shown in studies of Shapiro [83] with yeast cells. A series of diffraction patterns were taken from both a freeze-dried yeast cell at room temperature and a frozen hydrated yeast cell at cryogenic temperature. By monitoring the sizes of the speckles in certain spatial frequency range, the sizes of the cells in real space can be tracked as a function of radiation dose, as shown in Fig. 5.2. This study demonstrates

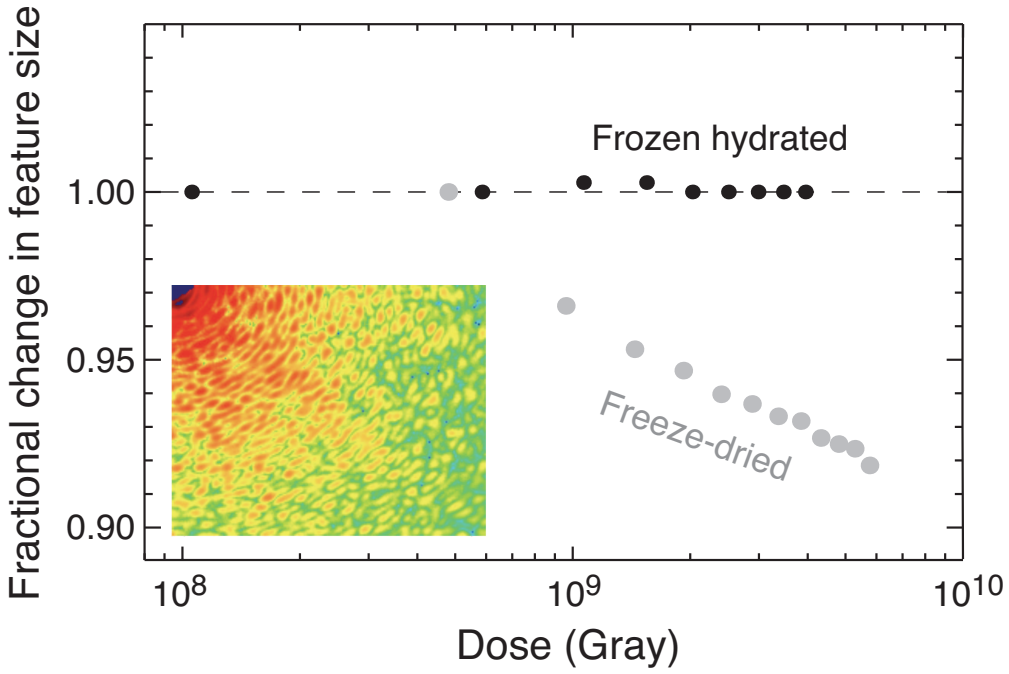

Figure 5.2: Demonstration of the stability of frozen hydrated yeast cells to 520 eV x-ray exposure for various absorbed doses in Gray [83]. Shown here are the fractional radial shifts of the centers of speckles in coherent diffraction patterns of yeast cells. The top curve is of cells that were viewed while frozen hydrated at -170°C, while the bottom curve is of cells that were freeze-dried and then exposed at room temperature. For the case of freeze-dried, room temperature cell, the center positions of speckles moved outwards from the diffraction pattern center, indicating a shrinkage of the object in real space.

significant stability of the diffraction patterns from the frozen hydrated cell out to doses up to 10^{10} Gray. In comparison, substantial specimen shrinkage was observed at room temperature before 10^9 Gray. Two separate groups have estimated that cryo XDM has the potential to deliver sub-10 nm resolution 3D images of whole hydrated cells within the limits of radiation damage [20, 21].

5.2 Frozen hydrated sample preparation

The XDM reconstruction algorithms require the specimen isolated from other scatterers. For frozen hydrated samples, the specimens are embedded or surrounded by ice. So we have to control the water on the sample grid to form vitreous ice, which has no crystalline structure and gives diffused diffraction signal.

5.2.1 Vitrification of ice

There are three major states for ice: hexagonal, cubic and vitreous. Hexagonal ice is a stable macro-crystalline modification at normal pressure, exhibiting the segregated compartments in a scale of 100 nm or more. Cubic ice is metastable microcrystalline, showing segregated compartments with diameters of about 20 nm, and it is usually the devitrification product of water-containing systems. Both of these two ice states diffract strongly, and thus do not satisfy our experimental requirement. Furthermore, the crystallization process can cause the solutes in cells to gain boundaries and result in potential structural artifacts. We want to control the water to form vitreous ice, which is amorphous. It has no detectable crystal structure, does not cause crystallization artifacts, and gives diffused diffraction signal.

The vitrification capability of a liquid is determined by its crystallization kinetics (nucleation and crystal growth rate) and the cooling rate. According the classical nucleation theory [101], the liquid crystallization generally takes place in two steps: a group of molecules forms an ice nucleus at the beginning, and then a consecutive growth around the nucleus will follow up rapidly. So, in order to obtain vitrified samples, the molecules have to be thermally settled

down before the ice nucleus is formed. The time required for vitrifying 1 μm^3 of pure water is in 10^{-4} sec range [102]. It has been shown that cells and biological tissues no thicker than 10 μm need a cooling rate more than 10^4 K sec^{-1} to be sufficiently vitrified [103].

5.2.2 Plunge freezing

Vitreous ice can be obtained by freezing the sample quickly. This can be done by plunge-freezing thin water layers into liquid ethane; in our case, we used a commercial instrument (FEI Vitrobot) to carry out this procedure.

The specimen is the yeast *Saccharomyces cerevisiae* carrying the *whi5* mutation, which is the same as in Chap. 4. The sample grid we used in the experiment is shown in Fig. 5.3, which is made from copper and designed for 3D data acquisition. It has seven 820×400 μm opening slots. The rectangular shape avoids the scattering from top and bottom edges for high rotation angles. The center bar in the center column is used for the 3D alignment, where the procedure is described in [83]. We coated this grid with a thin formvar film following the steps described in [35]. This film provides 98-99% transmission for 520 eV x-rays. It is also strong enough to support the specimen and has a reasonable surviving percentage from the sample preparation process.

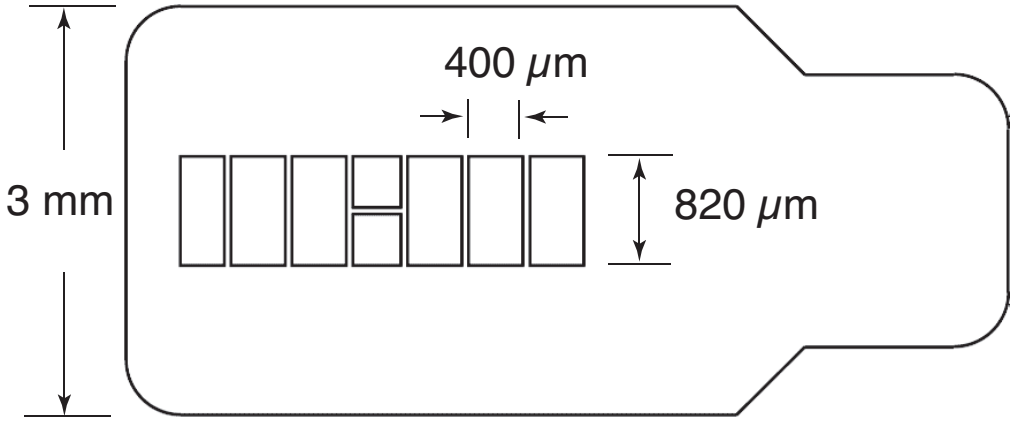

Figure 5.3: Sample grid used for Gatan 630 cryo-sample holder.

The cells were cultured in the same way as for the chemically dried cell in Sec. 4.2. The cell concentration was measured by Cellometer Disposable

Hemacytometer from Nexcelom [104]. We found that a concentration of about 20 cells in each 1×1 mm square of Cellometer gave good cell distribution on prepared grids.

Table 5.1: Plunging parameters and conditions of FEI Vitrobot for frozen hydrated sample preparation.

Cell concentration	20 per 1 mm^2 on Cellometer
Cell solution	5 μl
Oxygen plasma cleaning	20 sec
Vitrobot humidity	100%
Waiting time	30 sec
Blotting offset	2 mm
Blotting time	4 sec

In order to improve the hydrophilic property of the formvar surface and let the cell solution spread out uniformly, we cleaned the formvar coated grids using oxygen plasma for 20 sec. We then mounted the grid on the Vitrobot, where the blotting offset was set to 2 mm. The humidity of the closed chamber in the Vitrobot was set to be 100%. When the sample grid was pulled into the chamber, we added a 5 μl droplet of cell solution on to the grid using a pipette. We then waited for 30 sec to let cells settle down on the grid. The grid was then blotted by a pair of filter paper for 4 sec to remove extra liquid. After blotting, the sample grid was plunged into the cooling bath. There are 2 separated sections in the cooling bowl: the center part is filled with liquid ethane, and the outside ring section is filled with liquid nitrogen. The sample grid was plunged into liquid ethane first, and then transfered and stored into liquid nitrogen once the temperature of the grid was stabilized, which is judged by the cessation of bubbling. Table 5.1 summarizes the plunging parameters.

Although the temperature of liquid nitrogen is lower than that of liquid ethane, we cool the sample with liquid ethan first, because the cooling efficiency of liquid ethane is much higher than that of liquid nitrogen. Table 5.2 lists the freezing points and cooling efficiencies of some widely used cryogenic coolants, compared with liquid propane. We can see that the cooling efficiency of liquid ethane is one order higher than that of liquid nitrogen.

Table 5.2: Cooling efficiencies and freezing points of widely used cryogens in comparison with liquid propane [105–107]. Cooling efficiency greater than 1 indicates higher cooling rate than liquid propane, smaller than 1 means cooling rate lower than liquid propane. For boiling liquid nitrogen, the listed temperature is at its boiling point.

Cryogen	Freezing point (K)	Freezing point (°C)	Cooling efficiency
Ethane	91	-182	1.3
Propane	86	-188	1.0
Freon 13	92	-181	0.8
Freon 22	98	-175	0.7
Freon 12	116	-158	0.5
Isopentane	113	-160	0.5
LN_2	63	-210	0.2
Boiling LN_2	77	-196	0.1

The entire sample preparation, transfer, storage and data acquisition process has to be performed under at least -140°C (133 K). Electron microscopy studies have shown that vitrified samples start to devitrify at approximately 135 – 140 K [108, 109]. The devitrification and recrystallization process could cause conformational changes to the specimen.

5.3 Diffraction data and reconstruction

We collected diffraction data from a frozen hydrated yeast cell with 520 eV x-rays at Beamline 9.0.1 of the Advanced Light Source. We successfully reconstructed the phase information, and obtained the first image of an intact, eukaryotic cell using XDM [110] with a resolution better than 25 nm.

5.3.1 Diffraction data collection

Apart from the fact that the specimen was in a frozen hydrated state, the diffraction data were acquired in a manner similar to what was described previously for the studies of the chemically dried yeast cell in Chap. 4 and the freeze-dried yeast cell in [55]. A zone plate monochromator [84] was used at undulator beamline 9.0.1 to deliver a 520 eV x-ray beam to the experimental

apparatus [15]. By using a 5 μm pinhole located 2.5 cm upstream of the specimen, we were able to provide illumination with both the sufficient spatial coherence [87] and the required temporal coherence of $\lambda/\Delta\lambda = 500$.

By working at 520 eV, we were able to take advantage of the "water window" spectral region (as shown in Fig. 1.4) with low absorption in water and good contrast of organic materials [18, 72]

During data acquisition process, the sample grid temperature was controlled to stay at -170°C. In order to improve the vacuum quality and protect the sample grid from moisture and dust condensation, there is a liquid nitrogen cooled copper plate, which we called the "cold finger", installed in the chamber. The temperature on the cold finger was about -180°C. The pressure of microscope vacuum chamber was 4.0×10^{-7} torr.

For this particular specimen, we checked the transmission of the ice layer at a position near the cell, by measuring the transmitted beam flux using a photodiode and the incident flux with sample grid removed. This measurement indicates a transmission through the ice of about 90%, corresponding to an ice thickness of about 1 μm, calculated using Eq. 1.29.

The diffraction data were recorded with a 1340×1300 Princeton Instruments PI-MTE 1300B CCD with 20×20 μm pixel size [111], which was located 17.5 cm downstream of the specimen. The diffraction patterns were taken at multiple corner and beamstop positions again. We aligned the x-ray beam with the centers of corner and beamstop, which is called "high exposure" position for longest exposures (1, 10, 30 and 60 sec) and collecting highest spatial frequency signal. We aligned x-ray beam with the diagonal corners of corner and beamstop, which are called "top or bottom low" positions for shortest exposures (0.001, 0.005, 0.01 and 0.05 sec) and collecting lowest spatial frequency signal. The x-ray beam is also aligned at two "intermediate" positions which locate between the high and low positions for collecting signal in the intermediate spatial frequency range with medium exposure times (0.05, 0.1, 1 and 5 sec). From the diffraction patterns of the chemically dried sample shown in Chap. 4, we found that the overlapping of the beamstop arm at different locations can leave a CCD region with no effective signal reading. To solve this problem, we moved the beamstop 300 μm away from the high exposure

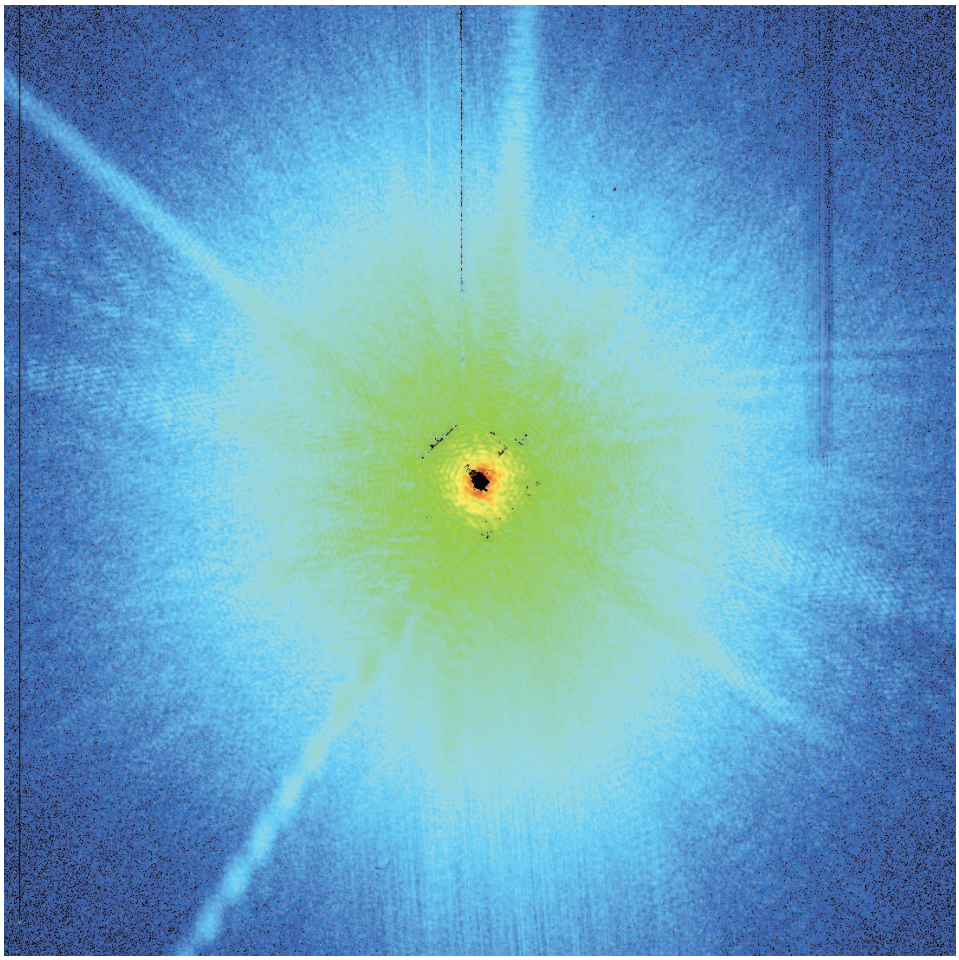

Figure 5.4: The assembled diffraction data from the frozen hydrated yeast cell. Array size is 1100×1100 with a 20×20 missing center.

position in Y direction, where we called it the "beamstop move" position and make sure that there was no beamstop arm overlapping with the high exposure position. The exposure times at this location were the same as at high exposure location. At each aligned position, each exposure time was repeated 5 times. The total exposure time for a 2D data set was 214.882 sec.

The photodiode reading of the incident beam flux was 47 nA. From Eq. 4.2, we can calculate the 520 eV photon flux to be about 2.1×10^{9} /sec. Following the dose estimation steps described in Sec. 4.4.2, the radius of the center Airy ring with 520 eV x-ray from a 5 μm pinhole placed 2.5 cm away form the sample grid is about 7.3 μm calculated from Eq. 1.49. Considering a cell with a radius about 1.5 μm located in the center of the Airy pattern from the pinhole, about 10% of the total photon flux is distributed in the cell area according to the calculation in [3]. This gives the photon flux in the cell region was about 3.0×10^{7} /sec/μm^2. Substituting the values

$$
\begin{aligned}
&E_{\text{photon}} = 520 \text{ eV} = 520 \times 1.6 \times 10^{-19} \text{ Joule} = 8.3 \times 10^{-17} \text{ Joule},\\
&\frac{\bar{n}}{\Delta^2} = 1.3 \times 10^{7} \text{ /sec/}\mu\text{m}^2 \times 214.882 \text{ sec} = 2.8 \times 10^{21} \text{ /m}^2,\\
&\rho = 1.35 \text{ g/cm}^3 = 1.35 \times 10^{3} \text{ kg/m}^3,\\
&\mu = \frac{4\pi\beta}{\lambda} = \frac{4\pi \times 2.6 \times 10^{-4}}{2.38 \text{ nm}} = 1.4 \times 10^{6}/\text{m},
\end{aligned}
\tag{5.1}
$$

into Eq. 1.52, we estimate the total radiation dose imposed on the cell is about 5.5×10^{8} Gray for a 2D data set. Using the method described in [83], the estimated dose value is 1.7×10^{8} Gray.

In order to remove the background from ice scattering and corner scattering, we collected 2 sets of background after taking data from the cell. As an ice background, we moved the sample grid 40 μm in Y direction and collected ice scattering data at that spot. We recorded another set of no-sample background with the sample grid completely removed.

The diffraction data from the cell, ice background and no-sample background were assembled separately. We found that the ice background data does not match the cell diffraction very well. This implies that the ice condition at the background taken position was not identical to that surrounding

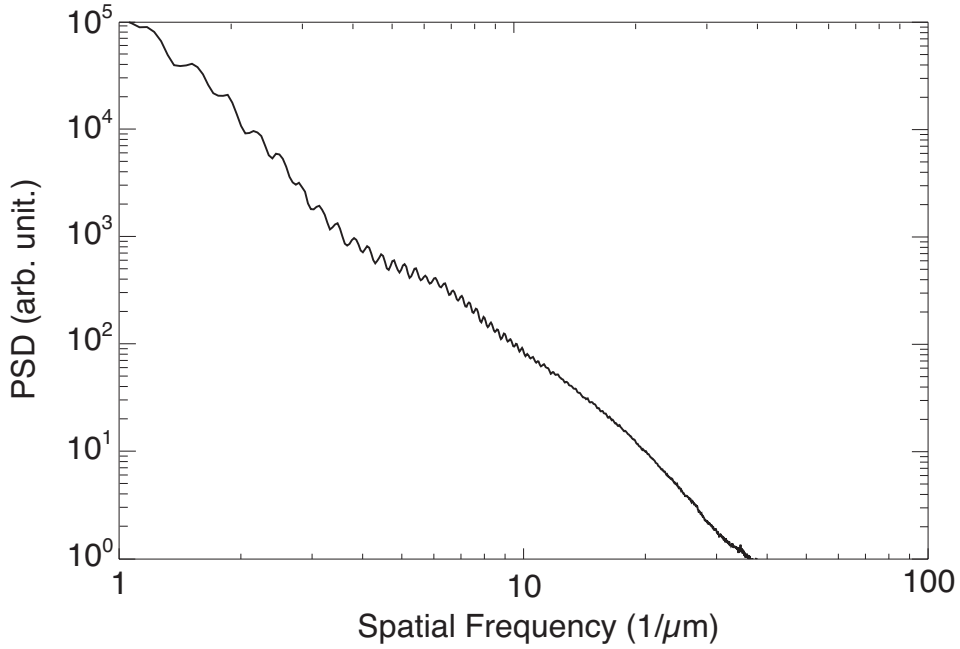

Figure 5.5: The power spectral density curve of the assembled diffraction data from the frozen hydrated yeast cell.

the cell specimen. The final data array was generated by subtracting the no-sample background from the initial data array. A 1100×1100 effective array was extracted from the initial 1340×1300 assembled array. The size of the missing center is about 20×20 pixels. Considering the oversampling ratio of this specimen is about 35, the missing speckle number is 11. According to the simulation result in Sec. 3.4, the difference map algorithm is able to give reasonable reconstructions under this condition. Fig. 5.4 shows the final assembled data array. The black pixels around the low spatial frequency area besides the missing center come from mismatching between data and no-sample background. The vertical lines on the right side of the assembled diffraction pattern are caused by damaged pixels on the CCD. The power spectral density curve is shown in Fig. 5.5.

The assembled diffraction pattern extends to 26 μm^{-1} spatial frequency at edges and 37 μm^{-1} at corners, which correspond to a half-period size of 19 nm at edges and 14 nm at corners. The pixel size in real space image is 19 nm.

5.3.2 Reconstruction

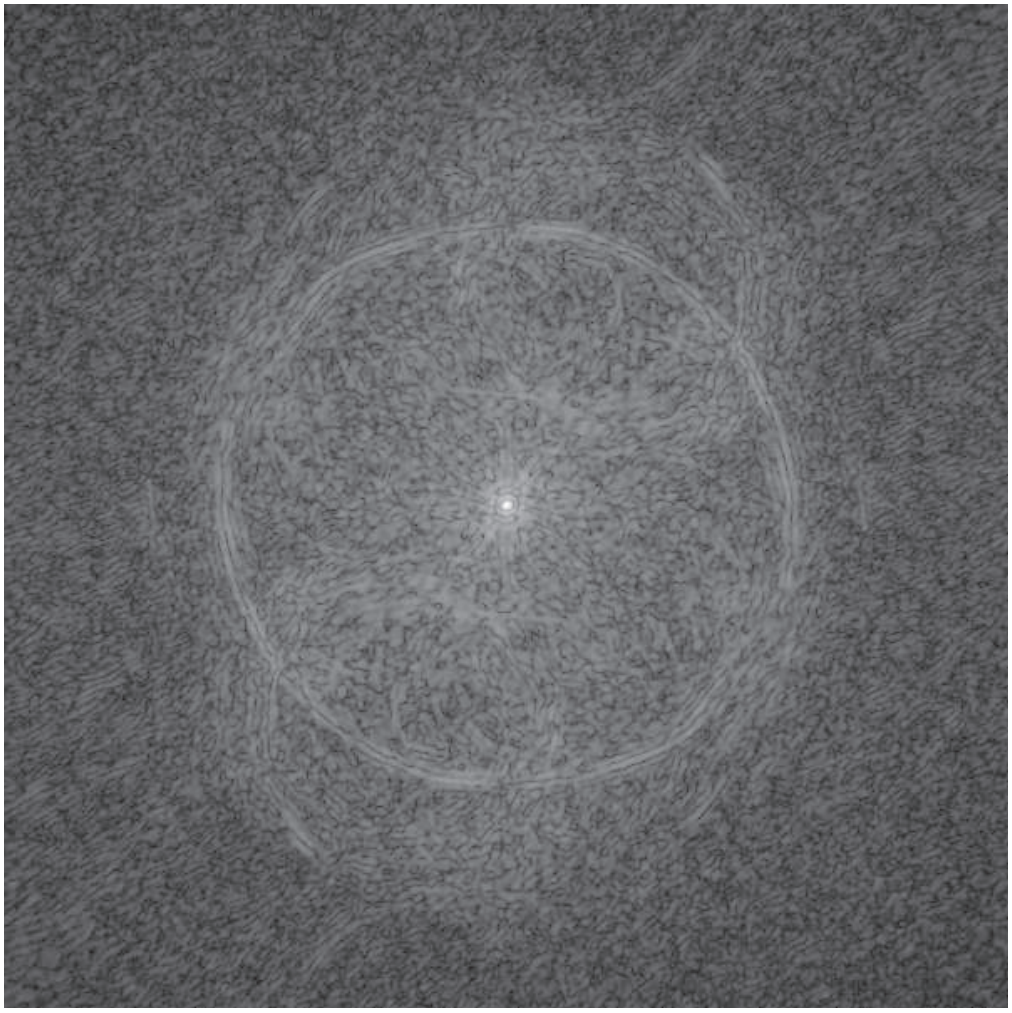

Figure 5.6: Autocorrelation image calculated from the assembled diffraction data of the frozen hydrated yeast cell.

The image in real space was retrieved from the assembled data using the Difference Map algorithm [45]. The original support guess was obtained from the shape of the ghost image in the autocorrelation picture, as shown in Fig. 5.6. The support was refined using the reconstruction outputs from the initial support. Once the best support was obtained, 10 independent reconstruction runs were performed with different random starts. Each reconstruction was run 10,000 iterations, and the averaging procedure was started after

8,000 iterations by summing outputs from every 20 iterations. The final reconstructed image was formed from the average of the outputs of all those 10 reconstructions. The global phase (Sec. 2.3.4) and the high pass filter (Sec. 2.3.3) were applied in the reconstruction and averaging process.

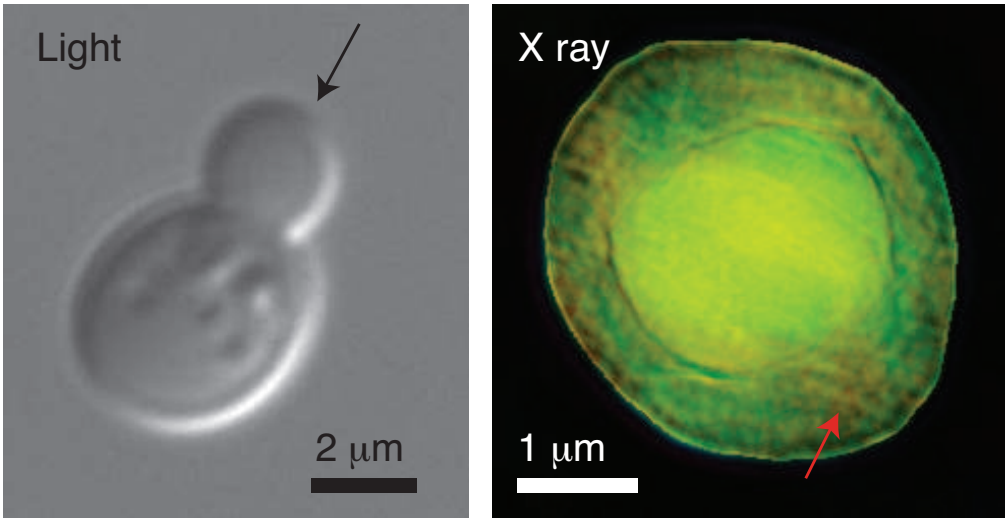

Figure 5.7: Images of *Saccharomyces cerevisiae* yeast cells. At left is shown a visible light DIC image of a budding yeast taken using a 100×, N.A.=1.3 immersion objective. The arrow indicates the assumed beam direction for the x-ray diffraction micrograph at right, which is of a different yeast cell. The x-ray diffraction micrograph is a complex wave reconstruction, where the magnitude is represented by brightness and the phase by hue. A possible mitochondrion is indicated with the red arrow.

The right side of Figure 5.7 shows the reconstructed complex image of a frozen hydrated yeast cell obtained using the method described above. For reference, a visible light micrograph of a budding yeast is also shown (obtained using a a Zeiss Axioplan2 microscope with a 100×, NA=1.3 immersion objective with DIC optics, and a mRM Axiocam with Zeiss Axiovision 7.1 software). In the x-ray diffraction micrograph, we see what appears to be two cell bodies lying on top of each other. Since this inner cell body is too large to be a nucleus in this cell type, we believe that the image shows a new-born bud produced as part of the division process in these cells, viewed from directly above the bud with the parent cell underneath (see the assumed illuminating beam orientation in Fig. 5.7 as indicated by the black arrow).

5.4 Reconstruction analysis

We verified the budding cell orientation using two approaches, both of which confirm that the bud is sitting on top the parent cell. We also estimated the reconstruction resolution with two methods, and concluded that the achieved resolution is better than 25 nm.

5.4.1 Budding orientation verification

We collected a limited data set with the sample rotated at 15 degree. While this second data set was inadequate to get a reconstructed image, it provides useful autocorrelation data, as shown in Fig. 5.8. As a comparison, we simulated two fake cells: one with a condensed core (A and B in Fig. 5.8), the other with a bud on its top (E and F in Fig. 5.8). We tilted the simulated cells to 0 and 15 degrees and calculated the autocorrelations at each angle. We found that there is no significant change in the autocorrelations at different degrees from the simulated cells with a core (C and D in Fig. 5.8). In the autocorrelation at 15 degree from the simulated cell with a bud, the circles slide one off another, compared with 0 degree (G and H in Fig. 5.8). The experimental autocorrelation data shows more curved outlines at 15 degree (J in Fig. 5.8), which is more analogous to that from a simulated cell with a bud on top.

Another evidence is available by "focusing through" the reconstructed image. Since we had reconstructed a complex wavefield at a depth plane where the outermost edges of the object within its support are sharpest [54, 112], we were able to use Fresnel propagation to generate the reconstructed wavefield at nearby depth planes. We picked two pairs of lines in the reconstructed image: the first pair is on the boundary of the bud (T1 and T2 in Fig. 5.9), the second pair is from the parent cell region (B1 and B2 in Fig. 5.9). If the bud is on top of the parent cell, these two pairs of lines should be focused on different focal planes. We propagated the reconstructed image from -3 μm to +3 μm, and picked the sharpest position for each line, which locates its focal plane. We found that the focal planes of T1 and T2 are almost at the same level, and B1 and B2 are focused on another plane. These two focal planes are

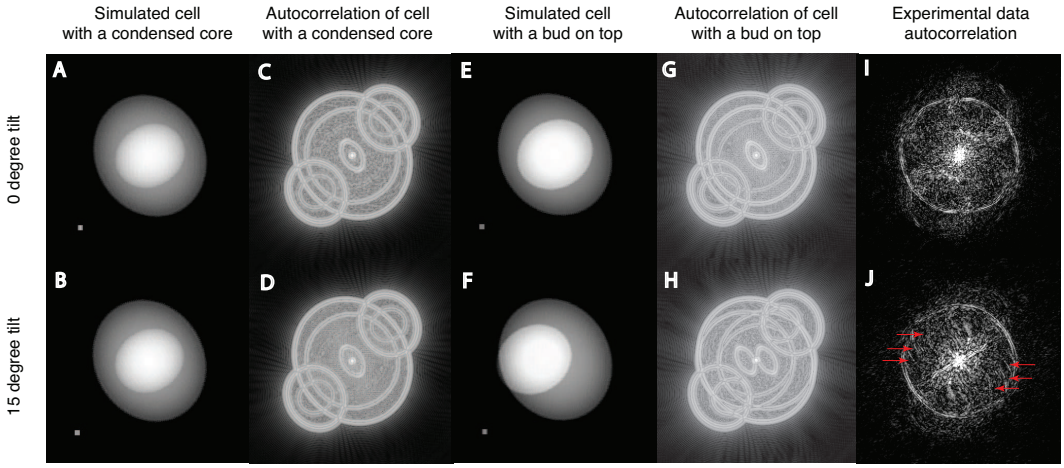

Figure 5.8: Autocorrelations from experimental data at 0 and 15 degrees support the assumption that the x-ray diffraction micrograph is of a budding yeast viewed end-on, though the 15 degree tilt x-ray data were inadequate to yield a reconstruction. (A and B) The simulated images of the optical density of two ellipsoids one inside the other representing a cell and its nucleus core viewed at 0 degree and 15 degree tilt. (C and D) The autocorrelations of diffraction intensities (like the Patterson function used in x-ray crystallography) from simulated cell with a core. There is no significant pattern change in the autocorrelations at different tilt degrees. (E and F) The simulated images of the optical density of two ellipsoids representing a cell and its bud on top viewed at 0 degree and 15 degree tilt. (G and H) The autocorrelations from simulated cell with a bud. The circles slide off one another in the autocorrelation at 15 degree tilt. (I and J) The autocorrelations of experimental data at 0 and 15 degrees respectively. More curved outlines are recognizable in the autocorrelation at 15 degree, indicated by red arrows in (J). The change in the autocorrelations from the experimental data at the two tilt angles is more analogous to that from a simulated cell with a bud on top.

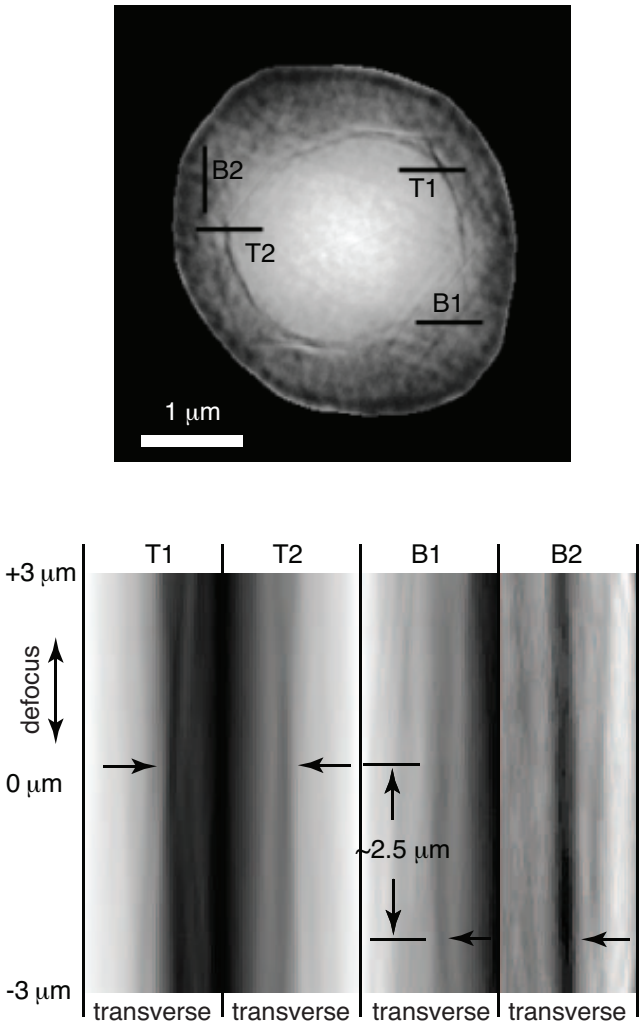

Figure 5.9: Through-focus imaging using the complex wavefront reconstructed in XDM. Four selected lines are shown on the magnitude-only representation of the reconstructed wavefront at top. The image at bottom shows line profiles of the reconstructed image magnitude as the wavefield is propagated from the reconstruction plane. In-focus edges look like the waist of an hourglass in such a representation; the line profiles from the inner and outer spherical objects in the reconstruction appear to be at different focal planes, consistent with the iterpretation that the larger parent cell is at lines B1 and B2, and the bud is at lines T1 and T2.

separated by about 2.5 μm (as shown in Fig. 5.9), which is about the same size of the bud.

Both of these two tests verified that we imaged a budding yeast cell with the bud sitting on top of the parent cell.

5.4.2 Resolution estimation

The reconstructed x-ray diffraction micrograph shown in Fig. 5.7 does not have the same degree of image contrast as the demonstration with the freeze-dried yeast [55]; we attribute this to the fact that the ice layer outside the cell was contributing some weak scattering which slightly violates the conditions required for imposition of a finite support constraint [113]. In spite of this limitation in our first frozen hydrated XDM demonstration, we are able to recognize sub-celluar features including what may be a mitochondrion in the parent cell (indicated by the red arrow in Fig. 5.7).

The resolution can be estimated to 25 nm or better using two independent measures. While the diffraction data extends to the edge of our CCD detector at a spatial frequency of 37 μm^{-1}, we do not claim this as representing the resolution of our reconstructed image. Instead, the magnitude ratio $M_{\text{recon}}/M_{\text{data}}$ (the phase retrieval transfer function or PRTF [36, 54, 55]) provides a good metric of the resolution of the reconstructed image. It does so by measuring the reproducibility of the phases recovered in the Fourier plane as the iterative reconstruction proceeds; phases that are reproducible lead to constructive interference when complex iterates are added together, while less reproducible phases lead to a lower value in the average. The spatial-frequency-dependent magnitude ratio $M_{\text{recon}}/M_{\text{data}}$ plot is shown at top in Fig. 5.10. The resolution cutoff was estimated at the spatial frequency where the PRTF drops below a value of 0.6. This provides one estimate of the half period resolution of 20 nm for the reconstructed x-ray diffraction micrograph.

Another measure of the resolution can be obtained by looking at the minimum width of features in the reconstructed image. Since the appearance of features in the image represents a convolution of their true shape with the point spread function of the imaging system, this measure is imperfect. Even

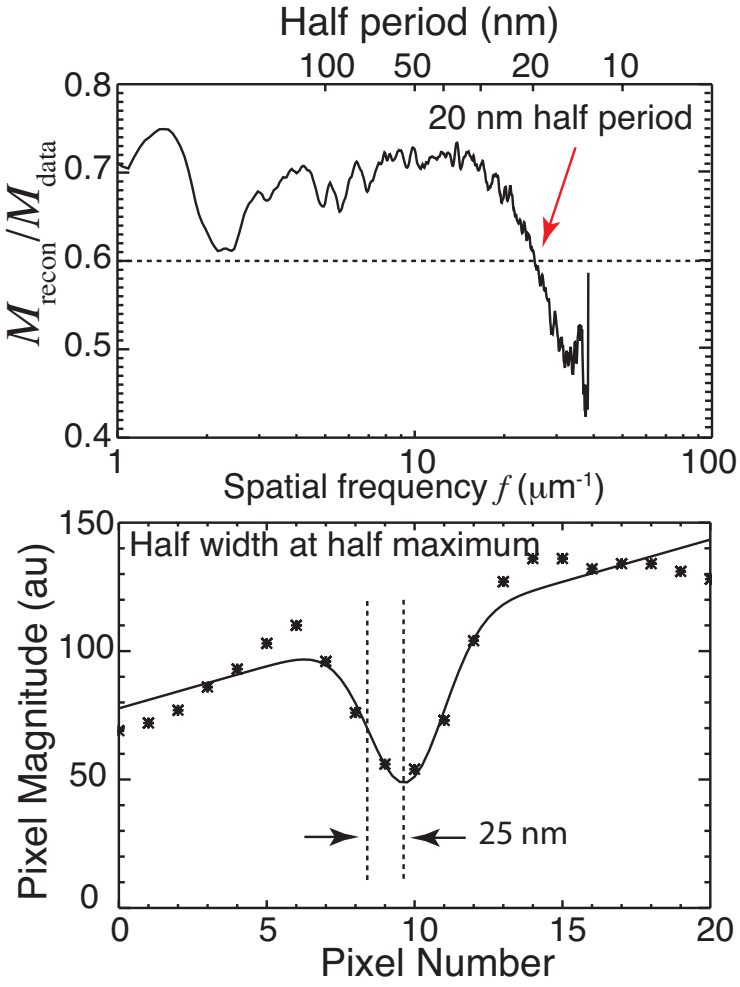

Figure 5.10: Estimation of the resolution of the x-ray diffraction micrograph. At top is shown both the azimuthal average of the magnitude ratio (or PRTF) $M_{\mathrm{recon}}/M_{\mathrm{data}}$. The PRTF measures the reproducibility of reconstructed pixel values as a function of spatial frequency; its decline at higher frequency provides an indication of the resolution. The resolution cutoff is estimated at the spatial frequency where the PRTF drops below a value of 0.6. This provides one estimate of the half period resolution of 20 nm. At bottom is shown a line scan across T2 in Fig. 5.9 at the plane of sharpest focus of this object. Also shown is a Gaussian-smoothed fit which indicates a half width at half max of 25 nm (or $\sigma = 21$ nm in $\exp(-0.5x^2/\sigma^2)$) for the combination of feature size and imaging resolution.

so, in Fig. 5.10 we also show a plot of the reconstructed intensity across a line (T2) in the image, along with a gaussian fit to the sharp feature seen. The Gaussian fit $\exp(-0.5x^2/\sigma^2)$ has $\sigma = 21$ nm, or a half width at half maximum of about 25 nm, again indicating that a high resolution image was obtained.

5.5 Anti-contamination device

During the data acquisition process from the frozen hydrated specimen, we noted that the diffraction speckles were gradually washed out by the scattering signal from accumulating ice. Because the sample grid is at very low temperature (-170°), any residual water vapor in the experiment vacuum chamber tend to condense on the grid and form frost and ice crystals, which will violate the object isolation requirement and degrade the sample's diffraction pattern over time. Although we have a cold finger serving as the coldest surface in the chamber, it is about 20 cm away from the grid, so it does not provide sufficient protection. We collected data at several different angles from the frozen hydrated cell, but only the first data set can be reconstructed.

Electron microscopy studies have shown that a cryogenic shield over the sample grid is important for imaging frozen samples [114]. To solve the contamination problem and protect the sample long enough for 3D data acquisition, we designed and installed an anti-contamination device (ACD) for the cryogenic x-ray diffraction microscope [15].

5.5.1 Mechanical design

Fitting cryo sample holders

The x-ray diffraction microscope [15] uses Gatan 630 and 914 high-tilt cryo-specimen holders, as shown in Fig. 5.11. The Gatan 630 holder uses rectangular grids with a 3 mm width (as shown in Fig. 5.3), and the Gatan 914 holder uses the standard electron microscope circular grid with a 3 mm diameter, while the grid holding frame is about 2 mm wider than grids. These holders are equipped with retractable slots to protect sample grids during the transfer

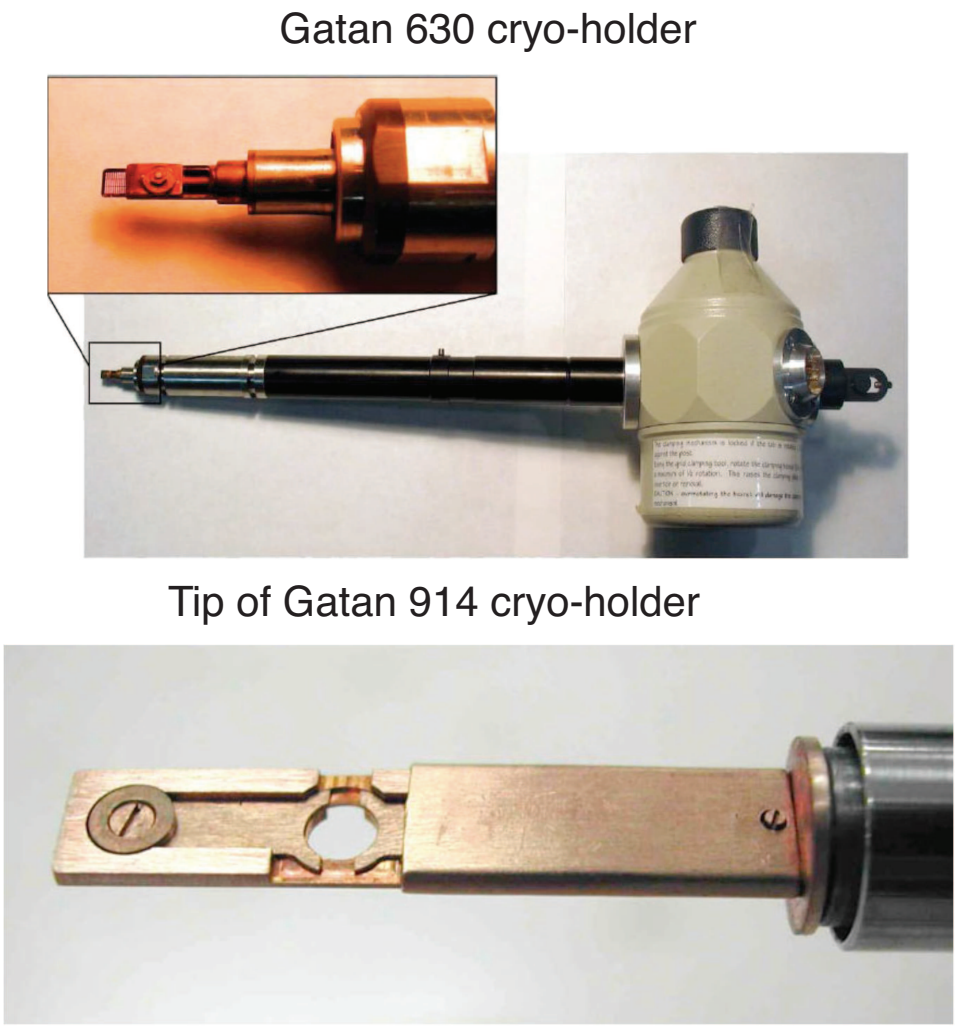

Figure 5.11: Gatan 630 and Gatan 914 cryo-sample holders. the Gatan 630 holder uses rectangular grids with a 3 mm width (as shown in Fig. 5.3), and the Gatan 914 holder uses the standard electron microscope circular grid with a 3 mm diameter, while the grid holding frame is about 2 mm wider than grids.

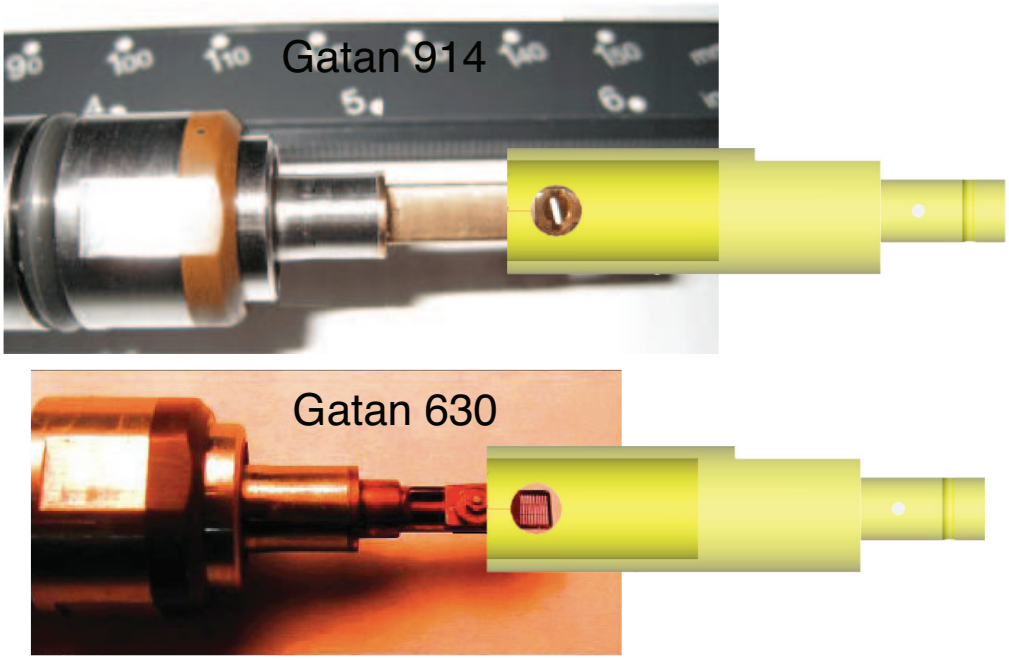

Figure 5.12: The inner diameter of the anti-contaminator is 8 mm. It fits both Gatan 914 and Gatan 630 cryo-sample holders. There are two 4 mm diameter windows on its side wall, which allow the x-ray beam to illuminate the sample grid and the diffraction signal to propagate without being obstructed.

process, but the grid is exposed to moisture in the residual gas during data aquisition.

To prevent ice building up on cryo specimens, the anti-contaminator, a liquid-nitrogen-cooled copper shield, was designed to surround the sample grid as close as possible with its temperature maintained at a level lower than that of the grid. The anti-contaminator is made from copper, and coated with a thin layer of gold, which protects the copper surface from oxidization and reduces the thermal emissivity of the surface. Its dimensions were determined by fitting the tips of both sample holders. To achieve the maximum shielding of the sample, the anti-contaminator was designed as a hollow cylinder of 8 mm inner diameter, and it is inserted coaxially around the sample grid, as shown in Fig. 5.12. The anti-contaminator shield is about 2.5 mm away from the grid edges. When the cylinder long axis is aligned with the rotation axis of the sample holder, the grid is able to be rotated with no conflicts for 3D data acquisition.

As the x-ray beam is perpendicular to the rotation axis of the sample holders, there are two 4 mm diameter windows on the side wall of the anti-contaminator, which allow the x-ray beam to illuminate the sample grid and the diffraction signal to propagate without being obstructed.

Mounting and positioning

The anti-contaminator is mounted on a Micos PP-30 piezo positioner [115] X-Y motor stage (shown in Fig. 5.13), which gives 30 mm travel ranges in both directions with 1 μm accuracy. The adjustment ability in X and Y directions helps align the anti-contaminator with the rotation axis of the grid, and align the 4 mm diameter side windows with the opening area of the grid as well. The anti-contaminator can also be fully removed from the grid in the X direction, when it is not in use. A motor in the Z direction is not required, because the X-Y stage mounting slot on the chamber is well matched with the grid holder in the Z direction.

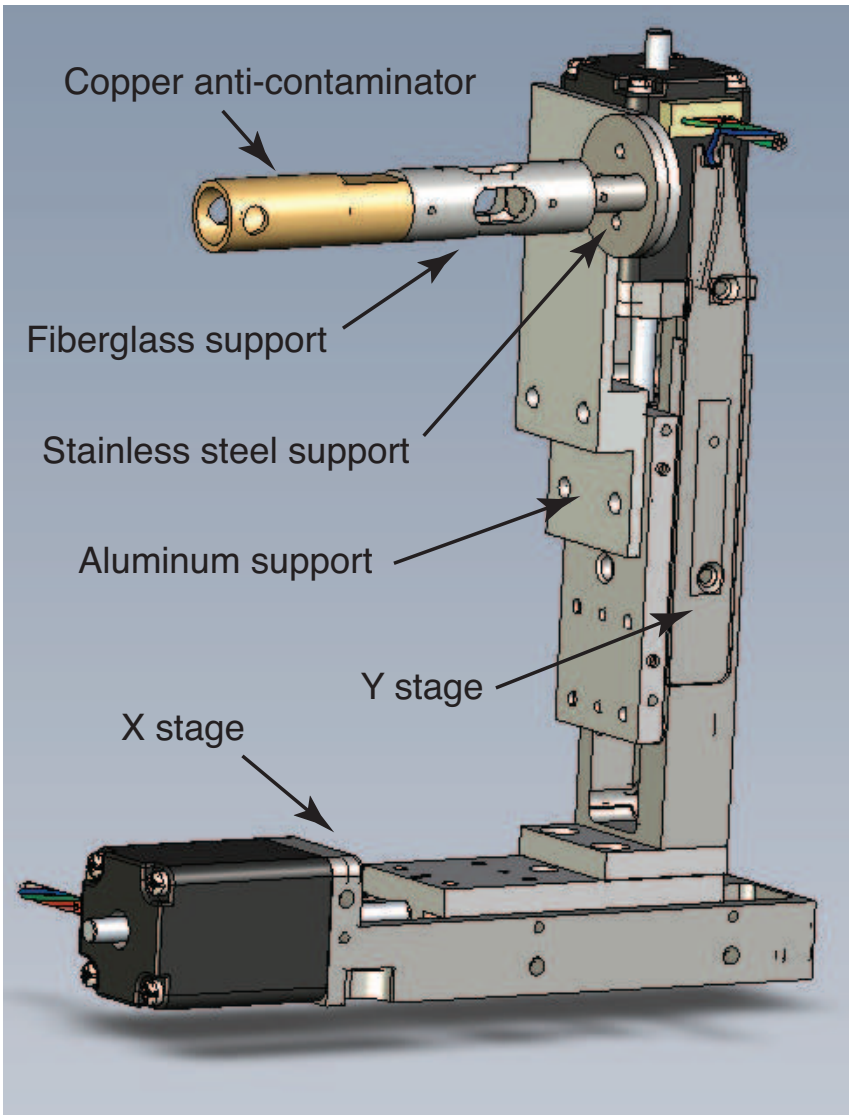

Figure 5.13: The anti-contaminator is a hollow copper rod coated with gold. It is mounted on a Micos PP-30 X-Y motor stage. The ACD is thermally isolated from the warm stage by a hollow fiberglass support and a stainless steel support.

5.5.2 Thermal design

The water molecules on sample grids can be rearranged to form cubic ice crystalline structure by warming up vitreous ice to approximately $-128°C$ – $-133°C$ [108, 109], and the residual water vapor can form cubic ice when depositing onto the grid surface in that temperature range. Based on both of these considerations, the temperature on the sample grid should never exceed -140°C during data acquisition. Normally, we control the grid temperature at -160°C.

To keep the ACD functioning properly, it is crucial that it should be cooled and maintained at a temperature lower than the cryogenic sample grid. We now consider what cooling power is required to keep the ACD operating at about $-170°C$.

Cooling path

The cooling power is provided by a cooling path, which consists of a liquid nitrogen dewar, a copper rod and a copper braid. The customized liquid nitrogen dewar functions as a heat sink sitting on the top of the microscope chamber as shown in Fig. 5.14, and can hold temperature for 4 hours after each refilling.

The dewar has a hollow aluminum "tail" at the bottom, which is filled with liquid nitrogen and connects to the inside of the chamber through a flange. From there, the cooling path is extended close to the sample grid via a 22 cm long, 1.27 cm diameter, solid copper rod, which is bent to fit the chamber. The copper rod is bolted firmly to the tail of the dewar with an indium film sealing the joint interface.

The other end of this copper rod is about 1.27 cm away from the anti-contaminator. They are connected using a 5 cm long copper braid (not shown in Fig. 5.14). The maximum traveling range of the ACD motor stage is $\sqrt{2}\times 30$ mm ($\sim$ 4.2 cm). The 5 cm copper braid provides the necessary flexibility between the fixed copper rod and the movable anti-contaminator.

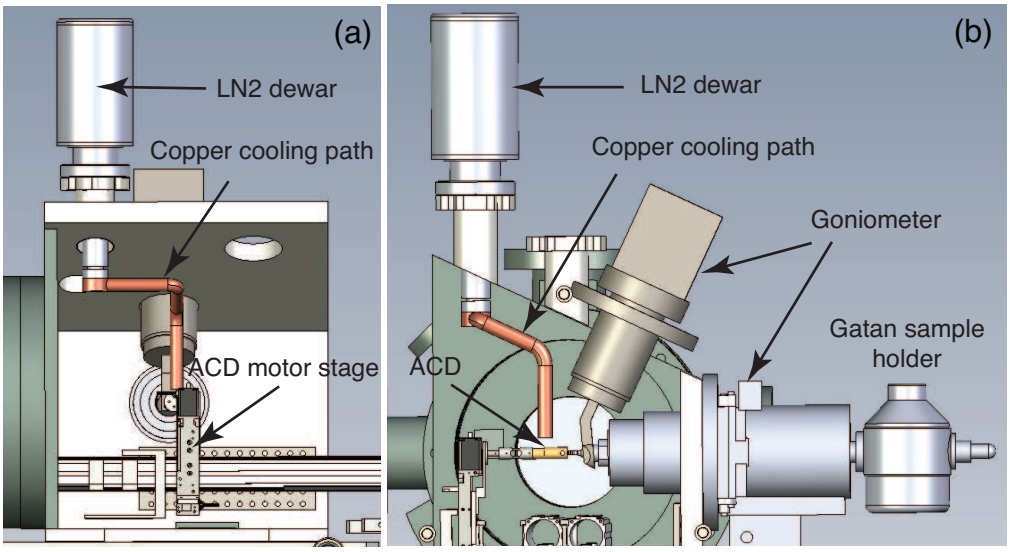

Figure 5.14: The anti-contaminator is cooled by a liquid nitrogen dewar, which is mounted on the top of the microscope chamber. A copper rod attached to the dewar bottom is bent to fit the chamber and extends to about one inch away from the anti-contaminator. The tail of the copper rod is connected to the ACD by a 5 cm long, 1.27 cm wide copper braid (not shown in the figure).

Thermal isolation

The anti-contaminator is cooled by liquid nitrogen, while the motor stage is at room temperature. A sufficient thermal isolation between the cold anti-contaminator and the warm motor stage is required to minimize the thermal conduction.

The anti-contaminator is attached to the motor stage through a fiber glass support, which has low thermal conductivity (about 0.05 W/(m·K)). This support is also hollow to the reduce effective thermal conduction cross-section. It is 30 mm long with 10 mm outer and 5 mm inner diameter, as shown in Fig. 5.13.

5.5.3 Heating power

The copper rod has a temperature close to liquid nitrogen $\sim -197°C$ at the side attaching to the dewar. To achieve the desired temperature $-170°C$

on the anti-contaminator, we consider the thermal efficiency to assume the temperature drops about 10 degree through the copper rod, and drops another 10 degree through the copper braid.

The heating power, which warms the ACD up, comes mainly from 2 sources: one is the thermal radiation power $P_{\rm rad}$ from the warm vacuum chamber to the cold anti-contaminator as well as other parts of the cooling path; the other is the thermal conduction power $P_{\rm cond}$ from the warm motor stage to the anti-contaminator.

Thermal radiation power

To estimate the thermal radiation power $P_{\rm rad}$, the anti-contaminator can be modeled as a 35 mm long, hollow copper cylinder with 10 mm outer diameter, as shown in Fig. 5.12. The anti-contaminator works at -170°C, while the chamber is at room temperature 20°C. The heat transfer power through thermal radiation from the chamber to the anti-contaminator $P_{\rm rad\_1}$ can be calculated as

$$P_{\rm rad} = \epsilon\sigma A \left(T_{\rm c}^4 - T_{\rm a}^4\right), \tag{5.2}$$

where ϵ is the emissivity of gold (about 0.02), σ is the Stefan-Boltzmann constant 5.67×10^{-8} W/(m^2·K^4), A is the total surface area of the hollow cylinder 2.2×10^{-3} m^2, $T_{\rm c}$ and $T_{\rm a}$ are temperatures in Kelvin of the chamber and the anti-contaminator, 293 K and 103 K, respectively. Substituting the numbers into Eq. 5.2, we obtain $P_{\rm rad\_1}$ to be approximately 18 mW.

Using the dimensions of the copper rod and the copper braid and estimating their average temperatures as -190°C and -175°C, respectively, the thermal radiation powers, between the vacuum chamber and the copper rod $P_{\rm rad\_2}$, and between the vacuum chamber and the copper braid $P_{\rm rad\_3}$, can also be calculated using Eq. 5.2 to be 73 mW and 46 mW, respectively. Then the total heating power through thermal radiation $P_{\rm rad}$ equals $P_{\rm rad\_1} + P_{\rm rad\_2} + P_{\rm rad\_3} = 137$ mW.

Thermal conduction power

One side of the fiber glass support is connected to the anti-contaminator at −170°C, while the other side is connected to the warm stainless steel support which is attached to the motor stage at room temperature 20°C. The heat transfer power through thermal conduction P_{cond} from the motor stage to the anti-contaminator can be calculated as

$$P_{\text{cond}} = \frac{kA\Delta T}{\Delta l}, \tag{5.3}$$

where k is the thermal conductivity of fiber glass 0.05 W/(m·K), A is the cross-section area 5.9×10^{-5} m^2, ΔT is the temperature difference between the two ends 190 K, and Δl is the length of the conduction path 0.03 m. P_{cond} is about 19 mW for this fiber glass support.

Other heating powers

At pressures below 10^{-3} torr, which is typical for cryogenic soft x-ray diffraction microscopy, the heat transfer power through convection is negligible compared to radiation and conduction [116].

With a typical beam flux of 10^9 incident photons per second for the x-ray diffraction microscope operated at 520 eV, the beam heating power by full absorption is

$$P_{\text{beam}} = 10^9 \text{ /sec} \times 520 \text{ eV} \times 1.6 \times 10^{-19} \text{ Joule/eV} = 8 \times 10^{-5} \text{ mW}, \tag{5.4}$$

which is also negligible compared with P_{rad} and P_{cond}.

5.5.4 Cooling power

The cooling power that the copper rod is able to provide can be estimated by Eq. 5.3 with $k = 500$ W/(m·K) for copper, $A = 1.27 \times 10^{-4}$ m^2, $\Delta T = 10$ K, and $\Delta l = 0.22$ m. The cooling power of the copper rod P'_{rod} is 2.9 W.

The copper braid contains 384×36 wires, each of which is of type AWG 36 or 127 μm in diameter. Suppose the temperature drops another 10 K across

the copper braid, which leaves the temperature on the anti-contaminator side of around $-170°C$. The cooling power of the copper braid P'_{braid} can then be estimated to be 18 W using Eq. 5.3.

As we can see, both P'_{rod} and P'_{braid} are orders of magnitude greater than the required amount $P_{\text{rad}} + P_{\text{cond}}$. The cooling path should provide sufficient cooling power to achieve the designed temperature on ACD.

5.5.5 Temperature measurement

To monitor how the ACD cools down, three silicon diode temperature sensors from Lakeshore [117] were mounted on the cooling path to measure temperatures: the first sensor was mounted near the connection interface between the tail of the liquid nitrogen dewar and the copper rod, the second sensor was mounted at the end of the copper rod away from the dewar, and the third sensor was mounted on the anti-contaminator.

The system was tested with the microscope chamber pumped down to 10^{-7} torr scale and the liquid nitrogen dewar filled with liquid nitrogen. When the temperatures stabilized, the readings from those three sensors using Lakeshore 218 Temperature Monitor [118] were $-195°C$, $-188°C$, and $-172°C$, respectively. This indicates that the ACD cools well as expected.

We also note that although the designed cooling power is much higher than the required amount, the achieved temperature is not remarkably better than the designed goal. This implies that the heat conduction efficiency is not perfect for the cooling path. In particular, the joints in the copper rod, and on either end of the copper braid, can provide thermal barriers that are only partially overcome through the use of indium foils.

5.5.6 Experimental performance

The ACD performance was tested by monitoring changes in the diffraction pattern of blank formvar grids at cryogenic temperatures across a time span comparable to 3D data acquisitions [36, 80]. Comparing the experimental data without ACD and with ACD, we conclude that the ACD significantly slows down moisture condensation and crystallization.

Test without ACD

The moisture condensation problem was tested before the ACD was installed [113]. A grid at room temperature was inserted into the microscope chamber, and then cooled down and kept at $-160°$C inside vacuum with the retractable slot covered. The diffraction patterns were recorded from an initially blank area, when the vacuum pressure was about 3×10^{-6} torr. The data were taken with 520 eV x-rays. The azimuthally averaged diffraction intensities of the initial diffraction image along with a second one taken an hour later at the same spot are shown as solid and dashed black lines in Fig. 5.15. The azimuthal averaging process smooths out the sharp variations due to individual speckles to reveal the average power scattered as a function of spatial frequency. The overall diffraction intensity is remarkably increased, and a ring of scattering signal was observed around a spatial frequency of 12 μm^{-1} (inset image of Fig. 5.15), which indicates that the scattering is dominated by this particular range of randomly oriented volume gratings. This doughnut-shaped ring is due to the scattering from either ice crystals formed after the grid was transfered into the chamber, or a nonuniform surface of an accumulated amorphous ice layer [87]. The result implies that without the ACD, significant moisture condensation and crystalline or amorphous ice formation occurred on the cryogenic test grid within one hour.

Test with ACD

The ice testing experiment was performed a second time after the ACD was installed in the cryogenic x-ray diffraction microscope. The vacuum pressure was observed to drop by one order of magnitude with the ACD cooled from 10^{-7} torr scale to 10^{-8} torr scale.

This test grid was prepared following the frozen-hydrated sample preparation steps on a formvar-coated grid except that distilled water was used instead of biological sample solution. The cold grid was then transfered into the microscope vacuum chamber, where it was maintained at $-160°$C. With the ACD cold, the chamber pressure stabilized at 5×10^{-8} torr. The diffraction data from a clean spot were taken with 520 eV x-rays after the grid temperature

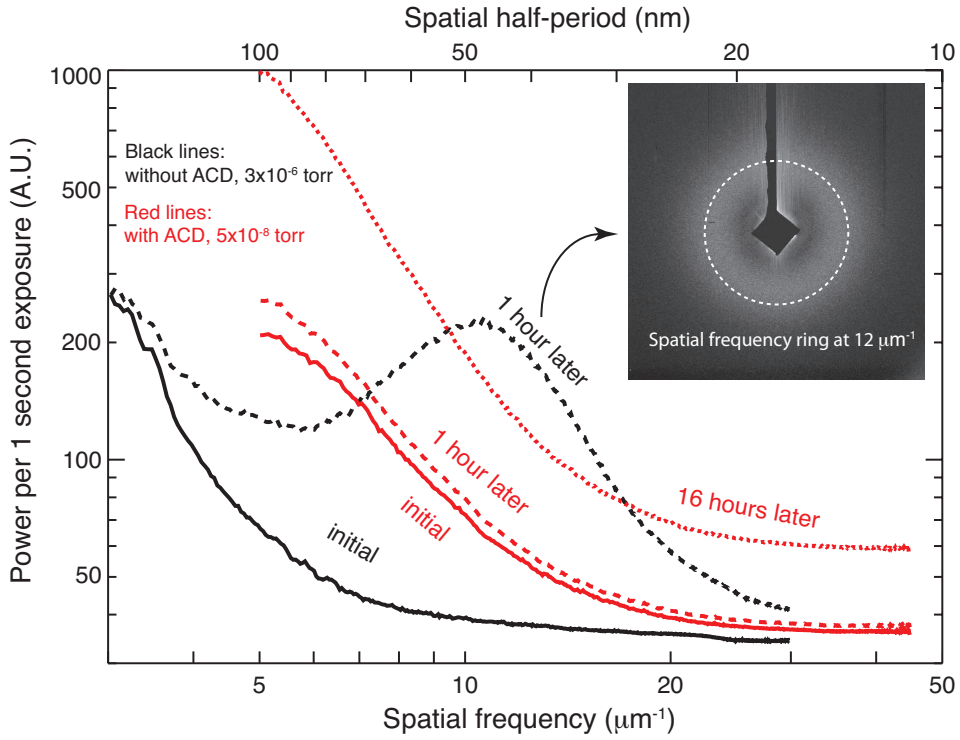

Figure 5.15: The azimuthally averaged curves of diffraction pattern without ACD at the beginning (black solid), without ACD 60 minutes later (black dashed), with ACD at the beginning (red solid), with ACD 60 minutes later (red dashed), with ACD 16 hours later (red dots). The vacuum pressure is improved by ACD. The ACD reduces moisture frosting significantly. It also prevents ice crystal formation for up to 16 hours. The inset image is the diffraction pattern taken one hour later without ACD. A ring of scattering signal was observed around a spatial frequency of 12 μm^{-1}, which indicates that the scattering from crystalline or amorphous ice is dominated by this particular range of randomly oriented volume gratings.

was stable, and again 16 hours later. The azimuthally averaged diffraction intensity curves are shown as red lines in Fig. 5.15. The red solid and fine-dashed lines in Fig. 5.15 show that after 16 hours the diffraction intensity increased almost uniformly and smoothly for most spatial frequencies, and no rings from ice scattering appeared. Assuming a linear increase of the condensation of moisture with time, we can calculate the expected power spectrum after 1 hour. This is plotted as the red coarse-dashed line in Fig. 5.15, which gives slightly higher diffraction intensities than the initial power spectrum.

Note that this grid was plunge-frozen and kept in liquid nitrogen before it was transfered into the microscope chamber. The ice thickness on this grid is therefore larger than on the previous grid used for testing ice accumulation without the ACD. It also possibly experienced exposures to the atmosphere environment during the preparation and transfer processes. These facts can explain why the total initial scattered power of the grid tested with the ACD (the red solid line in Fig. 5.15) is higher than that without the ACD (the black solid line in Fig. 5.15).

The experimental data show that the ACD significantly slows down moisture accumulation and crystalline or amorphous ice formation up to 16 hours, which is a time span comparable to 3D data acquisitions [36, 80]. It also improves vacuum pressure by an order of magnitude in torr. All these functions help to overcome the moisture contamination problem for cryo-XDM with soft x-rays, and enable the possibility to acquire data sets for 2D and 3D reconstructions on frozen-hydrated specimens.

Chapter 6

Outlook

Whole, eukaryotic yeast cells have been imaged in 2D in both chemically dried and frozen hydrated states at high resolutions using XDM. In this last chapter, we discuss the subtleties to be faced in doing 3D XDM reconstructions, and discuss recently developed methods to image extended objects, which can remove the isolation requirement.

6.1 XDM in 3D

A 2D reconstruction image of a 3D object compresses only a subset of the object's 3D structural information into a two-dimensional view. As the depth of focus is limited (Eq. 2.48), only a small portion of the whole object is displayed in focus in a 2D XDM reconstruction. A complete 3D reconstructed image will give much more structural information.

A 3D XDM reconstruction requires one to collect diffraction data at a series of angles, assemble these data into 3D data cube in reciprocal space, and perform a 3D phase-retrieval reconstruction [36, 80].

To collect data at multiple angles, more radiation dose is imposed on the specimen unless one exploits dose fractionation as proposed by Hegerl and Hoppe [119]. As discussed in Sec. 5.1.2 and illustrated in Fig. 1.5, the increased radiation dose can cause structural damage, and thus limit the achievable resolution. In this section, we study the relationship between the resolution and the angle range/step size of the collected data through simulation.

6.1.1 Simulation setup

The test object is the same as Cell B for the SNR simulation in Sec. 3.1. It is a 3D biological-like fake cell with a lipid membrane, protein bars and ellipses and a bud on the shoulder, with an array size reduced to 200×200×200 pixels. Instead of using one multiple-propagated exit wave of the complex 3D fake cell as in the SNR simulation, exit waves with incident illuminations from -90 to 90 degrees with one degree step size were generated for this simulation. The diffraction patterns for different illumination angles were then calculated from these exit waves.

The simulated diffraction patterns were assembled into the 3D data cube in reciprocal space, which was used for 3D reconstruction to retrieve the object image in 3D. Varying tilt ranges and increments were tested in this simulation. The reconstruction was performed using the Hybrid-Input-Output algorithm [43], because it consumes less computer memory than the Difference Map. The reconstruction qualities at different settings were compared.

6.1.2 3D assembling

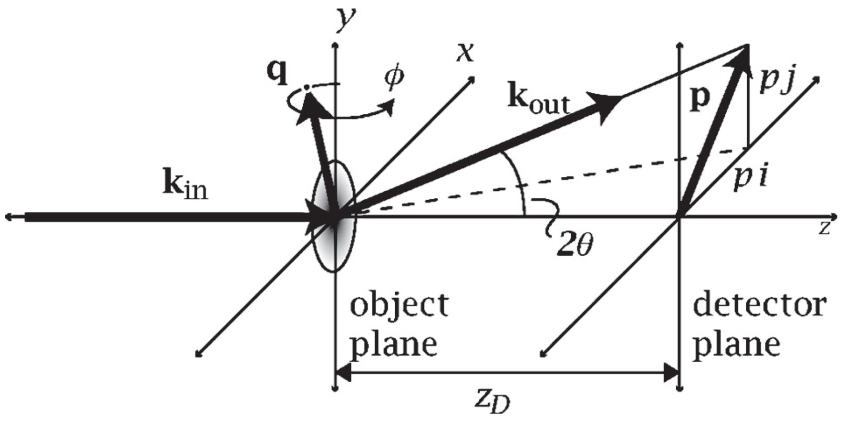

Figure 6.1: Illustration of scattering geometry for XDM, adapted from [36].

The 2D diffraction pattern were assembled into 3D Fourier data cube according the scattering geometry shown in Fig. 6.1. For elastic scattering, the incident wave number $\boldsymbol{k}_{\text{in}}$ and the outgoing wave number $\boldsymbol{k}_{\text{out}}$ have the same magnitude, and the wave transfer vector $\boldsymbol{q}$ equals $\boldsymbol{k}_{\text{out}} - \boldsymbol{k}_{\text{in}}$, which is located at the Ewald sphere and can be expressed as

$$\boldsymbol{q}_{\boldsymbol{i},\boldsymbol{j}} = \frac{1}{\lambda}\left(\frac{\boldsymbol{p}_{\boldsymbol{i},\boldsymbol{j}} + z_{\text{D}}\hat{\boldsymbol{z}}}{\sqrt{p_{i,j}^2 + z_{\text{D}}^2}} - \hat{\boldsymbol{z}}\right), \tag{6.1}$$

where $\boldsymbol{p}_{\boldsymbol{i},\boldsymbol{j}}$ is the pixel location on CCD with $\boldsymbol{p}_{\boldsymbol{i},\boldsymbol{j}} = \Delta(i\hat{\boldsymbol{x}} + j\hat{\boldsymbol{y}})$ where Δ is the CCD pixel size, z_{D} is the distance from the sample to CCD.

Note that the unit of $\boldsymbol{q}_{\boldsymbol{i},\boldsymbol{j}}$ is m^{-1}. In order to match $\boldsymbol{q}_{\boldsymbol{i},\boldsymbol{j}}$ onto a unit-less Cartesian coordinate, the voxel size in reciprocal space needs to be determined, which can be obtained as

$$\Delta_f = \frac{\Delta}{\lambda z_{\text{D}}}. \tag{6.2}$$

The 2D diffraction pattern can then be mapped onto the Ewald sphere by projecting $\boldsymbol{q}$ onto the coordinate system with unit of Δ_f and obtaining the coordinates on the Cartesian grid by nearest neighbor sampling.

The coordinates of 2D patterns at different orientation angles can be cal-

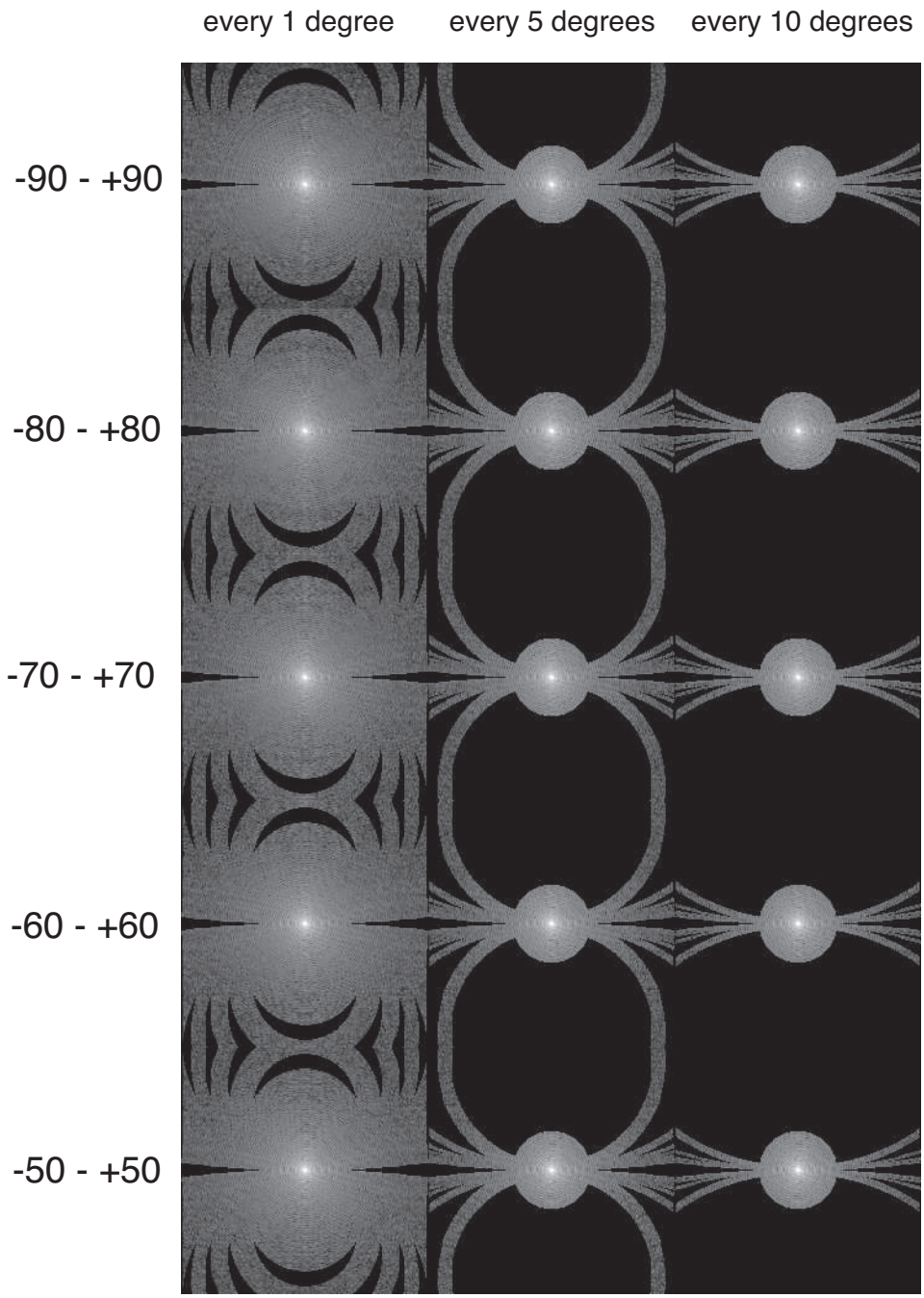

Figure 6.2: The center planes of (q_x, q_y) at $i_z = 100$ $(0 \leq i_z \leq 199)$ in reciprocal space of assembled 3D data cube.

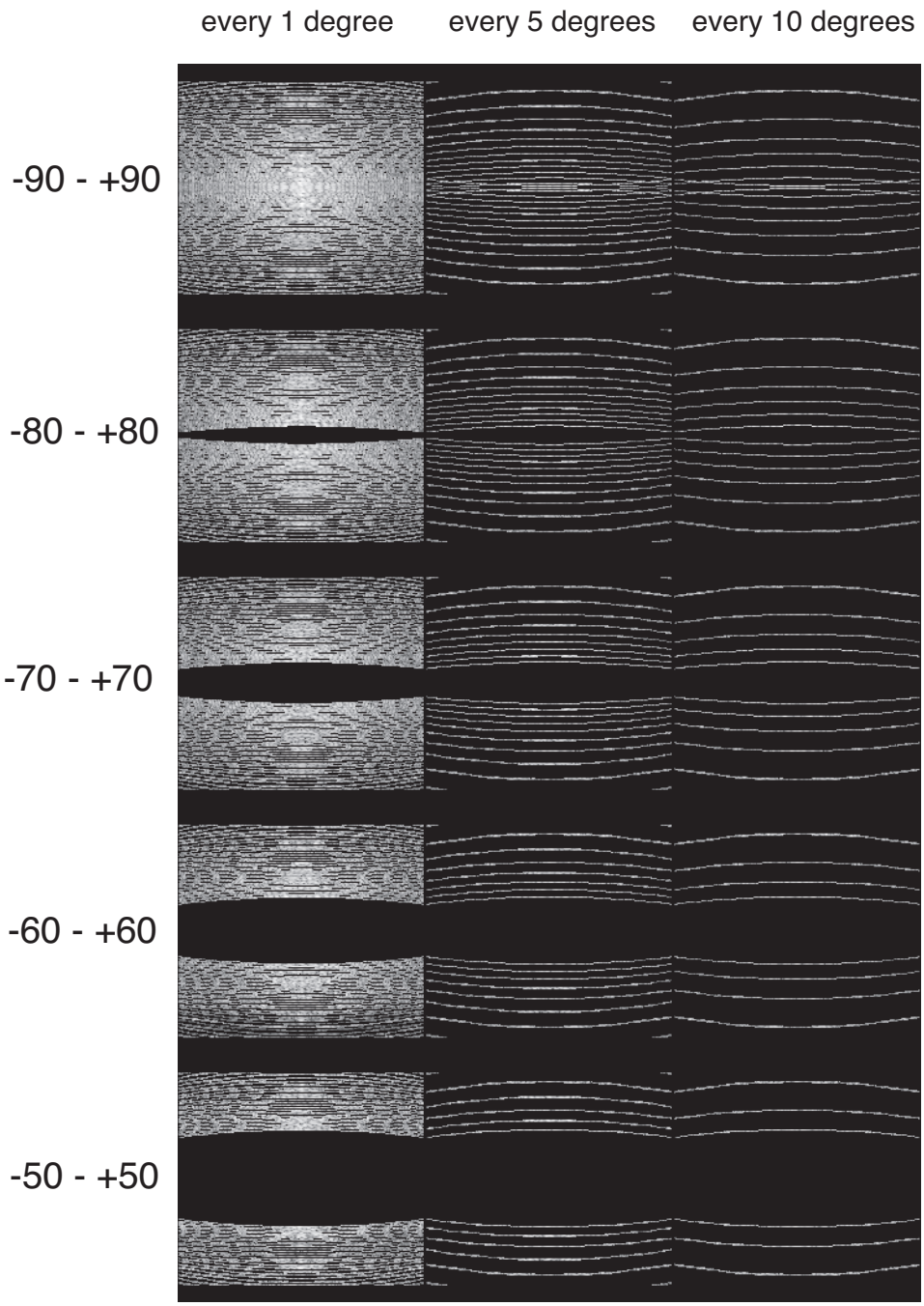

Figure 6.3: Planes of (q_x, q_y) at $i_z = 50$ $(0 \leq i_x \leq 199)$ in the assembled 3D data cube in reciprocal space.

culated by a 3D rotation matrix R_ϕ. Assuming that the specimen is rotated along the X axis in experiments, the rotation matrix can be expressed as

$$R_\phi = \begin{pmatrix} 1 & 0 & 0 \\ 0 & \cos\phi & -\sin\phi \\ 0 & \sin\phi & \cos\phi \end{pmatrix}, \tag{6.3}$$

where ϕ is the rotation angle.

In this simulation, the diffraction data range was tested at ±90, ±80, ±70, ±60 and ±50 degrees with step size of every 1 degree, every 5 degrees and every 10 degrees. Fig. 6.2 shows the center planes ($i_z = 100$) of the assembled data cubes. Fig. 6.3 shows the $i_z = 50$ planes of the assembled data cubes.

6.1.3 3D reconstruction and analysis

The 3D reconstruction was performed using the HIO algorithm with the perfect support. Each reconstruction was run 100 iterations, and averaged the output of every iteration after 80 iterations. Three image planes (i_z =80, 100, 120) of reconstructed images are shown in Fig. 6.5, Fig. 6.6, Fig. 6.7, Fig. 6.8 and Fig. 6.9. The object images at i_z =80, 100, 120 planes are shown in Fig. 6.4.

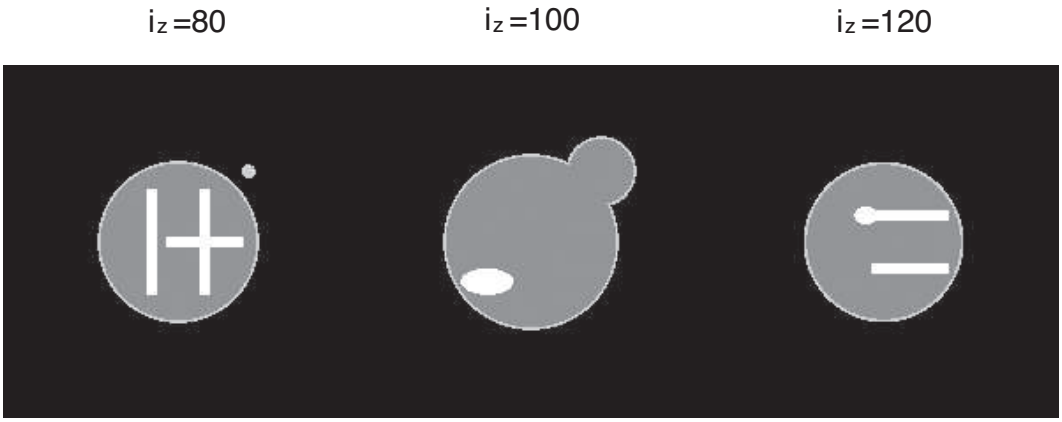

Figure 6.4: The i_z=80, 100, 120 planes ($0 \leq i_x \leq 199$) of the initial 3D object.

The oversampling ratio of this 3D object is about 15. In other words, 6.7% pixel values need to be determined. According to the oversampling theory,

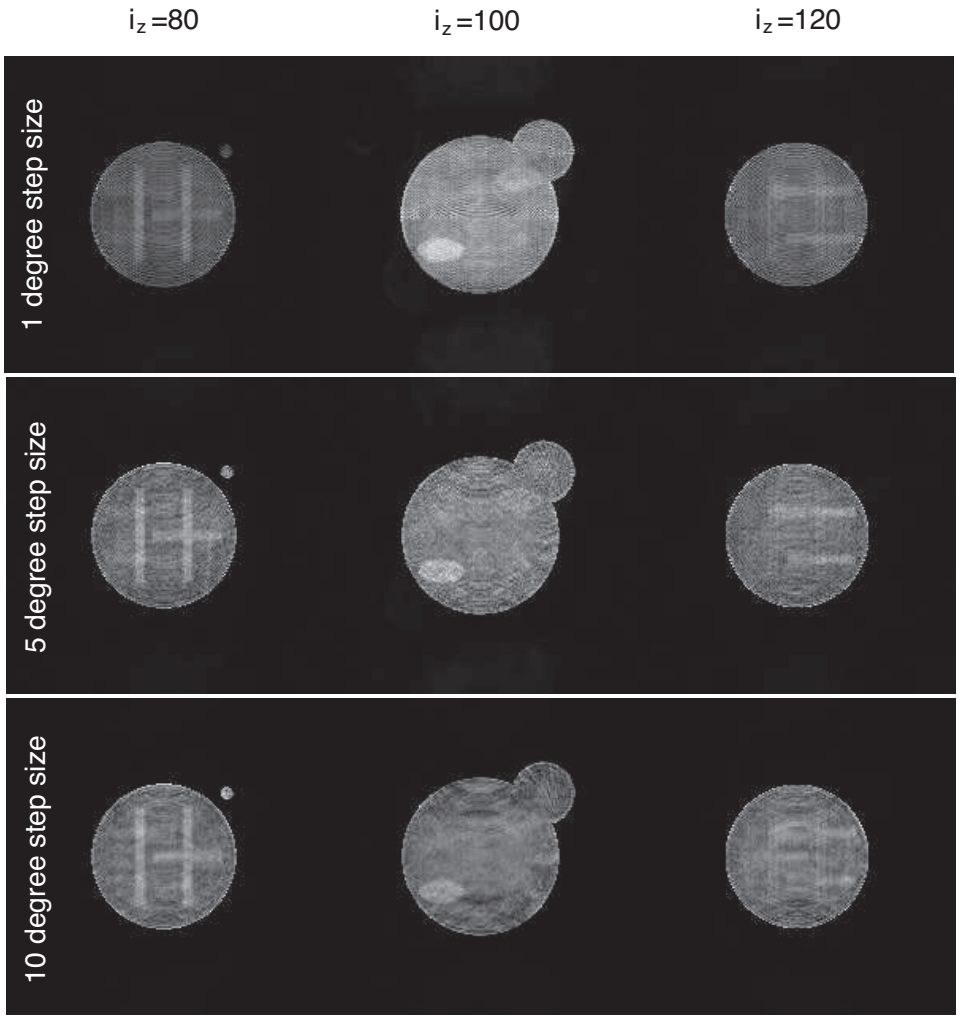

Figure 6.5: The i_z=80, 100, 120 planes of the reconstructed images with $\pm$90 degree data range.

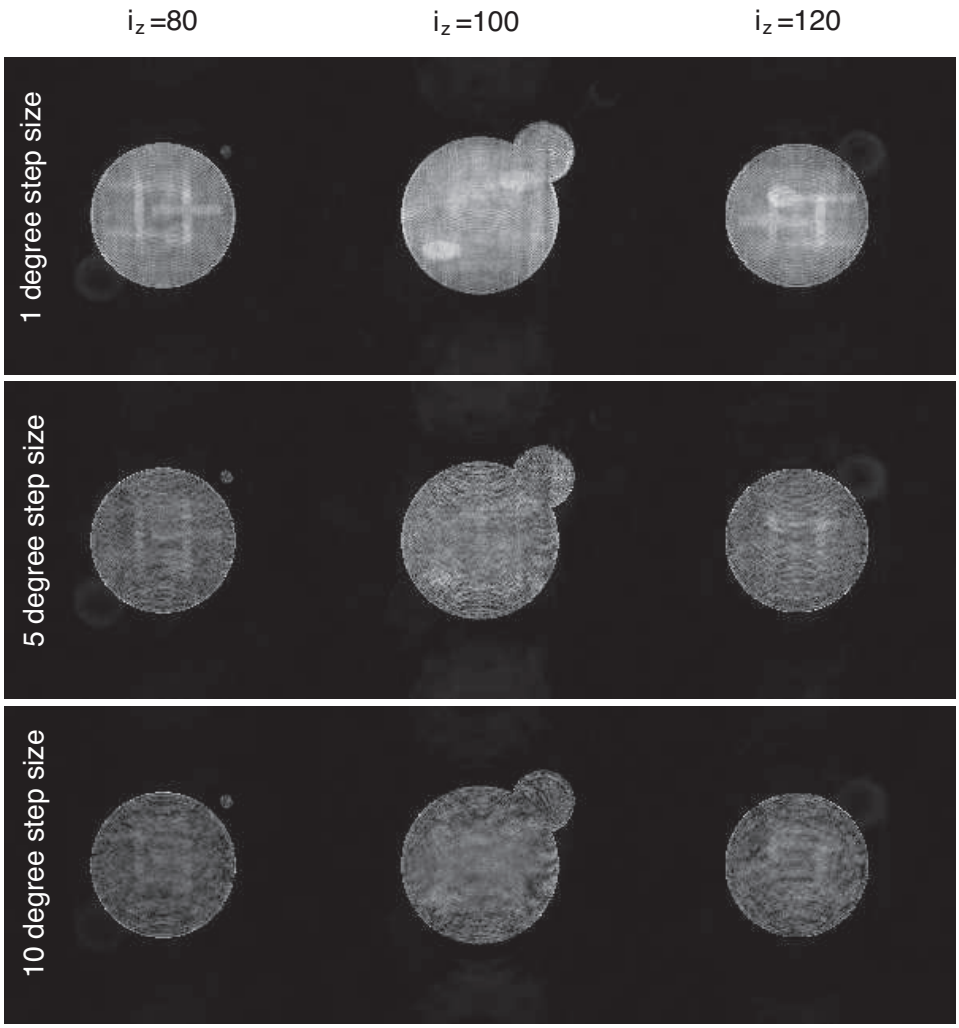

Figure 6.6: The i_z=80, 100, 120 planes of the reconstructed images with ±80 degree data range.

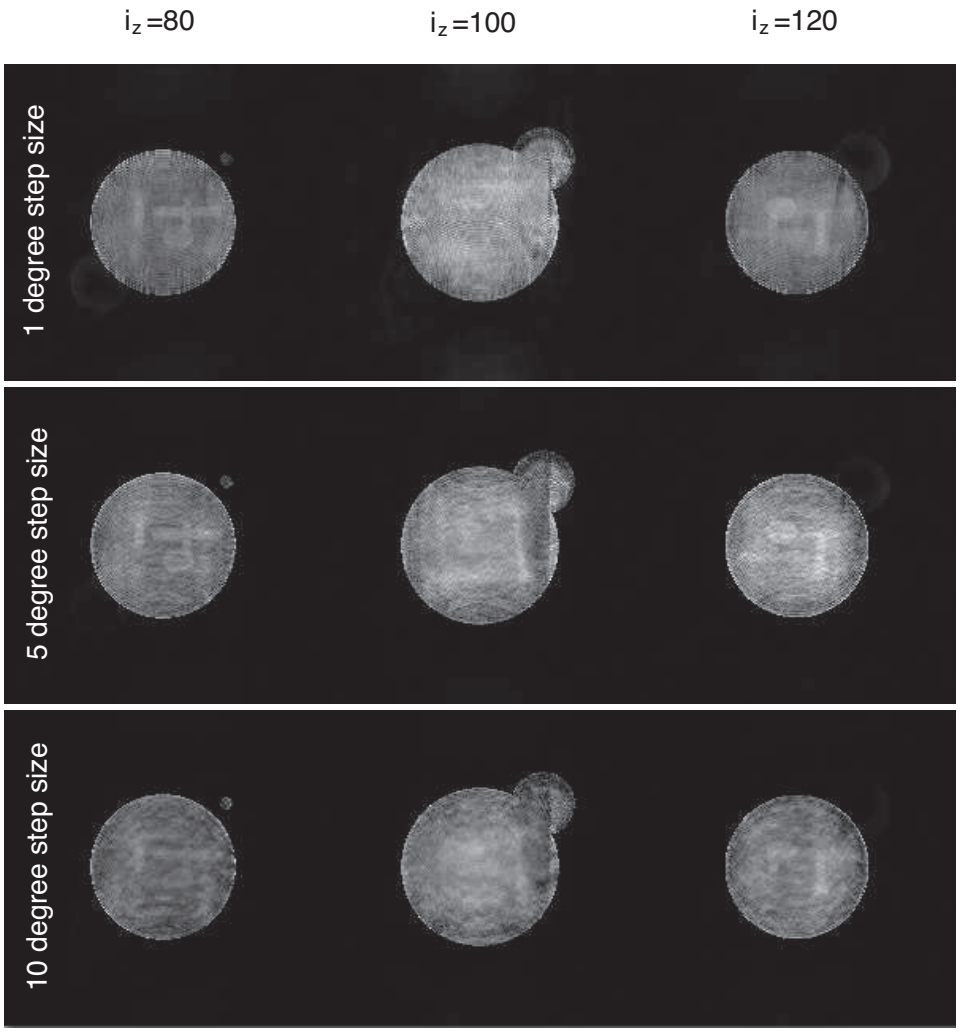

Figure 6.7: The i_z=80, 100, 120 planes of the reconstructed images with $\pm$70 degree data range.

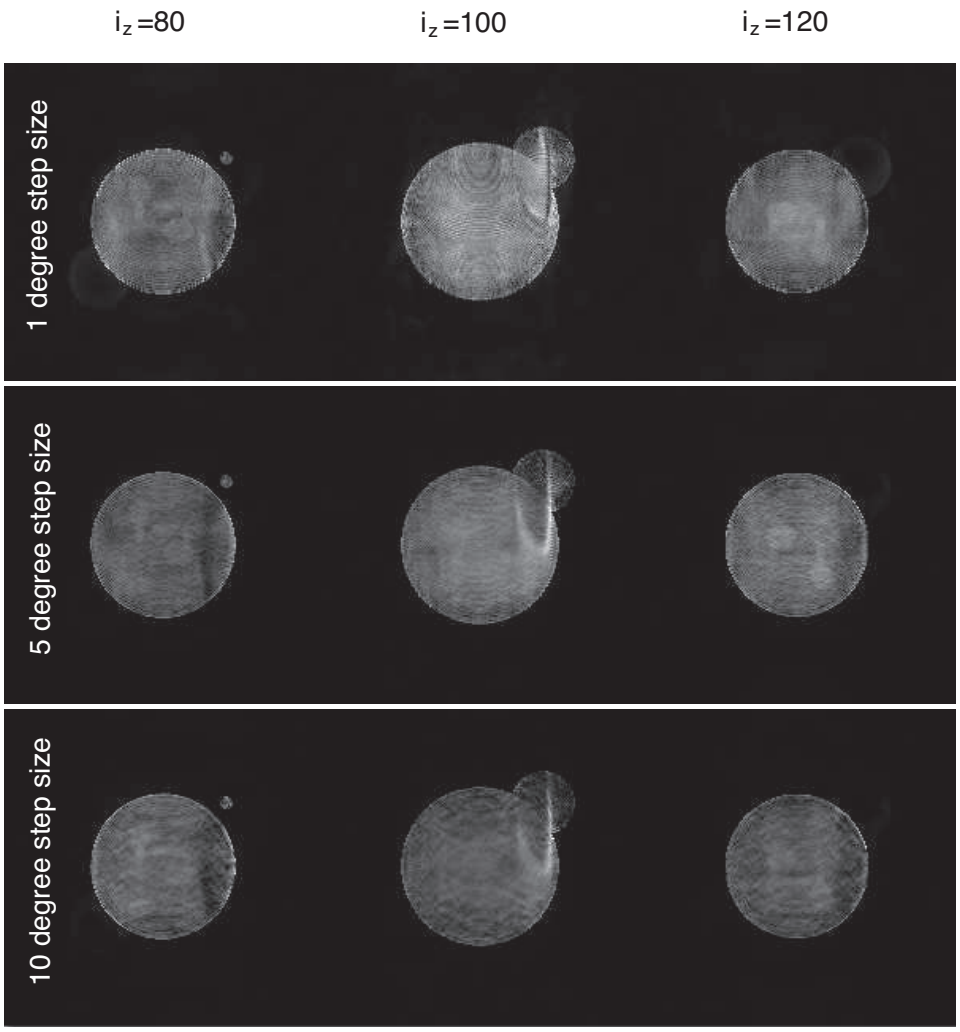

Figure 6.8: The i_z=80, 100, 120 planes of the reconstructed images with $\pm$60 degree data range.

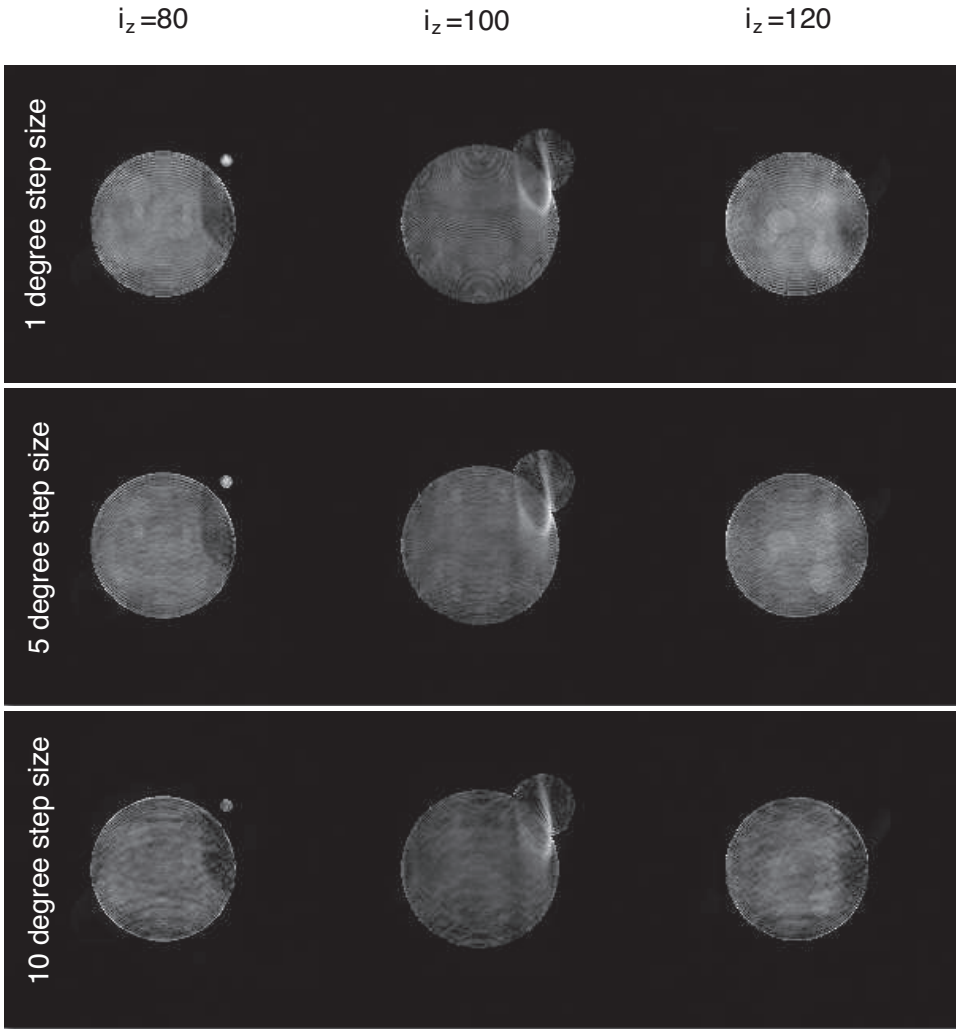

Figure 6.9: The i_z=80, 100, 120 planes of the reconstructed images with $\pm$50 degree data range.

it requires the percentage of the measured data at least 13.4%, or at most 86.6% unmeasured intensity voxels in the assembled data cube. Table 6.1 lists the percentage of unmeasured intensity voxels for each assembled data. Theoretically, the data sets with unmeasured intensity voxel percentage larger than 86.6% cannot be reconstructed. The reconstructed images are almost consistent with this conclusion. The exceptions happen at small angle ranges with finer step size and large angle range with rough step size. When the angle range is not sufficient, the finer step size does not help reconstruction. While for large enough angle range (for instance ±90 degrees), 10 degree step size can give fairly good reconstruction. This result implies that uniform sampling over larger Fourier space is more effective than finer sampling at a finite space. The chromosome experiment [80] also used the strategy of large data taking range (-70 to +60 degrees) with relatively sparse step size (every 2.5 or 5 degrees).

Table 6.1: Percentage of unmeasured intensity voxels for each assembled data.

	every 1 degree	every 5 degree	every 10 degree
±90	40.2%	83.8%	91.4%
±80	43.9%	85.4%	92.3%
±70	52.7%	87.2%	93.2%
±60	59.4%	88.9%	94.1%
±50	66.0%	90.7%	95.0%

For biological samples, data collections at a series of illumination angles can cause radiation damage problems. A promising solution involves dose fractionation [119, 120], which states that the radiation dose sufficient for a 2D reconstruction is also sufficient to generate a 3D reconstruction by distributing the 2D image dose uniformly over 3D tilt angles.

6.2 Diffraction microscopy on extended objects

In the XDM method, a CCD collects the far field diffraction pattern from an isolated object illuminated by a plane incident wave. The object image in real space is retrieved from this diffraction pattern using *a priori* known constraints. This approach has been shown to give unique solution [121–

123]. It has achieved great success, but it can be only applied on finite objects isolated from other scatterers. Additional limits include slow convergent speed and possible stagnation during iterative reconstructions.

Two new approaches for the diffraction microscope have been developed to extend this method to image objects with arbitrary sizes. They also improve the convergence property.

6.2.1 Ptychography

The ptychography method [124–128] uses multiple exposures from an illuminating beam that is smaller than the specimen, and which is scanned across the specimen. The scattering from a pinhole is used as the incident plane wave illumination. The center part of the Airy pattern from the pinhole is sufficiently localized to be used as a probe to define the imaged area. This illumination probe scans across the extended object, and the far field diffraction pattern is recorded at each scan point.

The ptychography reconstruction engine requires significant overlap between adjacent scan positions (normally $\geq$60% [129]). This reconstruction algorithm enforces that the reconstructed image in the overlapping area satisfies constraints on both scan positions. The abundant information in adjacent regions removes the reconstruction ambiguities and also improves convergent speed.

The modified ptychography technique, the scanning x-ray diffraction microscopy (SXDM) [69, 130], uses the focused x-ray beam from a zone plate as the probe. The object is scanned and imaged at the focal plane of the lens. Instead of assuming plane wave illumination, the SXDM method reconstructs both the extended object and the wave front of the incident focused illumination probe.

6.2.2 Keyhole CDI

Another diffraction method to image extended objects is called keyhole coherent diffraction imaging, or keyhole CDI [131, 132]. This approach places the object at a downstream position of the focal plane of the lens. The object

is then illuminated by a divergent beam emerging from the zone plate's focal plane. This illumination generates a Fresnel diffraction pattern at the far field detector plane, which can be used to reconstruct the object in the exposed area with the knowledge of the illumination wave front measured in advance [133]. The object can also be scanned in the divergent incident beam, and arbitrary regions of the object can be imaged.

The divergent incident beam has considerable phase curvature at the object plane, which is helpful to avoid reconstruction stagnation and speed up convergence.

Besides the difference in the illumination arrangements between ptychography and keyhole CDI, there is another important distinction in their reconstruction procedures. For the ptychography approach, the overlap of the illumination footprint at contiguous scanning positions is crucial, because the reconstruction algorithm uses the redundant information from adjacent regions to achieve a convergent reconstruction. The reconstruction quality is dependent on the amount of overlap at adjacent scanning positions. For the keyhole CDI, the reconstruction at each illumination position is independently achieved with the diffraction data measured at this scan location alone.

With the ability to image extended objects in 3D, x-ray diffraction microscopy is becoming a more powerful technique with great scientific applications.

Appendix A

Far field diffraction pattern from propagation theory

In Sec. 2.2, the Fourier transform relationship between the object and its far field diffraction pattern is derived following Born's approach by splitting the wave front to the unscattered part and scattered part. This far field diffraction pattern can be obtained from electromagnetic field propagation theory too.

A.1 Born approximation

We consider the propagation of the wave front exiting an object surface. Because x-rays interact with mediums weekly, the second order scattering can be ignored, which is known as the Born approximation as mathematically expressed in Sec. 2.2.2. The 2D exit wave of an object can be considered the overall modification of the incident illumination diffracted by the object along the transverse direction.

A.2 Fresnel and Fraunhofer approximations

Following the steps in Sec. 2.1.1, the wave front exiting the object surface can be considered as a collection of Huygens point sources. The propagation of each point source is modeled as a diverging spherical wave (Eq. 2.6). The wave front at a downstream plane is the summation of wave fronts from all those point sources (Eq. 2.1).

By applying the Fresnel approximation ($z^2 \gg (\xi-x)^2+(\eta-y)^2$), the wave function is simplified as (Eq. 2.3)

$$\boldsymbol{\psi}(x,y) = \frac{e^{ikz}}{z} e^{\frac{ik}{2z}(x^2+y^2)} \int\int \boldsymbol{\psi}(\xi,\eta) e^{\frac{ik}{2z}(\xi^2+\eta^2)} e^{\frac{-ik}{z}(x\xi+y\eta)} d\xi d\eta. \tag{A.1}$$

In far field diffraction condition, the Fraunhofer approximation is also satisfied, which gives $z^2 \gg \xi^2+\eta^2$. The wave function can be simplified further by dropping the quadratic phase term in the integral, or

$$\boldsymbol{\psi}(x,y) = \frac{e^{ikz}}{z} e^{\frac{ik}{2z}(x^2+y^2)} \int\int \boldsymbol{\psi}(\xi,\eta) e^{\frac{-ik}{z}(x\xi+y\eta)} d\xi d\eta. \tag{A.2}$$

Ignoring the decaying factor and the phase term outside the integral, the far field diffraction pattern is related to the exit wave of the object by a Fourier transform.

Note that the accurate forms for the Fresnel and Fraunhofer approximations are $z^3 \gg \pi[(\xi-x)^2+(\eta-y)^2]^2/(4\lambda)$, $z \gg \pi(\xi^2+\eta^2)/\lambda$, respectively.

A.3 Babinet principle

The exit wave from the object surface $\boldsymbol{\psi}(\xi, \eta)$ can be rewritten as

$$\begin{aligned} \boldsymbol{\psi}_{\text{ew}} &= \psi_0 e^{iknz'} = \psi_0 e^{ikz'} e^{ikz'(-\delta+i\beta)} \\ &\approx \psi_0 e^{ikz'}[1 + ikz'(-\delta + i\beta)], \end{aligned} \tag{A.3}$$

where z' is the thickness of the object, and $\delta z'$ and $\beta z'$ are denoted as the overall effects along the propagation direction. The Fourier transform of the first term of Eq. A.3 is a point-response $\delta(\boldsymbol{r})$ function in the center, and the core of the second term is $(-\delta + i\beta)$.

In Sec. 2.2.2, we see the far field diffraction pattern is related to the object's scattering potential $\boldsymbol{F}$ as expressed in Eq. 2.31. Noting that $\boldsymbol{F}$ is proportional to $(-\delta+i\beta)$ (Eq. 2.21), Eq. A.3 can be considered to add a uniform background "1" to $\boldsymbol{F}$. We obtain that the Fourier transform of the object's scattering potential $\boldsymbol{F}$ is identical to that of the object's exit wave $\boldsymbol{\psi}_{\text{ew}}$ up to a normalization factor, except for a point-response function in the center, or

$$\mathcal{F}(\boldsymbol{\psi}_{\text{ew}}) = C_b \mathcal{F}(\boldsymbol{F}) + \delta(\boldsymbol{r}), \tag{A.4}$$

where C_b is the complex scaling constant. This conclusion can be predicted by the Babinet principle, which states that the diffraction pattern of an opaque body is identical to that from a hole with the same size and shape, except for the central pixel.

Appendix B

Numerical derivation for SNR calculation

We discuss the details about the derivation of the formula to estimate SNR from correlation coefficient. The related properties of Poisson distribution are also briefly described.

B.1 Signal and noise in Poisson distribution

The Poisson distribution is a probability distribution of discrete random occurrences that happen during a given time interval. If the expected occurrence number is N, the probability of occurrence number x is equal to

$$f(x) = \frac{N^x e^{-N}}{x!}. \tag{B.1}$$

The mean value, or expected value of Poisson distribution can be calculated from definition as

$$\langle x \rangle = \int_0^\infty x f(x) dx = \int_0^\infty x \frac{N^x e^{-N}}{x!} dx = N. \tag{B.2}$$

The variance can be obtained from definition as

$$\sigma_p = \sqrt{\int_0^\infty (x - N)^2 f(x) dx} = \sqrt{N}. \tag{B.3}$$

The mean value of multiple measurements, can be considered as the signal, and the variance around this expected value is noise. The signal-to-noise ratio in this case is then $\sqrt{N}$. This result gives the same 0.5 scaling in log-log plot as Eq. 3.1.

B.2 Derivation of SNR

The 2D noisy image I_1 and I_2 are expressed in Eq. 3.5. The total signal and noise for the entire 2D array can be calculated from their variances:

$$\begin{aligned} \text{Signal}^2 &= \langle (S - \langle S \rangle)(S - \langle S \rangle)^* \rangle \\ &= \langle S S^* \rangle - \langle S \langle S \rangle \rangle - \langle \langle S \rangle S \rangle + \langle \langle S \rangle \langle S \rangle \rangle \\ &= \langle S S^* \rangle - \langle S \rangle^2 - \langle S \rangle^2 + \langle S \rangle^2 \\ &= \langle S^2 \rangle - \langle S \rangle^2, \end{aligned} \tag{B.4}$$

$$
\begin{aligned}
\text{Noise}^2 &= \langle (N_{1,2} - \langle N_{1,2} \rangle)(N_{1,2} - \langle N_{1,2} \rangle)^* \rangle \\
&= \langle N_{1,2} N_{1,2}^* \rangle - \langle N_{1,2} \langle N_{1,2} \rangle \rangle - \langle \langle N_{1,2} \rangle N_{1,2} \rangle + \langle \langle N_{1,2} \rangle \langle N_{1,2} \rangle \rangle \\
&= \langle N_{1,2} N_{1,2}^* \rangle - \langle N_{1,2} \langle N_{1,2} \rangle \rangle - \langle \langle N_{1,2} \rangle N_{1,2} \rangle + \langle \langle N_{1,2} \rangle \langle N_{1,2} \rangle \rangle \\
&= \langle N_{1,2}^2 \rangle, \qquad \text{(B.5)}
\end{aligned}
$$

where $\langle N_{1,2} \rangle = 0$ has been used. Notice that $I_{1,2}$, S and $N_{1,2}$ are real value intensities, so that $I_{1,2}^* = I_{1,2}$, $S^* = S$ and $N_{1,2}^* = N_{1,2}$.

The variances of image I_1 and I_2 can be calculated as

$$
\begin{aligned}
{\sigma_{1,2}}^2 &= \langle (I_{1,2} - \langle I_{1,2} \rangle)(I_{1,2} - \langle I_{1,2} \rangle)^* \rangle \\
&= \langle I_{1,2} I_{1,2}^* \rangle - \langle I_{1,2} \langle I_{1,2} \rangle \rangle - \langle \langle I_{1,2} \rangle I_{1,2} \rangle + \langle I_{1,2} \rangle \langle I_{1,2} \rangle \\
&= \langle I_{1,2} I_{1,2}^* \rangle - \langle I_{1,2} \rangle^2 - \langle I_{1,2} \rangle^2 + \langle I_{1,2} \rangle^2 \\
&= \langle I_{1,2} I_{1,2}^* \rangle - \langle I_{1,2} \rangle^2 \\
&= \langle (S + N_{1,2})(S + N_{1,2})^* \rangle - \langle S \rangle^2 \\
&= \langle S S^* \rangle + \langle S N_{1,2}^* \rangle + \langle N_{1,2} S^* \rangle + \langle N_{1,2} N_{1,2}^* \rangle - \langle S \rangle^2 \\
&= \langle S^2 \rangle + \langle N_{1,2}^2 \rangle - \langle S \rangle^2, \qquad \text{(B.6)}
\end{aligned}
$$

we used the fact that the cross terms $\langle S N_{1,2}^* \rangle$ and $\langle S^* N_{1,2} \rangle$ are in practice negligible compared to $\langle S S^* \rangle$. This would be expected for low contrast objects, but in practice it also applies to cases with objects with high contrast; in simulations, we find that $\langle S N_{1,2}^* \rangle$ and $\langle S^* N_{1,2} \rangle$ are several orders of magnitude lower than $\langle S S^* \rangle$ even with full contrast object. As a result, $\langle S N_{1,2}^* \rangle$ and $\langle S^* N_{1,2} \rangle$ are dropped in the last equality of Eq. B.6. As N_1 and N_2 obey the same Gaussian distribution, they have identical variances ($\langle N_1^2 \rangle = \langle N_2^2 \rangle$). So, we can denote $\sigma_1 = \sigma_2 = \sigma$.

The covariance between I_1 and I_2 can be derived as:

$$\begin{aligned} r\sigma_1\sigma_2 = r\sigma^2 &= \langle (I_1 - \langle I_1 \rangle)(I_2 - \langle I_2 \rangle)^* \rangle \\ &= \langle I_1 I_2^* \rangle - \langle I_1 \langle I_2 \rangle \rangle - \langle \langle I_1 \rangle I_2 \rangle + \langle I_1 \rangle \langle I_2 \rangle \\ &= \langle (S + N_1)(S + N_2)^* \rangle - \langle I_1 \langle S \rangle \rangle - \langle \langle S \rangle I_2 \rangle + \langle S \rangle^2 \\ &= \langle S S^* \rangle + \langle S N_2^* \rangle + \langle N_1 S^* \rangle + \langle N_1 N_2^* \rangle - \langle S \rangle^2 \\ &= \langle S^2 \rangle - \langle S \rangle^2, \end{aligned} \tag{B.7}$$

where $\langle N_1 N_2^* \rangle = 0$, because N_1 and N_2 are uncorrelated.

Appendix C

Corner and beamstop fabrication

In this section, we describe the steps of fabricating corners and beamstops from silicon wafers. We also discuss the attempt to fabricate a partially attenuating beamstop, which is called as the "Tower of Hanoi beamstop", to retrieve the data information in the missing center of diffraction pattern.

C.1 Corner and square beamstop

C.1.1 Design mask

The corners and square beamstops are made from silicon wafers. The initial pattern with the shapes and sizes of corners and beamstops are first drawn on a mask file. This pattern will be later transfered onto the wafer by UV or E-beam lithography. There is a open source software "Layout Editor" [134], which can be used to edit the mask files. Simple inversion of the mask contrast allows one to work with either positive or negative photoresists.

C.1.2 Fabrication steps

The shape of corners is a square aperture in the center of a silicon frame, while the beamstop is a square silicon piece. The typical sizes for a corner and a beamstop are 200×200 μm and 2×2 mm, respectively.

The silicon wafer we used is coated with a 200 nm thick silicon nitride layer. In order to transfer the pattern onto silicon layer, the designed pattern has to be transferred into the nitride layer first. The pattern transfer process from the mask file to the nitride layer is done by UV lithography. We used a negative photoresist in this fabrication process.

The fabrication steps are as follows:

1. Spin about 1-2 μm photoresist (Shipley S1811) on wafer.
2. Bake the wafer with photoresist on 115°C hot plate for 2 minutes.
3. Cover the wafer with the mask, and expose it with standard UV (λ = 365 nm) for 7 seconds.
4. Develop the exposed wafer in developer (Shipley MF312) for 30 seconds.
5. Post-bake the developed wafer on 115°C hot plate for 2 minutes.
6. Reactive ion etch off silicon nitride layer with SF_6 plasma for 2.5 minutes.
7. Wet etch silicon layer with KOH solution at 100°C for 8 hours.

This process is illustrated in Fig. C.1.

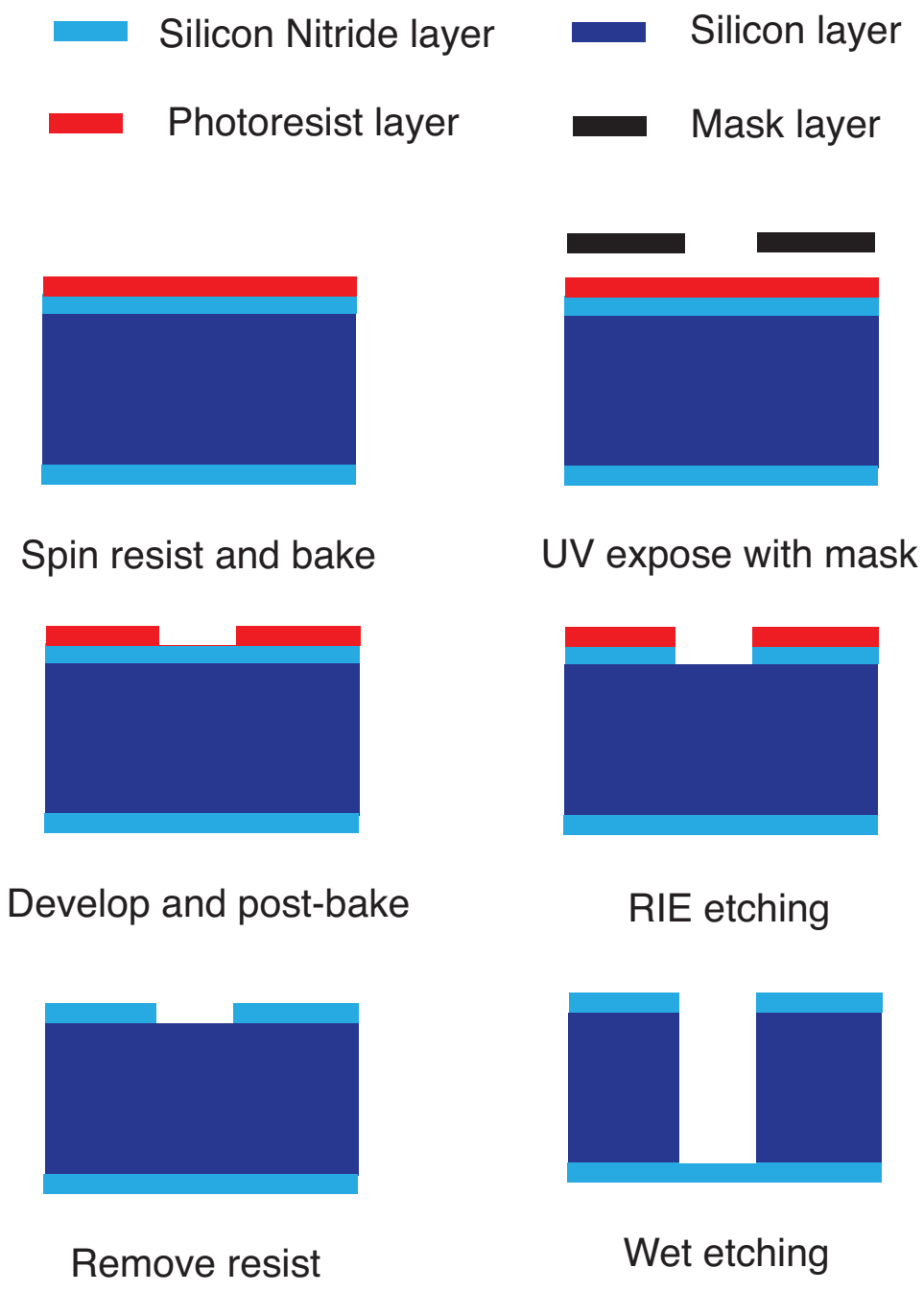

Figure C.1: Illustration of steps for corner and beamstop fabrication.

C.2 Tower of Hanoi beamstop

In XDM experiments, the far-field diffraction intensity is recorded by a CCD. The magnitude of diffraction intensity is about six orders in dynamic range, while the dynamic range od the CCD chip is only about 3000 : 1, which is not adequate for collecting the full ranges of intensities presented in the diffraction pattern. So the CCD is usually protected from the intense direct beam by a beamstop. The beamstop leaves a missing data region on the CCD, and it brings in problem of unconstrained modes in phase retrieval process, as discussed in Sec. 2.3.3 and Sec. **??**.

In order to retrieve the information blocked by the opaque beamstop, we propose to fabricate a partially attenuating beamstop with variable absorptions in steps, which is called as the "Tower of Hanoi" beamstop.

C.2.1 Attenuation length estimation

The Tower of Hanoi beamstop attenuates the central diffraction area, and reduces the intensities into the dynamic range of CCD. The attenuation length were estimated from experimental parameters by Enju Lima. This beamstop has three layers. The thickness and diameter of each layer are listed in Tables C.1. Fig. C.2 shows the side view of the beamstop that consists of three layers.

Table C.1: Dimensions of three layers of the Tower of Hanoi beamstop for 5 second exposure at 520 eV.

	Layer 3	Layer 2	Layer 1
Attenuation length	3	6	12
Diameter (μm)	1200	500	120
Net thickness if Si (μm)	1.4	2.8	5.6
Net thickness if Au (μm)	0.13	0.26	0.52

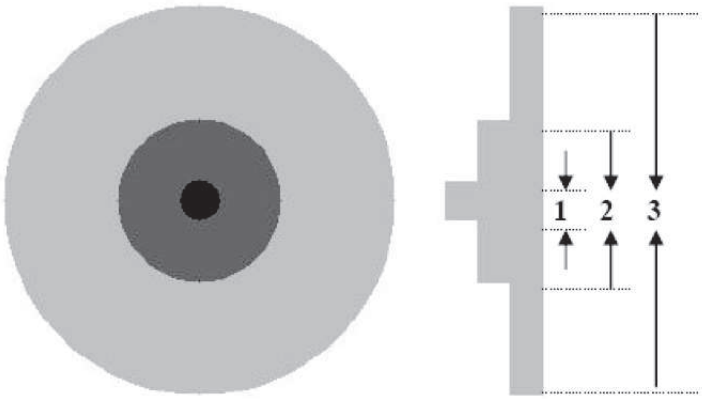

Figure C.2: Sketch of Tower of Hanoi beamstop with three layers.

C.2.2 Fabrication of Hanoi beamstop

The three-gold-layer structure was fabricated on top of 200 nm thick 2×2 mm silicon nitride window by electron beam lithography. The fabrication process requires multiple aligned mask exposures, etches, and thin film deposition techniques. The fabrication steps are:

1. Spin about 400 μm photoresist (ZEP 520A) on a silicon nitride window.
2. Bake the window with photoresist on 180°C hot plate for 3 minutes.
3. Expose the window with electron beam (30 keV, 1.25 nA) with the mask of 1 layer.
4. Develop the exposed window in developer (Xylenes) for 2 minutes.
5. Rinse the window in isopropanol for 45 seconds.
6. Evaporate 1 nm chrome, and then evaporate a gold layer with the thickness of this layer.
7. Dissolve the remaining photoresist layer in Posistrip 830 at 110 °C.
8. Repeat the entire list two more times with the other two layers.

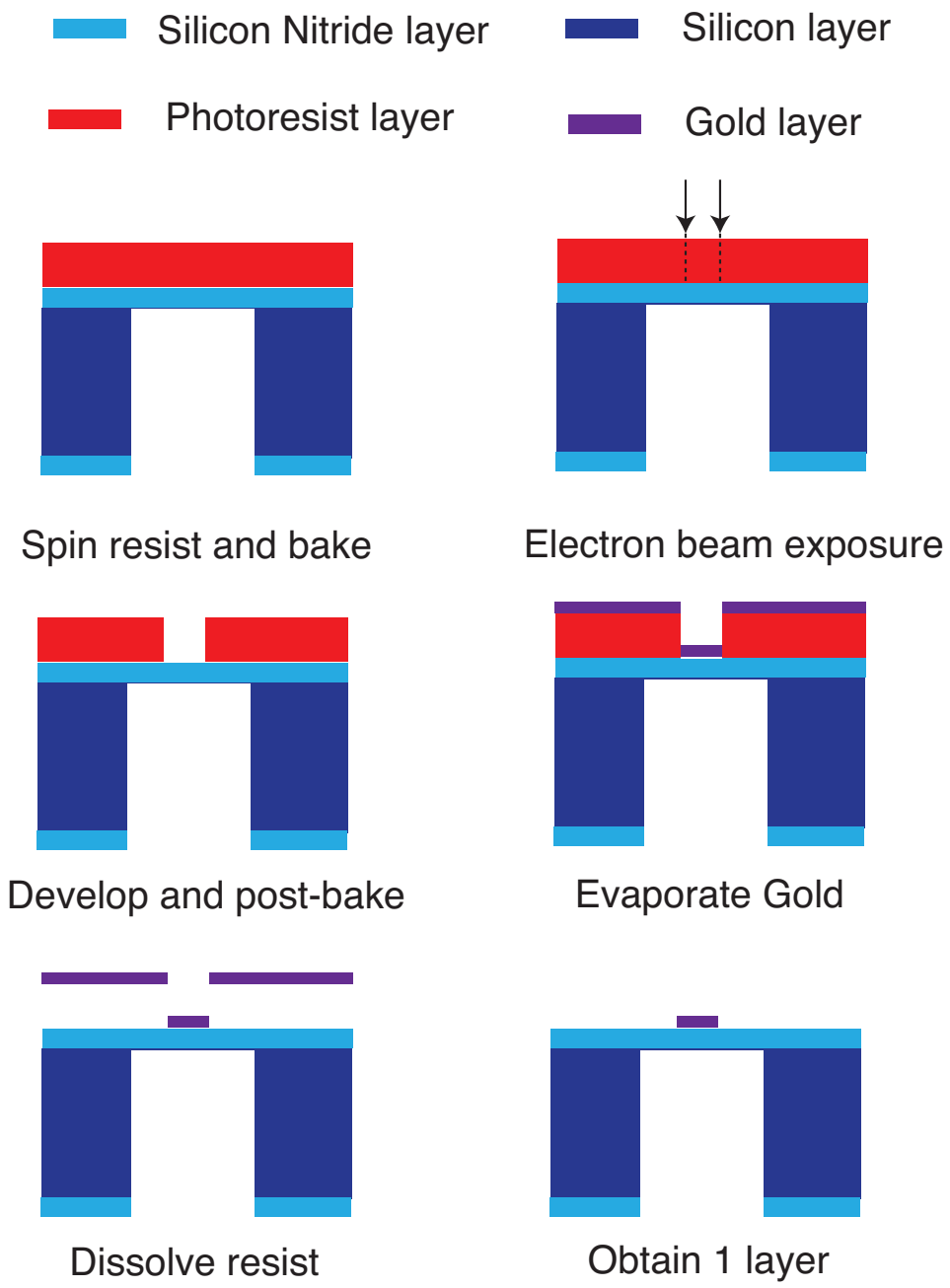

Figure C.3: Illustration of steps for fabricating one layer of the Tower of Hanoi beamstop. This process was repeated three times to obtain the three-layer structure.

This process is illustrated in Fig. C.3.

The masks for three layers are disks with specific diameters, and they control the exposure regions of the electron beam. In the evaporation step, the thickness of gold layer was controlled by timing, as the evaporation rate can be considered to be constant. The purpose for depositing a thin layer of chrome is because gold does not attach on silicon nitride window well, but attaches on chrome surface easily. The chrome layer also provides a conductive layer for a plating process (alternative to the evaporation process).

C.2.3 Structure diagnosis

SEM image

The fabricated Tower of Hanoi beamstop was imaged by SEM, as shown in Fig. C.4. The diameters for these three layers are 1150 μm, 475 μm and 112 μm, respectively, which match the designed values very well. The black squares near the edge of the second layer were used for disk alignment. In Fig. C.4 (c), we see some blemishes with small size.

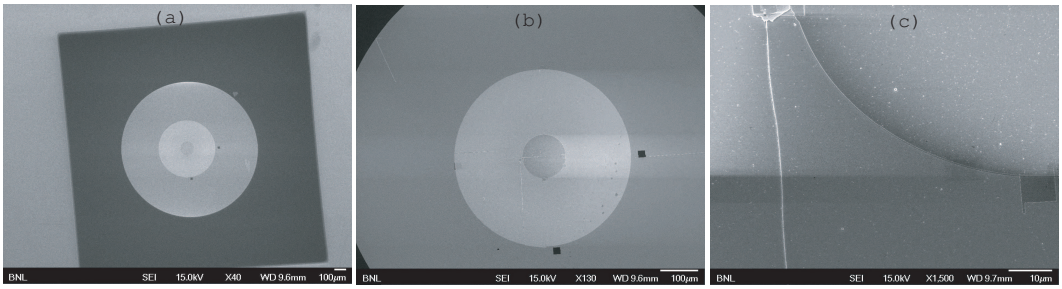

Figure C.4: SEM images of the Tower of Hanoi beamstop. (a) Over view of the three-layer structure. (b) Tow disks in the center. (c) Details at the disk edge.

STXM image

In order to check the thickness and roughness for each layer, several STXM images were taken from this Hanoi beamstop with 520 eV x-rays at Beamline

X1A of National Synchrotron Light Source at Brookhaven National Laboratory. The images are shown in Fig. C.5.

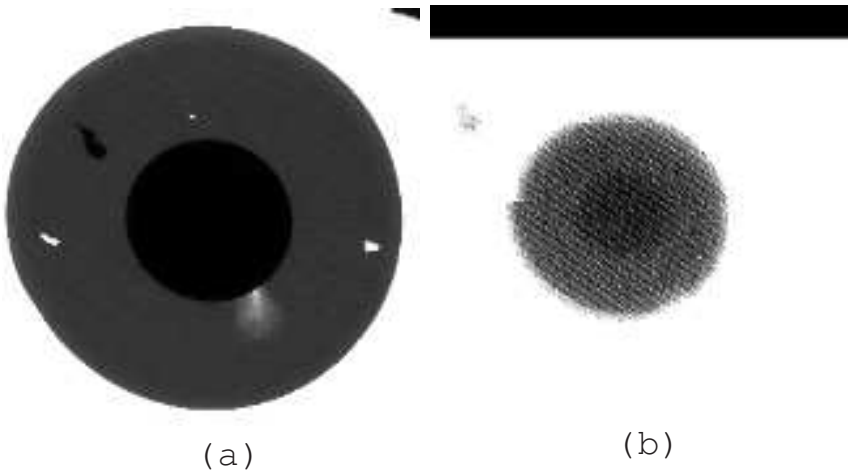

Figure C.5: STXM images of the Tower of Hanoi beamstop with 520 eV x-rays. (a) The first and second layers. (b) The second and third layers.

The averaged transmittance of each layer relative to silicon nitride background is: 6.06%, 0.21%, and 9.89×10^{-4}, respectively. Using Eq. 1.29, considering the β value of gold for 520 eV x-rays is about 0.0044, we obtain the thickness for each layer. They are 0.12 μm, 0.26 μm, and 0.30 μm, respectively. Compared with the numbers listed in Tables C.1, the first two layers are close to the desired values, but the third one is not thick enough.

To reduce the scattering from the Hanoi beamstop itself, the dick surface is required to be smooth and uniform. The histogram plot for each layer is displayed in Fig. C.6. The thickness range is estimated from the width of gaussian fit for each histogram.

The measurements from SEM and STXM images are summarized in Tables C.2.

C.2.4 Diffraction data

We mounted the Tower of Hanoi beamstop in the diffraction microscope apparatus at Beamline 901 at Advanced Light Source. We tested it by taking diffraction data from a frozen hydrated yeast cell grid with 520 eV x-rays. The

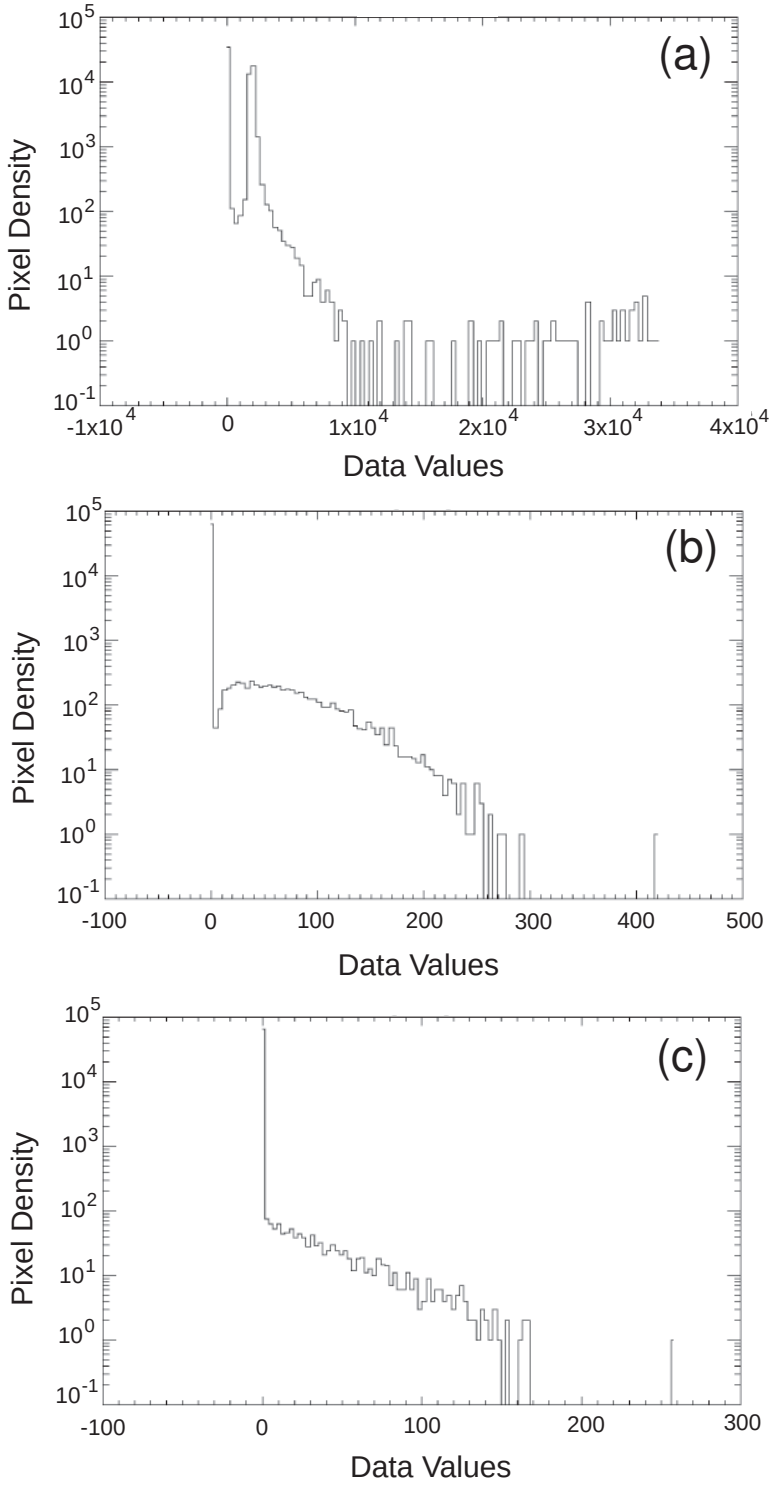

Figure C.6: Histogram for each layer of the Tower of Hanoi beamstop. (a) The first layer. (b) The second layer. (c) The third layer.

Table C.2: The Tower of Hanoi beamstop dimensions.

	Layer 1	Layer 2	Layer 3
Desired diameter (μm)	120	500	1200
Measured diameter (μm)	112	475	1150
Desired thickness with Au (μm)	0.52	0.26	0.13
Measured thickness with Au (μm)	$0.30^{+0.25}_{-0.04}$	$0.26^{+0.04}_{-0.02}$	$0.12^{+0.03}_{-0.02}$

images with the sample grid in and out are shown in Fig. C.7. (The right side of the silicon nitride window was blocked by the sample holder.)

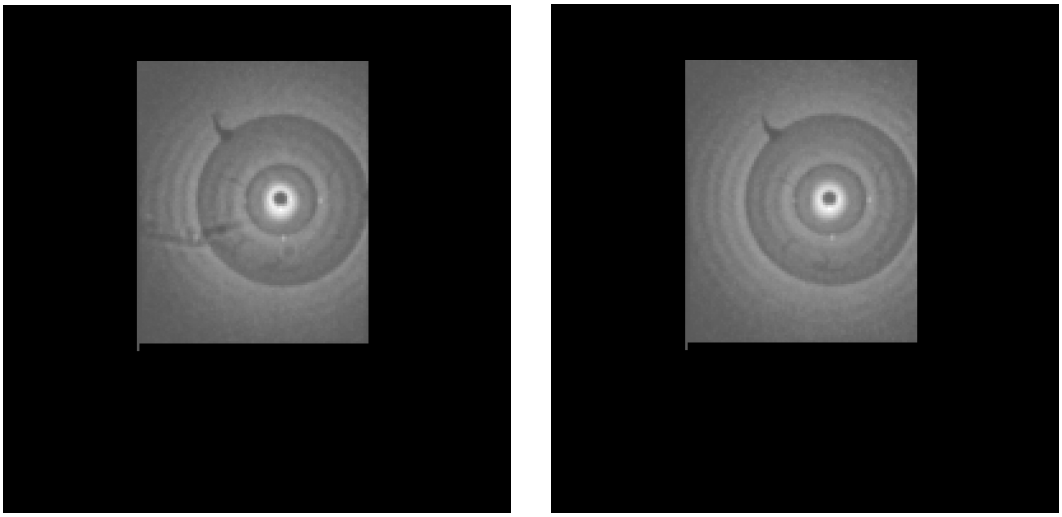

Figure C.7: Diffraction images of the Tower of Hanoi beamstop with 520 eV x-rays. Left, with the sample grid in. Right, with the sample grid out.

The attenuated net diffraction data was obtained by subtracting the grid-out background from the grid-in data (the left image in Fig. C.8). According to the measured thicknesses from STXM images, we can calculate the intensity before absorption of the Hanoi beamstop (the right image in Fig. C.8).

As only about 10% of direct beam is diffracted by the specimen, the count difference between data and background is very small. The statistical fluctuation could cause background pixel counts larger than data pixel counts. This effect leaves a lot of zero-value pixels in the net data image. The step shape of the Hanoi beamstop does not match the profile of the diffraction intensity optimally. The next generation of this partially attenuating beamstop could

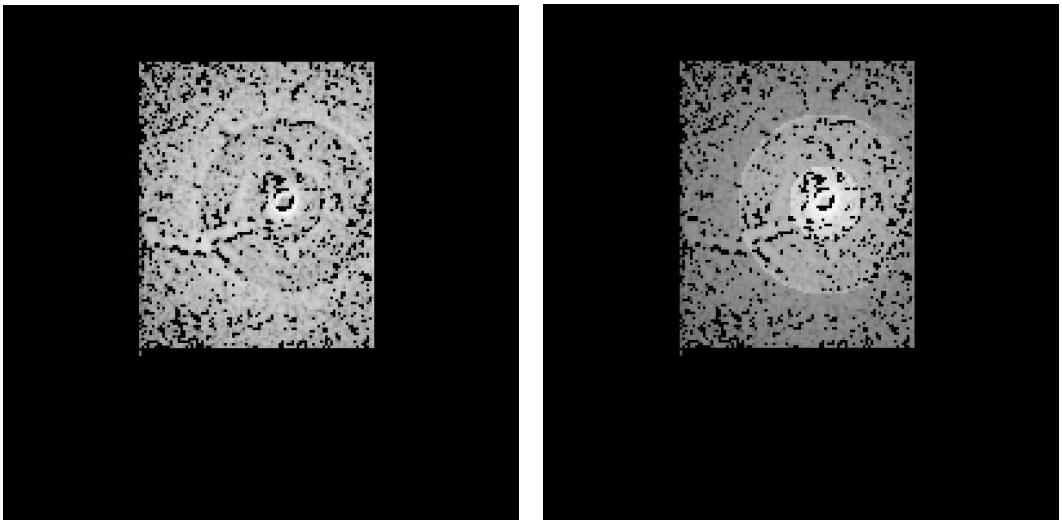

Figure C.8: Net diffraction data of the Tower of Hanoi beamstop with 520 eV x-rays. Left, attenuated data obtained by subtracting the grid-out background from the grid-in data. Right, calculated image without absorption using the measured thicknesses from STXM images.

have a thickness variation with a Gaussian shape.

Appendix D

Thermal calculation for ACD

We estimate the temperature on ACD as a function of the length of the cooling path. In the calculation, the thermal contact through the entire thermal path is assumed to be good enough to ignore the heat loss compared with other factors. The cooling mechanism is simplified as a copper rod or a copper braid contacting with a heat source (for instance, the liquid nitrogen dewar) at one end and the other end hanging in vacuum. Both the rod/braid and heat source are enclosed in a room temperature chamber. The temperature at the suspended end is estimated as a function of length the rod/braid.

D.1 Thermal conduction model

Considering a copper rod with length L and radius r, let's calculate the heat flux in a small section B with length Δx at position x (Fig. D.1).

D.1.1 Conduction

According to the law of heat conduction $\boldsymbol{q} = -k\boldsymbol{\nabla}T$, within time interval Δt, the heat flows into section B through intersection A ($Q_{\text{in\_cond}}$) and the heat flows out through intersection C ($Q_{\text{out\_cond}}$) are:

$$Q_{\text{in\_cond}} = q_{\text{in\_cond}}\pi r^2 \Delta t = -k\frac{\partial T(x,t)}{\partial x}\pi r^2 \Delta t, \tag{D.1}$$

$$Q_{\text{out\_cond}} = q_{\text{out\_cond}}\pi r^2 \Delta t = -k\frac{\partial T(x+\Delta x,t)}{\partial x}\pi r^2 \Delta t, \tag{D.2}$$

where $q_{\text{in\_cond}}$ and $q_{\text{out\_cond}}$ are heat flux densities, k is the thermal conductivity of copper, $T(x,t)$ is the temperature distribution in the rod, and πr^2 is the cross section area.

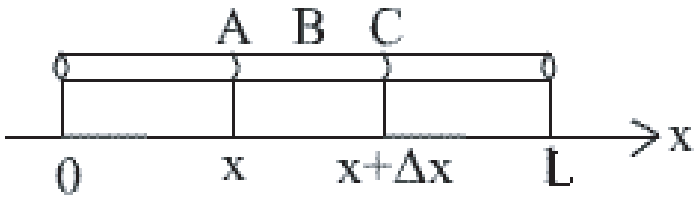

Figure D.1: Heat flux in section B with length Δx at position x.

D.1.2 Radiation

Because the surface temperatures of the rod and the vacuum chamber are different, they emit and absorb electromagnetic radiation at different rates. This effect causes heat transfer through radiation. Assume that the chamber is at room temperature T_{rm}. Within time interval Δt, the net transferred

energy by thermal radiation is given by Stefan-Boltzmann law as

$$Q_{\text{out\_rad}} = q_{\text{out\_rad}} 2\pi r \Delta x \Delta t = \epsilon\sigma[T(x,t)^4 - {T_{rm}}^4] 2\pi r \Delta x \Delta t, \qquad \text{(D.3)}$$

where ϵ is the emissivity, σ is the Stefan-Boltzmann constant, and $2\pi r\Delta x$ is the surface area of section B.

D.1.3 Convection

As there is a small amount of air molecules in the room temperature vacuum chamber, they can exchange energy with the cooling path by gas molecular collision. Newton's law of cooling [135] states that the rate of heat loss of an object through convection is proportional to the temperature difference between the object and its surroundings. Within the same time interval Δt, the heat loss of section B by exchanging energy with its surroundings is

$$Q_{\text{out\_conv}} = q_{\text{out\_conv}} 2\pi r \Delta x \Delta t = h[T(x,t) - T_{rm}] 2\pi r \Delta x \Delta t, \qquad \text{(D.4)}$$

where h is the heat transfer coefficient between copper and air, and again $2\pi r\Delta x$ is the surface area of section B.

D.2 Heat transfer equation and boundary conditions

The net heat gain in section B causes its temperature to rise by ΔT. Denoting c as the specific heat of copper and ρ as its density, we can write the heat conduction equation as

$$\begin{aligned} -k\frac{\partial T(x,t)}{\partial x}\pi r^2 \Delta t + k\frac{\partial T(x+\Delta x,t)}{\partial x}\pi r^2 \Delta t \;&-\; \epsilon\sigma[T(x,t)^4 - {T_{rm}}^4] 2\pi r \Delta x \Delta t - \\ h[T(x,t) - T_{rm}] 2\pi r \Delta x \Delta t \;&=\; c\rho\pi r^2 \Delta x \Delta T(x,t), \end{aligned} \qquad \text{(D.5)}$$

which can be simplified as

$$k\frac{\partial^2 T(x,t)}{\partial x^2}\pi r^2 - 2\pi r\epsilon\sigma[T(x,t)^4 - {T_{rm}}^4] - 2\pi rh[T(x,t) - T_{rm}] = c\rho\pi r^2\frac{\partial T(x,t)}{\partial t}. \tag{D.6}$$

We are interested in the heat equilibrium status, where the temperature distribution in the rod is static ($\partial T/\partial t = 0$). Under this condition, Eq. D.6 becomes

$$k\frac{\partial^2 T(x)}{\partial x^2}\pi r^2 = 2\pi r\epsilon\sigma[T(x,t)^4 - {T_{rm}}^4] + 2\pi rh[T(x) - T_{rm}]. \tag{D.7}$$

Denoting $\eta = 2\epsilon\sigma/(kr)$ and $\tau = 2h/(kr)$, then Eq. D.7 can be simplified further as

$$\frac{\partial^2 T(x)}{\partial x^2} = \eta[T(x,t)^4 - {T_{rm}}^4] + \tau[T(x) - T_{rm}]. \tag{D.8}$$

Solving this second order differential equation requires at least two boundary conditions. At $x = 0$, the rod temperature equals the heat source temperature T_{sc}

$$T(0) = T_{sc}. \tag{D.9}$$

At the other end ($x = L$), the boundary condition is that the heat flows into the tip surface equals the heat loss:

$$-k\frac{\partial T(L)}{\partial x}\pi r^2 = \epsilon\sigma[T(L)^4 - {T_{rm}}^4]\pi r^2 + h[T(L) - T_{rm}]\pi r^2. \tag{D.10}$$

Denoting $\xi = \epsilon\sigma/k$ and $\zeta = h/k$, Eq. D.10 can be expressed as

$$-\frac{\partial T(L)}{\partial x} = \xi[T(L)^4 - {T_{rm}}^4] + \zeta[T(L) - T_{rm}]. \tag{D.11}$$

D.3 Differential equation solution

Solving Eq. D.8 analytically may involve hypergeometric functions. Instead, the numerical solution can be obtained in a relatively easy way.

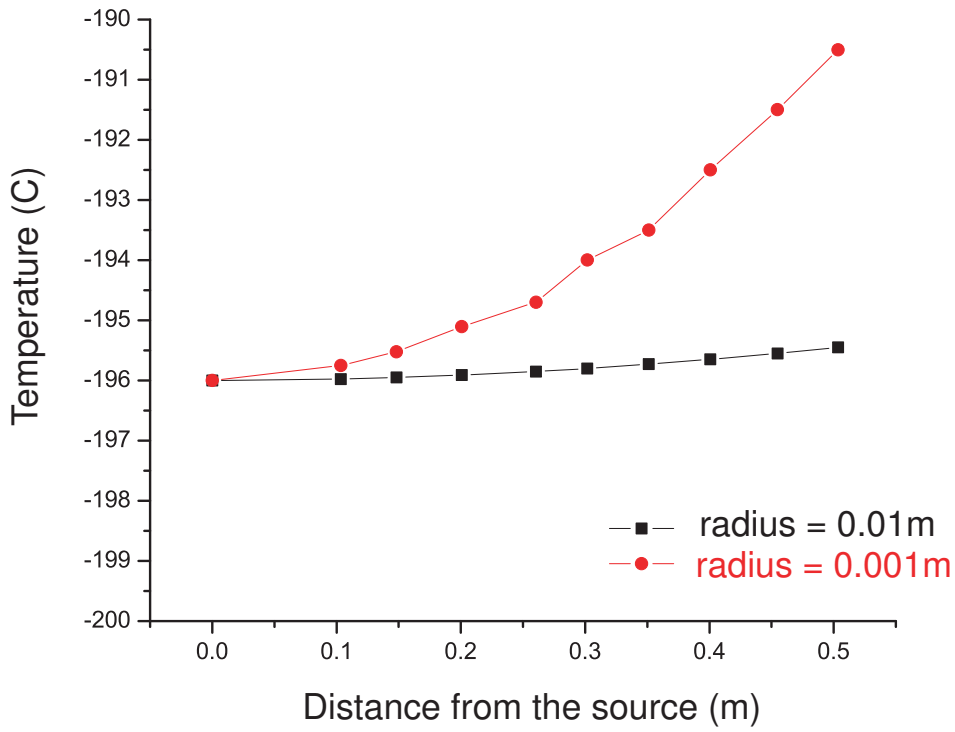

Figure D.2: Temperature distributions of solid copper rod with different radius.

At first, convert Eq. D.8 into lower order differential equation as

$$\partial\left(\frac{1}{2}\left(\frac{\partial T(x)}{\partial x}\right)^2\right) = \{\eta[T(x,t)^4 - {T_{rm}}^4] + \tau[T(x) - T_{rm}]\}\partial T. \tag{D.12}$$

Then integrate both sides of Eq. D.12 from x to L. This gives

$$\begin{aligned}\frac{1}{2}\left(\frac{\partial T(L)}{\partial x}\right)^2 \quad - \quad & \frac{1}{2}\left(\frac{\partial T(x)}{\partial x}\right)^2 = \frac{\eta}{5}[T(L)^5 - T(x)^5] - \eta {T_{rm}}^4[T(L) - T(x)] \\ + \quad & \frac{\tau}{2}[T(L)^2 - T(x)^2] - \tau T_{rm}[T(L) - T(x)].\end{aligned} \tag{D.13}$$

Substituting the second boundary condition Eq. D.11 into Eq. D.13, we obtain

$$\begin{aligned}\left(\frac{\partial T(x)}{\partial x}\right)^2 \quad = \quad & \{\xi[T(L)^4 - {T_{rm}}^4] + \zeta[T(L) - T_{rm}]\}^2 \\ - \quad & \frac{2\eta}{5}[T(L)^5 - T(x)^5] + 2\eta {T_{rm}}^4[T(L) - T(x)] \\ - \quad & \tau[T(L)^2 - T(x)^2] + 2\tau T_{rm}[T(L) - T(x)].\end{aligned} \tag{D.14}$$

Denote the right side of this equation as $F\{T(L), T(x)\}$. Take square root of Eq. D.14 and separate differential variables into different sides of the equation. Then integral both sides from 0 to L:

$$\int_{T(0)}^{T(L)} \frac{\partial T(x)}{\sqrt{F\{T(L), T(x)\}}} = \int_0^L \partial x = L. \tag{D.15}$$

We can test the left side integral with a series of $T(L)$ values. When the integral result matches the L value (which is the length of the copper rod), the corresponding $T(L)$ is the numerical solution that we are searching for.

D.4 Numerical estimation result

The heat conductivity of copper k is 450 W/(mK), the emissivity of highly polished copper is 0.023, and the heat transfer coefficient h between copper and air is about 0.04 mW/(mK) [116]. Set the room temperature T_{rm} to 20 °C. The heat source temperature T_{sc} at the tail of the liquid nitrogen dewar is

around -196 °C. The Stefan-Boltzmann constant is 5.67×10^{-8} W/(K^{4}m^2).

Fig. D.2 shows the temperature distributions of rod with 0.01 m and 0.001 m radius as a function of length. It shows the cooling effect of a solid copper rod is very good. The temperature does not rise too much up to 0.5 m in both cases.

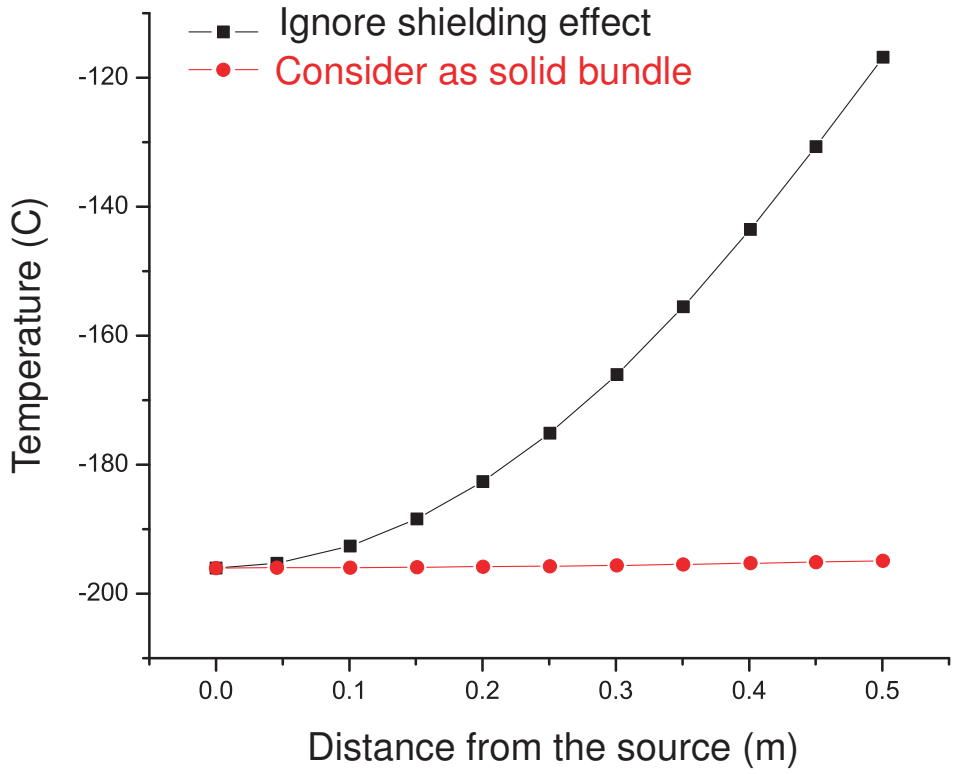

Figure D.3: Temperature distributions of copper braid consisting of 168×36 wires, each of AWG36 or 127 μm diameter. Black line: ignore shielding effect. Red line: consider all the wires as a solid bundle.

The ACD position needs to be adjustable. A copper braid can provide such a soft mechanical path with reasonable cooling ability. As an example, the temperature distribution is estimated on a copper braid consisting of 168×36 wires, each of AWG36 or 127 μm diameter. As the copper braid is a bundle of thin copper wires, the inside wires are shielded by the outside wire layers. The estimation is done at two extreme conditions, where one completely ignores the shielding effect, and where one considers wires to be part of a solid bundle,

shown in Fig. D.3. From the plot, we conclude that to avoid ice crystallization at around -140 °C, it is safe to use copper braid less than 0.4 m.

Appendix E

Liquid nitrogen autofill controller

The liquid nitrogen autofill system is meant to maintain liquid nitrogen levels in two separate reservoirs: one is the liquid nitrogen dewar for ACD, and the other is the dewar on the cryo-specimen holder. The autofill system works by using a pair of level sensors and a purge container used to pre-cool the transfer lines from a pressurized liquid nitrogen storage dewar. In this chapter, we describe the design and operation of this system.

E.1 Control panels

The valve control box can control two fill valves and one purge valve. Each valve has a manual control switch (labeled OPEN) and an enable switch (labeled ENABLE). The state of each ENABLE switch determines which valves will be enabled for either manual or automatic operation. Each FILL TANK represented schematically on the panel has three LED indicators. One LED indicates when power is supplied to open the solenoid valve. The other two LEDs indicate the status of the low level and high level liquid sensors. The PURGE tank is identical except that it lacks a high level sensor. The AUTO / MANUAL switch determines the operational mode of the controller, and the POWER LED indicates that the controller is powered.

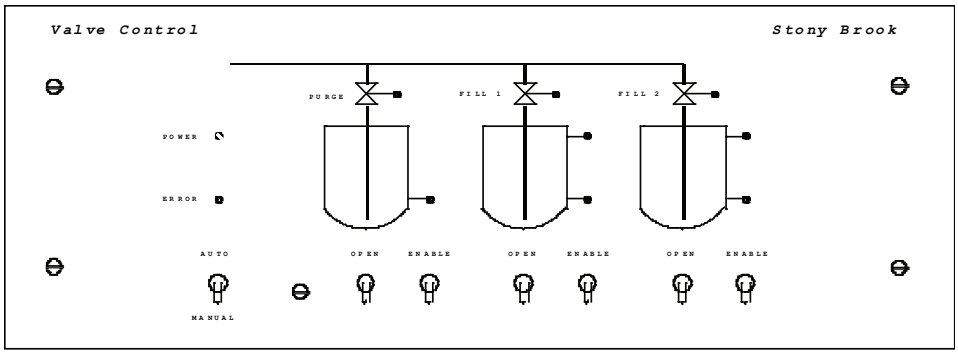

Figure E.1: Valve controller front panel.

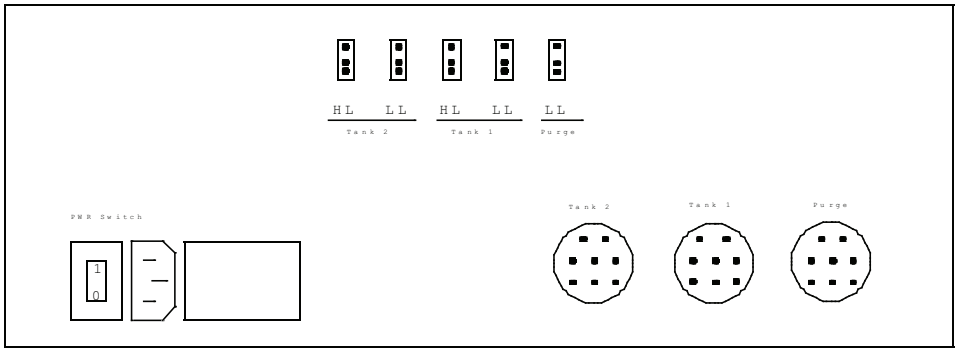

Figure E.2: Valve controller rear panel.

The support piece is mounted on the 10-inch flange holds a four-way

Swagelok connector, while each branch is equipped with a solenoid valve; the branches go to to the anti-contaminator, the cryo-holder dewar, and the pre-cooling bath via vacuum-sealed hoses.

The signals from the sensors are collected by a Parallax "Basic Stamp" IC, which is a programmable micro controller on a chip with 16 I/O lines, a built in clock, processor, Basic interpreter, and nonvolatile memory. The output commands control solenoid valves, which are powered by 12 VDC power supplies.

E.2 Operation modes

Manual mode gives full control over all valves:

1. Place 'AUTO/MANUAL' switch into 'MANUAL' mode.

2. Place the enable switch of the valve we want to operate into 'ENABLE'.

3. Hold the manual control switch in 'OPEN' position to open the valve, until releasing the manual control switch or the up level sensor giving signal.

Auto mode maintains a liquid level:

1. Place 'AUTO/MANUAL' switch into 'AUTO' mode.

2. Place the enable switch of the valve we want to operate into 'ENABLE'. (Refill tank 1: enable PURGE and FILL 1 valves; Refill tank 1 and 2: enable PURGE, FILL 1 and FILL 2 valves.)

E.3 Logic sequence

When the controller is placed in AUTO mode with at least one FILL valve enabled, the following logic sequence is performed:

1. If both the high level sensor and the low level sensor for an enabled valve are off, then proceed to step 2. Else wait at step 1.

2. If the PURGE valve is disabled, continue to step 3. If the PURGE valve is enabled and the PURGE tank liquid sensor is off, then open the PURGE valve and start the PURGE timer. If the PURGE tank liquid sensor senses liquid before the PURGE timer times out, close the PURGE valve and continue

to step 3. If the PURGE timer times out before the PURGE tank liquid sensor senses liquid, close all valves and indicate a PURGE TANK timeout error.

3. Open the FILL valve for any enabled tank whose liquid level is below the low level sensor. An independent FILL timer is started for each open valve. If at any time, the high level sensor senses liquid and the corresponding low level sensor does not sense liquid, all valves are closed and an error is indicated. If an enabled FILL timer times out before the associated tank is full, all valves are closed and a timeout error is indicated. If both the high level and low level sensors for an enabled tank sense liquid, the associated valve is closed. Once all valves are closed (without an error condition), continue to step 1.

E.4 Error message

The ERROR LED alerts an error condition or indicates that the controller is in "setup" mode. When the ERROR LED is flashing, it is reporting an error condition. Errors are detected and identified only when the controller is in AUTO mode. When an error occurs, all valves are closed. The error condition is reset when the AUTO / MANUAL switch is set to MANUAL. The ERROR LED identifies the error by flashing N times, then pausing for ∼1 second and then repeating the pattern. The value of N is determined by the source of the error:

N = 1, PURGE TANK timeout error

N = 2, FILL TANK ♯1 timeout error

N = 3, FILL TANK ♯2 timeout error

N = 4, FILL TANK ♯1 high level sensor on, low level sensor off

N = 5, FILL TANK ♯2 high level sensor on, low level sensor off

E.5 Timeout setting

The timeout for each tank can be programmed independently. The timeout is measured in seconds. A maximum value for the timeout parameter is 600 (ten minutes). To program the timeout for a particular valve, the process is

as following:

1. Disable all three valves by placing each ENABLE switch in the disable position.

2. Set the AUTO / MANUAL switch to AUTO.

3. Momentarily place all three manual valve switches in the OPEN position. The ERROR LED will come on to indicate that the controller is in 'setup' mode.

3. Now activate the ENABLE or OPEN switch for the tank to be programmed. The ERROR LED will proceed to blink once per second. When the desired timeout interval is reached, release the ENABLE or OPEN switch. The ERROR LED will turn off and the controller will return to operational mode. The new timeout value is stored in EEPROM and will remain in effect until reprogrammed.

Each tank can be programmed individually as described above. The default timeout parameters are 10 seconds for the PURGE tank and 1 minute for each of the FILL tanks. If one attempts to program a tank timeout of less than 3 seconds, the tank will revert to its default setting.

E.6 Electrical circuit schematics

Electrical circuit schematics are shown in Fig. E.3, Fig. E.4, Fig. E.5 and Fig. E.6.

E.7 System modification with continuous flow

The problem with the current refill system design is that the intensive flushing at the beginning of each refill cycle brings in vibration to the delicate microscope, and it might trigger level sensors accidentally. To avoid these side effects, instead of refilling the purge tank to cool the transfer hose, we can conduct a continuous cold nitrogen gas flow through the hose when the system is idling.

This involves modifications to two modes. In the idle mode, a relatively

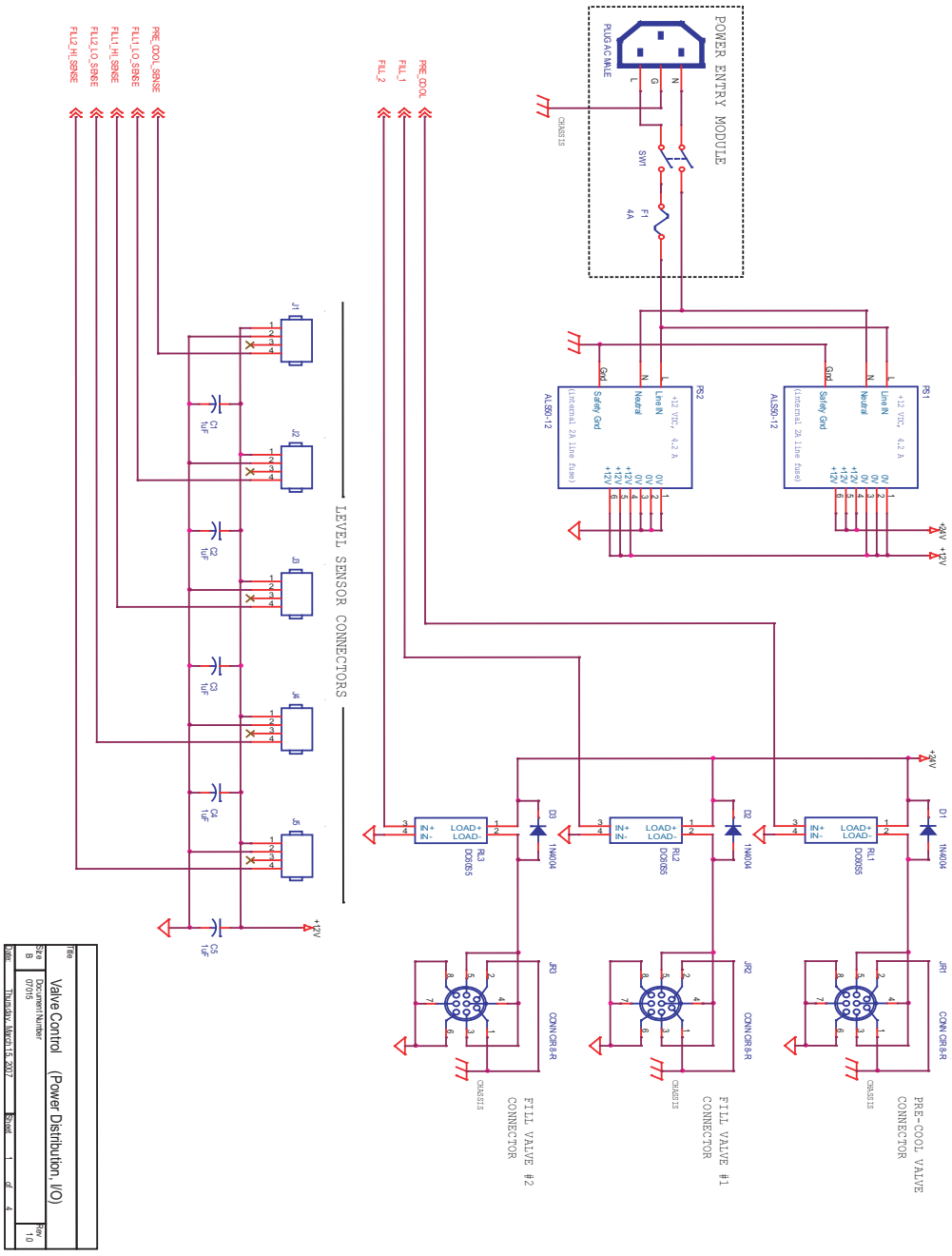

Figure E.3: Electrical schematic for valve controller power distribution.

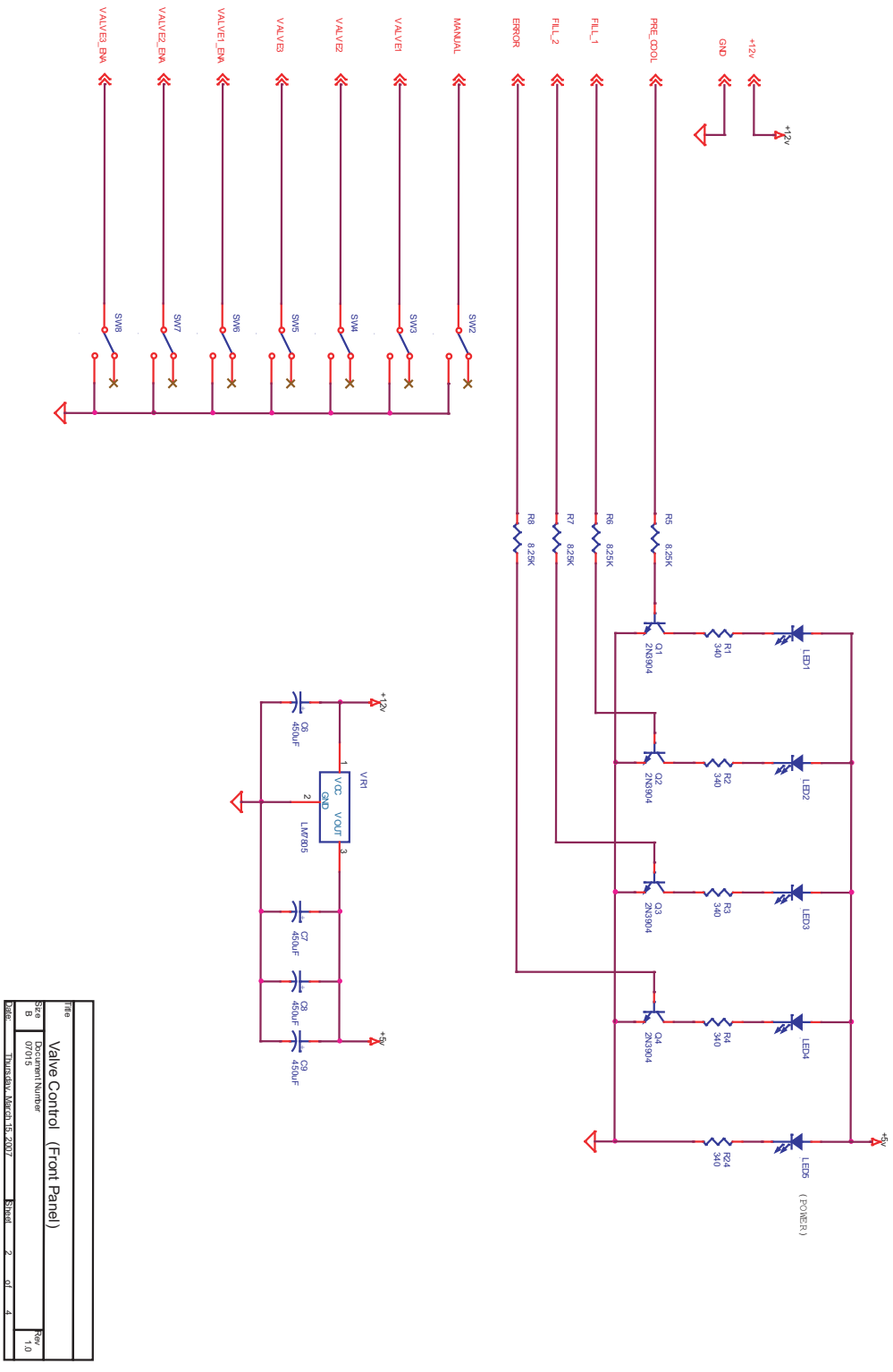

Figure E.4: Electrical schematic for valve controller front panel 1.

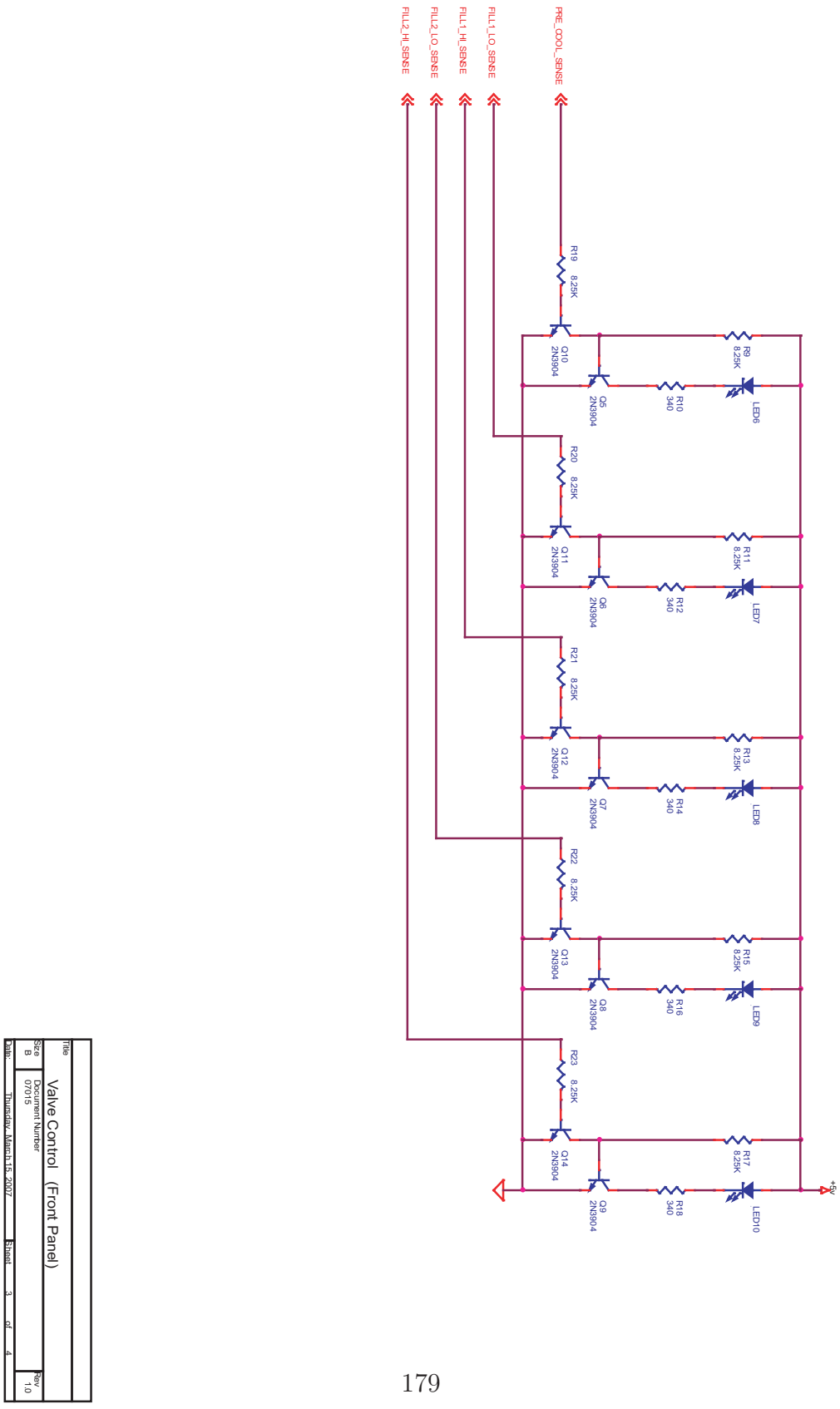

Figure E.5: Electrical schematic for valve controller front panel 2.

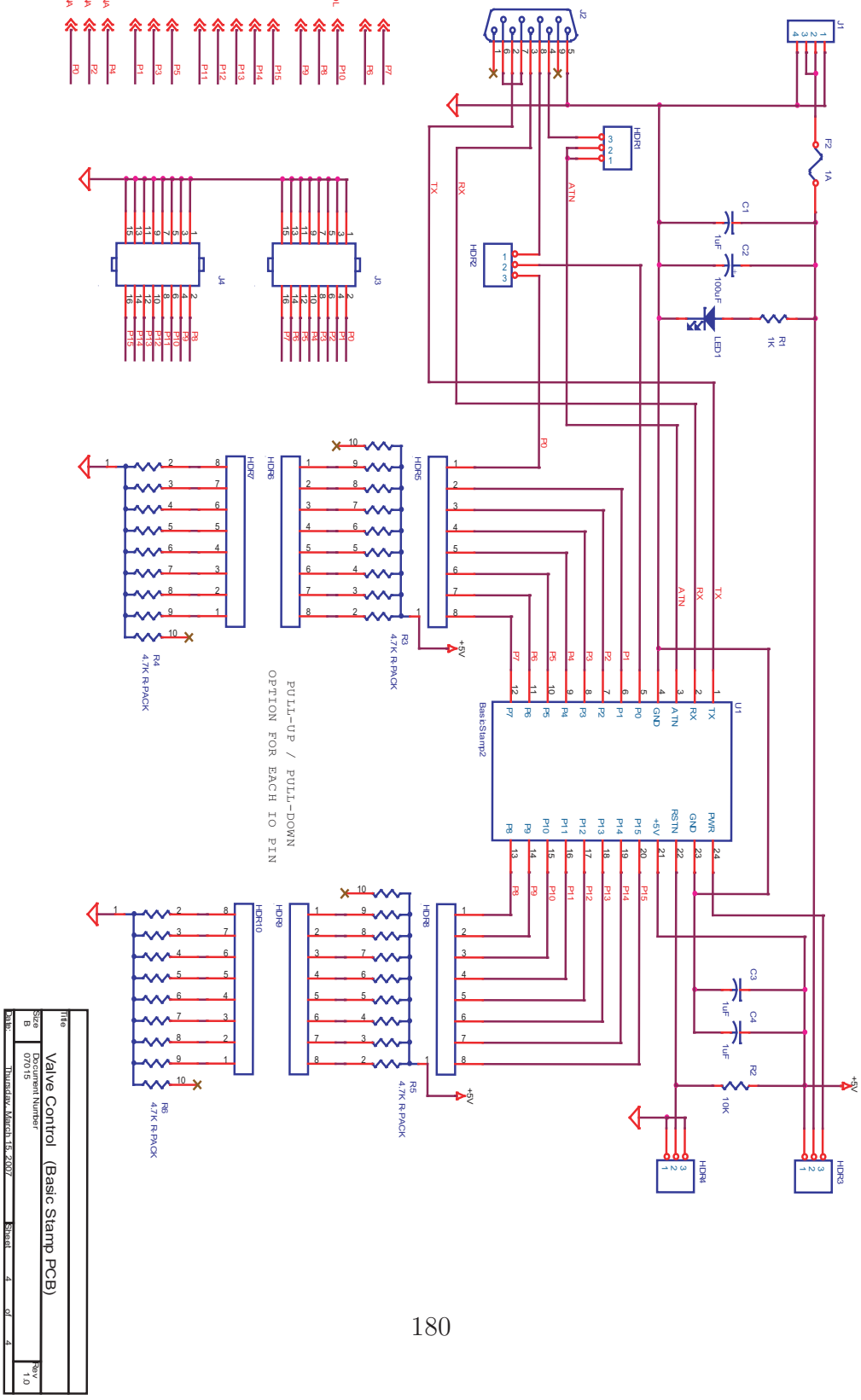

Figure E.6: Electrical schematic for valve controller basic stamp PCB.

low gas pressure ($\sim$ 1 PSI) in liquid nitrogen reservoir drives continuous cold nitrogen gas flow through the hose and keeps the hose cold; when the low sensor in the target tank gives a signal to refill, a relatively high pressure ($\sim$ 5 PSI) will be built up in the reservoir, which will drive a liquid nitrogen flux through the hose. Fig. E.7 sketches the working scheme of the new system.

A 3-way solenoid valve switches between those two working modes. When it is de-energized, it connects to the port with a 1 PSI release valve (controlling the pressure in the liquid nitrogen reservoir), and the system stays in the IDLE mode. When the valve is energized, it connects to compressed air. At this condition, the liquid nitrogen pressure is controlled by a 5 PSI release valve, and the system is triggered in the REFILL mode.

As there are electronic instruments located below the refilling tanks, liquid nitrogen over-flow should be avoided in any case. For this purpose, there is a over-flow sensor mounted near the opening edge of each target tank. When this sensor gives signal, the controller box will trigger evacuation valve on the liquid nitrogen reservoir and reduce the pressure down to atmosphere immediately, which will shut down liquid nitrogen flux in the hose.

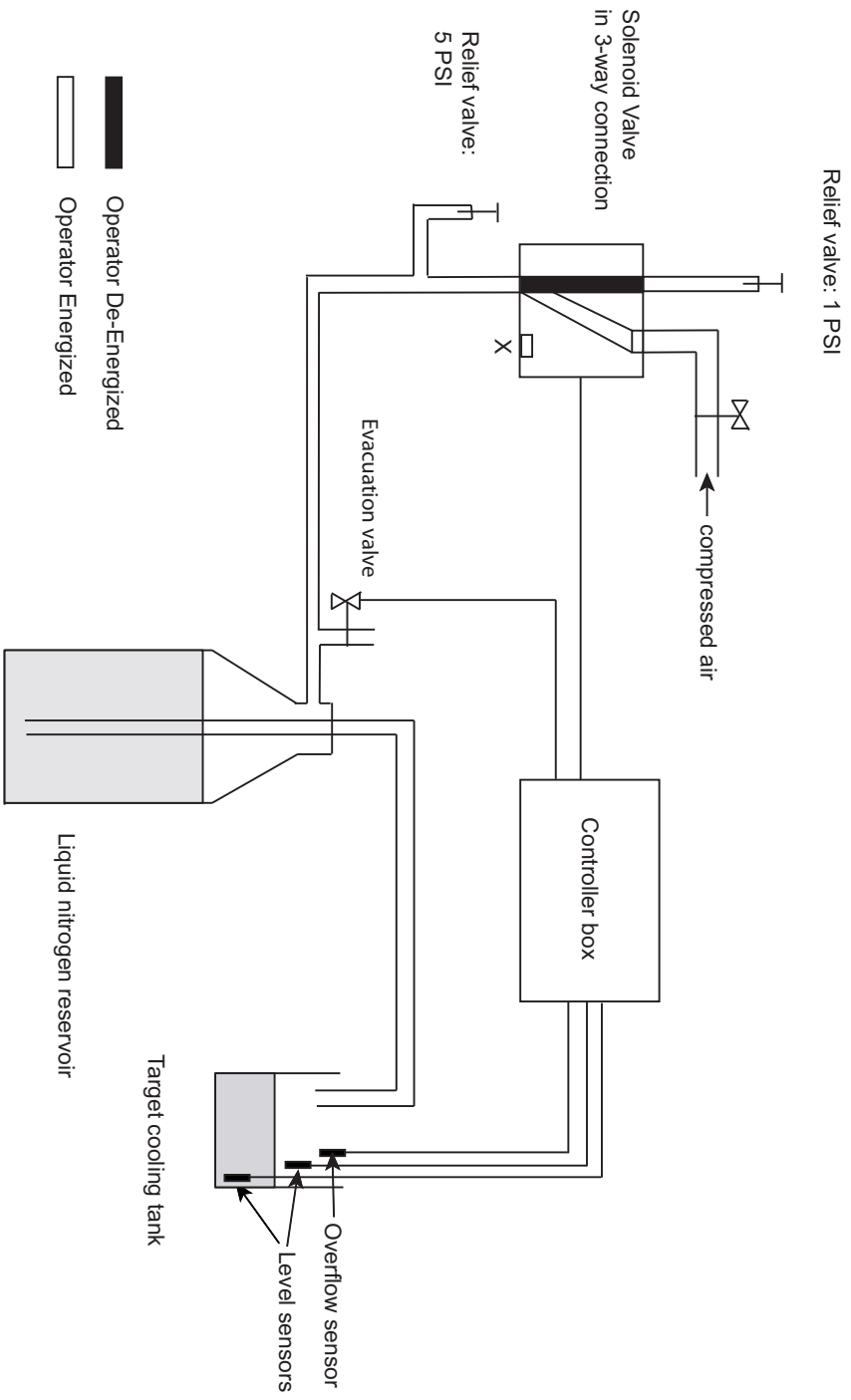

Figure E.7: Schematic drawing for the modified liquid nitrogen refill system with continuous flow.

Appendix F

Finding cells with CCD scan

The feasibility of using projection images to find cell locations is questionable, because the projection of a 3 μm cell on CCD is less than one pixel (20 μm). Ice balls on a sample grid can also generate round gray shadows on CCD, which can easily cause confusion. In this chapter, we discuss an approach for finding cells using CCD scans.

F.1 CCD scan speed control

The first challenge for CCD scan is that it is very time consuming. The scan speed is adjustable by using only parts of CCD pixels, which is determined by the parameter `ccd_unbinned_size`. For instance, when `ccd_unbinned_size` is set to be 512, only a 512×512 pixel array in the center of the entire CCD array is in use.

The size of the CCD scan image is controlled by another parameter pair: `col_binning` and `row_binning`. The default value of these two parameters is 2, which means every second column and row are actually read off to generate a final 256×256 CCD scan image with the textttccd_unbinned_size setting of 512.

In principle, we can increase CCD scan speed by reducing the read off image size as long as it is sensitive enough to find a cell. For this purpose, three parameter inputs are added in "CCD scan" widget for `ccd_unbinned_size`, `col_binning` and `row_binning`, respectively.

The scan speed has been tested as a function of those three parameters shown in Tables F.1. The scan timing is sensitive to the final generated image size. With different `ccd_unbinned_size` and `col/row_binning` combinations, as long as the image size is the same, the scan speed does not change much (values on diagonal lines of Tables F.1). The CCD read-out timing per pixel varies with the total pixel array size in use. Fig. F.1 shows the timing variation trend.

Table F.1: CCD scan speed test. 1 sec exposure, 5×5 scan array with 10 μm step size.

`col/row_binning`	128×128	256×256	512×512	1024×1024
1	1.4 min	1.9 min	2.9 min	
2	1.3 min	1.4 min	1.8 min	2.7 min
4	1.2 min	1.3 min	1.4 min	1.7 min
8	1.2 min	1.2 min	1.3 min	1.3 min

Besides the scan speed, the speckles on the scan images should be recognizable, and the field of view should be large enough as well. From the test, we found `ccd_unbinned_size` 512×512 with `col/row_binning` 4 was a

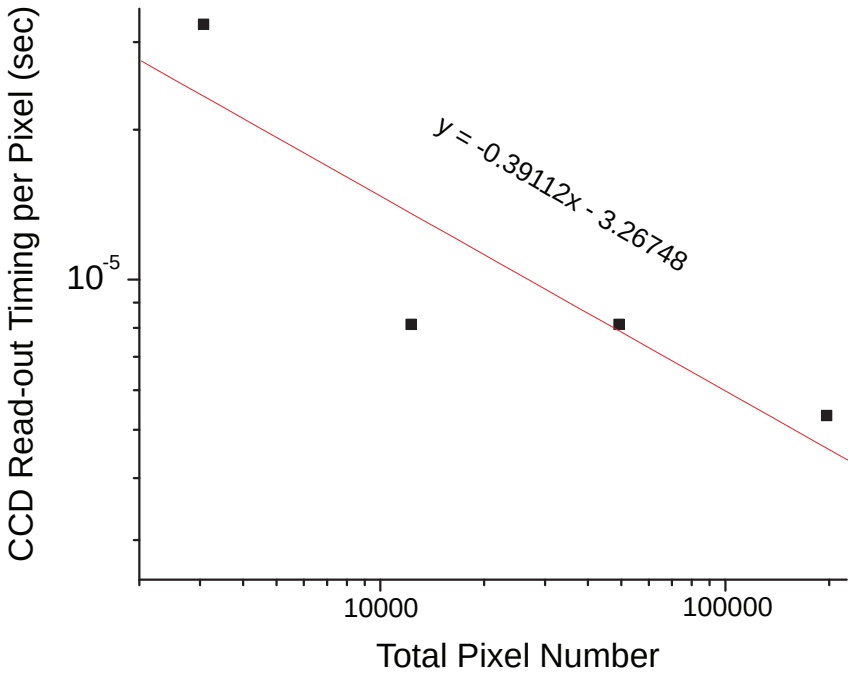

Figure F.1: CCD read-out timing versus total pixel number.

good setting to satisfy these requirements (left image in Fig. F.2) and gave reasonable timing. We tried a 25×25 scan with 10 μm step size using this set of parameter setting. It finished within about half an hour. Considering the entire scan area size was 250×250 μm which covered a majority of the grid opening window, the timing was quite good. From the CCD scan image (right image in Fig. F.2), several strongly scattering locations can be recognized.

F.2 Identifying cell using diffraction pattern

F.2.1 Simulation

In order to tell the similarity and difference in diffraction patterns between cells and ice, a fake cell and an ice ball were compared.

The fake cell was built and its exit wave was calculated in the same way as in Sec. 3.1.1 (shown in (a)(c)(e)(g) of Fig. F.3).

The ice ball was built in the same way as the fake cell and has the same

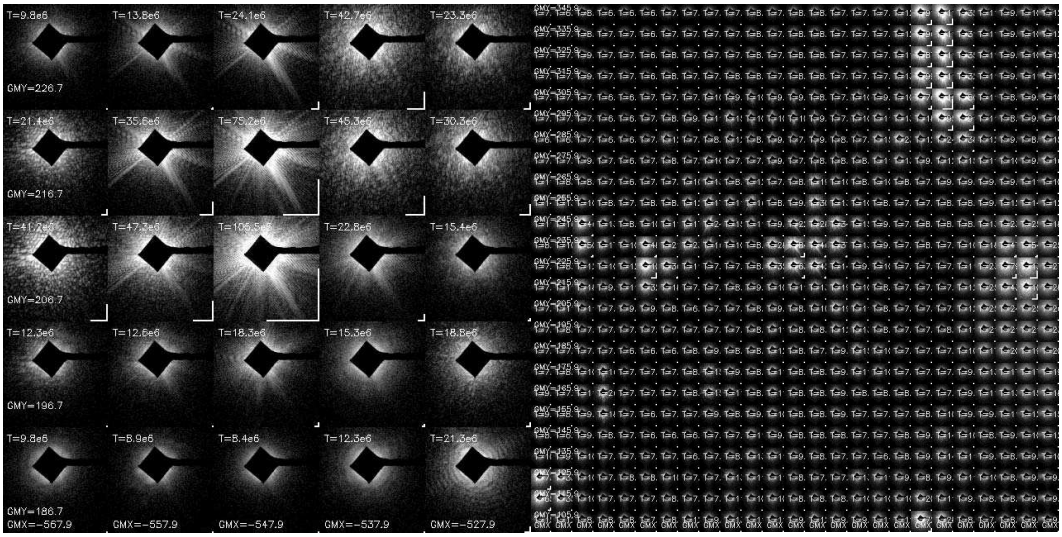

Figure F.2: CCD scan images with `ccd_unbinned_size` 512 × 512 with `col/row_binning` 4. Left: 5 × 5 scan with 10 μm step size; Right: 25 × 25 scan with 10 μm step size.

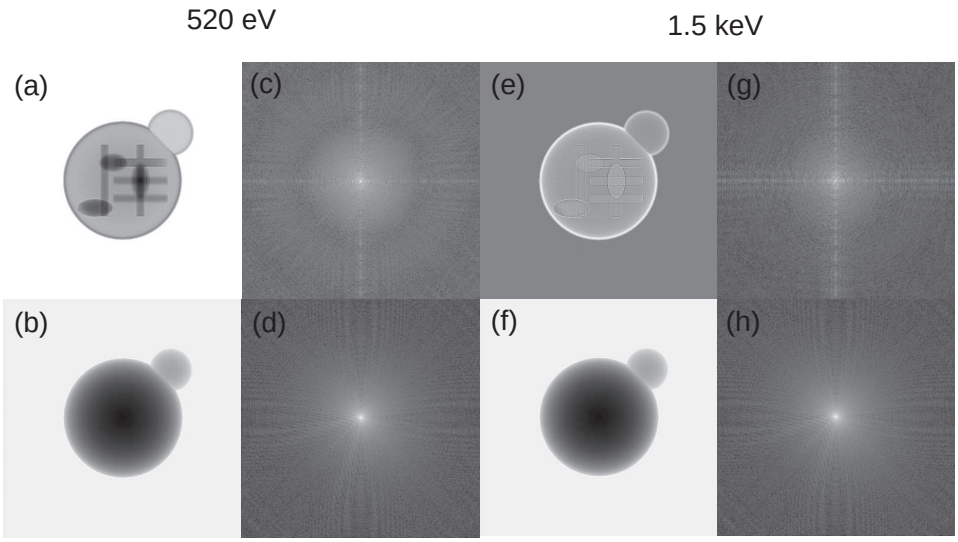

Figure F.3: Simulated exit waves and diffraction patterns at 520 eV ((a)-(d)) and 1.5 keV ((e)-(h)): (a)(e) exit wave of the fake cell, (b)(f) exit wave of the ice ball, (c)(g) diffraction pattern of the fake cell, (d)(h) diffraction pattern of the ice ball.

outline with the same pixel size of 15 nm, but filled with ice. The exit wave was also obtained by a multi-slice propagation (shown in (c)(f) of Fig. F.3).

The simulation was done at 520 eV and 1.5 keV with 1.0×10^4 incident photons per pixel. Fourier transforming both exit waves gave the far field diffraction patterns. The diffraction speckles did not show significant difference directly ((b)(d) and (g)(h) in Fig. F.3). Although we can see dark rings in the fake cell's 520 eV diffraction image, those rings were dismissed at 1.5 keV.

We then compared their power spectral density (PSD) curves as shown in Fig. F.4. In log-log plots, the PSD from the ice ball drops down smoothly with spatial frequency, while the PSD from the fake cell fluctuates more. At low spatial frequencies ($\leq 1\ \mu\text{m}^{-1}$), the fake cell PSD is 2 orders less than ice ball PSD at 520 eV, about 6 orders less at 1.5 keV.

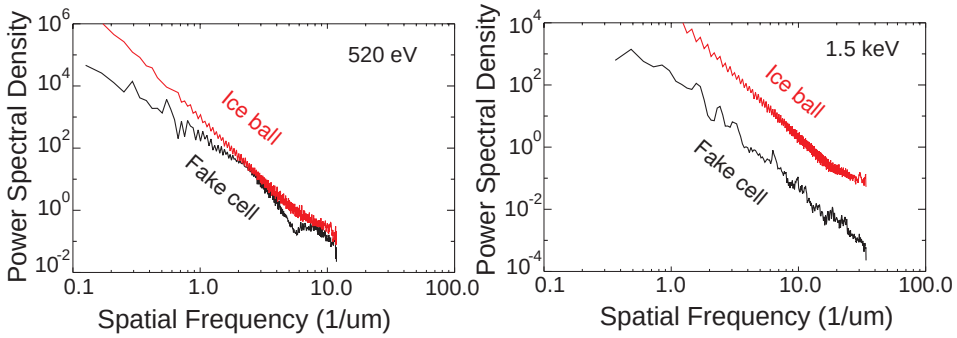

Figure F.4: Power spectral density curves of the fake cell and the ice ball at 520 eV (left) and 1.5 keV (right).

Considering the scattering pattern from an ice ball is more uniform than that from a cell, because the ice ball has no inside structure and no sharp boundary, the variations in the power spectral density curves should be smaller and can be used to identify the difference. Fig. F.5 shows that the PSD variation from the ice ball is indeed smaller than that from the fake cell in average, especially in the spatial frequency range $\leq 1.0\ \mu\text{m}^{-1}$ at 520 eV and in the entire range beyond $1.0\ \mu\text{m}^{-1}$ at 1.5 keV.

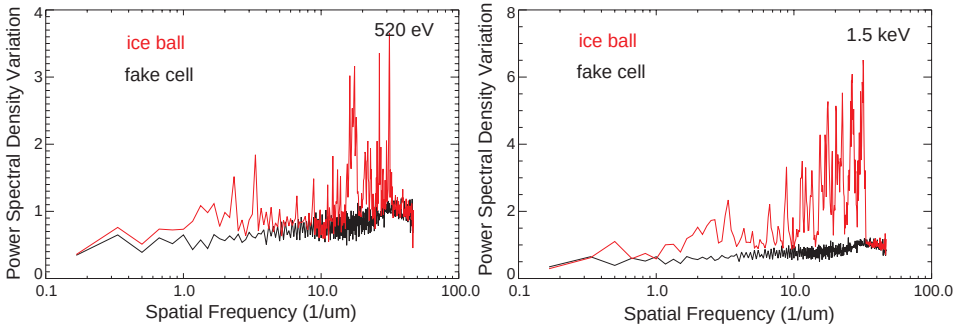

Figure F.5: Variations in power spectral density curves of the fake cell and the ice ball at 520 eV (left) and 1.5 keV (right).

F.2.2 Analysis on experimental scan data

We took a 25×25 CCD scan with 10 μm step size (shown in Fig. F.2) on a frozen hydrated yeast cell grid warmed up in vacuum chamber. We checked the intensities and PSD variations of the scan images.

We calculated the total scattering count for each image. Fig. F.6 displays the total count of each scan image as one pixel. The brightness of this 25×25 image demonstrates the relative scattering strength. Fig. F.6 (b) shows the locations of top 10 strongest scattering scan spots.

PSD variations were then calculated to represent diffraction pattern characteristics. Considering the CCD pixel size is about 20 μm, distance from sample to CCD is about 14 cm, and 520 eV x-ray wavelength is 2.38 nm, the pixel size in reciprocal space is about 16.7 μm^{-1}. The beamstop cutoff is about 5.6 μm^{-1}, and the outermost pixel spacial frequency is about 20.0 μm^{-1}. The PSD variation calculation was done in the range from 6.0 to 16.0 μm^{-1} range. It shows that the `ccd_unbinned_size` and `col/row_binning` combination was well chosen to cover this spacial frequency range. Fig. F.6 (c) shows the PSD variation for each scan image, and Fig. F.6 (d) shows top 10 locations with largest variations.

Fig. F.7 (a) shows one scan image that ranks in both top 10 lists of intensity (6th) and PSD variation (4th). Its diffraction pattern is contaminated by streaks, but speckles can be recognized. By checking its surrounding images, we found a scattered pattern with good speckles (Fig. F.7 (b)). This

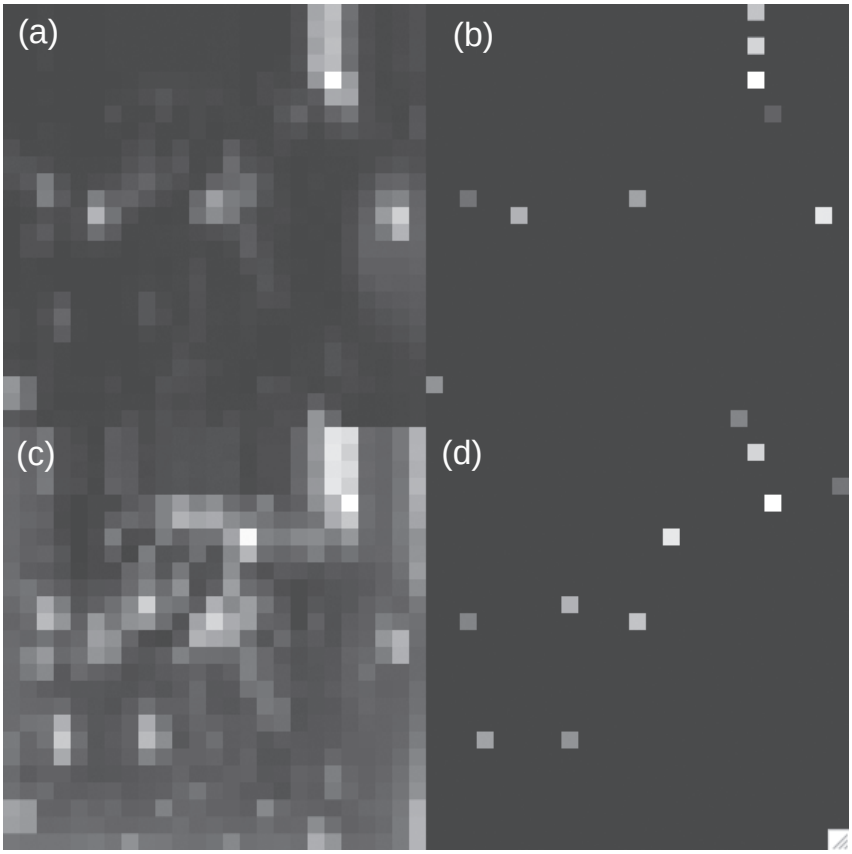

Figure F.6: (a) CCD scan image total counts. (b) Top 10 most strongly scattering positions. (c) PSD variations between 1.5 μm^{-1} and 4.0 μm^{-1}. (d) Top 10 largest PSD variation in the concerned range.

image is 10 μm away. With another CCD scan with smaller step size and `col/row_binning` settings, this promising specimen can be located more accurately.

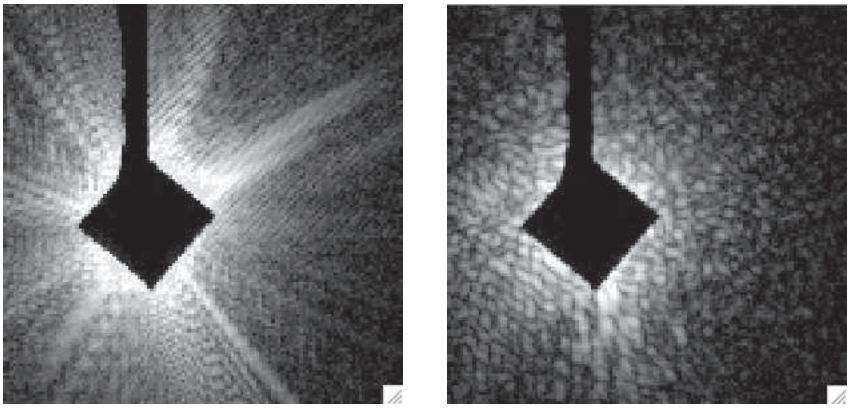

Figure F.7: (a) An image ranks in both top 10 lists of intensity and PSD variation. (b) The promising specimen 10 μm away from (a).

F.2.3 Conclusion

From simulation results, we conclude that: (1) it is unreliable to identify cell from its diffraction pattern directly; (2) the PSD curves of an ice ball is smoother than that of a fake cell and the fake cell PSD counts are several orders less at low spatial frequencies; (3) the PSD variation of an ice ball is consistently smaller than that of a fake cell.

Analysis of an experimental data shows than combining total scattering counts and PSD variation is functional to locate promising specimens. Fig. F.5 shows that PSD variation difference of a cell and an ice ball is larger at higher energy. This method could work better at higher energies.

Unfortunately, we did not collect finer scans over the picked up spot (Fig. F.7 (b)), and did not take a full 2D data set from this promising specimen. These two processes could be performed in future experiments, and they will provide further support to the conclusion.

Bibliography

[1] D. Attwood. *Soft X-rays and Extreme Ultraviolet Radiation*. Cambridge Univ. Press, 1999.

[2] J. D. Jackson. *Classical Electrodynamics*. Wiley, New York, third edition, 1998.

[3] M. Born and E. Wolf. *Principles of Optics*. Cambridge Univ. Press, 1999.

[4] B. L. Henke, E. M. Gullikson, and J. C. Davis. X-ray interactions: Photoabsorption, scattering, transmission, and reflection at E=50–30,000 eV, Z=1–92. *Atomic Data and Nuclear Data Tables*, 54:181–342, 1993.

[5] Rigaku x-ray tube. URL http://www.rigaku.com/generators/fre-plus.html, 2008.

[6] Rigaku x-ray tube bandwidth. URL http://www.rigaku.com/generators/cr-sad.html, 2008.

[7] Energetiq x-ray plasma laser. URL http://www.energetiq.com/html/xray.html, 2007.

[8] ALS bending magnet. URL http://www.als.lbl.gov/als/curves/sbend.html, 2002.

[9] ALS wiggler. URL http://www.als.lbl.gov/als/curves/W16.html, 2002.

[10] ALS undulator. URL http://www.als.lbl.gov/als/curves/U10.html, 2002.

[11] LCLS x-ray FEL. URL http://www-ssrl.slac.stanford.edu/lcls/technotes/lcls-tn-98-3.pdf, 1998.

[12] S. Krinsky, M. L. Perlman, and R. E. Watson. Characteristics of synchrontron radiation and of its sources. In E.-E. Koch, editor, *Handbook of Synchrotron Radiation*, volume IA, chapter 2. North-Holland, Amsterdam, 1983.

[13] K. Halbach. Physical and optical properties of rare eath cobalt magnets. *Nuclear Instruments and Methods*, 187:109–117, 1981.

[14] G. Brown, K. Halbach, J. Harris, and H. Winick. Wiggler and undulator magnets – a review. *Nuclear Instruments and Methods*, 208:65–77, 1983.

[15] T. Beetz, M.R. Howells, C. Jacobsen, C.-C. Kao, J. Kirz, E. Lima, T.O. Mentes, H. Miao, C. Sanchez-Hanke, D. Sayre, and D. Shapiro. Apparatus for x-ray diffraction microscopy and tomography of cryo specimens. *Nuclear Instruments and Methods in Physics Research A*, 545(1-2):459–468, 2005.

[16] ALS U10 undulator. URL http://www.als.lbl.gov/als/techspecs/insertdev.html, 2007.

[17] ALS U10 undulator parameters. URL http://www.osti.gov/bridge/servlets/purl/10187030-ORLBuI/webviewable/10187030.pdf, 1994.

[18] H. Wolter. Spiegelsysteme streifenden Einfalls als abbildende Optiken für Röntgenstrahlen. *Annalen der Physik*, 10:94–114, 286, 1952.

[19] J. Kirz, C. Jacobsen, and M. Howells. Soft x-ray microscopes and their biological applications. *Quarterly Reviews of Biophysics*, 28(1):33–130, 1995.

[20] Q. Shen, I. Bazarov, and P. Thibault. Diffractive imaging of nonperiodic materials with future coherent x-ray sources. *Journal of Synchrotron Radiation*, 11:432–438, 2004.

[21] M.R. Howells, T. Beetz, H.N. Chapman, C. Cui, J.M. Holton, C.J. Jacobsen, J. Kirz, E. Lima, S. Marchesini, H. Miao, D. Sayre, D.A. Shapiro, J.C.H. Spence, and D. Starodub. An assessment of the resolution limitation due to radiation-damage in x-ray diffraction microscopy. *Journal of Electron Spectroscopy and Related Phenomena*, 170:4–12, 2009.

[22] S. Williams, X. Zhang, C. Jacobsen, J. Kirz, S. Lindaas, J. van't Hof, and S. S. Lamm. Measurements of wet metaphase chromosomes in the scanning transmission x-ray microscope. *Journal of Microscopy*, 170: 155–165, 1993.

[23] J. W. Goodman. *Introduction to Fourier Optics*. McGraw-Hill, San Francisco, 1968.

[24] B. Niemann, D. Rudolph, and G. Schmahl. X-ray microscopy with synchrotron radiation. *Applied Optics*, 15:1883–1884, 1976.

[25] G. Schmahl, D. Rudolph, B. Niemann, and O. Christ. Zone-plate x-ray microscopy. *Quarterly Reviews of Biophysics*, 13:297–315, 1980.

[26] G. Schneider. Cryo x-ray microscopy with high spatial resolution in amplitude and phase contrast. *Ultramicroscopy*, 75:85–104, 1998.

[27] D. Weiß, G. Schneider, B. Niemann, P. Guttmann, D. Rudolph, and G. Schmahl. Computed tomography of cryogenic biological specimens based on x-ray microscopic images. *Ultramicroscopy*, 84(3–4):185–197, 2000.

[28] C.A. Larabell and M.A. Le Gros. X-ray tomography generates 3-D reconstructions of the yeast, *Saccharomyces cerevisiae*, at 60-nm resolution. *Molecular Biology of the Cell*, 15:957–962, 2004.

[29] H. Rarback, J. M. Kenney, J. Kirz, M. R. Howells, P. Chang, P. J. Coane, R. Feder, P. J. Houzego, D. P. Kern, and D. Sayre. Recent results from the Stony Brook scanning microscope. In G. Schmahl and D. Rudolph, editors, *X-ray microscopy*, volume 43, pages 203–215, Berlin, 1984. Springer-Verlag.

[30] J. Maser, A. Osanna, Y. Wang, C. Jacobsen, J. Kirz, S. Spector, B. Winn, and D. Tennant. Soft x-ray microscopy with a cryo STXM: I. Instrumentation, imaging, and spectroscopy. *Journal of Microscopy*, 197(1):68–79, 2000.

[31] A. L. D. Kilcoyne, T. Tyliszczak, W. F. Steele, S. Fakra, P. Hitchcock, K. Franck, E. Anderson, B. Harteneck, E. G. Rightor, G. E. Mitchell, A. P. Hitchcock, L. Yang, T. Warwick, and H. Ade. Interferometer-controlled scanning transmission x-ray microscopes at the Advanced Light Source. *Journal of Synchrotron Radiation*, 10(2):125–136, 2003.

[32] W. Chao, B. D. Harteneck, J. A. Liddle, E. H. Anderson, and D. T. Attwood. Soft x-ray microscopy at a spatial resolution better than 15 nm. *Nature*, 435:1210–1213, 2005.

[33] W. Chao, J. Kim, S. Rekawa, P. Fischer, and E. Anderson. Demonstration of 12 nm resolution Fresnel zone plate lens based soft x-ray microscopy. *Optics Express*, 17(20):17669–17677, 2009.

[34] D. Sayre. Prospects for long-wavelength x-ray microscopy and diffraction. In M. Schlenker, editor, *Imaging Processes and Coherence in Physics*, pages 229–235. Springer-Verlag, Berlin, 1980.

[35] E. Lima. *The Advancement of Biological Imaging Through X-ray Diffraction Microscopy*. PhD thesis, Department of Physics and Astronomy, Stony Brook University, 2006.

[36] H.N. Chapman, A. Barty, S. Marchesini, A. Noy, S. P. Hau-Riege, C. Cui, M.R. Howells, R. Rosen, H. He, J.C.H. Spence, U. Weierstall, T. Beetz, C. Jacobsen, and D. Shapiro. High resolution *ab initio* three-dimensional x-ray diffraction microscopy. *Journal of the Optical Society of America A*, 23:1179–1200, 2006.

[37] F. Natterer. An error bound for the Born approximation. *Inverse Probl*, 20:447–452, 2004.

[38] G. H. Stout and L. H. Jensen. *X-Ray Structure Determination*. Wiley, New York, 1989.

[39] H. Nyquist. Certain topics in telegraph transmission theory. *Trans. AIEE*, 47:617–644, 1928.

[40] C. E. Shannon. Communication in the presence of noise. *Proc. Institute of Radio Engineers*, 37:10–21, 1949.

[41] J. Miao, D. Sayre, and H. N. Chapman. Phase retrieval from the magnitude of the Fourier transforms of non-periodic objects. *Journal of the Optical Society of America A*, 15(6):1662–1669, 1998.

[42] R. W. Gerchberg and W. O. Saxton. A practical algorithm for the determination of phase from image and diffraction plane pictures. *Optik*, 35(2):237–246, 1972.

[43] J.R. Fienup. Reconstruction of an object from the modulus of its Fourier transform. *Optics Letters*, 3(1):27–29, 1978.

[44] J. R. Fienup. Phase retrieval algorithms: a comparison. *Applied Optics*, 21(15):2758–2769, 1982.

[45] V. Elser. Phase retrieval by iterated projections. *Journal of the Optical Society of America A*, 20(1):40–55, 2003.

[46] J. P. Abrahams and A. W. G. Leslie. Methods used in the structure determination of bovine mitochondrial f_1 atpase. *Acta Cryst D*, 52:30–42, 1996.

[47] H. H. Bauschke, P. L. Combettes, and D. R. Luke. Phase retrieval, error reduction algorithm, and Fienup variants: a view from convex optimization. *Journal of the Optical Society of America A*, 19:1334–1345, 2002.

[48] H. H. Bauschke, P. L. Combettes, and D. R. Luke. Hybrid projection-reflection method for phase retrieval. *Journal of the Optical Society of America A*, 20:1025–1034, 2003.

[49] D. R. Luke. Relaxed averaged alternating reflections for diffraction imaging. *Inverse Problems*, 21:37–50, 2005.

[50] R. Lyon, D. Luke, and J. Burke. Hybrid projection-reflection method for phase retrieval. *Journal of the Optical Society of America A*, 20(1): 40–55, 2003.

[51] S. Machesini. A unified evaluation of iterative projection algorithms for phase retrieval. *Review of Scientif Instruments*, 78:011301, 2007.

[52] G. J. Williams, M. A. Pfeiffer, I. A. Vartanyants, and I. K. Robinson. Effectiveness of iterative algorithms in recovering phase in the presence of noise. *Acta. Cryst. A*, 63:36–42, 2007.

[53] W.-B. Yun. *Contributions to soft x-ray diffraction imaging and diffractive optics*. PhD thesis, Department of Physics, State University of New York at Stony Brook, aug 1987.

[54] P. Thibault, V. Elser, C. Jacobsen, D. Shapiro, and D. Sayre. Reconstruction of a yeast cell from x-ray diffraction data. *Acta Crystallographica A*, 62:248–261, 2006.

[55] D. Shapiro, P. Thibault, T. Beetz, V. Elser, M. Howells, C. Jacobsen, J. Kirz, E. Lima, H. Miao, A. M. Neiman, and D. Sayre. Biological imaging by soft x-ray diffraction microscopy. *Proceedings of the National Academy of Science*, 102(43):15343–15346, 2005.

[56] J. R. Fienup. Invariant error metrics for image reconstruction. *Applied Optics*, 36(32):8352–8357, 1997.

[57] X. Huang, H. Miao, J. Steinbrener, J. Nelson, A. Stewart, D. Shapiro, J. Turnerand, and C. Jacobsen. Signal-to-noise and radiation exposure considerations in conventional and diffraction x-ray microscopy. *Optics Express*, 17(16):13541–13553, 2009.

[58] A. Rose. A unified approach to performance of photographic film, television pickup tubes, and human eye. *Journal of the Society of Motion Picture Engineers*, 47:273–294, 1946.

[59] A. Rose and P. Weimer. Physical limits to the performance of imaging systems. *Physics Today*, Sep:24–32, 1989.

[60] R. M. Glaeser. Radiation damage and biological electron microscopy. In B. M. Siegel and D. R. Beaman, editors, *Physical aspects of electron microscopy and microbeam analysis*, pages 205–227. Wiley, New York, 1975.

[61] D. Sayre, J. Kirz, R. Feder, D. M. Kim, and E. Spiller. Transmission microscopy of unmodified biological materials: Comparative radiation dosages with electrons and ultrasoft x-ray photons. *Ultramicroscopy*, 2: 337–341, 1977.

[62] N. Bershad and A. Rockmore. On estimating signal-to-noise ratio using the sample correlation coefficient. *IEEE Transactions on Information Theory*, 20:112–113, 1974.

[63] J. Frank and L. Al-Ali. Signal-to-noise ratio of electron micrographs obtained by cross correlation. *Nature*, 256:376–379, 1975.

[64] R. A. London, M. D. Rosen, and J. E. Trebes. Wavelength choice for soft x-ray laser holography of biological samples. *Applied Optics*, 28: 3397–3404, 1989.

[65] J. M. Cowley and A. F. Moodie. Fourier images. I. The point source. *Proceedings of the Physical Society B*, 70(5):486–496, 1957.

[66] G. Schneider, E. Anderson, S. Vogt, C. Knöchel, D. Weiss, M. Legros, and C. Larabell. Computed tomography of cryogenic cells. *Surface Review and Letters*, 9(1):177–183, 2002.

[67] A. Tkachuk, F. Duewer, H. Cui, M. Feser, S. Wang, and W. Yun. X-ray computed tomography in Zernike phase contrast mode at 8 keV with 50-nm resolution using Cu rotating anode x-ray source. *Zeitschrift Kristallographie*, 222:650–655, 2007.

[68] J. Kirz. Phase zone plates for X rays and the extreme UV. *Journal of the Optical Society of America*, 64:301–309, 1974.

[69] P. Thibault, M. Dierolf, A. Menzel, O. Bunk, C. David, and F. Pfeiffer. High-resolution scanning x-ray diffraction microscopy. *Science*, 321:379–382, 2008.

[70] G. J. Williams, H. M. Quiney, A. G. Peele, and K. A. Nugent. Coherent diffractive imaging and partial coherence. *Physical Review B*, 75(10): 104102, 2007.

[71] S. Marchesini, H. He, H.N. Chapman, S.P. Hau-Riege, A. Noy, M.R. Howells, U. Weierstall, and J.C.H. Spence. X-ray image reconstruction from a diffraction pattern alone. *Physical Review B*, 68(14):140101, 2003.

[72] D. Sayre, J. Kirk, R. Feder, D. M. Kim, and E. Spiller. Potential operating region for ultrasoft x-ray microscopy of biological materials. *Science*, 196:1339–1340, 1977.

[73] R. Grimm, M. Bärmann, W. Häckl, D. Typke, E. Sackman, and W. Baumeister. Energy filtered electron tomography of ice-embedded actin and vesicles. *Biophysical Journal*, 72:482–489, 1997.

[74] C. Jacobsen, R. Medenwaldt, and S. Williams. A perspective on biological x-ray and electron microscopy. In J. Thieme, E. Umbach G. Schmahl, and D. Rudolph, editors, *X-ray Microscopy and Spectromicroscopy*, pages II–93–102, Berlin, 1998. Springer-Verlag.

[75] P. Kirkpatrick. The x-ray microscope. *Scientific American*, 180:44–47, 1949.

[76] A. V. Baez. A study in diffraction microsopy with special reference to x-rays. *Journal of the Optical Society of America*, 42:756–762, 1952.

[77] J. Miao, K.O. Hodgson, T. Ishikawa, C. A. Larabell, M. A. LeGros, and Y. Nishino. Imaging whole *escherichia coli* bacteria by using single-particle x-ray diffraction. *Proceedings of the National Academy of Sciences*, 100:110–112, 2003.

[78] G.J. Williams, E. Hanssen, A.G. Peele, M.A. Pfeiffer, J. Clark, B. Abbey, G. Cadenazzi, M.D. de Jonge, S. Vogt, L. Tilley, and K.A. Nugent. High-resolution x-ray imaging of *Plasmodium falciparum*-infected red blood cells. *Cytometry Part A*, 73A(10):949–957, 2008.

[79] C. Song, H. Jiang, A. Mancuso, B. Amirbekian, L. Peng, R. Sun, S. Shah, Z. H. Zhou, T. Ishikawa, and J. Miao. Quantitative imaging of single, unstained viruses with coherent x rays. *Physical Review Letters*, 101(15): 158101, 2008.

[80] Y. Nishino, Y. Takahashi, N. Imamoto, T. Ishikawa, and K. Maeshima. Three-dimensional visualization of a human chromosome using coherent x-ray diffraction. *Physical Review Letters*, 102(1):018101, 2009.

[81] J. Miao, P. Charalambous, J. Kirz, and D. Sayre. An extension of the methods of x-ray crystallography to allow imaging of micron-size non-crystalline specimens. *Nature*, 400:342–344, 1999.

[82] M. Tyers, G. Tokiwa, and B. Futcher. Comparison of the *Saccharomyces cerevisiae* G1 cyclins: Cln3 may be an upstream activator of Cln1, Cln2, and other cyclins. *European Molecular Biology Organization Journal*, 12:1955–1968, 1993.

[83] D. Shapiro. *Biological imaging by soft x-ray diffraction microscopy*. PhD thesis, Department of Physics and Astronomy, Stony Brook University, 2004.

[84] M.R. Howells, P. Charalambous, H. He, S. Marchesini, and J.C.H. Spence. An off-axis zone-plate monochromator for high-power undulator radiation. In D.C. Mancini, editor, *Design and Microfabrication of Novel X-ray Optics*, volume 4783, pages 65–73, Bellinghan, WA, 2002. SPIE.

[85] B. Niemann, D. Rudolph, and G. Schmahl. Soft x-ray imaging zone plates with large zone numbers for microscopic and spectroscopic applications. *Optics Communications*, 12:160–163, 1974.

[86] J. Thieme. Theoretical investigations of imaging properties of zone plates and zone plate systems using diffraction theory. In D. Sayre, M.R. Howells, J. Kirz, and H. Rarback, editors, *X-ray Microscopy II, volume 56 of Springer Series in Optical Sciences*, pages 70–79. Springer-Verlag, Berlin, 1980.

[87] H. Miao. *Studies on X-ray Diffraction Microscopy*. PhD thesis, Department of Physics and Astronomy, Stony Brook University, 2008.

[88] Princeton instruments PI-MTE 2048B CCD. URL http://www.princetoninstruments.com/Uploads/Princeton/Documents/

Datasheets/Princeton_Instruments_PI-MTE2048B_M1_6.09.pdf, 2009.

[89] T. Beetz. *Soft x-ray diffraction imaging with and without lenses and radiation damage studies*. PhD thesis, Department of Physics and Astronomy, Stony Brook University, 2004.

[90] J. R. Fienup and C. C. Wacherman. Phase-retrieval stagnation problems and solutions. *Journal of the Optical Society of America*, 3(11):1897–1907, 1986.

[91] E. O'Toole, G. Wray, J. Kremer, and J. R. McIntosh. High voltage cryomicroscopy of human blood platelets. *Journal of Structural Biology*, 110:55–66, 1993.

[92] E. Kellenberger. The response of biological macromolecules and supramolecular structures to the physics of specimen cryopreparation. In Steinbrecht and Zierold [97], pages 35–63.

[93] K. Taylor and R. Glaeser. Electron diffraction of frozen, hydrated protein crystals. *Science*, 106:1036–1037, 1974.

[94] K.A. Taylor and R.M. Glaeser. Electron microscopy of frozen hydrated biological specimens. *Journal of Ultrastructure Research*, 55:448–456, 1976.

[95] R. M. Glaeser and K. A. Taylor. Radiation damage relative to transmission electron microscopy of biological specimens at low temperature: a review. *Journal of Microscopy*, 112:127–138, 1978.

[96] M. Stewart and G. Vigers. Electron microscopy of frozen-hydrated biological material. *Nature*, 319:631–636, 1986.

[97] R. A. Steinbrecht and K. Zierold, editors. *Cryotechniques in Biological Electron Microscopy*, Berlin, 1987. Springer-Verlag.

[98] O. Medalia, I. Weber, A. Frangakis, D. Nicastro, G. Gerisch, and W. Baumeister. Macromolecular architecture in eukariotic cells visualized by cryoelectron tomography. *Science*, 298(8):1209–1213, 2002.

[99] V. Lučić, A.H. Kossel, T. Yang, T. Bonhoeffer, W. Baumeister, and A. Sartori. Multiscale imaging of neurons grown in culture: from light microscopy to cryo-electron tomography. *Journal of Structural Biology*, 160:146–156, 2007.

[100] T. Beetz and C. Jacobsen. Soft x-ray radiation-damage studies in PMMA using a cryo-STXM. *Journal of Synchrotron Radiation*, 10(3):280–283, 2003.

[101] F. Franks. The properties of aqueous solutions at subzero temperatures. In F. Franks, editor, *Water: a comprehensive treatise*, volume 7, pages 215–338, New York, London, 1982. Plenum.

[102] J. Dubochet, M. Adrian, J. J. Chang, J. Lepault, and A. W. McDowall. Cryoelectron microscopy of vitrified specimens. In Steinbrecht and Zierold [97], pages 114–131.

[103] H. Moor. Theory and practice of high pressure freezing. In Steinbrecht and Zierold [97], pages 175–191.

[104] Cellometer: Disposable hemacytometer from nexcelom. URL http://www.nexcelom.com/Products/DisHemacytometer.html, 2009.

[105] H. Site, L. Edelmann, and K. Neumann. Cryofixation without pretreatment at ambient pressure. In Steinbrecht and Zierold [97], pages 87–113.

[106] M.J. Costello and J.M. Corless. The direct meansurement of temperature changes within freeze-fracture specimens during quenchin in liquid coolants. *Journal of Microscopy*, 112:17–37, 1978.

[107] K.P. Ryan, D.H. Purse, S.G. Robinson, and J.W. Wood. The relative efficiency of cryogens used for plunge-cooling biological specimens. *Journal of Microscopy*, 145:89–96, 1987.

[108] J. Dubochet and A.W. McDowall. Vitrification of pure liquid water for electron microscopy. *Journal of Microscopy*, 124:RP3–RP4, 1981.

[109] J. Dubochet and J. Lepault. Cryo-electron microscopy of vitrified water. *Journal of Physics*, C7:85–94, 1984.

[110] X. Huang, J. Nelson, J. Kirz, E. Lima, S. Marchesini, H. Miao, A. Neiman, D. Shapiro, J. Steinbrener, A. Stewart, J. Turner, and C. Jacobsen. Soft x-ray diffraction microscopy of a frozen hydrated yeast cell. *Physical Review Letters*, 103(19):198101, 2009.

[111] Princeton instruments PI-MTE 1300B CCD. URL http://www.princetoninstruments.com/Uploads/Princeton/Documents/Datasheets/Princeton_Instruments_PI-MTE1300B_M1_6.09.pdf, 2009.

[112] J.C.H. Spence, U. Weierstall, and M. Howells. Phase recovery and lensless imaging by iterative methods in optical, x-ray and electron diffraction. *Philosophical Transactions of the Royal Society of London A*, 360: 875–895, 2002.

[113] H. Miao, K. Downing, X. Huang, J. Kirz, S. Marchesini, J. Nelson, D. Shapiro, J. Steinbrener, A. Stewart, and C. Jacobsen. Cryo diffraction microscopy: ice conditions and finite supports. *Journal of Physics: Conference Series*, 186:012055, 2009.

[114] A. Cheng, D. Fellmann, J. Pulokas, C.S. Potter, and B. Carragher. Does contamination buildup limit throughput for automated cryoEM? *Journal of Structural Biology*, 154(3):303–311, 2006.

[115] Micos piezo positioner PP-30. URL http://www.micos.ws/web2/en/1,4,830,pp30.html, 2009.

[116] R.F. Barron. *Cryogenic Heat Transfer*. Taylor & Francis, Philadelphia, 1999.

[117] Lakeshore DT-400 series silicon diodes temperature sensor. URL http://www.lakeshore.com/temp/sen/sd400_ts.html, 2009.

[118] Lakeshore model 218 temperature monitor. URL http://www.lakeshore.com/temp/mn/218po.html, 2009.

[119] R. Hegerl and W. Hoppe. Influence of electron noise on three-dimensional image reconstruction. *Zeitschrift für Naturforschung*, 31 a:1717–1721, 1976.

[120] B. F. McEwen, K. H. Downing, and R. M. Glaeser. The relevance of dose-fractionation in tomography of radiation-sensitive specimens. *Ultramicroscopy*, 60:357–373, 1995.

[121] Y.M. Bruck and L.G. Sodin. On the ambiguity of the image reconstruction problem. *Optics Communication*, 30:304–308, 1979.

[122] M.H. Hayes. The reconstruction of a multidimensional sequence from the phase or magnitude of its Fourier transform. *IEEE Transactions on Acoustics, Speech, Signal Process*, ASSP-30:140–154, 1982.

[123] R. H. T. Bates. Fourier phase problems are uniquely solvable in more than one dimension. I. Underlying theory. *Optik*, 61:247–262, 1982.

[124] J.M. Rodenburg, A.C. Hurst, A.G. Cullis, B.R. Dobson, F. Pfeiffer, O. Bunk, C. David, K. Jefimovs, and I. Johnson. Hard-x-ray lensless imaging of extended objects. *Physical Review Letters*, 98:034801, 2007.

[125] H.M.L. Faulkner and J.M. Rodenburg. Movable aperture lensless transmission microscopy: a novel phase retrieval algorithm. *Physical Review Letters*, 93:023903, 2004.

[126] J.M. Rodenburg and H.M.L. Faulkner. A phase retrieval algorithm for shifting illumination. *Applied Physics Letters*, 80:4795, 2004.

[127] H.M.L. Faulkner and J.M. Rodenburg. Error tolerance of an iterative phase retrieval algorithm for moveable illumination microscopy. *Ultramicroscopy*, 103:153–164, 2005.

[128] J.M. Rodenburg, A.C. Hurst, and A.G. Cullis. Transmission microscopy without lenses for objects of unlimited size. *Ultramicroscopy*, 107:227–231, 2007.

[129] O. Bunk, M. Dierolf, S. Kynde, I. Johnson, O. Marti, and F. Pfeiffer. Influence of the overlap parameter on the convergence of the ptychographical iterative engine. *Ultramicroscopy*, 108:481–487, 2008.

[130] P. Thibault, M. Dierolf, O. Bunk, A. Menzel, and F. Pfeiffer. Probe retrieval in ptychographic coherent diffractive imaging. *Ultramicroscopy*, 109:338–343, 2009.

[131] B. Abbey, K.A. Nugent, G.J. Williams, J.N. Clark, A.G. Peele, M.A. Pfeiffer, M. de Jonge, and I. McNulty. Keyhole coherent diffractive imaging. *Nature Physics*, 4(5):394–398, 2008.

[132] B. A. Abbey, K. A. Nugent, G. J. Williams, J. N. Clark, A. G. Peele, M. A. Pfeiffer, M. de Jonge, and I. McNulty. Quantitative coherent diffractive imaging of an integrated circuit at a spatial resolution of 20 nm. *Applied Physics Letters*, 93(21), 2008.

[133] H.M. Quiney, A.G. Peele, Z. Cai, D. Paterson, and K.A. Nugent. Diffractive imaging of highly focused x-ray fields. *Nature Physics*, 2:101–104, 2006.

[134] Layout editor software. URL http://www.layouteditor.net/, 2009.

[135] Y.A. Cengel. *Heat transfer: A Practical Approach*. McGraw-Hilll, New York, 2003.